Luminescent Solar Concentrators:

A Study of Optical Properties,

Re-absorption

and

Device Optimisation

Lindsay Robert Wilson, B.Sc.

Submitted for the degree of

Doctor of Philosophy (Ph.D.)

on completion of research conducted at the

Department of Mechanical Engineering
School of Engineering & Physical Sciences
Heriot-Watt University
Edinburgh EH14 4AS
United Kingdom

May 2010

Abstract

This thesis presents the results of work on the optical properties and design optimisation of the luminescent solar concentrator (LSC).

The optical properties of a range of fluorophores were measured and it was found that the Lumogen F Rot 305 organic dye exhibited properties which make it ideal for use in LSCs, namely a wide absorption range (300-650 nm), 100 % quantum yield at concentrations up to 1700 ppm, and the highest photostability of all the Lumogen F dyes, although the overlap of the absorption and emission spectra results in re-absorption (RA) losses.

Despite these optimum properties, a detailed analysis showed that LSCs based on Rot 305 cannot compete with conventional glass/glass laminate modules on grounds of either cost or embodied energy. Since Rot 305 represents an optimum dye, this suggests it is unlikely that LSCs based on organic dyes will ever be competitive with conventional technologies. The only solution is the use of a fluorophore with greatly reduced RA losses, for example a rare-earth (RE) complex. The RA losses of a europium-containing complex were found to be less than those of the Rot 305 dye, despite the lower quantum yield of the complex (86 %).

The solar-to-electric conversion efficiencies of several LSC modules based on Rot 305 were measured. Modules with dimensions of 10 cm x 10 cm and 60 cm x 60 cm had efficiencies of 2.7 % and 1.84 % respectively, both measured without a back reflector. In addition, the technique of current-matching the edge cells was successfully demonstrated, resulting in a 15 % increase in power output from an edge using matched cells relative to an edge using unmatched cells.

Acknowledgements

Firstly, my greatest love and thanks to my parents, whose continuous help and support has sustained me throughout this project and allowed me to bring it to a successful conclusion.

My sincere thanks to my supervisors Bryce Richards and Andrew Moore for their assistance throughout and also to Darren Bagnall & John Wilson, who were my external and internal examiners.

My thanks also to Brenda Rowan - your help and friendship have been invaluable!

I am extremely grateful to the people at the Department of Chemistry, University of Edinburgh, both for their endless help on photochemistry questions and also for access to equipment. My special thanks to Anita Jones, Neil Robertson and Patricia Richardson. You made me realise how little I knew of photochemistry!

I would like to acknowledge the invaluable help and services provided by several companies -

BASF. My thanks to Axel Grimm and Matthias Klueglein for supplying the Lumogen F and NIR dyes which were a central component of this project. My thanks also for supplying the initial PMMA samples which allowed me to start experiments.

Lucite. Huge thanks to Ian Fraser, Neil Kirtley, Lesley Minto and John Lynch for PMMA sheet casting, technical advice, and supply of raw materials. Thanks to your support, what originally seemed a black art became a quick and painless process! Your speed and quality of service will always be remembered. Thanks also to Garry Phillipson for performing accelerated weathering.

NaREC. My great thanks to Tim Bruton, Alex Cole, Ian Baistow and Keith Heasman for the design and supply of the solar cells used in the project, and also for access to the solar simulators for testing the LSC performance.

Horiba Jobin-Yvon. Simon Fitzgerald, Gerard Freeman, Ramji Senghani - a huge thank you for your help in choosing and using the integrating sphere, which forms a major part of this thesis. Thanks also to Andrew Beeby and Lars-Olof Pålsson of the Department of Chemistry, Durham University for your advice and use of your

Flurolog!

Edinburgh Instruments. Thanks to Nick Leeson, Roger Fenske and Robbie Thomas for both access to the F900 equipment and help in customising our own machine. Congratulations on making a great machine!

I am grateful for the DTA-funded scholarship provided by the Department of Mechanical Engineering, Heriot-Watt University.

Many people have made my experience easier and enjoyable - thank you Dalila, Gavin, Dave, Laura, Pas, Nabin, Alban, Ricardo, Panos, Gudrun, and many others, for your friendship and conversation. I am grateful to all the technicians for their support; Richard, Ian, Curtis, John, Chris, Kenny, Mark - thank you for your help in making the hardware of my project, and for many interesting discussions on model engineering! I am extremely grateful to superintedent George Smith for allowing me access to the workshop machines - this speeded things up hugely.

If I have, by accident, omitted any person here - you know who you are, and you have my thanks!

Finally, I reserve my warmest thanks for my colleague and fellow PhD student, Thimios. $Ευχαριστω$, my friend, for our many conversations and your help!

ACADEMIC REGISTRY
Research Thesis Submission

Name*:*	Lindsay Robert Wilson		
School/PGI:	School of Engineering and Physical Sciences, Dept. of Mechanical Engineering		
Version: *(i.e. First, Resubmission, Final)*	Final	Degree Sought (Award **and** Subject area)	PhD Mechanical Engineering

Declaration

In accordance with the appropriate regulations I hereby submit my thesis and I declare that:

1) the thesis embodies the results of my own work and has been composed by myself
2) where appropriate, I have made acknowledgement of the work of others and have made reference to work carried out in collaboration with other persons
3) the thesis is the correct version of the thesis for submission and is the same version as any electronic versions submitted*.
4) my thesis for the award referred to, deposited in the Heriot-Watt University Library, should be made available for loan or photocopying and be available via the Institutional Repository, subject to such conditions as the Librarian may require
5) I understand that as a student of the University I am required to abide by the Regulations of the University and to conform to its discipline.

* *Please note that it is the responsibility of the candidate to ensure that the correct version of the thesis is submitted.*

Signature of Candidate*:*		Date:	

Submission

Submitted By *(name in capitals):*	LINDSAY ROBERT WILSON
Signature of Individual Submitting:	
Date Submitted:	

For Completion in Academic Registry

Received in the Academic Registry by *(name in capitals):*			
Method of Submission *(Handed in to Academic Registry; posted through internal/external mail):*			
*E-thesis Submitted (**mandatory for final theses from January 2009)***			
Signature:		Date:	

Please note this form should bound into the submitted thesis.

Updated February 2008, November 2008, February 2009

Contents

Publications resulting from this thesis (to date)

Journal

L.R. Wilson, B.C. Rowan, N. Robertson, O. Moudam, A.C. Jones, and B.S. Richards. Characterization and reduction of reabsorption losses in luminescent solar concentrators. *Appl. Opt.*, 49(9):1651-1661, 2010.

L.R. Wilson and B.S. Richards. Measurement method for photoluminescent quantum yields of fluorescent organic dyes in polymethyl methacrylate for luminescent solar concentrators. *Appl. Opt.*, 48(2):212-220, 2009.

B.C. Rowan, L.R. Wilson, and B.S. Richards. Advanced material concepts for luminescent solar concentrators. *IEEE J. Selected Topics in Quantum Electronics*, 14(5):1312-1322, 2008.

Conference

B.C. Rowan, L.R. Wilson, and B.S. Richards. Visible and near-infrared emitting Lanthanide complexes for luminescent solar concentrators. In *Proceedings of the 23rd European Photovoltaic Solar Energy Conference and Exhibition*, Hamburg, Germany, pages 346–349, 2009.

L.R. Wilson and B.S. Richards. High-efficiency dyes for luminescent solar concentrators - photostability, modelling and results. In *Proceedings of the 22nd European Photovoltaic Solar Energy Conference and Exhibition*, Valencia, Spain, pages 510-512, 2008.

E. Klampaftis, B.S. Richards, L.R. Wilson, K.R. McIntosh, A. Cole, and K. Heasman. Improving spectral response of mc-Si cells via luminescent down-shifting of the incident spectrum. In *Proceedings of PVSAT-4*, Bath, UK, pages 59-62, 2008.

L.R. Wilson, B.S. Richards, A.C. Jones, P.R. Richardson, A. Cole, I. Fraser, N. Kirtley, L. Minto. Quantum yield measurements of high-efficiency dyes for luminescent solar concentrators. In *Proceedings of PVSAT-4*, Bath, UK, pages 101-104, 2008.

Chapter 1

Introduction

Solar energy can provide a clean, reliable, renewable source of electric power. However, the present increasing cost of silicon requires that we find a more efficient means of utilising available silicon resources. We will see how this might be achieved through the use of the luminescent solar concentrator (LSC). The LSC can also aid with another problem of conventional PV, that of building integration, as it is possible to combine an LSC with components such as windows, doors or façades to result in a more appealing structure.

1.1 The case for solar power

As the environmental impact of mankind's increasing fossil fuel usage becomes ever more apparent, the search for alternative sources of energy has developed greater urgency.

The amount of power available from sunlight is significant - the maximum possible insolation is around $1000\,\mathrm{W/m^2}$, measured at noon on a cloudless midsummer's day at the equator[1]. This decreases at higher latitudes, dropping to around half at 60° latitude[1]. The goal of converting this power directly to electricity using photovoltaic cells has occupied researchers for the past half century, with silicon-based cells dominating the field.

Until recently, the cost of polysilicon, the starting material for solar cell produc-

tion, has shown a steady increase, and this has motivated researchers to attempt to economise on the amount used per peak watt of power production. Fig. 1.1 shows both historical and forecast prices for polysilicon. Historical data (1995-2008) from Hemlock Semiconductor Group, a major polysilicon manufacturer, do indeed show a rapid increase in the polysilicon price, more than doubling in only a few years. However, a recent study by the market research group iSuppli has suggested the possibility of sharp *decrease* of the price in the near future[2]. The study concluded that the price would decrease as a result of major new production capacity coming on-line, primarly in the Far East. Indeed, a company in Taiwan is claimed to currently produce polysilicon for as little as \$50-\$100/kg[2]. The predicted future polysilicon price is shown by the dashed line in Fig. 1.1. It may be that, in several years' time, the price will have dropped sufficiently to render the need for economising on silicon use redundant. However, this remains to be seen.

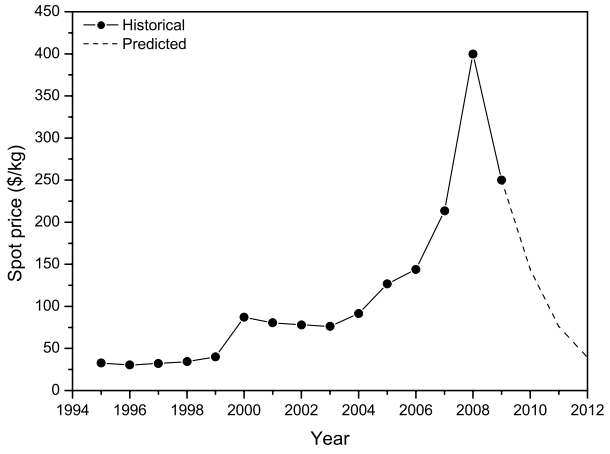

Figure 1.1: Spot price of polysilicon, showing historical[3] and predicted[2] data.

A possible solution to the challenge of minimising the amount of silicon required is to use a concentrating system[4] to collect sunlight over a large area and direct it on to a small area of solar cells. This reduces the amount of silicon used, while still producing the same power output. Efficiencies can actually be higher, because of the increased illumination intensity that the cell experiences[5, 6]. So-called "imaging" concentrators use lenses, mirrors or a combination of both to focus sunlight on to the cells. While capable of achieving extremely high concentrations (several hundred

suns), these require precise tracking to follow the sun across the sky and keep the cells illuminated. Also, these are unable to make use of diffuse solar radiation.

An alternative is to use a "non-imaging" concentrator. There are several different ways of achieving this[6, 7]. We explore here one of these options - that of the luminescent solar concentrator (LSC) - a device originally proposed more than thirty years ago[6] which uses a sheet of luminescent material to trap both direct and diffuse solar radiation and transfer this energy to smaller areas of silicon cells mounted on the edges to generate electricity.

1.2 The LSC - past, present and future

A schematic of a luminescent solar concentrator (LSC) is shown in Fig. 1.2. It consists of a sheet of transparent material which has been doped with a fluorophore capable of absorbing incident solar radiation and emitting fluorescence photons. Solar cells are attached to the edges of the sheet to convert the trapped fluorescence emission into electricity.

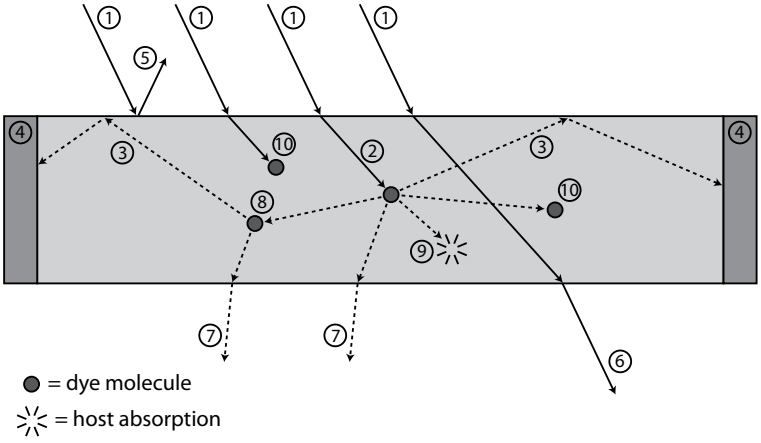

Figure 1.2: Cross-section of a luminescent solar concentrator, showing incident sunlight (①), absorption by a fluorophore molecule (②), trapped emission (③) and edge-mounted solar cells (④). Loss mechanisms shown are - surface reflection (⑤), unabsorbed solar radiation (⑥), escape-cone losses (⑦), re-absorption (⑧), host absorption (⑨) and non-radiative decay (⑩).

Sunlight (①) incident on the front surface of the sheet can be transmitted into the sheet and absorbed by a fluorophore molecule (②), such as an organic dye. Fluorescence is then emitted by the fluorophore (subject to quantum yield, which determines

the probability of emission) and is transported to the edge via total internal reflection (③) if the emission angle is greater than the critical angle. The fluorescence is collected by the solar cells (④).

Several loss mechanisms are present which reduce the amount of fluorescence reaching the solar cells. A small fraction (∼4 %) of incident sunlight is reflected from the front surface of the sheet (⑤) because of Fresnel reflection. If the fluorophore has a limited absorption range, some sunlight can pass through the sheet unabsorbed (⑥). Fluorescence emission is only trapped inside the sheet if the angle of incidence with the surface is greater than the critical angle. If it is less, the light leaves the sheet in what is termed the escape cone and is lost (⑦).

Fluorescence emission can also be re-absorbed by other fluorophore molecules if their absorption spectrum overlaps the emission (⑧). This can again result in fluorescence being emitted and transported to the edge (③) or leaving the sheet via the escape cone (⑦). Re-absorption results in a loss because fluorescence which was originally trapped within the sheet may be directed out of the sheet and lost. Fluorescence can also be absorbed by the host material and lost (⑨). Finally, if the fluorophore has a non-unity quantum yield, emission may not occur and the absorbed photon is lost (⑩).

The LSC was first proposed in the late 1970s as a means of concentrating solar radiation[8, 6, 9, 10], although the concept of trapping fluorescence inside a transparent body by total internal reflection (TIR) was known as early as 1949[11]. Extensive studies were made of LSC technology through the 1980s until the limitations of the fluorescent dyes available at that time hindered further development[12, 13, 14, 15, 16]. Wittwer *et. al.*[17] achieved a record solar-to-electric efficiency of η_{LSC}=4.0 % for a large-area (40 cm x 40 cm x 0.3 cm) two-sheet system consisting of a short-wavelength emitting plate coupled to gallium arsenide (GaAs) solar cells placed above a long-wavelength emitting plate coupled to silicon (Si) solar cells with an air gap between the plates. Friedman[18] used a mixed-dye thin-film module (14 cm x 14 cm x 0.3 cm) to achieve η_{LSC}=3.2 % with Si cells and η_{LSC}=4.5 % with GaAs cells, the higher efficiency with GaAs being a result of the higher open-circuit voltage. More recently, Slooff *et. al.*[19] obtained η_{LSC}=7.1 % with GaAs cells and Goldschmidt *et. al.*[20]

obtained η_{LSC}=6.7 % with gallium indium phosphide (GaInP) cells. However, both of these high efficiencies are mainly a result of the small module sizes (5 cm x 5 cm x 0.5 cm and 2 cm x 2 cm x 0.6 cm, respectively) and the use of a diffuse reflector placed behind the module. These record efficiencies are summarised in Table 1.1.

Table 1.1: LSC record efficiencies

Year	Author	Sheet size (cm)	η_{LSC} (%)	Cells	Comments
1984	Wittwer *et. al.*[17]	40 x 40 x 0.3	4.0	Si/GaAs	Two separate sheets
1980	Friedman[18]	14 x 14 x 0.3	3.2 4.5	Si GaAs	Mixed-dye thin-film
2008	Slooff *et. al.*[19]	5 x 5 x 0.5	7.1	GaAs	Mixed-dye
2009	Goldschmidt *et. al.*[20]	2 x 2 x 0.6	6.7	GaInP	Two bonded sheets

It has been estimated that LSC devices could produce electricity at around 30-50 % of the cost of conventional PV[21], although this analysis does not account for module framing or front/rear covers which are required to protect the surfaces of the LSC sheet from damage. Despite the possibility of reduced cost (in terms of $/W), a greater area of LSCs is required to produce the same power as conventional silicon PV because of their lower efficiency, currently only 20-30 % of regular PV, and the decision on their use depends on whether the user is limited in terms of cost or of coverage area[21]. Another consideration is photostability, since both the flurophores and host material can suffer photodegradation under exposure to solar radiation. For LSCs to be competitive they must exhibit outdoor lifetimes comparable to that of conventional PV (>20 yr).

The advent of novel luminescent materials such as quantum dots[22], rare-earth materials[23] and semiconducting polymers[24] has renewed interest in LSC development. Techniques to reduce the losses within the devices by using, for example, liquid crystals[25] or photonic layers[26] are under investigation. The maximum efficiency of an LSC was estimated by Friedman[18] to be η_{LSC}=8-10 %, assuming that all sunlight in the range 300-900 nm was absorbed. However, these efficiencies were not reached because of limitations outlined in subsequent sections.

1.3 Losses in LSC devices

Several different loss mechanisms were mentioned above in the description of LSC operation. The reduction or elimination of these losses is one of the major challenges in LSC development. In this section we look at each loss mechanism in detail and discuss their relative magnitudes. In later sections, a range of different options for each component of the LSC is reviewed (for example, choice of fluorophore, choice of sheet material) and their impact on these loss mechanisms discussed.

The overall optical efficiency of an LSC, η_{opt}, defined as the fraction of incident solar power which reaches the edges, can be expressed as the product of the efficiencies of the different processes present inside the LSC as shown in Eqn. (1.1), originally proposed by Goetzberger *et. al.*[27]. The values he obtained for the process efficiencies are listed in Table 1.2 for a square LSC sheet of dimensions 40 cm x 40 cm x 0.3 cm containing a single organic dye. Note that Eqn. (1.1) is only approximate, since each of the different efficiencies is interdependent[27].

$$\eta_{opt} = (1 - R)\, P_{TIR}\, \eta_{abs}\, \eta_{PLQY}\, \eta_{Stokes}\, \eta_{host}\, \eta_{TIR}\, \eta_{self} \tag{1.1}$$

Table 1.2: Experimental process efficiencies for a 40 cm x 40 cm x 0.3 cm LSC (Goetzberger *et. al.*[27])

Quantity	Value
$1 - R$	0.96
P_{TIR}	0.75
η_{abs}	0.2 - 0.3
η_{PLQY}	0.95 - 1.0
η_{Stokes}	0.75
$\eta_{host} + \eta_{TIR}$	0.9 - 0.95
η_{self}	0.75
η_{opt}	**0.07 - 0.12**

The significance and magnitude of the contribution of each efficiency term to the total are discussed in detail below.

Fraction of incident light transmitted into sheet $(1 - R)$. There is a small loss of incident light due to Fresnel reflection from the front surface of the LSC sheet. The

reflectivity is given by the usual expression $R = (n-1)^2/(n+1)^2$, and is around 4 % for a refractive index of $n = 1.5$. Reflection from the rear surface of the sheet is less important, as most of the useful range of incident wavelengths has been absorbed by the time the light reaches the rear surface.

Probability of total internal reflection (P_{TIR}). Fluorescence is only trapped inside the LSC when the the light strikes the internal surface of the sheet at an angle greater than the critical angle. The critical angle, θ_C, can be calculated from Eqn. (1.2), where n is the refractive index of the host material.

$$\theta_C = \sin^{-1}\left(\frac{1}{n}\right) \tag{1.2}$$

The probability that fluorescence emission is trapped inside the sheet, P_{TIR}, is given by Eqn. (1.3).

$$P_{TIR} = \frac{\sqrt{n^2-1}}{n} \tag{1.3}$$

For a sheet of refractive index of $n = 1.5$, there is a ∼25 % probability that a fluorescence photon will be emitted within either the front or the rear escape cone and will be lost from the sheet[6]. This problem is increased with the presence of re-absorption, as each photon emitted from subsequent re-absorption events also has a ∼25 % probability of being lost in one of the escape cones. Although difficult to reduce, as it depends on the refractive index of the sheet which is nearly always in the range 1.3-1.5, attempts have been made which have resulted in an increase in efficiency[25, 28, 29, 20, 26, 30, 31, 32, 33]. These are discussed later.

Absorption efficiency (η_{abs}). An LSC sheet will, by design, absorb a narrower range of wavelengths than will, for example, a Si solar cell. To maximise the power output, the LSC sheet has to absorb the greatest possible range of incident solar wavelengths with corresponding photon energies greater than the bandgap of the solar cells at the edges of the sheet. A sheet which can absorb all incident wavelengths below 550 nm, for example, has $\eta_{abs} = 0.26$, since 26 % of the AM1.5g solar spectrum lies below this wavelength[27]. For optimum performance with Si cells, the sheet should ideally

absorb all wavelengths <950 nm and emit in the 950-1000 nm range which corresponds to the maximum spectral response of the cell[34]. If it becomes possible to absorb all wavelengths <950 nm, η_{abs} increases to 0.71.

Quantum yield (η_{PLQY}). The photoluminescent quantum yield (PLQY) (also called quantum yield (QY), luminescent quantum efficiency (LQE) or fluorescence quantum yield (FQY)) determines the probability that an excited fluorophore molecule will decay by the emission of a fluorescence photon (as opposed to, for example, dissipating the energy in thermal vibrations), as shown in Eqn. (1.4).

$$\eta_{PLQY} = \frac{\text{No. emitted photons}}{\text{No. excited molecules}} \times 100\,\% \tag{1.4}$$

A high (near-unity, 95-100 %) quantum yield is essential for good LSC performance, especially for fluorophores which have a large spectral overlap and large re-absorption losses. Since the same quantum yield applies to all re-absorption events, the effects of a non-unity quantum yield are magnified by multiple re-absorptions. For example, if a fluorophore has 95 % quantum yield, the probability of a photon being emitted after, for example, five re-absorption events is only $0.95^5 = 0.77 \equiv 77\,\%$.

"Stokes efficiency" (η_{Stokes}). In the fluorescence process, the emitted photon always has a longer wavelength (lower energy) than the absorbed photon. As a result, there is a net *energy* loss during fluorescence, even if the fluorophore has 100 % PLQY. The fraction of energy remaining after the fluorescence process is denoted by η_{Stokes} (alternatively, the fraction of energy *lost* during fluorescence is $1-\eta_{Stokes}$). Since this is an inherent feature of the wavelength-shifting process which occurs in an LSC, it is always present and η_{Stokes} will remain $\sim$0.75.

"Host efficiency" (η_{host}). As shown in Fig. 1.2, one possible loss mechanism is absorption of trapped fluorescence by the host material. η_{host} represents the fraction of fluorescence transmitted by the host (the fraction absorbed or scattered is $1-\eta_{host}$). While of little importance at visible wavelengths, where most polymers and glasses are highly transparent[35], care must be taken when operating at near-infrared (NIR) wavelengths above 700 nm, as many polymers exhibit strong absorption in this region from harmonics of CH and CO bond stretches[36]. For a PMMA host with fluorescence

in the visible region, η_{host} is typically 0.95-0.98. The effect of different materials on the host absorption losses is discussed later (Section 1.5.1).

Efficiency of total internal reflection (η_{TIR}). Theoretically, total internal reflection should be 100 % efficient. However, the presence of foreign particles such as dust or moisture droplets on the surface of the sheet can cause light to be scattered out of the sheet. Physical damage to the sheet surface, such as scratching, will obviously result in the loss of trapped light, although the magnitude of this effect does not appear to have been studied. In addition, the surface may posess a microstructure, depending on the method of manufacture, which will also lead to a loss. Thomas *et. al.*[37], studying carefully-cleaned PMMA surfaces, measured fractional losses as low as 0.0002 per reflection, corresponding to $\eta_{TIR} = 0.9998$. He also observed surface microstructure in the 0.1-1 μm size range. It was concluded that this formed during the shrinkage of the PMMA in the glass-plate mould, despite the PMMA remaining in contact with the surface of the glass[37]. Whatever the cause of the loss, it only results in an extremely small decrease in trapped fluorescence, even after several hundred reflections (for example, the fraction remaining after 200 reflections is $0.9998^{200} = 0.96$ - still a large fraction).

Self absorption (η_{self}). η_{self} applies to only the fraction of fluorescence photons reaching the edges of the LSC sheet without being lost due to re-absorption. Re-absorption occurs with fluorophores that have overlapping absorption and emission spectra, for example, organic dyes or quantum dots. The separation between the peak absorption and emission wavelengths is called the Stokes shift (Lakowicz[38] p.5). Fluorescence emission from one molecule can be absorbed by another molecule of the same fluorophore. Although subsequent emission will still occur, subject to quantum yield, it will be emitted in a random direction and there is again a probability of its leaving the sheet via the escape cones. Re-absorption leads to a reduction in LSC efficiency as trapped photons which would have reached the edge can be re-directed out of the sheet and lost[39, 40]. Although it may seem at first that re-absorption could help to reduce escape-cone losses by re-directing escape-cone photons back into the sheet, this is less likely to occur as the pathlengths involved are on the order of the thickness of the sheet, rather than the length or width. Photons in an LSC

can experience multiple re-absorption events, each one increasing the chance of the photon being lost. η_{self} for an LSC containing an organic dye is typically on the order of 40-80 %, although this depends greatly on concentration and PLQY.

Dominant factors. The largest contributions to the overall losses come from P_{TIR}, η_{abs}, η_{Stokes} and η_{self}. These must be improved to achieve higher LSC efficiencies. To increase P_{TIR} is difficult, since it depends only on the refractive index of the host, which varies little (most polymers and glasses are in the range 1.3-1.5). However, several techniques can be used to recapture some of the escape-cone losses and direct them back into the sheet. These techniques, which include hot mirrors, photonic filters, and oriented dyes, are discussed in detail in Section 1.5.3. η_{abs} can be increased by using a mixture of several dyes in either the same or multiple LSC sheets to increase the absorption range, although problems arise because of the generally lower PLQY of longer-wavelength dyes (Section 1.4.1). The use of multiple dyes and multiple sheets is discussed in Section 1.5.4. η_{Stokes} cannot be improved, as it is inherent in the wavelength-shifting process which occurs in an LSC. In fact, if the absorption range is increased, η_{Stokes} will decrease, as there is a larger average decrease in energy in the absorption/emission process. Finally, η_{self} can be improved with the use of fluorophores which have larger Stokes shifts and lower spectral overlaps to reduce re-absorption losses. Rare-earth materials offer one solution and these are discussed in Section 1.4.3.

1.4 Fluorophores

The different fluorophores used in LSCs can be broadly categorised into three types: organic dyes, quantum dots and rare-earth materials. Each type is discussed below and the impact of their properties on the LSC design challenges described.

1.4.1 Organic fluorescent dyes

Fig. 1.3 shows the energy-level (Jablonski) diagram of an organic dye. Upon absorption of a photon, an electron from the ground electronic state, S_0, is excited to

one of the vibrational levels of the first excited electronic state, S_1. It then decays non-radiatively by internal conversion to the lowest vibrational level of S_1. From there, it decays to one of the vibrational levels in S_0 by emission of a fluorescence photon. Transitions between the different vibrational levels of the molecule give rise to peaks in the absorption and emission spectra. Fig. 1.4 shows the absorption and emission spectra of a typical organic dye (BASF Lumogen F Orange 240). Because of the symmetry of the absorption and emission processes, the positions of the peaks in the absorption and emission spectra are also nearly symmetrical (peak separation $\sim$0.17 eV), although of different magnitudes.

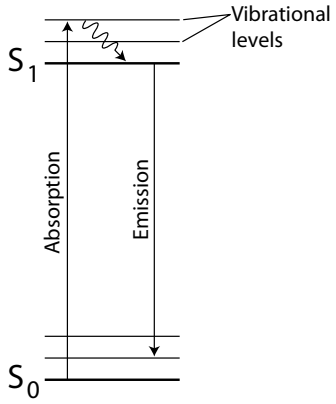

Figure 1.3: Jablonski energy-level diagram for an organic dye[38].

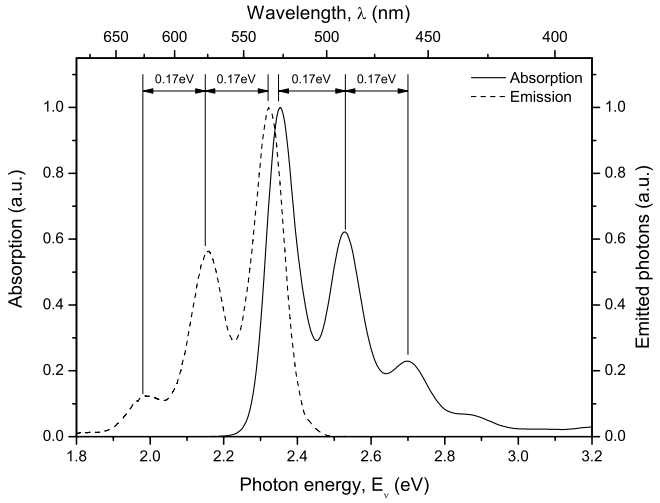

Figure 1.4: Absorption and emission spectra of Lumogen F Orange 240 dye.

Organic dyes offer the simplest means of incorporating a fluorophore in a LSC, as

they can easily be dissolved in a range of organic polymers, such as poly(methyl methacrylate) (PMMA), which are then cast into sheet form. Initial LSC research[6, 9, 16, 41, 42, 43] used dyes originally developed for use in dye lasers, such as Rhodamine 6G, DCM and Coumarin, as they were widely available and had well-characterised properties. Many visible-emitting laser dyes have near-unity quantum yields (for example, η_{PLQY}=98 % for Rhodamine 6G[16]), making them ideally suited to LSC use, although they have limited photostability.

To maximise the efficiency of an LSC, the emission wavelength of the dyes used should ideally be in the NIR region of the spectrum[34], where the spectral response of silicon solar cells is greatest. However, an increase in the emission wavelength of the dye is invariably accompanied by a decrease in its quantum yield[44]. This is shown in Fig. 1.5 (adapted from Zastrow[44]), which plots the quantum yield of a range of different organic dyes versus their peak emission wavelength. The decrease has been attributed to the increased probability of non-radiative decay occurring at longer wavelengths and the decreased probability of radiative transitions[45]. It has been found that deuteration of either the dye molecule or the solvent can lead to an increase in quantum yield[45]. The larger deuterium atom lowers the energy of bond vibrations (such as C-H) and reduce the probabiliy of non-radiative decay.

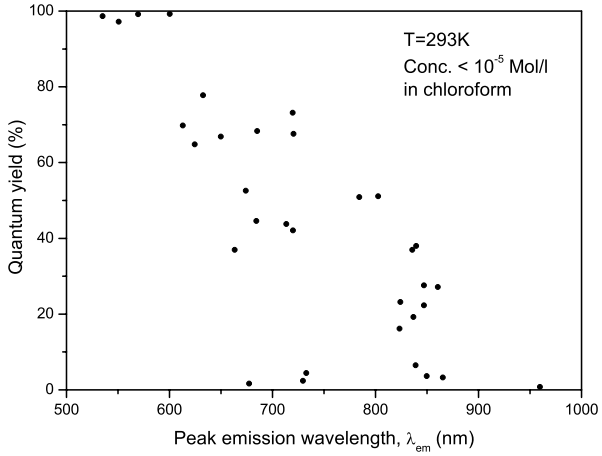

Figure 1.5: Quantum yields of organic dyes versus peak emission wavelength (adapted from Zastrow[44])

Although the development of NIR-emitting dyes with high quantum yields has been

difficult, several dyes based on terrylenediimides and violanthrones have been developed which can emit in the range 700-800 nm and are claimed to have high quantum yields (50-90 %)[46, 47, 48]. Other derivatives of the basic perylene molecule have also been produced with emission wavelenghs up to 1000-1100 nm[49, 50, 51, 52].

All organic dyes exhibit an overlap of their absorption and emission spectra (Fig. 1.4) and will therfore exhibit re-absorption when incorporated in an LSC sheet. Because of this, the effects of non-unity quantum yield become significant, especially for NIR-emitting dyes which show a greater spectral overlap[45], as successive re-absorption events increase the probability that a photon is lost by non-radiative decay of the dye molecule.

To reduce the spectral overlap and the degree of re-absorption, the emission spectrum can be red-shifted by the addition to the host matrix of molecules which have high mobility[53], such as dimethylsulfoxide (DMSO). These stabilise the excited state[53], lowering its energy and resulting in a red-shifted emission spectrum. The absorption spectrum is unaffected since absorption transitions occur between the ground state and an unstabilised excited state[53]. However, although re-absorption can be reduced with this technique (but not eliminated), the optical properties and stability of the host material are compromised by the amount of mobile molecules which needs to be added; Sah *et. al.*[53] found that concentrations of 5-10 % of DMSO were required to achieve red-shifts of 50-100 nm.

Organic dyes typically have an absorption bandwidth of only 100 nm, as can be seen from Fig. 1.4. However, to maximise LSC performance, it is necessary to absorb a much wider range of solar wavelengths, ideally all wavelengths <950 nm. No single dye can achieve this because of their limited absorption range. It has been demonstrated, however, that multiple dyes with different absorption ranges can be incorporated into the same sheet to increase the overall absorption range[54, 55, 56]. Up to 70 % of the solar spectrum can be absorbed by a sheet using a mixture of dyes[15]. Photons are absorbed and emitted by successively longer-wavelength dyes, creating a cascade effect where any absorbed photon passes through the chain of dyes and is emitted by the longest-wavelength dye, regardless of its initial wavelength[34]. Efficiencies as high as 4.4 % have been predicted for an LSC with a sheet containing multiple organic

dyes[34].

The organic laser dyes which were originally studied suffered from poor photostability[15], with some dyes lasting the equivalent of only a few weeks under solar illumination[43]. The best lasted 1-2 years[17, 57]. While not a problem for their original intended use, where fresh dye solution is continuously circulated through the laser, it shortens the usable lifetime of an LSC greatly. Even though dyes may have near-unity quantum yield, which is one of the requirements, they must be stable in LSCs for 10-20 years. However, dyes have been developed[48, 58, 59, 60] which appear to have stability of many years under exposure[61, 62]. These are from the Lumogen F range of dyes which were originally developed by BASF[63] to have high quantum yields and good photostability for use in LSCs[48]. These dyes have been used in a variety of situations including LSCs[64, 65, 66, 29, 20, 25, 67, 28] and daylighting applications[68, 69, 70, 61].

Dye stability can be affected by the host material. A recent study by Kinderman[71] showed that better stability was achieved in pure PMMA coatings on glass plates compared with bulk PMMA samples. It was thought that this was caused by additives in the bulk PMMA samples but may also be a result of the bulk samples being cured with UV light, which can cause photodegradation of the dyes. Co-polymers of polystyrene and PMMA have shown an increase in dye stability[72], with the lifetime of one of the dyes, coumarin, increasing from 361 min in PMMA to 1964 min in the co-polymer[72]. Reisfeld[73] found that LSCs constructed from thin films of sol-gel glasses doped with the BASF Lumogen F dyes exhibited improved photostability, with samples exhibiting 65 % of their initial fluorescence intensity after the equivalent of five years outdoor exposure[73]. It has also been suggested that the presence of oxygen during device manufacture can lead to a reduced stability because of photooxidation[74].

1.4.2 Quantum dots

Nanocrystals of inorganic compounds such as lead sulphide (PbS) or lead selenide (PbSe) (called quantum dots) exhibit broad absorption spectra, high absorption co-

efficients and emission wavelengths which can be tuned from 850 nm to 1900 nm by simply altering the diameter of the quantum dot[75, 76]. Although quantum yields of up to 80 % have been achieved for laboratory-produced quantum dots[77], commercial quantum dots are limited to 30-50 % quantum yield[78, 79, 80] and are both expensive (£800-£3000 per gram[78, 79] compared with £5-£20 per gram for the Lumogen dyes[81]) and exhibit poor photostability[82, 83, 84, 85, 86].

Fig. 1.6 shows absorption and emission spectra of both cadmium selenide/zinc sulphide (CdSe/ZnS) quantum dots with a diameter of 5 nm and PbS quantum dots with a diameter of 8 nm. The PbS dots are capable of absorbing all wavelengths below 900 nm which would appear to make them ideally suited for LSC use. However, despite the wide absorption range, there is still a large overlap of the absorption and emission spectra. Combined with the relatively low quantum yield (compared with the near-unity quantum yield of the Lumogen organic dyes[63]), this results in large re-absorption losses. The widths of the absorption and emission spectra (and hence the amount of spectral overlap) are determined by the distribution of diameters in a quantum dot sample[87]. Improvements in quantum dot production techniques which result in a narrower size distribution could result in lower re-absorption losses from quantum dot samples[24].

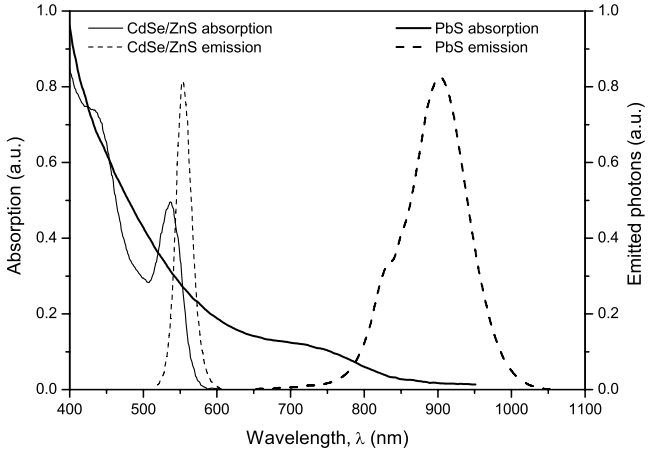

Figure 1.6: Absorption and emission spectra of CdSe/ZnS and PbS quantum dots (adapted from Rowan *et. al.*[88])

Several authors have constructed LSC devices using quantum dots[82, 89, 80, 90, 22,

91, 92, 93, 94]. While offering some advantages, such as an emission wavelength in the NIR, their low quantum yield and large re-absorption losses resulted in low efficiencies. In addition, quantum dots are susceptible to oxidation and photodegradation[82], as well as aggregation at high concentrations which reduces their quantum yield[86] and it was concluded that major improvements need to be made in quantum dot efficiency before they can perform with any degree of efficiency in LSC modules[90].

1.4.3 Rare-earth materials

Rare-earth (lanthanide) ions such as Nd^{3+} and Yb^{3+} can exhibit reduced re-absorption losses, high quantum yields and excellent photostability, making them highly suitable for use in LSCs[12, 95]. The properties of a range of lanthanide ions, as well as non-lanthanide ions such as chromium and uranium, have been studied in a variety of host materials such as glass[12, 96, 95, 97, 98], glass-ceramics[99, 100] and sol-gels[101, 102, 103, 104, 105, 106, 107]. Quantum yields in the range 90-100 % have been measured for the Nd^{3+} ion in silicate[108] and fluoride[109] glasses and YAG crystal[108, 110, 111], although they vary with host material and concentration.

As an example of the optical properties of a commonly-used rare-earth ion, the absorption and emission spectra of the Nd^{3+} ion are shown in Fig. 1.7.

The absorption spectrum exhibits a multitude of peaks over the range 300-900 nm, corresponding to transitions from the $^4I_{9/2}$ ground state of the ion to different excited states. The emission spectrum consists of three peaks at 880 nm, 1064 nm and 1330 nm, with 75 % of the emitted photons occurring in the main peak at 1064 nm. Emission occurs from the $^4F_{3/2}$ excited state. It will be seen from Fig. 1.7b that there is a peak in the absorption spectrum at 880 nm, corresponding to the $^4I_{9/2} \rightarrow ^4F_{3/2}$ absorption transition, which is the inverse of the $^4F_{3/2} \rightarrow ^4I_{9/2}$ emission transition. As a result, emission at 880 nm will be re-absorbed by the ion, leading to re-absorption losses at this emission wavelength. However, the two longer-wavelength peaks at 1064 nm and 1330 nm do not suffer from re-absorption, since the terminal states of the corresponding emission transitions ($^4F_{3/2} \rightarrow ^4I_{11/2}$ and $^4F_{3/2} \rightarrow ^4I_{13/2}$, respectively) are above the ground state and are unpopulated in a ground-state ion, save for a

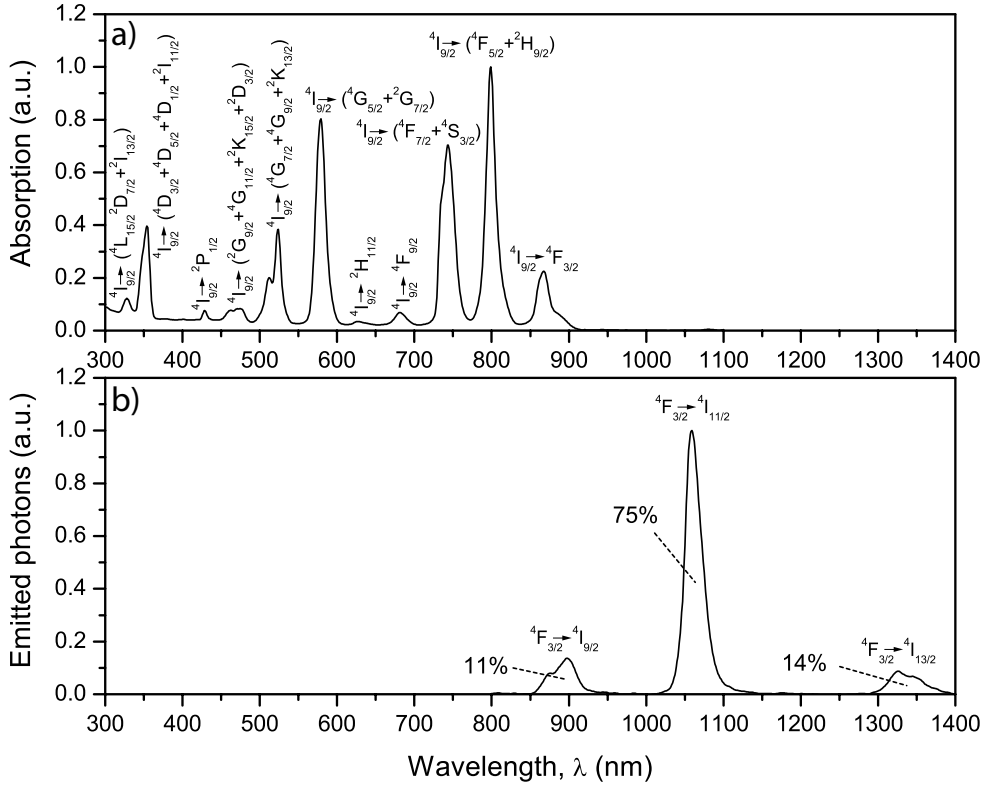

Figure 1.7: (a) Absorption and (b) emission spectra of Nd^{3+} ion, excited at 578 nm (adapted from de Sousa *et. al.*[112]). The percentage contribution of each emission peak to the total emission spectrum is indicated.

small amount of thermal electrons. Therefore, the corresponding absorption processes $^4I_{11/2} \rightarrow ^4F_{3/2}$ and $^4I_{13/2} \rightarrow ^4F_{3/2}$ cannot occur.

However, the situation is different for other ions such as Yb^{3+} or Er^{3+}, as the terminal state of the emission transitions in these ions *is* the ground state and absorption *can* occur at the same wavelength as the emission. For example, Yb^{3+} exhibits a single emission peak at 970 nm, corresponding to the $^2F_{5/2} \rightarrow ^2F_{7/2}$ emission transition[113]. Since the terminal state of this transition is the $^2F_{7/2}$ ground state, absorption can also occur at 970 nm and this is confirmed by the single peak in the absorption spectrum at 970 nm caused by the $^2F_{7/2} \rightarrow ^2F_{5/2}$ absorption transition. The Er^{3+} ion (ground state $^4I_{15/2}$) shows similar behaviour, with a main emission peak at 1550 nm ($^4I_{13/2} \rightarrow ^4I_{15/2}$) and a corresponding absorption peak also at 1550 nm ($^4I_{15/2} \rightarrow ^4I_{13/2}$).

Re-absorption of the emission is again a problem with rare-earth ions, but there are techniques to reduce the losses, specifically by using a rare-earth complex to increase

the absorption coefficient and reduce the amount of rare-earth ion required. This is discussed below.

Although the Nd^{3+} ion has a wide absorption range (from 300-900 nm), its main emission wavelength of 1064 nm is not ideally matched to the peak spectral response of silicon solar cells, which occurs at 900-950 nm. At 1064 nm, the spectral response is only around 50 % of its peak value. Conversely, the Yb^{3+} ion has an emission wavelength of 970 nm which *is* well-matched to the cell response but it lacks a wide absorption range, with the only absorption occurring at 970 nm. It is possible to combine the wide absorption range of Nd^{3+} with the optimum emission wavelength of Yb^{3+} by doping both of the ions into the glass host[95, 114, 115, 116, 117, 118]. In this combination, light is absorbed by the Nd^{3+} ion and the energy transferred to the Yb^{3+} ion which emits with a broad single peak at 970 nm. Up to 20 % of the solar spectrum in the range 440-980 nm can be absorbed using such a combination[95], and transfer efficiencies as high as 90 % have been measured between the two ions[95].

The absorption can be increased still further by the addition of chromium ion (Cr^{3+}) to the mixture of Nd^{3+} and Yb^{3+} to form a triple-doped glass[119, 120, 121, 97]. Cr^{3+} exhibits absorption bands covering most of the visible spectrum[97] and performs a similar function to Nd^{3+} in that it transfers its energy to the Yb^{3+} ions which then emit. The combination of Cr^{3+} and Nd^{3+} absorption results in a higher overall absorption across the visible spectrum. Neuroth *et. al.*[119] found that it was possible to absorb 62 % of the solar radiation in the region 400-950 nm with a 0.5 cm-thick sheet of triple-doped glass, and that this could be increased to 79 % by the use of a back reflector[119]. Fig. 1.8 shows the internal transmittance (corrected for surface reflection) and emission spectra of such a sheet, demonstrating the high absorption in the visible region. Overall quantum yields of 20-44 % were measured, depending on the exitation wavelength[119].

Because of the difficulty of casting bulk samples of glass or ceramic doped with lanthanide ions, which involves high-temperature melting/casting[100, 122], cutting, diamond grinding and polishing, research has been carried out to develop nanoparticles of lanthanide compounds which can be dispersed in polymer hosts instead, as this has applications in the photonics/telecoms field[123, 124, 125, 126, 127, 128, 129, 130, 131,

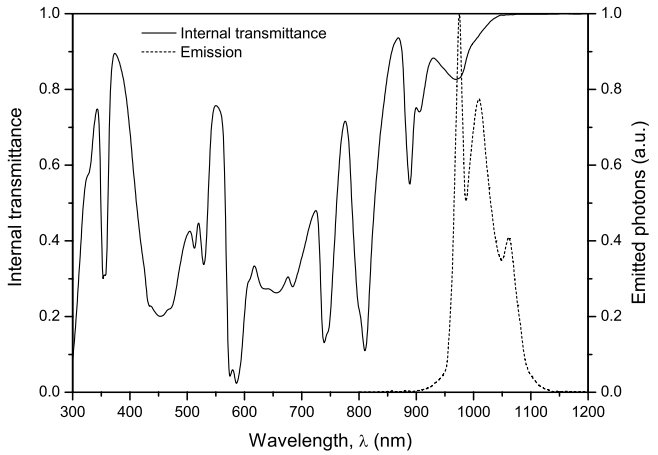

Figure 1.8: Internal transmittance and emission of a 0.5 cm-thick sheet of Cr-Nd-Yb triple-doped glass (adapted from Neuroth *et. al.*[119])

132]. The particles are of lanthanide-doped compounds such as Eu^{3+}-doped LaF_3 and have diameters of ∼10 nm, sufficiently small to prevent scattering of incident light. These can be dispersed in a monomer prior to its polymerisation, in much the same manner as organic dyes are dissolved.

Although bulk lanthanide-doped glasses possess high absorption coefficients of the order of $5\,cm^{-1}$ (calculated from the transmittance of the Cr-Nd-Yb glass shown in Fig. 1.8), the *mass* absorption coefficients of the rare-earth nanoparticles are extremely low, of the order of $5x10^{-6}\,ppm^{-1}cm^{-1}$ (since bulk material is equivalent to a "concentration" of 1,000,000 ppm), to be contrasted with a typical organic dye which has a mass absorption coefficient in the range 0.1-0.5 $ppm^{-1}cm^{-1}$. Therefore, high concentrations of nanoparticles are required in an LSC sheet to absorb a sizeable fraction of incident sunlight. Required concentrations can be as high as 50 % by weight of host material. Although the cost of rare-earth materials is comparable to that of organic dyes (for example, Nd_2O_3 powder is typically £1-£5 per gram[133]), the much higher concentration required results in an expensive device, and some means must be found of reducing the amount of rare-earth material needed. In addition, there still exist problems with re-absorption of the fluorescence by the rare-earth ions.

A promising solution to the problems of limited absorption range, high required concentration, and re-absorption of fluorescence is the use of a complex or chelate of an

organic dye molecule (or molecules) and a rare-earth ion[134, 135, 136, 137, 23, 138, 113, 139, 140, 141, 142, 143, 144, 145, 146, 147, 148, 149, 150, 151, 152, 153, 154]. The organic ligand absorbs radiation and transfers the energy to the ion which then emits. Complexes have been formed with Nd^{3+} and Yb^{3+}, which exhibit absorption in the visible and quantum yields in the range 0.012-0.03 % for Nd^{3+} and 0.14-0.23 % for Yb^{3+}[23, 138, 113]. Quantum yields for Eu^{3+} complexes as high as 50 %[139] and, more recently, 86 %[140] have been measured.

Fig. 1.9 shows the absorption and emission processes for a Eu^{3+} complex, although the process is similar for other ions and ligands. Light is absorbed by the ligand, exciting it to the first singlet state. Energy is transferred to the triplet state of the ligand via inter-system crossing (ISC) and thence to an excited state of the Eu^{3+} ion, as the presence of the rare-earth ion increases energy transfer from the triplet state of the ligands[155]. The decay of the ion to the $^7F_{J=0,1,2,3,4}$ levels[136] gives rise to five narrow peaks in the emission spectrum at 578, 592, 613, 650 and 697 nm as shown in Fig. 1.10.

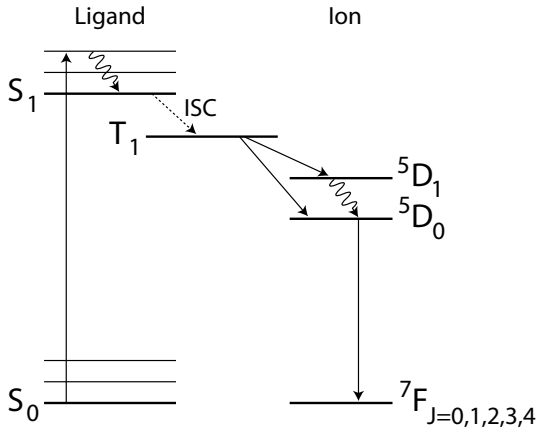

Figure 1.9: Jablonski energy-level diagram for a Eu^{3+} complex

Rare-earth complexes exhibit several desirable features. Because an organic absorbing ligand is used, mass absorption coefficients are high (similar to those of organic dyes) compared with those of the rare-earth nanoparticles. The greatly increased absorption allows a much lower concentration of rare-earth ion to be used, with a consequent reduction in the re-absorption losses caused by re-absorption of fluorescence by the rare-earth ion. Required concentrations decrease from around 500,000 ppm in the case of rare-earth nanoparticles to around 200 ppm for the rare-earth complexes, with

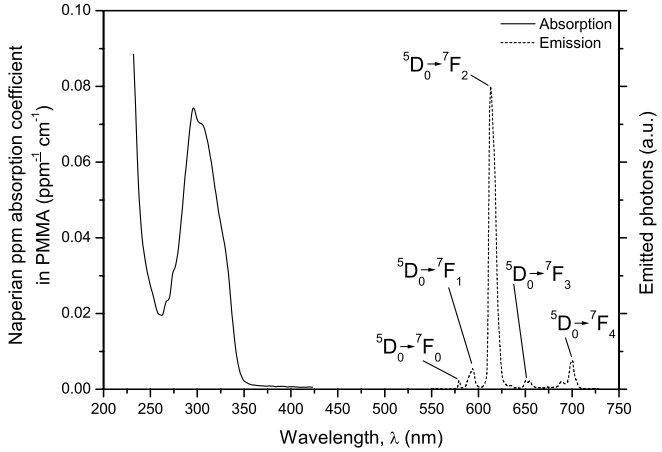

Figure 1.10: Absorption (solid) and emission (dashed) spectra of a Eu^{3+} complex. Emission transitions are indicated.

a similar reduction in re-absorption losses. If the mass absorption coefficient of the ion itself is of the order of $5\text{x}10^{-6}\,\text{ppm}^{-1}\text{cm}^{-1}$, then the absorption coefficient of the doped material at the ion absorption wavelength is only $200 * 5\text{x}10^{-6} = 10^{-3}\,\text{cm}^{-1}$. This is less than, for example, the absorption of PMMA (which may be used as a host material), indicating that re-absorption by the rare-earth ion is of little concern in an LSC using rare-earth complexes.

Another major benefit of rare-earth complexes is their large Stokes shift. As can be seen from Fig. 1.10, which shows the absorption and emission spectra of a Eu^{3+} complex, the Stokes shift is ∼300 nm, with zero overlap of the absorption and emission spectra. This is to be contrasted with organic dyes which have a Stokes shift of 10-50 nm (Fig. 1.4). As a result, re-absorption losses are completely eliminated. The requirement for a near-unity quantum yield becomes less critical. Indeed, it is shown later in this thesis (Section 5.3.3) that a LSC sheet containing a Eu^{3+} complex with 86 % quantum yield exhibits lower losses than a similar sheet containing an organic dye with 100 % quantum yield.

Complexes formed with single types of ligands still suffer from the problem of limited absorption bandwidth, similar to that of individual organic dyes. It may be possible to extend the absorption range by complexing the ion with several different ligands which have different absorption ranges.

1.5 LSC sheet(s)

Many materials and configurations have been used in the construction and development of LSC devices. For example, different host materials, variations in size/thickness and shape, different types of solar cells and the use of back reflectors or hot mirrors. An overview of these is presented in the following sections.

1.5.1 Material

The host material of the LSC sheet serves both as a medium into which the fluorophores are doped and as a structural support. The material choice influences both the optical properties of the fluorophore and the parasitic host absorption.

By far the most common host material is the polymer poly(methyl methacrylate), also known as PMMA, Plexiglas, Lucite, or simply "acrylic". This is the material originally used by Goetzberger[6] and many others since[8, 9, 10, 16, 43, 80, 156, 64, 20]. Its main advantages are its low cost, high optical clarity[35, 72, 71] and the ease of doping with fluorophores as these can simply be dissolved in the monomer prior to polymerisation. It also has good photostability, with lifetimes of up to 17 years[157, 15].

However, although PMMA exhibits good optical transparency in the visible region of the spectrum, it begins to show absorption peaks above 700 nm. These are caused by harmonics and overtones of the C-H and C-O bond vibrations in the molecule[36, 158] and are common to all polymers in which these bonds are present. Host absorption losses therefore become significant when using fluorophores with emission wavelengths >700 nm. In addition to host absorption, the C-H and C-O vibrations can lead to an increased probability of non-radiative relaxation of the flurophore when the energy gap of the fluorophore corresponds to the bond frequencies, leading to a reduction in quantum yield[159]. These problems can be reduced by either deuterating or fluorinating the host polymer[160, 161, 162, 36]. The larger, heavier deuterium and fluorine atoms shift the absorption peaks to lower energies (longer wavelengths), reducing the probability of host absorption and leading to an increase in quantum yield[160, 154].

Two-component clear epoxy resins have been used which exhibited around 30 % lower

absorption in the visible region than than PMMA[82]. This is certainly an advantage for fluorophores which may be sensitive to temperature. Unlike PMMA casting, which requires heat to cure the polymer, epoxy resins can set at room temperature. However, epoxy resins have a poorer photostability compared with PMMA.

Several authors[6, 16] used a liquid as the host material. The liquid was contained between two glass plates to form a large, thin cuvette. The main motivation was the limited photostability of the organic dyes which were used. Using a solution of the dye made it possible to easily replace the dye once it had photodegraded. However, the availability of dyes with good photostabilities renders this an uneccessary and impractical method.

Glass has also been used as a host material[18, 12, 95, 96, 97, 8]. Because it is an inorganic material, it has a higher transparency at NIR wavelengths (>700 nm) compared with organic polymers and is not subject to photodegradation. However, as the glass must be prepared from a melt at high temperatures (usually >600°C)[100, 122], the choice of fluorophores is restricted to rare-earth ions and other inorganic compounds which can withstand the required temperatures. Organic dyes, rare-earth complexes and quantum dots cannot be incorporated into the glass.

Instead of producing glass from a melt, it can also be prepared from a sol-gel, which allows the process to be carried out at room temperature[163, 101]. It becomes possible to incorporate a range of different fluorophores into the glass material, including organic dyes[164, 103, 73, 107] and rare-earth or inorganic ions[106, 104, 105, 123, 124]. Since they are entirely inorganic, sol-gel glasses do not suffer from photodegradation and show improved transparency in the NIR compared with polymers. The range of pore sizes in the final glass is in the range 1.5-10 nm[163, 102], which is much smaller than the wavelength of visible light. As a result, they are transparent and exhbit little scattering at wavelengths above about 250 nm[163, 102].

Although perhaps not optimum for use with NIR-emitting fluorophores, PMMA will be used throughout this thesis as a host material because of the ease with which it can be cast into sheet form.

1.5.2 Shape

Although a square LSC sheet would seem the obvious first choice because of the ease of construction and tiling, a square sheet produces a non-uniform intensity distribtion along the edge of the sheet (and hence along the solar cell). The intensity is 20-30 % greater in the centre of the edge compared with the ends[165, 12].

Since the maximum length of a solar cell is 10-12 cm (determined by the maximum wafer size), an LSC module of a practical size requires several solar cells placed along its edges. To achieve adequate operating voltages, these cells need to be connected in series[166]. However, in a series combination of cells, the maximum current is limited by the cells with the lowest illumination which, in an LSC, are those nearest the corners. The non-uniform illumination therefore reduces the maximum current which can flow, reducing efficiency by around 20 %[166]. Non-uniform illumination of an individual cell can also reduce operating efficiency[167, 168]. It is possible to reduce this problem by varying the size (length) of the cells on the edges in proportion to the amount of light they receive by using longer cells nearer the edges and shorter cells in the middle[166, 169]. The effect of shape on the uniformity of edge illumination has been studied[165, 170, 12, 166] and, while it was found that shapes such as right-angled triangles with a reflector on the hypotenuse resulted in improved uniformity, the best shape was a circular sheet[166, 165] as this is totally symmetrical and the intensity is constant around the perimeter. However, this would require bending the solar cells to fit them to the edges. The best compromise is therefore a hexagonal shape. This allows straight solar cells to be used, while still providing good illumination uniformity. A hexagonal module can also be tiled to cover 100 % of available surface area. Although a hexagonal shape is optimum for a production module, research has been focussed on square and rectangular modules because they are simpler to construct manually. We will therefore concentrate on square or rectangular sheets in this thesis.

Sheet thicknesses are typically in the range 0.2-0.5 cm. This is primarily because sheet material (glass, PMMA) is readily available in these thickness, or can be produced with relative ease. Too thin a sheet will lack the strength to support it over the width of the LSC. Conversely, a thicker sheet will increase the weight and embodied energy

of the LSC module. A thicker sheet can result in a higher efficiency, as the required fluorophore concentration can be decreased, thus reducing re-absorption losses. However, this must be balanced against the increased embodied energy and material cost. A thin-film device, where a layer of fluorescent material is coated on to a transparent substrate, may offer a solution, as the substrate could be rigid (for example glass) and could be made thin while still offering support. However, the higher dye concentration required in a thin-film device may case problems with fluorescence quenching and a reduction in efficiency. Later (Chapter 6), the effects of thickness and size are studied in detail using computer simulations.

1.5.3 Escape-cone losses

In Section 1.3, the probability P_{TIR} that an emitted photon is trapped was calculated from the critical angle inside the LSC [Eqn. (1.3)]. For a material with refractive index $n = 1.5$, typical for a polymer such as PMMA, P_{TIR} =75 %, implying that three-quarters of fluorescence emission is trapped inside the sheet[9], with a total of a quarter lost from both the front and rear escape cones. This probability also applies to re-absorption events, since they also rely on the emitted light being incident at greater than θ_C for trapping to occur. Each re-absorption event has a 75 % probability of emitting a photon which becomes trapped in the sheet. The probability of a photon remaining trapped after several re-absorption events is the product of the P_{TIR} for each event. For example, the probability of a photon remaining trapped after five re-absorption events is $0.75^5 = 0.24 \equiv 24\,\%$. Clearly, the combination of re-absorption and escape-cone losses can lead to a large reduction in the number of photons trapped inside the LSC.

The simplest way to reduce escape-cone losses is to use a mirror (either a simple specular or diffuse reflector, or an advanced reflector such as a hot mirror or photonic crystal) to reflect the escape-cone losses back into the sheet[6, 16, 14, 41, 26, 30, 171, 172, 29]. Fig. 1.11 shows different processes associated with a back reflector which are discussed presently. The advantages and disadvantages of different types of back reflector are discussed below, but first there are two important points which relate to the use of any type of reflector.

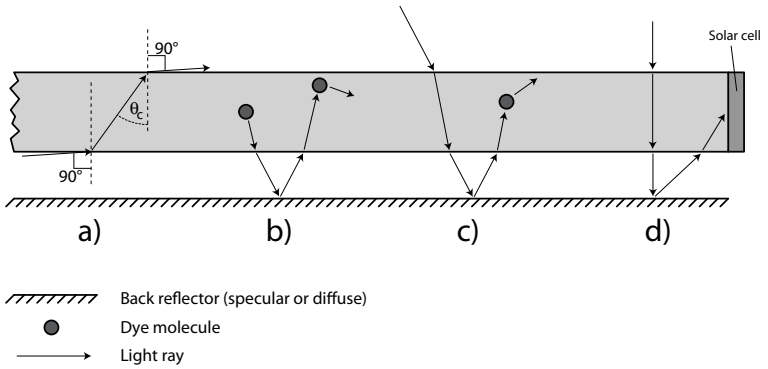

Figure 1.11: Use of a back reflector showing a) the limit of entry angles into the sheet b) re-absorption of rear escape-cone losses c) reflection of unabsorbed sunlight d) direct reflection of sunlight on to the solar cell. Sunlight is incident on the top surface of the sheet.

Firstly, it is highly important to separate the reflector from the LSC sheet and not attach it directly to the surface. In an LSC sheet, a trapped fluorescence photon can make as many as a hundred reflections from the front and rear surfaces before reaching the edge (an approximate relation for the maximum number of reflections is half the side length divided by the sheet thickness). Normally these reflections (if due to TIR) are 100 % efficient. If a mirror coating is applied to the surface, the reflectivity drops, as no mirror coating is 100 % reflective. Even if the coating is 99 % reflective, the percentage of photons remaining after, for example, 100 reflections is only $0.99^{100} = 0.36 \equiv 36\,\%$. Reports of an observed gain when a mirror is attached to the sheet surface[41] can be explained by the small dimensions of the LSC sheet. The number of internal reflections is much lower and a gain is possible in this case.

Secondly, it is impossible to use a reflector to direct photons back into the LSC sheet in such a way that they become trapped by TIR, *unless* they are absorbed and emitted by a dye in the sheet. The angle of incidence of photons on the external surface of the sheet must lie between 0° and 90°. Therefore, the angle of incidence on the internal surface must be between 0° and θ_C. The photons will pass straight out the other side of the sheet, even at the maximum angle of incidence, as shown in Fig. 1.11a. If, however, they are absorbed by a dye while in the sheet, there is a probability of P_{TIR} that they will be re-directed so that they are trapped by TIR inside the sheet. In short, to make use of the escape-cone photons, they must be re-absorbed after they are reflected back into the sheet.

Nearly all authors have used a "back reflector" - a totally-reflecting mirror placed behind, but separated from, the LSC sheet - to increase the efficiency[6, 41, 28, 19, 62]. This can be either specular or diffuse. A back reflector improves the efficiency in two ways. Firstly, it reflects rear escape-cone photons back through the LSC sheet (Fig. 1.11b), giving them a small chance (due to the weak absorption) of being re-absorbed by the dye and subsequently trapped in the sheet. Secondly, and more importantly, it reflects unabsorbed solar photons back through the sheet (Fig. 1.11c), effectively doubling the thickness of dyed material through which they pass. As a result, the dye concentration can be halved while still absorbing the same number of solar photons, albeit at the additional cost of using a back reflector. This halves the re-absorption losses. As far as escape-cone photons are concerned, there is no difference in improvement between the specular and diffuse reflectors, as escape-cone photons are already randomly directed when they leave the LSC sheet. However, a diffuse reflector will result in an increased number of absorbed solar photons compared with a specular reflector, since it reflects solar photons at random angles and increases the average pathlength of these in the LSC sheet, increasing the probability of absorption. A diffuse reflector also has the beneficial side-effect of reflecting solar photons directly on to the edge-mounted solar cells (Fig. 1.11d). This is the main reason for the high efficiencies measured in small LSC modules[20]. The behaviour of both specular and diffuse back reflectors is studied in detail later (Section 6.1.2).

Although specular and diffuse total reflectors can be used to recycle the rear escape cone losses, they obviously cannot be placed in front of the sheet as they would block incident sunlight. Instead, a wavelength-dependent mirror such as a hot mirror, photonic band-stop filter or photonic crystal must be used. The mirror is transparent to short wavelengths, allowing incident sunlight to pass through and strike the LSC sheet, but is reflective at longer wavelength where the fluorophore emits. As a result, the front escape-cone losses are reflected back into the sheet and can be re-absorbed[26, 30, 20, 32, 25, 28, 29, 31, 33]. Goldschmidt *et. al.*[29, 20] obtained a 20 % relative increase (from 2.6 % to 3.1 %) in the efficiency of a 5 cm x 5 cm LSC module when using a photonic structure placed on top of the LSC. Rugate filters and three-dimensional photonic structures such as opal have also been studied for use with LSCs[31]. Although they do result in an improvement in efficiency, hot mirrors, pho-

tonic crystals and rugate filters can be difficult to manufacture over a large area[173] and can also result in reducing the amount of sunlight reaching the LSC, as they can exhibit increased reflection (compared with a bare host:air interface) over the absorption range of the dye[31]. Peters *et. al.*[31] found that a photonic filter exhibited 20-30 % reflectivity over the absorption range of the dye, decreasing the light reaching the LSC by a similar amount[31]. The reflection properties are also angle-dependent, which can result in greater reflection losses at large angles of incidence[31].

Although the fluorescence emission from a bulk sample of dye-doped material is isotropic, emission from individual dye molecules is not. Each molecule has a preferred emission direction because of the existence of an emission dipole. It is possible to align the dye molecules in an LSC sheet so their emission direction is preferentially towards the edges[25]. This leads to a reduction in escape-cone losses. Alignment was achieved using a liquid crystal and a 15 % increase in the edge output was measured compared with an isotropically-emitting LSC sheet[25]. However, alignment of the dye molcules such that their emission is directed in the plane of the LSC can also lead to a reduction in the absorbed solar radiation because of the orientation of their absorption dipoles[25].

In conclusion, the optimum combination of technologies to either reduce or utilise escape-cone losses would appear to be the use of a diffuse reflector placed behind the LSC to reflect rear escape-cone loss and unabsorbed sunlight, a photonic bandstop filter placed in front to allow incident sunlight to be transmitted but longer-wavelength escape-cone losses to be reflected, and, finally, oriented dye molecules to actually reduce the fraction of fluorescence which is emitted into the escape cones.

1.5.4 Multiple dyes

One of the criteria for good LSC performance is a wide absorption range, to absorb as much as possible of the incident solar spectrum. As we have seen, individual organic dyes have an absorption range of only ∼100 nm. To increase the absorption range, mixtures of dyes have been used[54, 15, 34, 43, 56, 156, 16, 27]. When combined in the same sheet, the absorption spectra of each dye add together to form

a wide absorption bandwidth. Short-wavelength absorbed photons cascade through the different fluorescent dyes until they are finally emitted by the longest-wavelength dye in the mixture[34]. Since all photons are emitted by the longest-wavelength dye, the efficiency of the LSC is strongly dependent on the quantum yield of this dye. While not a problem in, for example, mixtures of the Lumogen F visible-emitting dyes which all have near-unity quantum yields, the addition of an NIR-emitting dye with a low quantum yield results in a significant drop in overall efficiency[34], despite the increased range of absorbed solar wavelengths.

To overcome this problem, a stack of several LSC sheets can be used, with dyes of lower quantum yield being placed in subsequent sheets separated with an air gap[6, 34]. The sheets are stacked to ensure that sunlight strikes sheets containing dyes with higher quantum yields and shorter emission wavelengths first. Electrical output is taken separately from each sheet and combined externally. This has the advantage that the low-quantum yield dyes do not affect the photon transport inside the sheets with high-quantum yield dyes. Wittwer[17] obtained optical efficiencies of 15.8 % for a three-sheet stacked system compared with only 10 % for a single-sheet system. Stacked sheets can also result in lower escape-cone losses, as the losses from one sheet can be re-absorbed by an adjacent sheet if the dye in the adjacent sheet has a suitable absorption range.

An additional advantage of a multi-sheet system is the possibility of matching the edge emission wavelength of each sheet to a different type of solar cell. For example, Goetzberger[9] proposed a four-sheet stack with germanium (Ge), silicon (Si), gallium arsenide (GaAs) and gallium phosphide (GaP) cells attached to each of the four sheets, resulting in a predicted efficiency of 23.7 %. The peak spectral response of each cell type was matched to the emission wavelength of each sheet.

Although multi-sheet LSC systems may result in a higher efficiency, this increase must be balanced against the extra energy and cost involved in adding the extra sheets[18]. We will see later (Section 6.2) that a multi-sheet system actually results in a higher embodied energy compared with a single-sheet system, despite the higher efficiency. The extra embodied energy comes mainly from the material of the second LSC sheet and the extra solar cells.

Multi-sheet systems can also result in lower operating temperatures of the LSC sheets as the thermal loading is spread across several sheets[9, 34]. By matching the edge-mounted solar cells to the emission wavelength ranges of each sheet, thermal losses in the cells can also be reduced, increasing the efficiency.

1.5.5 Thin-film

Instead of using a bulk-doped LSC sheet, it has been suggested that a thin film of luminescent material coated on a transparent substrate such as glass or PMMA might be used[12, 174, 175, 41, 94]. It has been proposed that this configuration reduces re-absorption losses by confining all re-absorption to the thin dye-doped film[174, 175, 176, 88]. The trapped photons spend a large proportion of their path inside the clear, undoped substrate. However, both analysis and experiment show that the thin-film device shows no gain or loss in efficiency compared with a bulk-doped device of identical optical density[94]. This can easily be seen by considering the dye concentration required in the thin film. If, for example, a 0.3 cm-thick bulk-doped LSC requires 100 ppm of dye for efficient operation, a thin-film LSC with a 0.01 cm-thick dye-doped film would require 3000 ppm of dye to achieve the same optical density (30x smaller thickness, therefore 30x higher concentration). If we then consider the path of the trapped photons, we can see that, although they spend only 1/30th of their path in the doped film, the dye concentration in the film is 30x greater than the bulk device, therefore the probability of re-absorption occurring is exactly the same. A possible disadvantage is the extremely high dye concentrations required in the thin film which may lead to quenching and a drop in quantum yield.

The main advantage of a thin-film device is the possibility of reducing host absorption losses in the NIR region of the spectrum by depositing the film on to a substrate such as low-iron or borosilicate glass or fused silica which have lower absorption in the NIR region than polymeric hosts such as PMMA or polycarbonate. Even if the thin film is made of a polymer which exhibits host absorption, the proportion of a trapped photon's path spent inside the film is minimal. This becomes important for NIR-emitting fluorophores, where a deuterated or fluorinated polymer may be needed to achieve a high quantum yield. Using a thin film minimses the amount of

polymer required. A thin-film device will also reduce the embodied energy, as the substrate could be made from glass, which has a lower energy content than polymers (the embodied energy for glass[177, 178] is typically 10-25 MJ/kg whereas that for polymers[177, 179, 180, 181] is in the range 80-200 MJ/kg).

A factor which is often not considered is the flammability of many polymers, especially PMMA. Indeed, PMMA's high flammability[182] is the main reason it is not used for window glazing, despite its excellent optical qualities. Polycarbonate, which is self-extinguishing[183], is used instead. By using a thin film of polymer on a glass substrate, the problem of polymer flammability is eliminated.

Despite the possible advantages of thin-film devices, only bulk-doped devices are considered in this thesis, mainly because it is easier to cast a sheet of PMMA rather than trying to spin-coat a thin film on a PMMA or glass substrate (variations in thickness, surface quality, stress cracking of underlying PMMA).

1.6 Solar cells

The spectral bandwidth of the emission from the edges of an LSC is small - typically <200 nm for an organic dye and <50 nm for a rare-earth ion. This is much smaller than the range of wavelengths to which a conventional solar cell is normally designed to respond (the visible and NIR portion of the solar spectrum from 300-1100 nm). Fig. 1.12 compares the emission from an organic dye (Rot 305) with the AM1.5g solar spectrum and clearly demonstrates the narrow bandwidth of the fluorescence emission.

Solar cells for use in photovoltaic panels are optimised to utilise a wide range of solar wavelengths and, as a result, compromises must be made in the efficiency of the cell. However, because of the narrow-band emission from the LSC, the cells can be optimised for a much smaller range of wavelengths and the efficiency increased[184]. For example, in the design of an anti-reflection coating (ARC), it is possible to achieve a lower reflectance if the range of wavelengths over which the ARC must operate is reduced. As a result, more light is absorbed by the cell. Cell parameters such as

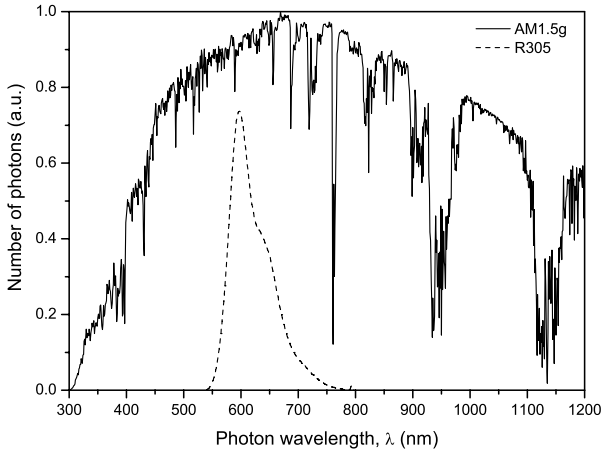

Figure 1.12: Comparison of AM1.5g solar spectrum and Rot 305 fluorescence emission spectrum (not to scale)

doping concentration and junction depth can also be optimised better for narrowband illumination.

There is clearly scope for optimisation of solar cells for use with LSCs[185, 184] but it is not intended to study this here as we are primarily concerned with the optical properties and behaviour of different fluorophores, rather than solar cells.

Although silicon cells have been widely used in LSC research, other cells such as gallium arsenide (GaAs) or gallium indium phosphide (GaInP) can result in a higher efficiency. Reisfeld[41], for example, compared the performance of both Si and GaAs solar cells attached to an LSC consisting of a 10x10 cm PMMA sheet doped with an orange-emitting fluorescent organic dye. The ratio of the short-circuit current from an edge-connected cell to the current from an identical cell facing the sun directly was measured for the two cell types. This ratio was 1.7 for Si cells and 2.98 for GaAs - almost double. This is because GaAs has a larger bandgap than Si (GaAs: 1.43 eV, Si: 1.11 eV) and therefore less energy will be wasted as heat in the GaAs cell. The open-circuit voltage is also higher (GaAs: $\sim$1 V Si: $\sim$0.6 V), leading to a higher power output and efficiency. The solar cell should ideally be chosen on the basis of matching the semiconductor's bandgap as well as possible to the emission wavelengths of the LSC sheet. However, for convenience, silicon cells are used throughout this thesis.

Because of the difficulty in attaching solar cells to the edge of a LSC sheet (solar cells

for LSC use are typically long and narrow, for example 10 cm long and 0.3 cm wide), several authors have attempted to texture or shape either the surface of the sheet or the sheet edges in an attempt to enable the use of larger, more easily handled solar cells[6, 186, 10, 187, 188, 189]. Details of several different construction profiles are shown in Fig. 1.13.

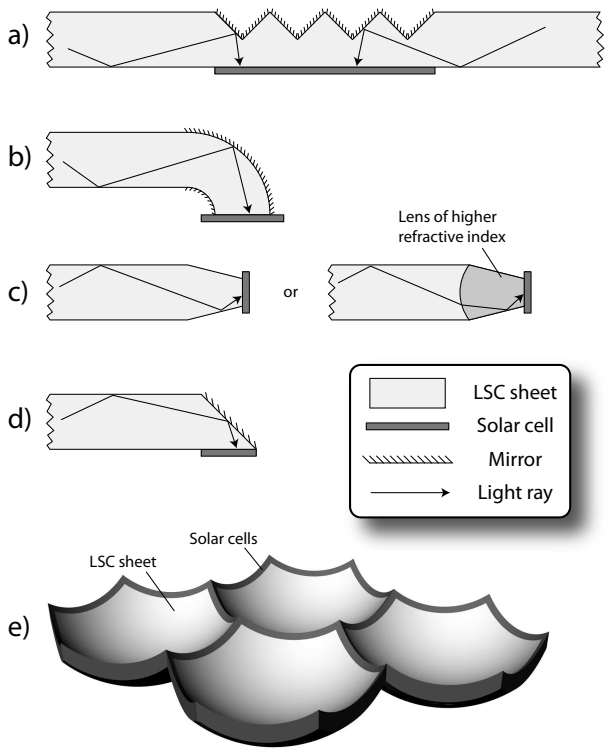

Figure 1.13: Different LSC sheet profiles. a) Mirrored "V"-grooves[186]. b) Bent edges[186]. c) Tapered or lensed edges[10]. d) Chamfered edges[187]. e) Hexagonal "dished" sheets[189].

Goetzberger[186] used mirrored V-shaped grooves cut into the front surface of the LSC sheet to reflect the fluorescence light trapped inside the sheet on to a solar cell attached to the rear surface of the sheet (Fig. 1.13a). A single, large sheet of LSC material could then be used, with solar cells attached at locations across the surface of the sheet. However, the resulting illumination intensity across the solar cell is highly non-uniform. Bent edges were also tried[186] so the solar cell could be mounted in a plane parallel to the LSC sheet (Fig. 1.13b). However, trapped fluorescence would be able to escape the sheet at the corner of the bend, and this would reduce the amount of light reaching the cells. Goetzberger[10] used a taper or lens on the edge of the sheet to increase the concentration ratio obtained (Fig. 1.13c); however, this is difficult to manufacture accurately. Boling[187] cut the edges of the sheet at 45°

and polished or mirrored them in an attempt to again reflect fluorescence light on to a solar cell attached to the rear surface of the sheet near the edge (Fig. 1.13d). Zewail[189] used hexagonal concentrator sheets "dished" into a concave shape which was claimed to reduce the proportion of fluorescence light lost from the surfaces of the sheet (Fig. 1.13e). The edges were also tapered and mirrored.

Although these techniques may increase the amount of light reaching the cells or the ease with which they are attached, the extra processes involved in, for example, cutting a taper on the edge of a sheet, polishing and mirroring outweigh any benefits gained. The best solution is still to attach the cells directly to the edges so they are at right-angles to the plane of the sheet. The edges of the sheet can then be finished simply with a diamond edge polisher, which can also create a tapered or bevelled edge if required.

The use of mirrors on the edges of the LSC sheet has been suggested (for example, Slooff *et. al.*[19] and Weber *et. al.*[8]) as a means of reducing the number of edges to which solar cells need to be attached. By placing solar cells on two adjacent edges of a square LSC sheet and mirrors on the other two edges, fluorescence which reaches the mirrored edges is reflected back towards the cells on the opposite edges. However, this effectively doubles the pathlength of the trapped fluorescence and doubles both the re-absorption and host absorption losses. The simplest solution is to attach cells to all edges of the sheet.

1.7 Measurement of quantum yield

We have seen that one of the requirements for an LSC to have a high efficiency is a fluorophore with near-unity quantum yield. It is also essential that the quantum yield is known accurately, as the effect of small errors in quantum yield is magnified by the multiple re-absorption events which occur with, for example, an organic dye. This is especially important if the performance of a LSC is to be modelled using a ray-tracing simulation program with a view to optimising module parameters.

Quantum yield is defined as the fraction of excited fluorophores which emit a fluores-

cence photon upon decay, as opposed to releasing the energy as heat by, for example, vibrational relaxation. We therefore need some means of accurately measuring the number of photons emitted by a sample and comparing this with the number of photons absorbed, which is equivalent to the number of excited fluorophores. A brief history of quantum yield measurement is presented below and two techniques of particular interest in this thesis are described.

An excellent review of a wide range of quantum yield measurement techniques is given by Demas and Crosby[190] and the reader is referred to that paper and its references for detailed descriptions of historical methods. Quantum yield measurement techniques can be broadly divided into two categores - those that compare the emission of the unknown sample to emission or scattering from a reference sample and those that do not rely on the use of a reference.

Vavilov[191] was the first to describe a technique for measuring quantum yields. In his technique, which was later developed by Melhuish[192, 193], a monochromatic source of excitation light is focussed on to a cuvette containing an optically dense solution of the dye under study and the emission spectrum measured with a monochromator. The cuvette is then replaced, at exactly the same position, with a magnesium oxide (MgO)-coated plate which scatters the excitation light. The scattered excitation is measured using the same monochromator settings. From the two measurements, the quantum yield can be calculated[191]. However, there are several sources of error which limit the accuracy of his technique. The main source of error is the assumption that the MgO scatterer is 100 % reflective and scatters isotropically. In practice, the reflectance depends on the thickness of the coating and also decreases with age. Problems also arise from polarisation of the fluorescence emission, reflection losses at optical interfaces and re-absorption of fluorescence within the sample, the latter being a consequence of the requirement for an optically dense sample. It is certainly a "tedious"[190] method and is capable of, at best, ± 10 % accuracy in the results. Instead of solid scattering reference samples, solution scatterers have also been used[194, 195], such as colloidal silica[195] or a suspension of glycogen[194]. An advantage of using a solution scatterer is that the measurements can be carried out on optically dilute solutions, thus minimising the effects of re-absorption. Despite

this, there are still many sources of error which limit the method's accuracy[190].

To avoid the need for a standard scattering reference sample, techniques have been developed which instead compare the emission of the dye under study with the emission of a dye of known quantum yield[196, 197]. Samples of both the unknown dye and the reference are made up in solution in separate cuvettes and the emission spectra from both recorded at a range of different concentrations. The quantum yield can be calculated from this data and knowledge of the sample absorbances[196, 197]. However, the accuracy is no better than that of the technique using a scattering reference, as the quantum yields of the reference samples must still be determined by comparison with a scattering reference. In addition, the reference sample must emit in the same wavelength region as the unknown dye and this limits the range of emission wavelengths which can be studied to below about 600 nm because of the lack of standards which emit above this wavelength[190]. Quantum yield "standards" are notoriously difficult to determine, as the yield can vary strongly with environmental factors such as solvent, pH, temperature and concentration[190].

The techniques described thus far rely on the use of a reference sample of known properties. They are also only really suitable for use with liquid samples in a cuvette. It would clearly be advantageous to avoid the need to use a reference sample and to also be able to measure solid samples and samples of different shapes and sizes. Fluorescence properties depend on the solvent[53] and it is therefore important to measure them in the actual material of an LSC. Several additional techniques offer greater flexibility in choosing sample format - these are classed as either calorimetric or photon-counting techniques.

Calorimetric methods rely on measuring, directly or indirectly, the temperature rise of a sample of dye when irradiated with light and comparing this with the temperature rise obtained from a non-fluorescent (zero quantum yield) reference sample. It is assumed that the only ways in which absorbed energy can be dissipated are by either fluorescence emission or by dissipation of the energy as heat. Other processes, such as photochemical reactions, are assumed not to occur[190]. In the non-fluorescent reference sample, all of the absorbed energy is turned into heat. The ratio of the temperature rises of both samples gives the fraction of absorbed energy which is

turned into heat in the fluorescent sample, which is the complement of the quantum yield. It should be noted that, even in a sample with 100 % quantum yield, heat is still deposited because of the difference in energy between absorbed and emitted photons.

Although a reference sample still must be used, the only property it must have is zero quantum yield, which is a far less stringent requirement than having an accurately characterised quantum yield. Materials such as fluorescein quenched with potassium iodide, collodial graphite and aniline black are all suitable for non-fluorescent reference samples[198].

The temperature rise can be measured directly using a thermocouple or thermopile[199, 48, 200, 198, 201, 202]. However, this requires that the sample be placed in a well-insulated chamber to isolate it from temperature flucuations of the surrounding atmosphere. Construction of chambers with sufficiently low heat loss is difficult[190]. Along with the difficulty of measuring the small temperature changes (on the order of milliKelvin[190]), this limits the accuracy of direct thermal measurements to around ±10 %.

By using a modulated exciation source (for example, a chopped xenon lamp, or a pulsed laser), the sample can be made to undergo periodic variations in temperature. This results in periodic expansion and contraction of the sample. The sound wave produced in the surrounding atmosphere can be detected using a sensitive microphone, for example a gas microphone[108]. This technique is called photoacoustic spectroscopy. Put simply, the magnitude of the sound wave detected is proportional to the amount of heat deposited in the sample by the nonradiative relaxation of the dye molecules. By comparing the magnitudes obtained from both the fluorescent sample and the non-fluorescent reference, the quantum yield can again be determined[108]. The accuracy is again around ±10 %. This technique, however, while more convenient than direct measurement of temperature, still requires specialised equipment (anechoic chamber, sensitive microphone).

The temperature rise of the sample can also be determined by measuring the change in refractive index, as most materials exhibit a change in refractive index with temperature. For example, dn/dT for PMMA is -1.1x10^{-4} K^{-1}[203]. The decrease is

attributed to expansion of the material and the increasing intermolecular distance. This basic principle is used in a technique called thermal-lens spectrometry to determine the quantum yield of a fluorescent sample[204, 205, 206, 207, 208, 209]. Samples for this technique can be either solid or liquid but must be non-scattering and have optical-quality flat, parallel surfaces[204]. This is ideally suited to measuring fluorophores in PMMA, as this host material is usually cast in thin sheets in a glass mould. A Gaussian laser beam, of suitable wavelength to excite the fluorophore, is passed through the sample. A fraction of the beam is absorbed and excites the fluorophore molecules in the illuminated region. Any heat released by non-radiative relaxation is deposited in the host material and raises its temperature. This results in a change in refractive index of the host material, which is greatest at the centre of the laser beam where the intensity is highest. This refractive index gradient acts as a lens and causes the laser beam to diverge if dn/dT is negative. The rate of formation of this "thermal lens" is proportional to the amount of heat deposited in the sample. Once again, the fluorescent sample can be compared with a non-fluorescent reference and the quantum yield determined from the relative amounts of heat deposited.

It is claimed this method has accuracies approaching $\pm 3\,\%$[204]. However, its applicability is limited by the need for optically flat, non-scattering samples within a certain range of thicknesses[210, 211, 212]. Sample and reference must be carefully placed relative to the waist of the focussed laser beam and, if a separate probe beam is used to detect the thermal lens, both excitation and probe beam must be accurately aligned[213].

The thermal-lens technique is described in detail in Chapter 3, where a dual-beam system is constructed. However, despite a good experimental setup, it was found impossible to obtain results which were either repeatable or which agreed with values obtained from other methods. The reasons for this remain unknown.

The final technique for measuring quantum yields described here is based on photon-counting using an integrating sphere[214, 215, 216, 217, 218, 219] and is the method used for determining the quantum yields presented in Chapter 4. A spectrofluorometer is used to both excite the fluorescent sample and to measure its emission. The sample is placed at the centre of an integrating sphere which averages the emission over all

directions, eliminating errors due to non-isotropic emission. The detection monochromator is operated in photon-counting mode. The number of photons absorbed by the sample is calculated from the difference in the excitation spectra recorded both with and without a sample present in the sphere. The number of photons emitted is obtained from the emission spectrum. From this, the quantum yield can be obtained from a simple calculation[216].

The main advantages of the integrating-sphere technique are its applicability to a wide range of sample configurations, both solid and liquid. Samples do not need optical-quality surfaces and scattering can be tolerated. It is also unneccesary to use a reference sample of either known or zero quantum yield, unlike previous methods. Single-measurement accuracies using this technique are also $\pm 10\,\%$, although some groups claim as low as $\pm 3\,\%$[218, 220, 219]. We will see later that it is possible to achieve a better accuracy by studying the progression of measured quantum yields with increasing re-absorption. This technique is described in detail in Chapter 4.

1.8 Thesis overview and goals

We have seen the history and development of the luminescent solar concentrator and also the challenges in improving device performance. This thesis presents the results of several areas of research on different aspects of LSC design.

The equipment and materials used in the project, including the different fluorophores studied, optical measurement equipment, PMMA casting techniques, Monte-Carlo ray-tracing simulation programs, and LSC construction and characterisation techniques, are described in Chapter 2. Several novel construction details are proposed, including techniques of cell solder and attachment of the cells to the sheet edges.

One of the criteria for a successful device is a high fluorophore PLQY, which is especially important if the fluorophore exhibits re-absorption losses. The PLQY and optical properties of the fluorophore must be known accurately, and must also be measured in the actual LSC host material, if the performance of the LSC is to be studied or simulated with a view to optimisation. To this end, the optical properties

of a range of different fluorophores were studied in PMMA hosts using a variety of techniques. Initially, the thermal-lens technique was attempted in order to measure PLQY, but proved unreliable. A detailed description of the technique and the results are, however, presented in Chapter 3. The integrating-sphere technique was used instead and the PLQYs of the different fluorophores were successfully measured. The absorption and emission spectra were also measured using traditional spectrophotometry. The results of these measurements are presented in Chapter 4 and allow the suitability of the fluorophores for LSC use to be determined.

A major loss mechanism in LSCs is re-absorption, as described previously. To accurately study the re-absorption losses in an LSC containing an organic dye, the absorption spectrum must be known to a high degree of accuracy, because of the long pathlengths involved. In Chapter 5, a technique is devised to measure both the absorption spectrum of the dye and also the re-absorption losses, based on fluorescence measurements from a strip sample of LSC material. The losses for both an organic dye and a rare-earth complex are compared and it is found that, despite the lower PLQY, a rare-earth complex can result in a higher number of photons reaching the edge because of the absence of re-absorption. This demonstrates that rare-earth complexes are an extremely promising step in LSC development.

In Chapter 6, a ray-tracing simulation program is used to simulate LSC modules containing a range of different dyes and dye mixtures (both visible- and NIR-emitting), with a view to maximising the efficiency. A detailed study is also performed of the effects of a range of module parameters (for example, back reflector, dye concentration, module dimensions) on the device efficiency and operating losses. This is essential, as all parameters of an LSC device are interdependent (for example, the effect of sheet thickness changes depending on the dye concentration). An analysis of the cost and embodied energy of LSC modules is also carried out and compared with conventional PV.

Finally, in the logical conclusion, the information gained from the optimsation simulations performed in Chapter 6 is used to design and construct several LSC modules using organic dyes and the performance of these is measured under illumination with a solar simulator. The results are presented in Chapter 7. The technique of current

matching of the edge cells is successfully demonstrated.

Chapter 2

Materials and methods

This chapter details the main experimental materials and techniques used in this project, including the different fluorophores used, spectrometry, PMMA casting, ray-tracing simulations, solar cells and LSC construction and characterisation methods. The sections overlap somewhat, as different experiments may require the use of the same equipment.

2.1 Fluorophores

Four main classes of luminescent fluorophores were studied in this project: visible-emitting organic dyes, NIR-emitting organic dyes, rare-earth nanoparticles and rare-earth complexes. The history and development of these have been described previously (Section 1.4). More specific details, such as naming and structure, are discussed here.

2.1.1 Visible-emitting organic dyes

Five visible-emitting organic dyes were chosen from the Lumogen F range developed and manufactured by BASF[63, 48]. Their names and formulae are listed in Table 2.1. Both the full name (e.g. Violett 570) and the abbreviation (e.g. V570) will be used in this thesis.

Table 2.1: BASF Visible Organic Lumogen Dyes

Name	Abbrev.	Type	Formula
Violett 570	V570	Naphthalimide[63]	4,5-dimethyloxy-N-(2-ethyl hexyl) naphthalimide[221]
Gelb 083	G083	Perylene[63]	isobutyl 4,10-dicyanoperylene-3,9-dicarboxylate[222, 221]
Gelb 170	G170	Perylene[223]	N/A (not currently a commercial product)
Orange 240	O240	Perylene[63]	perylene-3,4,9,11-tetracarboxylic acid bis-(2',6'-diisopropylanilide)[221]
Rot 305	R305	Perylene[63]	perylene-1,8,7,12-tetraphenoxy-3,4,9,10-tetracarboxylic acid bis-(2',6'-diisopropylanilide)[221]

The dyes are based on either perylene or naphthalimide structures and are readily dissolved in a wide range of organic solvents (such as dichloromethane, toluene, methyl methacrylate, chloroform or acetone), which makes their incorporation into a range of polymeric hosts possible. They are also resistant to temperature, as they were developed to be suitable for injection-moulding processes where temperatures may reach several hundred degrees. The densities and molecular weights of the dyes are listed in Table 2.2.

Table 2.2: Lumogen dye densities and molecular weights

Dye	Density (g/cm^3)	Mol. wt. (g/mol)
Violett 570	1.28	370
Gelb 083	1.27	503
Gelb 170	1.31	507
Orange 240	1.36	711
Rot 305	1.4	1079

2.1.2 NIR-emitting organic dyes

Three NIR-emitting organic dyes were studied in this project. These were developed by BASF for use in LSCs and are designated by KF402, NIR1 and NIR3. The chemical structures of each of the dyes, along with the reference where they were published, are shown in Table 2.3 and their molecular weights in Table 2.4. Their quantum yields

are claimed to be as high as 92 % for KF402[48].

Table 2.3: NIR dye structures

Dye	Structure	Type	Reference
KF402	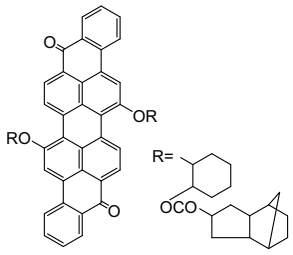	Isoviolanthrone	7e of Seybold[48]
NIR1	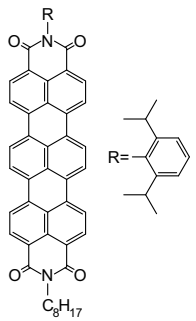	Terrylenimide	4a of Holtrup[46]
NIR3	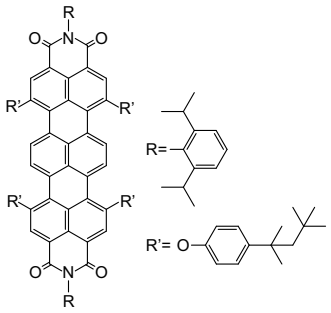	Terrylenediimide	20a of Nolde[47]

Table 2.4: NIR dye molecular weights

Dye	Mol. wt. (g/mol)
KF402	825
NIR1	1540
NIR3	835

2.1.3 Rare-earth nanoparticles

Rare-earth nanoparticles have been developed by Clemson University[125, 126, 127, 128]. They consist of tiny particles (5-10 nm diameter) of LaF_3 doped with either neodymium or ytterbium in varying proportions. To dope the particles into PMMA, they are first dispersed in a small amount of tetrahydrofuran (THF) with ultrasonic agitation and then added to the monomer. Although the particles do not actually dissolve (since they are inorganic), they do not scatter light because their diameter is much smaller than visible wavelengths.

The four different nanoparticle compositions studied are:

- NdF_3
- $Nd_{0.5}La_{0.5}F_3$
- $Nd_{0.2}La_{0.8}F_3$
- $Yb_{0.15}La_{0.85}F_3$

2.1.4 Rare-earth complexes

A rare-earth complex containing europium as the emitting ion was studied in this thesis. It is designated as "MO49" and its structure is shown in Fig. 2.1. It was developed and produced by Edinburgh University[140]. It can be doped into PMMA in the same manner as the organic dyes, by dissolving in the monomer prior to polymerisation. The combination of a bis(2-(diphenylphosphino)phenyl)ether oxide (DPEPO) ligand and three hexafluoroacetylacetonate (hfac) co-ligands results in a single absorption peak at 300 nm[140, 154].

2.2 Spectrometry

Several different spectrophotometers and spectrofluorometers have been used to measure the optical properties of the host PMMA and the fluorophores.

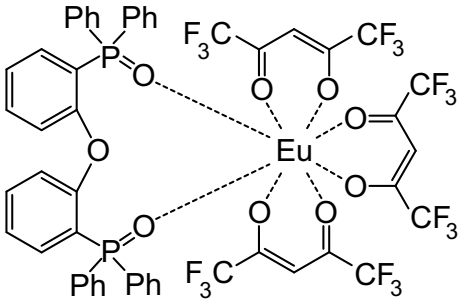

Figure 2.1: Structure of MO49 europium complex

A standard UV/visible spectrophotometer (Shimadzu UV-1601) was used for measuring the host absorption coefficient and refractive index and for determining the absorption spectra of the different fluorophores. This is a single-beam instrument, capable of scanning from 300 nm to 1100 nm using both tungsten-halogen and deuterium lamps as light sources. The detector is a silicon photodiode. Although the control software is capable of calculating "absorption coefficient" directly, it was unclear whether this referred to Decadic or Napierian coefficients (see below). Therefore, the spectrometer was always used to measure the percent transmission of samples and calculations were performed manually later to determine the absorption coefficient.

There is often confusion in the literature about which type of absorption coefficient is being referred to, whether it is Decadic or Napierian. Decadic coefficients are based on using the power of 10 in the Beer-Lambert law[224, 38], while Napierian coefficients use the power of e instead[225]. To avoid confusion, all coefficients referred to in this thesis are **Napierian**.

By measuring the transmittance of samples, it is possible to use the Beer-Lambert law to calculate the host absorption coefficient, host refractive index, and the absorption coefficient of the dye or fluorophore. These procedures are described below.

2.2.1 Spectrophotometry

In order to calculate the absorption coefficient of dyes in a host matrix, it is necessary to know the reflectance of the host material at different wavelengths. Reflectance varies with wavelength, since refractive index is wavelength-dependent. It is possible

to calculate both the host refractive index (and hence reflectance) and absorption coefficient simultaneously by measuring the fractional transmittances of two samples of the undoped host material of different thickness (for example, as used later in Section 2.3.4, 23.9 mm and 3.25 mm).

Eqns. (2.1) and (2.2) are the Beer-Lambert law for the two samples of different thickness. T_1 & T_2 are the fractional transmittances, R is the reflectance of a single host:air boundary, α is the Napierian absorption coefficient (units of cm^{-1}) of the host material and t_1 & t_2 are the thicknesses.

$$T_1 = (1-R)^2 e^{-\alpha t_1} \tag{2.1}$$

$$T_2 = (1-R)^2 e^{-\alpha t_2} \tag{2.2}$$

Rearranging, we obtain expressions for both α and R, shown in Eqns. (2.3) and (2.4).

$$\alpha = \frac{ln\left(\frac{T_1}{T_2}\right)}{t_2 - t_1} \tag{2.3}$$

$$R = 1 - \sqrt{T_1}\left[\frac{T_1}{T_2}\right]^{\frac{t_1}{2(t_2-t_1)}} \tag{2.4}$$

The refractive index can then be calculated from $n = (1+\sqrt{R})/(1-\sqrt{R})$. As shown later (Section 2.3.4), the Cauchy relation can be used to determine the refractive index, and hence reflectivity, at any measurement wavelength.

Once the host reflectance has been calculated, it becomes possible to measure the absorption coefficient of the dye or fluorophore present in the sample. Since it has become common practice in this project to produce dyed samples on the basis of a concentration of dye in parts-per-million by weight (ppm), it was decided to calculate the "Napierian ppm absorption coefficient" with units of ppm^{-1} cm^{-1}.

To determine the dye absorption coefficient, it is necessary to correct for the absorption of the host material. To achieve this, the fractional transmittance spectra of both

a clear (sample #1) and a dyed (sample #2) sample are measured. Eqns. (2.5) and (2.6) are the fractional transmittances of the undyed and dyed samples, respectively.

$$T_1 = (1-R)^2 e^{-\alpha t_1} \tag{2.5}$$

$$T_2 = (1-R)^2 e^{-\alpha t_2} e^{-\varepsilon c t_2} \tag{2.6}$$

Here, ε is the Naperian ppm absorption coefficient of the dye and c is its concentration in ppm by weight. ε can be obtained from Eqn. (2.7), obtained by rearranging Eqns. (2.5) and (2.6).

$$\varepsilon = \frac{1}{ct_2} ln \left\{ \frac{(1-R)^2}{T_2} \left[\frac{T_1}{(1-R)^2} \right]^{\frac{t_2}{t_1}} \right\} \tag{2.7}$$

Note that the absorption coefficient determined in this way is only valid for the host material in which the data were measured (because it is based on a concentration in ppm by weight). The absorption coefficient in another material depends on the relative densities of the two materials and can be calculated from $\varepsilon_{other} = (\rho_{other}/\rho_{original})\varepsilon_{original}$.

Another way of quantifying the amount of fluorophore present in a sample is by the optical density (OD). This is related to the transmittance T by $OD = -log_{10}T$ (note the base-10 logarithm, which is normal for the standard definition of OD[225]).

2.2.2 Measurement of fluorescence spectra

To measure the emission spectra and quantum yield of fluorescent samples, two different spectrofluorometers were used, differing mainly in the range of emission wavelengths detectable. The first, a Jobin-Yvon Fluoromax 3, was used for measurements on the visible-emitting fluorophores, with emission wavelengths up to 850 nm. This was the limit of detection of the photomultiplier tube used (Hamamatsu R928). Later in the project, access was gained to an Edinburgh Instruments F900 spectrofluorometer. This used both visible (Hamamatsu R928) and infrared (Hamamatsu R5509)

photomultipler detectors, enabling emission measurements up to 1600 nm to be performed. This was used for quantum yield and emission measurements of the NIR-emitting organic dyes.

Both spectrofluorometers use a 150W xenon arclamp as the excitation source. Excitation wavelengths in the range 250-1000 nm were available by adjusting the excitation monochromator. When making measurements of emission spectra, care was taken to avoid second-order detection of scattered excitation light. This is a feature of all monochromators - in addition to passing the primary wavelength, they will also pass multiples. For example, if a sample is excited at 400 nm and some of this is scattered into the detection monochromator, a peak will be recorded at 800 nm (twice the excitation wavelength). This can easily be avoided by placing a long-pass filter between the sample and the detection monochromator to block the excitation light but transmit the fluorescence being measured. Correction must then be made for the transmission spectrum of the filter.

Difficulties were experienced in measuring the PLQY of some of the NIR-emitting organic dyes. To calculate the PLQY, both excitation and emission spectra need to be recorded. However, the measurement of these spectra for the NIR-emitting dyes required the use of both the UV/Vis and NIR detectors, since neither can detect both the excitation and emission wavelengths. Since the NIR detector requires a different calibration file and slit widths, the raw data from it cannot be compared directly with that from the visible detector. To correct the data, both the visible and NIR detectors were used to measure the emission from a compound in a region where both detectors are sensitive - the sample used was one containing 94 ppm of NIR1 and the wavelength region scanned was 700-750 nm. By dividing the spectra obtained from each detector, it was possible to obtain a correction factor which could be applied to data from the NIR detector to normalise it to the visible detector and make it possible to calculate the quantum yield.

For measurement of the edge-emission spectra from sheet samples (Section 5.3), a Jobin-Yvon iHR320 spectrometer equipped with a R928 photomultiplier detector was used. The light source was a combined 150W xenon / 80W tungsten-halogen lamp with a monochromator (Bentham). Light delivery was provided by a 6 mm diameter

fibre optic bundle.

When attempting to measure the molecular emission spectrum of a luminescent species which has a small Stokes shift, it is important to minimise the effects of re-absorption of the emitted light within the sample. In organic dyes, for example, this leads to an apparent reduction in the intensity of the low-wavelength end of the emission spectrum and an overall red-shift. Two measures were taken to prevent this when measuring the molecular emission spectrum. Firstly, samples with an extremely low concentration of fluorophore were used. The peak optical density of the sample was typically on the order of 0.01. Although this optical density is very low, there was still sufficient emission present to give a detectable signal.

Secondly, the sample was excited close to its edge and emission light detected from the same region. This ensures that the pathlength of the emission light within the sample is at its absolute minimum and that the amount of re-absorption is also minimised.

The excitation/emission arrangement is shown in Fig. 2.2. The disc samples (Section 2.3.5) made for the integrating sphere were used. These were held in the sample compartment of the spectrofluorometer using a bulldog clip. Excitation and emission are at right angles. A long-pass filter was used, when required, to prevent second-order detection of scattered excitation light.

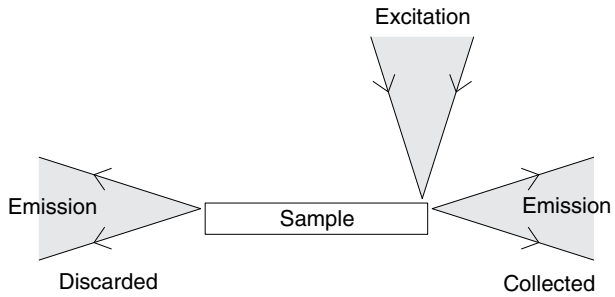

Figure 2.2: Measuring molecular emission spectrum

2.2.3 Integrating sphere

The integrating sphere was used for measuring the photoluminescent quantum yield (PLQY) of different fluorophores. The sphere used here was supplied by Jobin-Yvon for use with their Fluoromax 3 spectrofluorometer but it was also used with the

Edinburgh Instruments F900. It consists of a perfect hollow sphere, 10 cm diameter, machined from a solid piece of Spectralon diffuse reflecting material[226]. This material is based on sintered PTFE and exhibits an extremely high Lambertian reflectance over the visible/NIR region. A plot of its reflectance is shown in Fig. 2.3. The reflectance is greater than 99 % over the range 350-1300 nm.

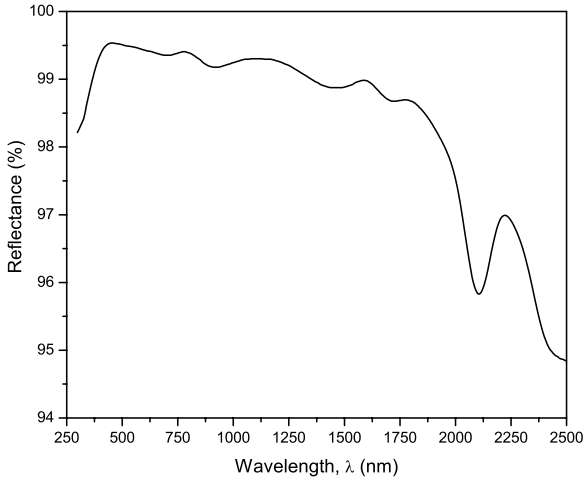

Figure 2.3: Reflectance of Spectralon material[226]

Two 20 mm diameter ports are machined into the sphere, giving a port area of 2 % of the total sphere surface area. These serve as entrance and exit ports for the excitation light and fluorescence emission, respectively. Either solid (11 mm diameter discs) or liquid (5 mm diameter cylindrical fused silica cuvette) samples can be mounted at the centre of the sphere. A circular baffle of Spectralon is placed over the exit port to prevent light emitted from the sample from reaching the detector directly and thus ensuring that all detected light has made at least one reflection from a Spectralon surface. A photo and internal diagram of the sphere and holders is shown in Fig. 2.4.

The sample holder can be rotated from outside the sphere. It was found that a variation in angular position of the holder of 5° did not affect the PLQY results obtained. The holder for solid samples was positioned so that any specularly reflected excitation light struck the wall of the sphere instead of being reflected back out the entrance port.

The theory and use of the integrating sphere are described in detail in Chapter 4, where it is used to measure the PLQY of both the organic dyes and rare-earth com-

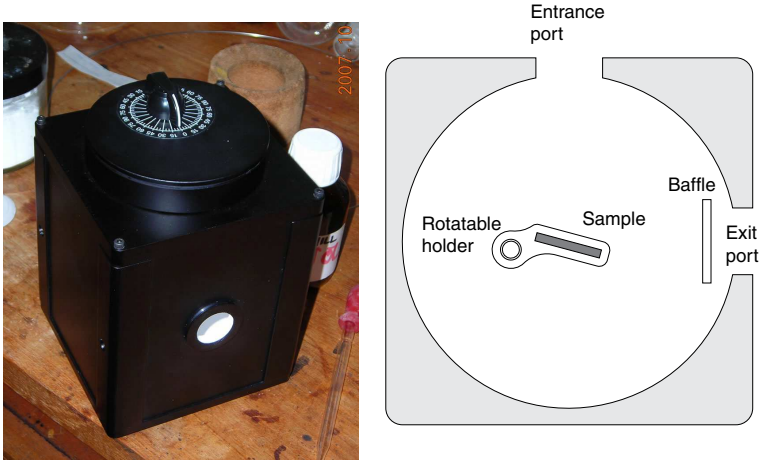

Figure 2.4: Integrating sphere

pounds.

2.2.4 Intensity-stabilised lamp

For some experiments, an intensity-stabilised light source was required which could illuminate at least a 10 cm x 10 cm area (the size of a typical experimental LSC module) with a uniform intensity. The author constructed a system based on a standard 500 W halogen outdoor floodlamp using pulse-width modulation (PWM) to regulate the lamp intensity. The circuit diagram of the system is shown in Fig. 2.5.

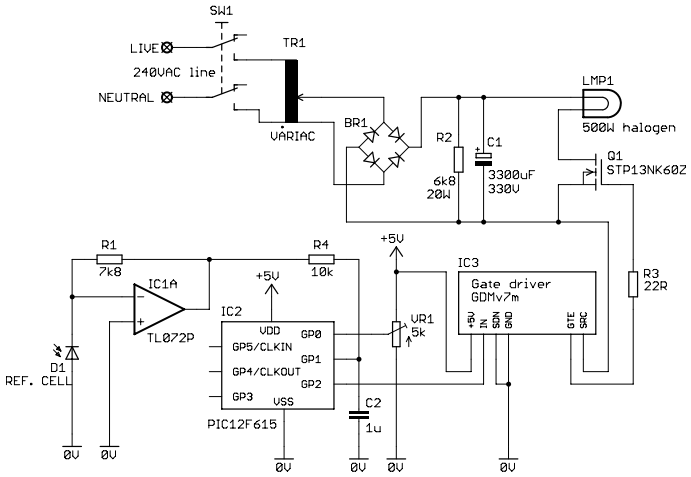

Figure 2.5: Intensity-stabilised lamp circuit

The output from variable transformer TR1 is rectified and smoothed to provide a DC supply on C1. Power MOSFET Q1 is used to switch the lamp current in response

to the PWM signal. The lamp is normally intended for operation from 240 VAC mains. The DC link voltage was therefore set slightly higher than this, at 270 V. When the lamp is operated at its rated intensity, the duty cycle of the PWM signal is approximately 90 %. This allows for some variation in the mains voltage whilst still providing intensity regulation.

The lamp is placed approximately 3 m from the sample to be illuminated to ensure a uniform intensity. A small solar cell D1 is placed near the sample, pointing towards the lamp. This measures the lamp intensity. IC1A and R1, configured as a current-to-voltage converter, turn the short-circuit current from D1 into a voltage proportional to the lamp intensity. Pot VR1 provides an adjustable setpoint voltage. Both the setpoint and the current lamp intensity are measured by IC2, a PIC microcontroller. The GP2 output pin is configured as a PWM output with a base frequency of around 8 kHz. IC3, the gate driver, provides isolation between the logic-level PIC circuit and the MOSFET/lamp circuit, which is floating at mains voltage.

The PIC runs a simple regulation loop. During each cycle of the loop, it measures the reference cell output and the setpoint. It then increases or decreases the PWM duty cycle by an amount proportional to the difference between the two. This can be represented by the iterative equation $duty_{new} = duty_{old} - [gain \times (current - setpoint)]$, where the error gain *gain* is found by experiment. It is chosen to achieve a stable, damped response to any fluctuations in mains voltage.

The stability of the lamp output both was measured both with and without regulation, as shown in Fig. 2.6. The PIC regulates the intensity to ± 0.03 %, compared with ± 1.5 % without regulation - an improvement of 50 times.

2.3 PMMA casting and properties

PMMA provides an ideal medium for LSC construction because of its high transparency and the ease of incorporation of fluorophores into the material. It can be cast in either bulk or sheet form. Sheets cast in a glass-plate mould (described below) have optical-quality flat surfaces. The basic casting chemistry and procedure will be

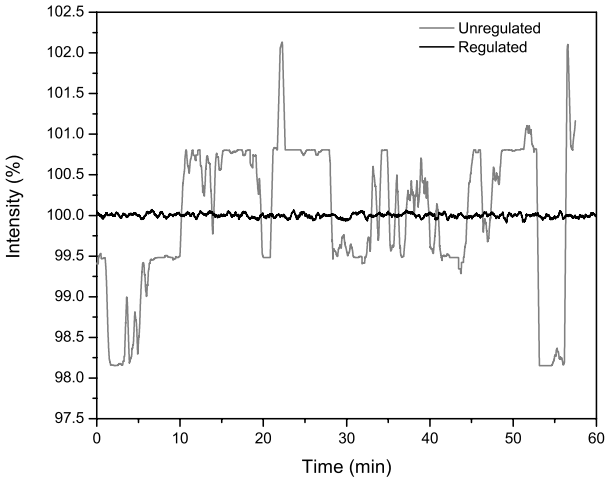

Figure 2.6: Stabilty of lamp with and without regulation

described in the following sections.

The structures of both methyl methacrylate and poly-(methyl methacrylate) are shown in Fig. 2.7. The monomer is liquid at room temperature. To induce polymerisation, a free-radical initiator such as benzoyl peroxide (BPO) or azobisisobutyronitrile (AIBN) is used. Under the action of heat, the initiator decomposes and generates free radicals which cause the monomer to polymerise[227].

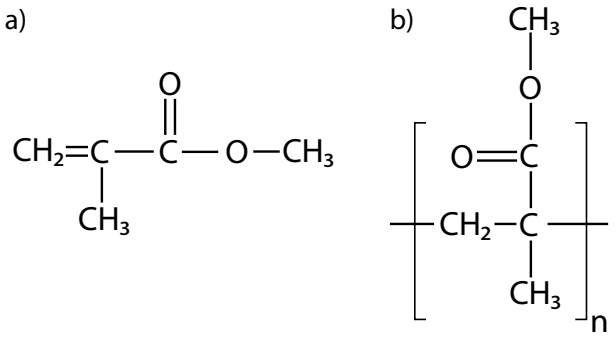

Figure 2.7: Structures of a) monomer and b) polymer

The reaction is exothermic and, if the temperature is not controlled, the monomer can reach boiling point. To prevent this, an autoclave can be used to pressurise the reaction mixture and raise the boiling point. Alternatively, a water bath, which conducts heat away from the reaction mixture, can be used to keep the temperature constant.

The density of the polymer (1.19 g/cm^3) is greater than that of the monomer (0.94 g/cm^3). As a result, the reaction mixture shrinks in volume by around 20 % upon polymerisation[227]. The shrinkage can be reduced slightly by starting with a polymer/monomer syrup instead of pure monomer, but it is still present and allowances have to be made for this in the design of the casting mould.

Two casting techniques (waterbath and autoclave) are described next. Because it is widely used in industry and the commercial production of PMMA sheet, the waterbath process was the main one used to prepare PMMA samples used in this project. The autoclave process is described briefly for completeness, as it is the method the author initially used before learning of the waterbath process.

2.3.1 Waterbath casting

This technique is used predominantly to cast flat sheets of PMMA. A monomer/polymer mixture is used as the precursor. As this already contains polymer, it helps to reduce shrinkage. In addition, because this mixture has a high viscosity, it is easier to handle and pour into the mould.

The mould consists of two plates of float glass, separated by a resilient gasket which allows the plates to move together as the reaction mixture shrinks. This technique was first invented by O. Rohm in 1937[228, 229]. The glass plates are normally made of toughened glass (for large-scale casting), but it is sufficient to use normal soda-lime float glass for small ($\sim$20 cm square) sheets. The glass should be quite thick, >6 mm, to prevent bending.

The design of the gasket is critical. It must be soft enough to allow the plates to move together, yet must also seal the mould successfully and prevent leakage. Lucite use a gasket made from extruded plasticized PVC. Although this remains attached to the edge of the PMMA sheet once cast, it can be easily cut off and discarded. Several different thicknesses of gasket are shown in Fig. 2.8. The final thickness of the PMMA sheet cast from a mould using these gaskets is less than the original thickness of the gasket, as a result of both physical compression of the gasket by the clips holding the mould together and the shrinkage of the PMMA itself. The long

side of the "L" shaped cross-section provides good adhesion to the glass and prevents the gasket slipping in the mould.

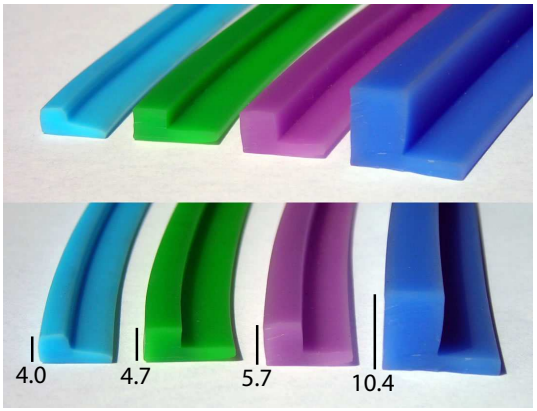

Figure 2.8: Mould gaskets. Thickness (in mm) shown.

The gasket is placed around three sides of the mould plates and the plates are clamped together with standard "fold-back" stationery clips. This leaves an open edge, into which the casting syrup will be poured, and a free gasket tail. To fill the mould, it is placed vertically and a funnel made from rolled-up overhead transparency film is used. Once the mould has been filled, the tail is pressed in between the plates and another clip is applied to that edge to keep the mould closed.

An example of a mould before and after filling is shown in Fig. 2.9. This mould is used for casting small (∼5 cm square) sheets. For larger moulds, several clips are placed along each edge.

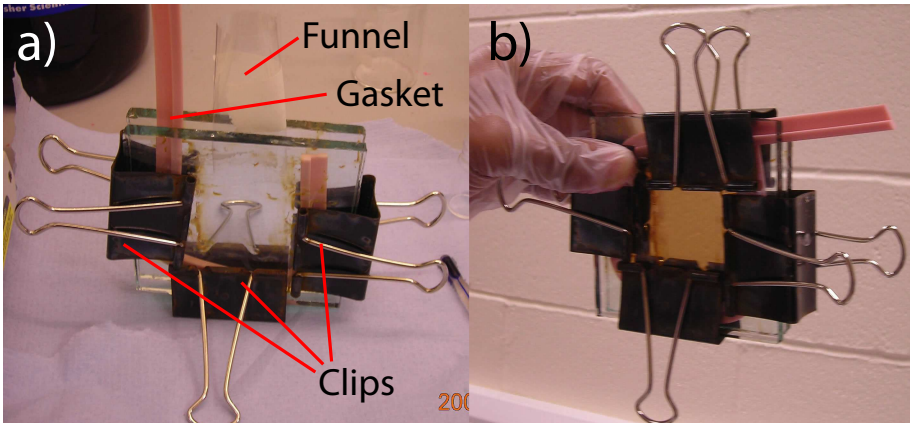

Figure 2.9: Casting mould a) before and b) after filling

The water bath used (Mega Electronics) was originally designed for PCB processing.

It was chosen for its large depth/width aspect ratio which makes it ideal for curing the plate moulds. Moulds up to 30 cm square have been cast in this tank.

The casting procedure is described below. Monomer and polymer powder were obtained from Lucite. The monomer contains 5 ppm w/w of Topanol inhibitor to prevent the monomer polymerising by itself in storage. The initiator which is added later overcomes this inhibitor. The polymer powder is pure PMMA. The initiator used was AIBN, also obtained from Lucite.

1. Monomer and polymer are weighed out in the ratio 9:1 of monomer to polymer. Enough is made to fill the mould used. The polymer powder will later be dissolved in the monomer to form a casting syrup.

2. If a dye needs to be incorporated into the final product, it is dissolved into the bulk of the monomer at this stage, rather than attempting to dissolve it in the syrup later. The lower viscosity of the pure monomer makes it easier to dissolve. An ultrasonic bath was found to help dissolving.

3. The monomer is heated to 60°C on a heated magnetic stirrer and the polymer powder added gradually while stirring to prevent clumping. The mixture is stirred vigorously for around 1 hr. After this time, the polymer powder will have dissolved, yielding a clear, syrupy liquid. This is the casting syrup. It only contains monomer, polymer and dye. Initiator is added next.

4. The syrup is removed from the heat source and allowed to cool to room temperature (either naturally or with a cold water bath). If initiator were added when the syrup was still hot, polymerisation would start and the syrup would thicken, making it difficult to pour into the mould. The amount of initiator (AIBN) used is 0.08 % by weight of the casting syrup. It is weighed into a small bottle and then dissolved with a small amount of pure monomer. This is then added to the casting syrup which is stirred thoroughly again using the magnetic stirrer to disperse the initiator throughout the mixture. The casting syrup is now ready to pour into the mould.

5. The mould has been prepared previously as described above. It is held vertically with the open edge uppermost. The casting syrup is poured in a continuous

stream (to prevent trapping bubbles) into the mould. Once filled, the loose tail of gasked material is tucked in. Care is taken to ensure the gasket squeezes a little of the syrup out the top of the mould - this ensures there are no air spaces inside the mould. Clips are then placed on the top edge of the mould to hold it closed.

6. The waterbath is heated to 60° and the mould placed in the water. This will start the polymerisation. The mould is normally left in the bath for about 18 hours to complete the first stage of polymerisation - the mould is usually placed in the bath in the evening and removed the next morning.

To summarise:

1. Weigh out monomer and polymer powder in 9:1 ratio
2. Dissolve dye in monomer if required
3. Using a heated magnetic stirrer at 60°, dissolve polymer in monomer to make syrup
4. Cool syrup to room temp and add 0.08 % w/w of AIBN initiator
5. Fill mould and seal
6. Place in waterbath at 60° for 18 hours to cure

A sample produced by this technique is shown in Fig. 2.10. The gasket is still attached to the edges. However, it can easily be cut off (Section 2.3.5).

Although this will result in a solid product, the sheet still needs to be post-cured to remove the residual monomer. This is described later in Section 2.3.3.

Nearly all of the samples used in this thesis were prepared using the waterbath technique. The several samples which were made using the autoclave are identified where they appear in the text.

Figure 2.10: Sample produced using waterbath casting

2.3.2 Autoclave casting

This was the first technique the author used. While this technique is simpler than the waterbath, it is limited to small samples, because they need to be cured inside an autoclave, and is only described here for completeness.

The technique is based on mixing equal quantities of monomer and an initiator-containing polymer powder (type D-88/S, Makevale Ltd.). The monomer is the same as in the waterbath technique. However, the PMMA polymer powder contains 0.3 % w/w of BPO initiator. Extra initiator does not need to be added.

Because of the much higher proportion of initiator, the reaction rate is much faster compared with the waterbath method. However, because of the higher rate, more heat is generated in the polymerisation and there is a risk of the monomer boiling. To prevent this, an autoclave is used to raise the boiling point of the monomer.

This method was mainly used to make "bulk" samples of PMMA in the form of blocks or cylindrical bars, instead of sheets. The monomer and polymer powder were mixed in a glass test-tube and were cured in the same test-tube. Once cured, it was then broken to remove the rod-shaped PMMA sample, as PMMA releases well from a glass surface.

The procedure is as folllows:

1. Weigh out equal quantities of monomer and polymer powder. Place the powder in a test-tube.
2. Dissolve any dyes required in the monomer at this stage.
3. Add the monomer all at once to the polymer powder in the test-tube. Use a glass stirring rod to agitate the mixture and prevent the polymer settling out. Place the test-tube in a water bath at 50°C and continue stirring. The mixture will start to thicken. Once it is the consistency of syrup, it can be cooled and set aside. If it is desired to pour the mixture into another mould, do so now. Otherwise, leave the mixture in the test-tube. The mixture will appear cloudy - this is because of the suspended polymer powder. It will turn clear once cured.
4. The test-tube is placed in an autoclave and pressurised to 10 bar with pure, dry nitrogen (air cannot be used as oxygen inhibits polymerisation). The autoclave is heated to 75°C for 5 hours using a modified hot-air oven.
5. Once cured, remove the test-tube from the autoclave. The tube should be broken immediately to release the cured PMMA. Otherwise, upon cooling to room temperature, the tube can shatter violently because of the different contraction rates.

To summarise:

1. Measure equal weights of monomer and polymer powder
2. Dissolve dye in monomer
3. Add monomer to polymer in test-tube, heat to 50° on water bath whilst stirring
4. Place in autoclave, pressurise to 10 bar with nitrogen and cure for 5 hours at 75°
5. Remove test-tube and break to remove PMMA

An example of the sample produced by the autoclave casting method is shown in Fig. 2.11. It is formed closely to the shape of the test-tube. The large hollow visible in the middle is because of the shrinkage of the PMMA on curing.

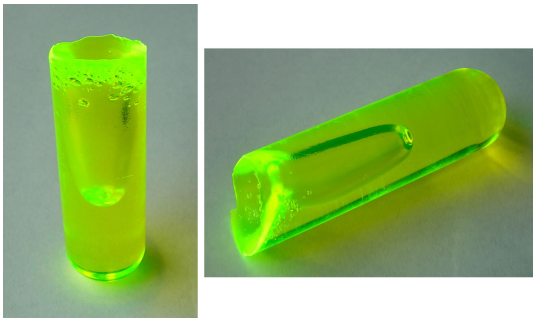

Figure 2.11: PMMA sample produced using autoclave

An autoclave of the required specification could not be purchased at a reasonable cost so a custom-designed one was built. It is shown in Fig. 2.12. A K-type thermocouple monitors the temperature and a release valve set at 13 bar provides protection against over-filling.

Figure 2.12: Casting autoclave

2.3.3 Post-curing

As the polymerisation progresses, the viscosity of the reaction mixture increases. Eventually, the viscosity reaches a point where free radicals produced by the thermal

breakdown of the initiator can no longer reach the monomer and polymer molecules to continue the reaction. The polymerisation stops. However, not all of the initial monomer has been polymerised. Around 15 % of the mixture by weight is unreacted monomer. This increase in viscosity and the associated change in polymerisation rate is called the Trommsdorff effect[230].

The residual monomer content can be determined by gas chromatography. The amount of residual monomer affects both the light stability and optical transparency of the PMMA. An acceptable value in industry is less than 0.5 % of residual monomer.

To continue the polymerisation, the PMMA must be heated above its glass transition temperature (softening point) to allow the free radicals from the initiator to reach the unreacted monomer. This stage is called post-curing and is normally performed in a hot-air oven.

The success of post-curing depends on the mobility of the free radicals produced by the initiator. AIBN generates smaller, higher-mobililty radicals than BPO, so post-curing PMMA prepared using AIBN and the waterbath technique is more effective and results in a lower residual monomer content[231, 227].

Moulds are removed from the waterbath and immediately placed in a hot-air oven at 80°C. The temperatures and times used in the post-curing cycle are shown in Fig. 2.13.

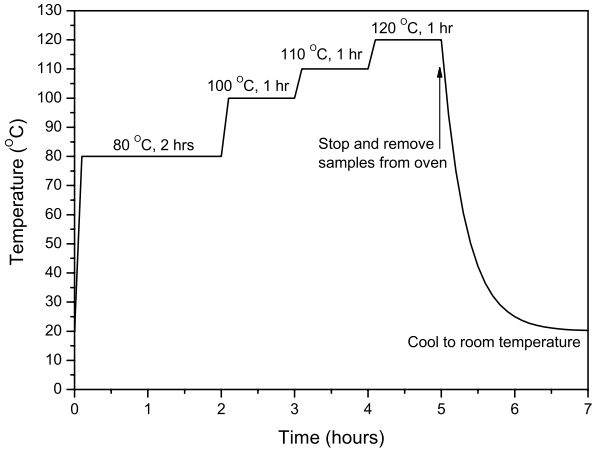

Figure 2.13: Post-curing temperature regime

Once removed from the oven at 120°C, the moulds are allowed to cool to room temperature. The clips are removed and the two mould plates can then be prised apart to remove the PMMA sheet. The PVC mould gasket remains attached, but this can be cut off manually.

After post-curing, the residual monomer content of sheets prepared using the waterbath technique was in the range 0.3-0.5 % w/w. The residual monomer content of PMMA samples from two other manufacturers, Rohm & Haas (Germany) and Chilin (Taiwan) was also measured. Rohm & Haas material had a content of 0.6 %, while Chilin material had a content of 4-6 %. This shows that the Chilin material has not been properly post-cured.

The optical properties of the PMMA are now described.

2.3.4 Optical properties

The absorption coefficient and refractive index of the PMMA sheet prepared using the waterbath method were measured as described in Section 2.2.1. Two samples of PMMA of widely different thicknesses (23.9 mm and 3.25 mm) were used.

The measured absorption spectrum is shown in Fig. 2.14.

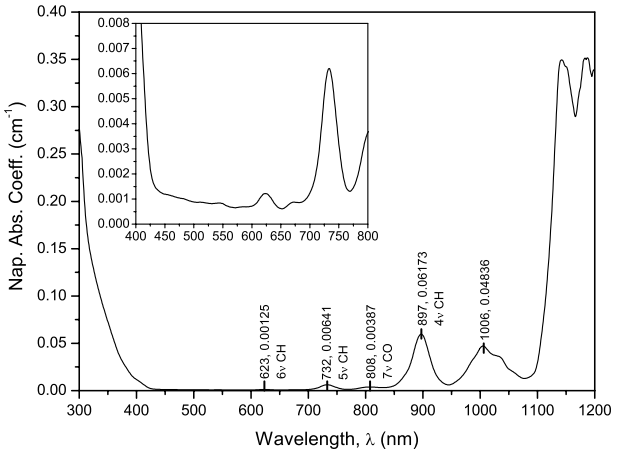

Figure 2.14: PMMA absorption spectrum. Inset: closeup of 400-800 nm.

The inset shows a magnification of the region from 400-800 nm, showing the low

absorption coefficient in the visible part of the spectrum. At wavelengths above ∼700 nm, absorption peaks due to harmonics of the bond stretches become visible. Several of these are identified in Fig. 2.14 as the 4th, 5th & 6th harmonics of the CH stretch and the 7th harmonic of the CO stretch, as calculated by Ballato *et. al.*[36] (Table 1 of that paper). Both the magnitude and profile of the absorption spectrum are in close agreement with that obtained previously (Batchelder [232], Fig. 2, and Friedman[233]).

We will demonstrate briefly how transparent PMMA is to fluorescence light travelling in an LSC. In square LSC modules, the average pathlength for trapped fluorescence light is approximately half the side length. For a 30 cm square module (a typical size), this is 15 cm.

The average absorption coefficient in the visible region is about 0.001 cm^{-1}. Over the 15 cm pathlength, this is equivalent to 98.5 % transmission - extremely high. Moving further into the NIR, the absorption increases. At the 808 nm peak, the absorption is 0.004 cm^{-1}. The transmission over 15 cm is now down to 94 %. At longer wavelengths still, host absorption becomes sufficient to prevent the use of fluorophores emitting at these wavelengths. For example, at 980 nm, the emission wavelength of the ytterbium ion, transmission over 15 cm is now only 52 %.

In short, PMMA can be used satisfactorily for emission wavelengths up to ∼800 nm. Wavelengths above this experience too much absorption to be usable. However, the amount of absorption in the NIR region can be reduced by using deuterated or fluorinated polymers instead [160, 162]. The larger mass of the deuterium and fluorine atoms shifts the bond vibrations to longer wavelengths (lower energies) and reduces the absorption.

Next, the refractive index of the PMMA was calculated from the thick and thin samples. Experimental data were used to obtain values for the refractive index over the range 400-900 nm, where the absorption is relatively small. In order to calculate the refractive index over a wider range, the Cauchy relation[224] was used to fit a curve to the experimental data. The Cauchy equation for the refractive index is given by Eqn. (2.8). The three Cauchy coefficients A, B and C are for wavelengths, λ, in nanometers.

$$n = A + \frac{B}{\lambda^2} + \frac{C}{\lambda^4} \tag{2.8}$$

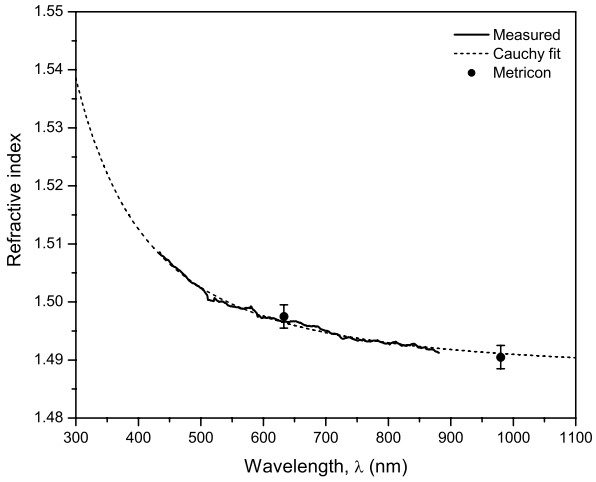

Figure 2.15: PMMA refractive index

The following values for the coefficients were obtained from the fitted curve:

A 1.488

B 3.230×10^3

C 1.216×10^8

These values are in agreement with published values for PMMA [234]. The refractive index was also measured at two discrete wavelengths (632.8 nm and 980 nm) using a Metricon prism coupler[235]. This is based on measuring the critical angle of reflection between the PMMA surface and an optical prism[236, 237]. The two measurement wavelengths were determined by the light sources available - a He-Ne laser and a 980 nm laser diode. The two measured refractive indices are shown on Fig. 2.15 - there is good agreement between them and both the Cauchy and measured refractive index curves.

The refractive indices of some of the Chilin samples were also measured with the Metricon analyser. Refractive indices in the range 1.47-1.48 were obtained. These values are lower because of the higher residual monomer content of the Chilin samples. The refractive index of monomer is 1.41 and this lowers the overall refractive index of the sample.

2.3.5 Sample preparation

The integrating sphere accepts solid samples in the form of a disc, 11 mm diameter and 1.9 mm thick. A lathe was used to turn discs of these dimensions from either the sheet waterbath samples or the bulk autoclave samples. For the waterbath samples, a small piece of sheet was clamped between a rod in the chuck and the revolving centre in the tailstock and turned to diameter. It was then held in a split clamp (Fig. 2.16) and faced off to the correct thickness. Autoclave samples were simply held in the lathe chuck directly and turned down to the required dimensions. The final sample is shown in Fig. 2.17.

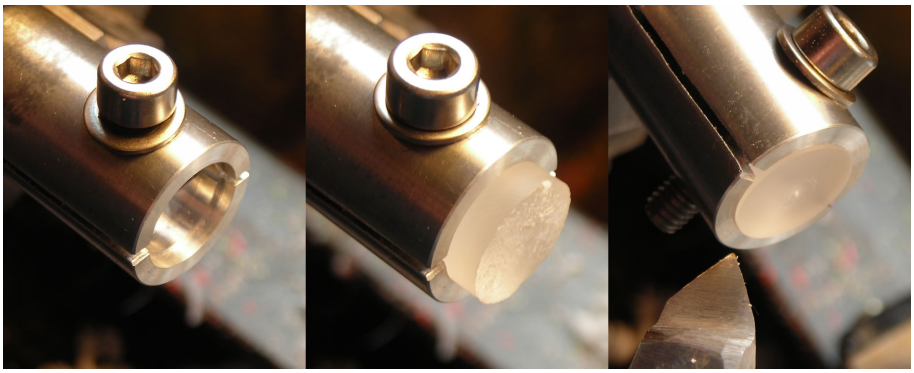

Figure 2.16: Split clamp for machining discs

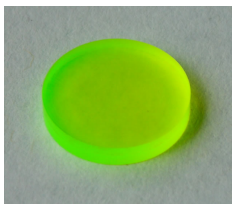

Figure 2.17: Sample for integrating sphere

To prepare square or rectangular sheets suitable for constructing LSC modules or for measurements of the edge-emission spectra, the waterbath sheets need to be cut to an exact size and the edges either machined or polished smooth. The procedure is described briefly here.

When the sheets are removed from the glass-plate moulds, the surfaces are bare PMMA and are prone to scratching when handled. To prevent this, a low-tack protective film (Artcoe[238] "Friskfilm") is applied to both faces. This prevents scratching,

yet can easily be removed later without leaving a residue. The surface is then marked (Fig. 2.18) and a rough square or rectangle cut out by hand with a coping saw.

Figure 2.18: PMMA sheet before cutting, with protective film.

The sheet is then clamped to the bed of a computer-controlled router[239]. The clamping arrangement is shown in Fig. 2.19. The PMMA sheet is sandwiched between two wooden plates which ensure a good clamping force over the entire sheet area. The sheet is then milled to the final dimensions with a milling cutter in the spindle[240].

If it is intended to glue solar cells to the edges of the sheet, the edges are left as-machined, since the slightly rough finish helps the glue to hold. It does not affect the optical path since the glue acts as an index-matching medium. However, if optical measurements are to be performed on the edges they are finished with a diamond edge polisher (Mutronic[241] "Diaplain 6300"). This uses a single-point diamond cutter rotating at ∼20,000 rpm to remove a small amount of material (0.2 mm) and leave a polished edge. The sheet is drawn across the rotating cutter by hand. Fig. 2.20 shows a photo of both the machine and a close-up of the cutting head.

Figure 2.19: PMMA sheet being machined on router

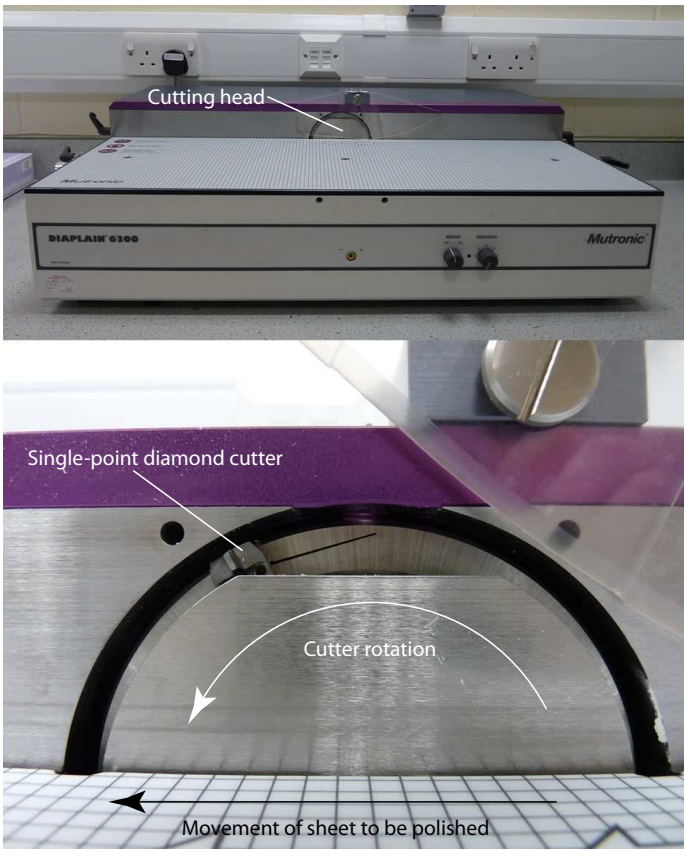

Figure 2.20: Mutronic diamond edge polisher

2.4 Monte-Carlo simulations

In order to optimise the design of luminescent concentrator sheets and, more generally, to predict the behaviour of trapped photons inside LSC sheets, it is vital to have some means of modelling photon transport inside an LSC. A powerful way of doing this is by Monte-Carlo simulations, where a large number of randomly-directed photons are generated by a computer program and followed as they undergo interactions with dye molecules, the host material, reflections from planes in the LSC and detection by solar cells[40, 156, 242, 243, 34].

Two different simulation programs were used in this project. The first, "Raylene", was written in a combination of Microsoft Excel and Visual Basic[34]. Although this has a large number of features and is easy to use, speed is an issue. A batch of simulations to look at different combinations of dye concentrations may have several hundred simulations to run. Depending on the number of rays simulated, this can take weeks to run using Raylene. In addition to limited simulation speed, it does not directly output spectra in terms of photons (for example, the number of photons lost through the escape cones, or the number reaching a back reflector, or the number detected by the solar cells).

The second program, "Raytracer" was written by the author to address these issues. It is written entirely in C++ (Code::Blocks) and is purely text-based. There are several advantages over Raylene. It has a slightly improved model for calculating solar cell electrical output. There is the ability to simulate a back reflector, which can be either diffuse or specular. It can also simulate two LSC sheets in a "stacked" configuration (for example, a visible-only sheet and an NIR-only sheet). Unlike Raylene, it performs the simulation by considering individual photons, rather than "bundles" of several thousand. Each photon can be "tagged" by its type - fluorescence or incident solar. This allows photons to be distinguished when they are detected. For example, it is possible to detect only fluorecsence photons and discard solar photons, despite both types being incident on the solar cells.

The programs were both tested on several different kinds of LSC model to check the results of the author's program. In all cases, Raytracer gave exactly the same results

(within the simulation error) as Raylene. It was also around 40 x faster than Raylene (e.g. one simulation took 350 s in Raylene and 8.5 s in Raytracer).

Although only Raytracer was used to obtain the simulation results presented in this thesis, both programs are described here for completeness. In the section on Raytracer, a detailed explanation is given of several important programming issues relating to the prediction of photon paths.

2.4.1 Raylene

A screenshot of the user page of the program is shown in Fig. 2.21. The different inputs and outputs are described below.

Module dimensions. Two different layers are specified. The bottom layer contains the dye molecules, while the top layer is clear. This is useful, for example, for simulating a thin-film LSC, where a thin layer of luminescent material is applied to a clear sheet. Thicknesses and dimensions are specified.

Incident illumination. The intensity, direction, location and spectrum of the incident illumination can be specified. The program has stored several different solar spectra (AM1.5g, AM1.5d). It can also accept as illumination the fluorescence emission of a previous simulation in an attempt to simulate multiple sheets.

Layer material. The host material of the LSC. Raylene loads the absorption coefficient and refractive index for the selected material from an external file. Again, different materials for the two layers can be specified.

Solar cell parameters. Solar cells will normally be attached to all the edges of the LSC sheet. Their type, fill-factor and open-circuit voltage are specified here. The EQE and reflectance curves for the selected cell type are loaded from another worksheet. It can model mc-Si, sc-Si, CdTe, CIGS, and several others. An assumption is made that the open-circuit voltage of the solar cell is constant and equal to the 1-sun voltage, regardless of the illumination intensity. This is not a valid approximation, because the open-circuit voltage will decrease at lower illumination intensities. A better model is used in Raytracer.

Dyes. Dye concentrations in the bottom layer are entered here. Concentrations are in terms of optical density through the thickness of the sheet. If the sheet thickness is changed, the actual concentration (in ppm) will be changed to keep the OD constant.

Coating material. The different surfaces of the LSC can be coated with different materials. Normally, the top and bottom surfaces are bare (PMMA:air interface) and the sides coated with solar cells.

Convergence params. Here, the number of initial rays and convergence limits are defined. Raylene operates by simulating ray "bundles" which contain several thousand photons. If the "intensity" of the bundle drops below a certain point, then it is discarded. This is supposed to speed up simulations by avoiding following uneccessary rays. However, as described later, Raytracer follows *every* photon to its conclusion (either detected or lost) yet this doesn't affect speed.

Operational outputs. Raylene calculates several module parameters. The most important is module efficiency, which describes the solar-to-electric conversion efficiency of the module (it is assumed the cells are operated at maximum power point). Other outputs include geometrical concentration (edge/surface area ratio) and optical efficiency (fraction of light hitting module which reaches the solar cells).

Power breakdown. Different power losses are calculated here, such as incident power reflected from the module, parasitic absorption by the host material, losses due to non-unity dye quantum yield and absorption by solar cells.

The different graphs show the spectra incident on the front of the module, the total optical density of the sheet, number of dye interactions per initial ray and effective module EQE.

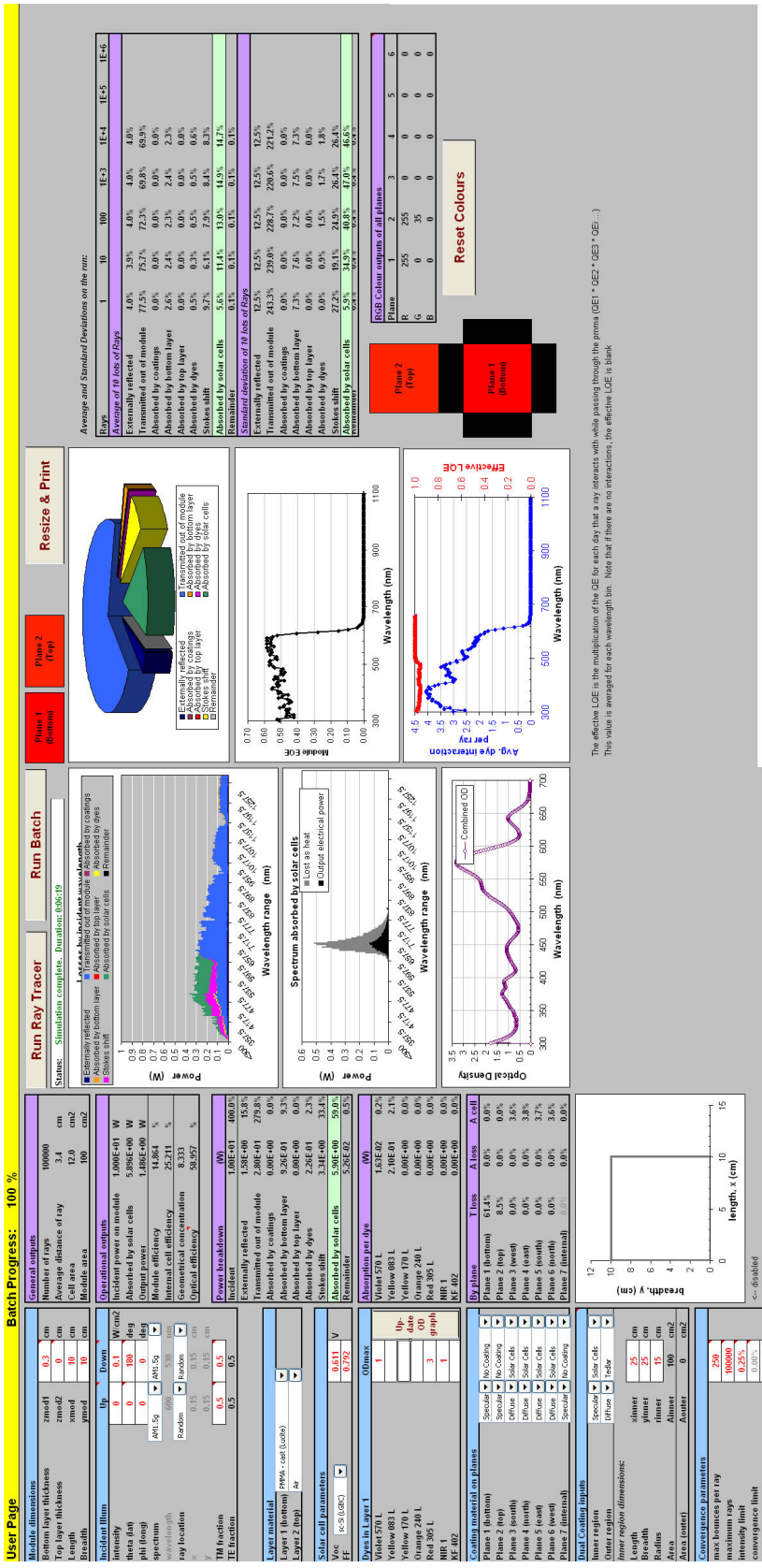

Figure 2.21: Raylene screenshot

2.4.2 Raytracer

Fig. 2.22 shows a flowchart diagram of the author's program. This, with minor changes, is the same basic procedure which all raytracing software uses[40, 156, 242, 243, 34]. The stages are described below and details are then given of some specific problems of simulating photon transport in code.

First, the program loads data for dye absorption coefficients, host material absorption coefficient and refractive index, solar cell EQE and reflectance, plane coatings and module dimensions. Concentrations are specified by the user.

An iteration loop is run to generate a certain number of incident solar photons. These are generated striking at random locations across the surface of the LSC module. By default, they strike at normal incidence. Their wavelengths are randomly distributed across the chosen input spectrum (for example AM1.5g).

Next, interaction distances are calculated. Three things can happen to a photon - it can strike a plane of the LSC, it can be absorbed by a dye molecule, or it can be absorbed by the host. The program calculates the interaction distances of the current photon with each of the planes of the LSC and then calculates likely interaction distances with the dye and host. Depending on which interaction distance is shortest, the photon either continues on its path inside the LSC, is detected or is lost.

When the photon interacts with a plane, the program checks to see if that plane is covered with a solar cell. If it is, and the photon is absorbed by the cell, an entry is added to the detected photon array and the program loops back to generate a new solar photon. Otherwise, the photon is transmitted or reflected from the plane and the new trajectory calculated accordingly.

If the photon is absorbed by a dye molecule, a new (fluorescence) photon is generated, subject to the dye quantum yield. This new photon is emitted in a random direction and has a random wavelength distributed across the relevant dye emission spectrum. The program is able to distinguish between different dyes and can simulate up to eight different dyes. If a photon is emitted, the program loops back to calculating interaction distances again.

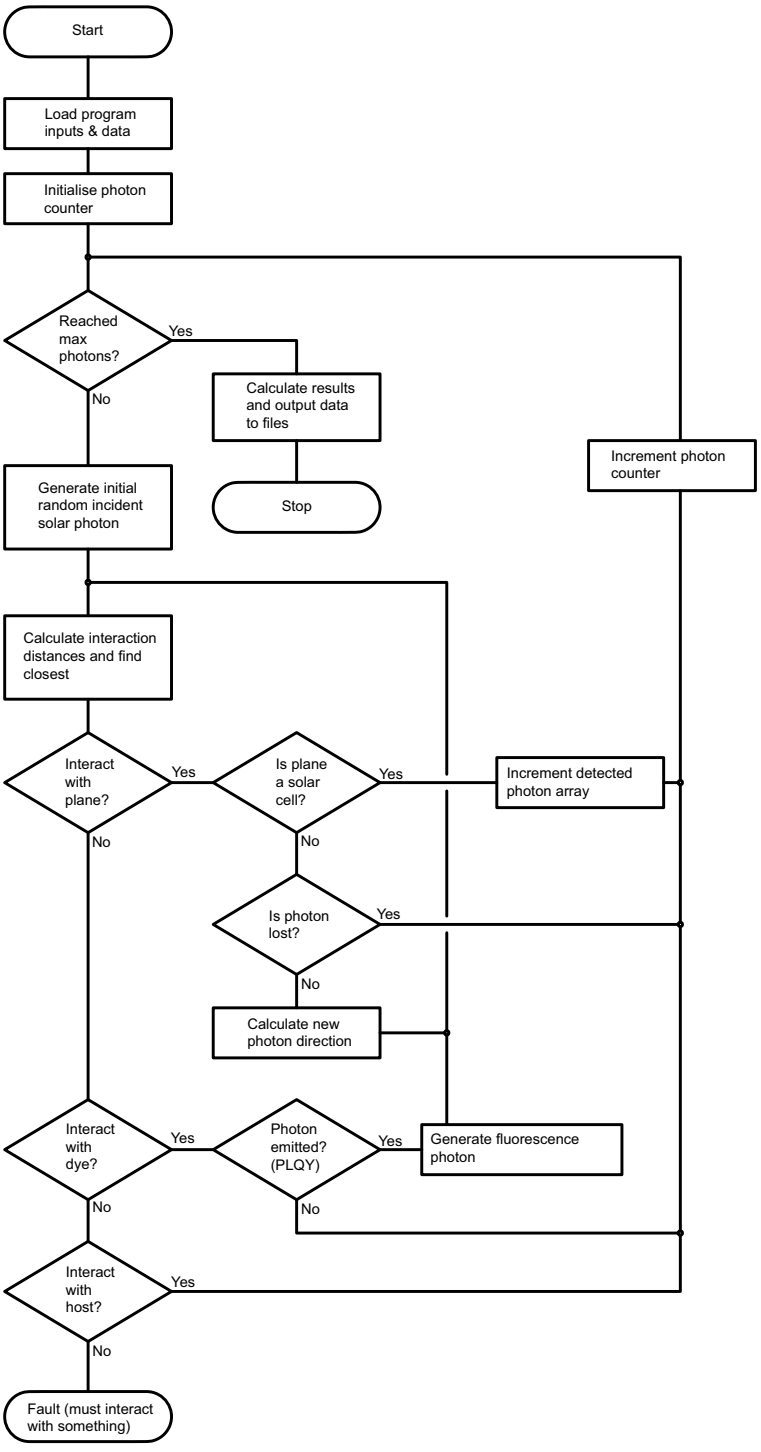

Figure 2.22: Raytracer flowchart

Finally, if the photon is absorbed by the host, it is lost and the program once again loops back to generate a new solar photon. If, for some reason, the photon does not interact with the host either, then the program exits with a fault as the photon must interact with something.

The complete C++ software code of this program is provided on the enclosed CD, including all required data files containing the optical properties of dyes, host materials and illumination spectra.

Several aspects of the program code are now described.

Random number generation

The entire Monte-Carlo simulation process is based on random number generation. They are used to determine a photon location and wavelength, whether a photon is reflected from a boundary, whether a dye emits a fluorescence photon etc. The inbuilt C++ function `rand()` returns a random `long` variable between `0` and `RAND_MAX`. The value of `RAND_MAX` varies between compilers, but for Code::Blocks with the MingW compiler, it is 32767. This is the maximum number of different random numbers which can be generated. When this is used to generate, for example, a random emission direction for an emitted photon, the emission directions are discretised into steps of about 1° because of the limited number of possible random numbers. To improve the resolution of the generated emission directions, the range of random numbers can easily be increased by taking two successive random numbers, multiplying the first by `RAND_MAX` and then adding the second. This results in a maximum of $\texttt{RAND\_MAX}^2$ different possible random numbers.

The subroutine `rnd()` below returns a `double` random number between 0 and 1 inclusive. The two `long` variables `rndnum1` and `rndnum2` must be declared before the start of the program.

```
double rnd(void)
{
    rndnum1=(double)rand()*RAND_MAX/((RAND_MAX*RAND_MAX)+RAND_MAX);
    rndnum2=(double)rand()/((RAND_MAX*RAND_MAX)+RAND_MAX);
    return(rndnum1+rndnum2);
}
```

It is also advisable to seed the random number generator with the current system

time at the start of each program - this ensures the sequence of random numbers is never repeated. This can be done using `srand((unsigned)time(NULL));`.

Photon trajectories and planes

It is simplest to represent photon trajectories and planes using vector notation. Intersection distances can then be calculated easily using dot products. The word "ray" will also be used to refer to a photon trajectory.

A photon trajectory is defined by $\mathbf{r} = \mathbf{a} + \lambda\widehat{\mathbf{m}}$, where $\mathbf{a}$ is the origin point of the ray, λ is the distance from the origin point of the ray and $\widehat{\mathbf{m}}$ is a unit vector in the direction of the ray. C++ cannot directly store a vector format, but it is easy to either create a data structure to hold the i,j,k components or to store the components as separate variables.

A plane (e.g. of the LSC module, or a back reflector) is identified by its distance from the origin and a unit vector normal to the plane. The plane equation is $\mathbf{r} \cdot \widehat{\mathbf{n}} = d$, where $\widehat{\mathbf{n}}$ is the unit normal vector and d is the distance of the plane from the origin. All elements of the normal vector should be positive. The distance from the origin can have either sign.

We can easily find the distance from a ray's origin point to where it intersects a given plane. This is found from $\lambda = (d - \mathbf{a} \cdot \widehat{\mathbf{n}})/(\widehat{\mathbf{m}} \cdot \widehat{\mathbf{n}})$. The point of intersection can then be calculated.

When a photon passes through a plane, it is refracted (changes direction). This is only relevant for the top and bottom planes of the LSC in this model. For a horizontal plane, the i & j components of the ray direction vector should be multiplied by n_1/n_2 where n_2 is the refractive index of the material which the ray is *entering*. The new k component can be calculated from $\sqrt{1 - (i^2 + j^2)}$.

To determine whether a photon is reflected at an interface, we simply work out a random number and check whether it is less than the reflectance. If it is, then the photon is reflected.

Generating a random isotropic emission direction

When a photon is emitted from a dye molecule, the program assumes that it is emitted isotropically. This is obviously not true for an individual dye molecule, as the emission direction is determined by the orientation of the emission dipole moment[67, 244, 245]. However, when many molecules are dissolved with random orientations in a host material, it can be assumed that the net emission does occur isotropically.

The direction is initially specified in spherical polar coordinates, using θ and ϕ. Here, ϕ is the angle from the +X axis in the horizontal XY plane and takes values from 0 to 2π. θ is the vertical angle from the XY plane and takes values from $-\frac{\pi}{2}$ to $\frac{\pi}{2}$.

Calculating a random value for ϕ is simple: $\phi = 2\pi \times$ `rnd()`. However, the same procedure cannot be used for calculating θ. If it were, there would be a greater density of ray directions around the two extreme values of θ. Instead, θ has to be weighted towards 0. The expression $\theta = sin^{-1}(2(\texttt{rnd()} - 0.5))$ returns values with a suitable weighting distribution.

C++ does not have either sin^{-1} or cos^{-1} functions. Instead, tan^{-1} has to be used. If we need to calculate $sin^{-1}(x)$, then this can be done using $tan^{-1}\left[x/\sqrt{1-x^2}\right]$ or `atan(x/sqrt(1-pow(x,2)));` in C++.

Generating a random emission wavelength

To simulate either the incident solar spectrum or a dye fluorescence spectrum, random wavelengths have to be generated such that the distribution of wavelengths matches the spectrum in question. The wavelengths need to be weighted towards certain areas of the spectrum. The simplest way of achieving this is by making use of cumulative frequency.

Let all spectra be defined in wavelength steps of 1 nm. Define an emission spectral intensity array `em_int[1201]`. This holds the shape of the spectrum required to simulate. The upper limit of 1200 nm is chosen as an example and can be any value. If the total area of this spectrum is normalised to 1 (i.e. the sum of all the elements of `em_int[]` is 1), then the value in `em_int[n]` represents the probability that a photon

is generated with a wavelength of $n \leq wavelength < n + 1$.

We now create a cumulative frequency array for the emission spectrum, called `em_cf[1202]`. Note that the size of `em_cf[]` is 1 larger than `em_int[]`. Each element of the cumulative frequency array `em_cf[n]` is the sum of all elements of the emission spectral array from `em_int[0]` to `em_int[n-1]`. Therefore, `em_cf[n]` represents the probability that a photon is generated with a wavelength less than n.

To generate a random photon wavelength, we first generate a random number using `rnd()`, then go through `em_cf[]` starting from the lowest index until we find the element whose value is closest to the random number. The generated wavelength is then set equal to the index of that element. In C++ code this can be done by the following:

```
rannum=rnd();
for(wavelength=0;wavelength<=1200;wavelength++)
{
    if(rannum>=em_cf[wavelength] and rannum<em_cf[wavelength+1])
    {
        output_wavelength=wavelength;
        break;
    }
}
```

The distribution of `output_wavelength` will match the actual emission spectrum stored in `em_int[]`. This technique can be used for either a fluorescence photon or a solar photon.

Calculating a probable absorption distance

When working out the interaction distances of a ray with the planes, dyes and host, we need to calculate the probable distance the photon will travel before it is absorbed. Again, this needs to be randomly distributed, but with a weighted distribution towards shorter distance.

Consider a piece of material with an absorption coefficient of α, for example PMMA. α has units of cm^{-1}. A number of initial photons N_0 is incident on the material at distance $x = 0$.

The number of photons which reach a distance x inside the material is $N_0 e^{-\alpha x}$, calculated from the Beer-Lambert law. The number of photons that are absorbed in a further small distance δx is $N_0 e^{-\alpha x}\left[1 - e^{-\alpha \delta x}\right]$.

The "density" of absorbed photons per unit length is this expression divided by δx: $\left[N_0 e^{-\alpha x}\left(1 - e^{-\alpha \delta x}\right)\right]/\delta x$. As $\delta x \to 0$, this expression becomes $\alpha N_0 e^{-\alpha x}$. If this is then divided by N_0 (the total number of initial photons), we get $\alpha e^{-\alpha x}$. This is the probability that a photon will be absorbed at a distance x. And indeed, the integral of this w.r.t. x from zero to infinity is unity, as it should be.

This probability is similar to the probability of a photon being emitted at a certain wavelength, as used in the calculations to generate a random photon wavelength. Likewise, we now calculate a cumulative frequency expression for the fraction of photons which are absorbed between 0 and x. This can be obtained either by integrating the probability expression or from Beer-Lambert law. The cumulative probability is therefore $1 - e^{-\alpha x}$. To generate a random distance, we generate a random number between 0 & 1 using `rnd()` and set this equal to the cumulative probability. We then work out what distance this corresponds to. In short, the distance is calculated from $x = -ln(\texttt{rnd()})/\alpha$.

Calculating solar cell outputs

The simulation program works out the number and wavelengths of photons striking the solar cells attached to the edges of the LSC sheet. The actual electrical output of the cells must be calculated from this.

The current produced by a cell is calculated from the solar cell equation, Eqn. (2.9).

$$I = I_{SC} - I_0\left[e^{\frac{qV}{nkT}} - 1\right] \tag{2.9}$$

Under normal conditions, the exponential term is dominant so the -1 term in the

brackets can usually be ignored. n is the ideality factor which we will assume to be 1. We will also assume an operating temperature of 300 K. If this is now written in terms of current densities and we consider open-circuit operating conditions (total current, I is zero), we can obtain an expression for J_0, the dark current density [Eqn. (2.10)].

$$J_0 = \frac{J_{SC}}{e^{\frac{qV_{OC}}{nkT}} - 1} \tag{2.10}$$

For the NaREC laser-grooved buried contact (LGBC) cells (Section 2.5) under 1-sun illumination, V_{OC}=0.611 V and J_{SC}=33.6 mA/cm^2. Therefore, J_0=1.828e-12 A/cm^2. We can now, given a particular J_{SC}, calculate the I-V curve and hence the maximum power point. This value of J_0 actually gives a slightly higher fill factor than was measured (83 % instead of 79 %). This is because no resistive losses (shunt/series) are accounted for.

There is unfortunately not a simple theoretical expression to calculate the MPP. However, the fill factor changes very little over a wide range of J_{SC} and we can assume it to be constant. We can then calculate the MPP from the open-circuit voltage, short-circuit current and the fill factor.

The open-circuit voltage can be calculated from Eqn. (2.11).

$$V_{OC} = \frac{nkT}{q} ln \left[\frac{J_{SC}}{J_0} + 1 \right] \tag{2.11}$$

For example, if we have a J_{SC}=10 mA/cm^2, V_{OC} is 0.58 V. If we assume a fill factor of 79 %, the maximum power produced is then 4.58 mW/cm^2.

It only remains to calculate the short-circuit current from our simulation outputs. Since we know the number and wavelengths of the photons which strike the cell, we can use the reflectivity and IQE to calculate the number of electrons produced inside the cell, and hence the total charge produced. In order to calculate the current, we need to know over what length of time this charge is generated.

Over the course of the simulation, a record is kept of the total energy (in J) of the solar

incident photons which strike the LSC module. This will vary according to the number of initial photons simulated. Since we know the intensity (in W/m^2) of solar radiation incident on the module, for example $1\,kW/m^2$, the time it takes for the photons to strike is simply $(Total\ incident\ solar\ energy)/(Incident\ intensity\ \times\ Module\ area)$. The short circuit current can then be calculated.

2.4.3 Repeatability

The repeatability of both simulation programs was checked and compared by performing 100 identical simulations of module efficiency using both programs. A 10 cm x 10 cm x 0.3 cm LSC sheet containing a mixture of 50 ppm Violett 570 and 350 ppm Rot 305 was used. The cells used on the edges were laser-grooved buried contact (LGBC), described in detail later (Section 2.5). A total of 100,000 initial photons was used in both programs. Fig. 2.23 shows a histogram of the results from both programs.

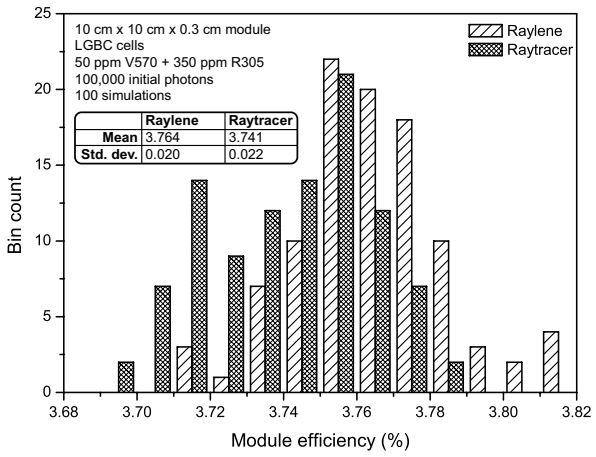

Figure 2.23: Distribution of module efficiencies over 100 identical runs of both simulation programs

The standard deviation (SD) of the results is similar (∼0.02) in both cases, as might be expected from using the same number of initial photons. To reduce the SD and the error, a larger number of photons can be simulated. The mean of the results from Raytracer is slightly lower than that from Raylene (around 0.6 % relative), explained by the different solar cell model used. Unlike Raylene, which assumes a constant

V_{OC} regardless of the cell illumination intensity, Raytracer calculates the V_{OC} for the intensity the cell experiences. The average V_{OC} values calculated from Raylene and Raytracer are 0.611 V and 0.6 V, respectively. Therefore, Raytracer will, in this situation, result in a slightly lower efficiency.

Apart from the small difference caused by the different solar cell calculations, both programs agree to within ∼1 % relative.

2.5 Solar cells

The solar cells used for constructing LSC modules in this project were manufactured by NaREC[246] using the laser-grooved buried contact (LGBC) process[247, 248, 249, 250, 251, 252, 253] and were monocrystalline. The main consideration in choosing this type of cell was the ease and flexibility of manufacturing sizes suitable for mounting on the edges of an LSC, typically long (10 cm) and narrow (0.5 cm).

Unlike the majority of silicon solar cells which usually have screen-printed front contacts and need to be mechanically scribed to break them into suitable sizes, LGBC cells use a Nd:YAG laser to scribe grooves into the surface of the cell which are then electroless-plated with copper/silver to form the fingers of the front contact. This results in reduced shading losses, as the fingers extend into the wafer and can be made narrower than screen-printed fingers. In addition, the same Nd:YAG laser can be used to cut the cells to the final dimensions. Because the fingers and outline cutout are both done with a computer-controlled laser, different electrode patterns and shapes can easily be made, as there is no need to manufacture a different screen for each electrode pattern. The surface of the cells is textured using an anisotropic etch during manufacture. This forms many small pyramidal structures on the surface of the cell, which help to reduce reflection losses. They should also help form a stronger bond with coupling adhesive because of the greater surface area. Conversion efficiencies as high as 17-19 % have been reported[253, 252]. A cross-sectional diagram of a LGBC cell is shown in Fig. 2.24.

A photograph of several of the cells is shown in Fig. 2.25. The busbar is formed from a

series of many closely-spaced fingers. When tabbing is soldered to this, solder bridges all of the fingers forming a continuous connection. Fig. 2.26 shows the dimensions of the cells produced for use in this project. The busbar is visible at the top and is covered with tabbing. The active width of 3.2 mm is slightly greater than the LSC sheet thickness and ensures that the cell covers the entire edge of the sheet. The overall length of the cells is 10 cm.

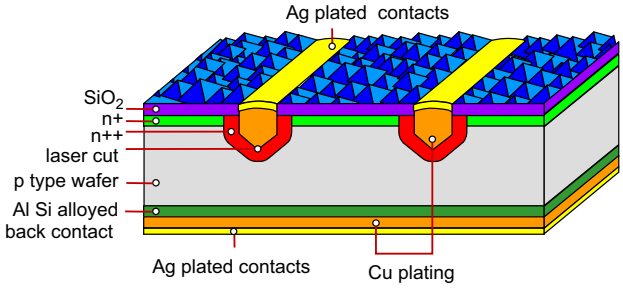

Figure 2.24: Structure of LGBC cells (from Vivar *et. al.*[252])

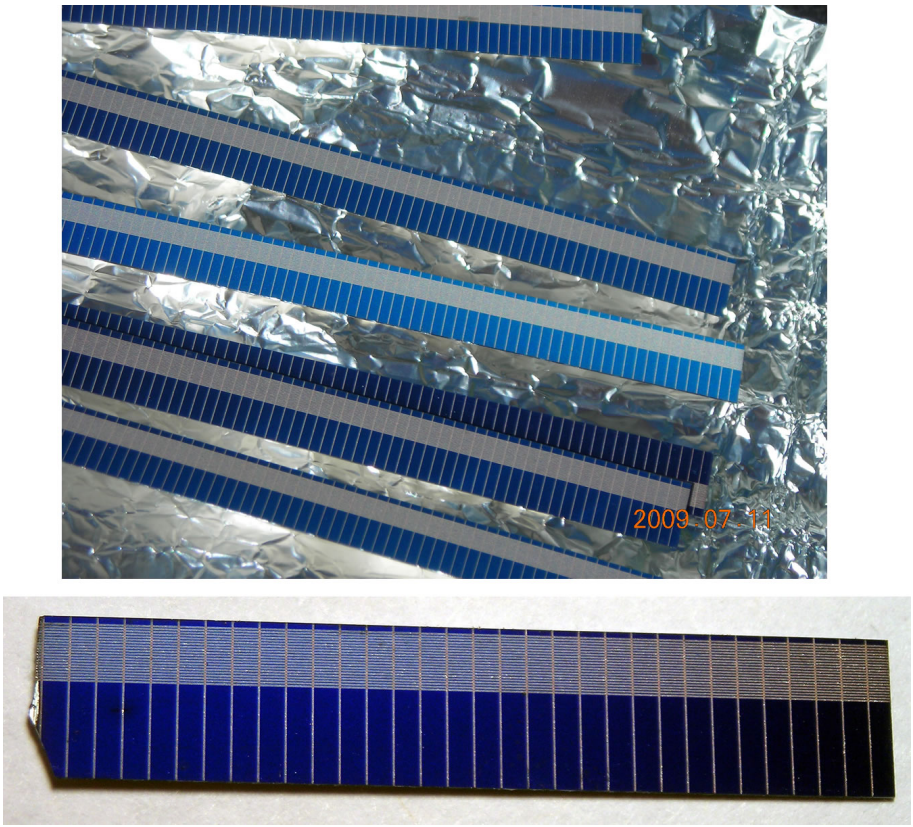

Figure 2.25: LGBC solar cells for LSC use

The spacing of the front-contact fingers varies depending on the illumination intensity under which the cell is designed to work. Since LSCs are concentrating devices, it

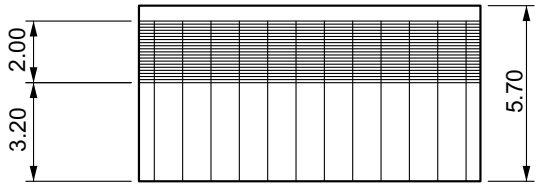

Figure 2.26: LGBC solar cell dimensions (in mm)

was decided to use cells optimised for 5x concentration (this value being determined from simulations of predicted module efficiency). Before the optimised cells became available, non-optimised cells with the same dimensions but designed for 10x concentration were used to experiment with different methods of module construction. These naturally had a closer finger spacing and higher shading losses. It emerged that the concentration ratio of the 10 cm x 10 cm LSC modules constructed in Chapter 7 was, at best, ∼1.8x; therefore, cells designed for 1-sun illumination would have been suitable and would have exhibited lower shading losses. However, the 60 cm x 60 cm module constructed in Chapter 7 exhibited a concentrtation ratio of ∼5x. The cells are therefore an excellent match to this size of module.

The finger spacing, width and shading losses are listed in Table 2.5 for a 1-sun full-wafer cell (such as those used in PV module construction) and both the optimum and non-optimum LSC cells. The groove width is constant, as this is a feature of the laser and focussing arrangement used to cut the groove. However, the metal plating is wider on the cells designed for higher concentrations - this ensures a lower-resistance contact. As a result, the shading losses are greater.

The simulation program does not account for the increase in shading losses at higher concentrations as a result of the closer finger spacing. This will result in over-estimating the actual conversion efficiency of the module.

Table 2.5: LGBC cell dimensions

Type	Conc.	Groove width (μm)	Metal width (μm)	Finger spacing (μm)	Shading (%)
Full-wafer	1x	15	35	1545	2.3
Optimum LSC	5x	16	72	915	7.9
Non-optimum LSC	10x	15	70	645	10.9

2.5.1 IQE and reflectance

The Monte-Carlo simulation programs (Section 2.4) used to predict LSC module performance require data on the properties of the solar cells used, specifically the internal quantum efficiency (IQE) of the cell and the reflectance at the boundary between the host material of the LSC and the cell's surface. The IQE of a cell cannot be measured directly: it must be calculated from the external quantum efficiency (EQE) and the cell's reflectivity.

The external quantum efficiency (EQE) of these cells have been measured both by NaREC and at Heriot-Watt and the data are shown in Fig. 2.27. There is good agreement between them

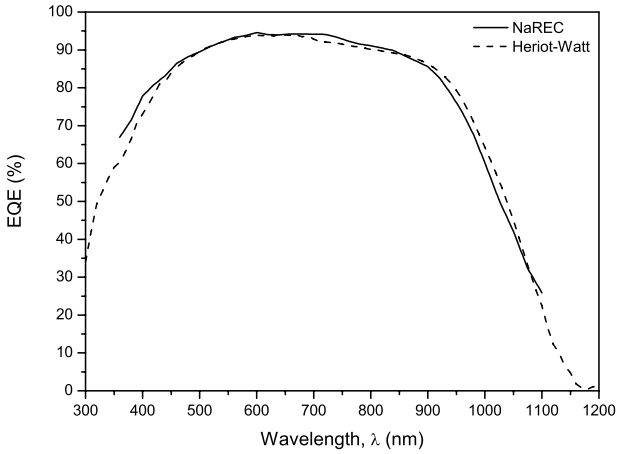

Figure 2.27: Solar cell EQE

IQE (the number of electron-hole pairs generated and collected per photon *absorbed by the cell*) is related to the EQE (the number of electron-hole pairs generated and collected per photon *incident on the cell*) and the surface reflectance, R, by Eqn. (2.12).

$$IQE = \frac{EQE}{1 - R} \tag{2.12}$$

In order to calculate the IQE, we need to measure the reflectance of the solar cell's surface. This was done using an integrating-sphere attachment for a standard UV/Visible

spectrophotometer. A sample of $BaSO_4$-coated aluminium (reflectance above 99 %) was placed in the sphere first as a reference. The signal obtained when a piece of solar cell is placed in the sphere is then equivalent to the surface reflectance of the cell. It should be noted that, because an integrating sphere is used, the reflectance data are averaged over all angles of incidence. In reality, the reflectance will change depending on the angle of incidence, mainly because of the pyramidal surface texture which follows the crystal planes of the wafer. However, since the computer simulation can only use isotropically-averaged reflectance data, this is not a problem.

The EQE of the cell was originally measured with the bare cell in contact with air. Similarly, to calculate the IQE of the cell, the reflectance needs to be measured in contact with air. However, for the simulation, the cell is obviously optically coupled to the host material of the LSC sheet. The reflectance of a host:cell interface is used in the simulation. Once the air:cell reflectance has been measured, the effective refractive index of the cell is calculated at each wavelength using $n_{cell} = \left(1 + \sqrt{R_{air:cell}}\right) / \left(1 - \sqrt{R_{air:cell}}\right)$ where $R_{air:cell}$ is the reflectance. The reflectance at the host:cell boundary is then found from the usual expression $R_{host:cell} = [(n_{cell} - n_{host})/(n_{cell} - n_{host})]^2$.

The measured reflectance $R_{air:cell}$ and the calculated IQE and $R_{host:cell}$ for a PMMA host are shown in Fig. 2.28. The PMMA:cell reflectance is lower because of the higher refractive index of PMMA. Note that the reflectance is negligible at wavelengths $>$ 550 nm, where edge-emission light from the LSC is usually located. No additional optimisation of the anti-reflection coating on the surface of the cells is required for use with LSCs.

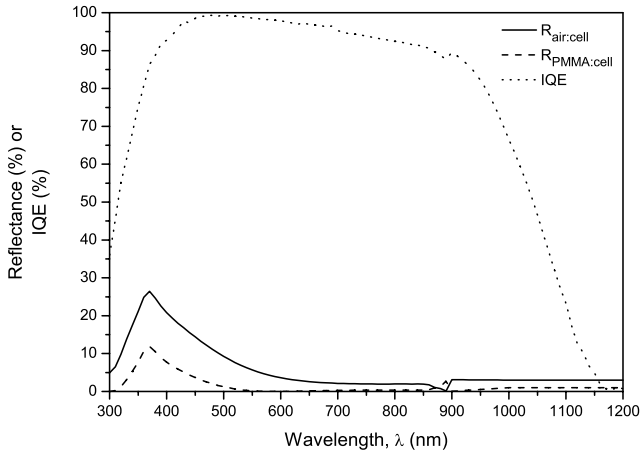

Figure 2.28: Solar cell IQE and reflectance

2.6 LSC construction

The construction of LSC modules requires great care, both in making electrical connections to the cells and in bonding the cells to the edges of the LSC sheet. Small errors in attachment (for example, excess adhesive) can have an adverse effect on the module performance. Few details are often given in the literature of the precise details of module construction. As this is an important topic, the sections below describe the various aspects of construction in detail, including cell tabbing and cell attachment.

2.6.1 Electrical connections

In the production of solar panels and modules constructed from many cells connected together, electrical connection to cells is most often made by thin tin-plated copper strips, or "tabbing". This is soldered to the busbars on the front and rear surfaces of the cell. Although ideally suited to joining large, full-wafer cells (such as those used in solar panels), the soldering technique has to be adapted for use in making connections to the long, narrow cells used for LSCs.

Tabbing is soldered either manually or by an automatic process which passes cells under a roll of tabbing which is continually unwound. Soldering processes are in the range 200-300°C, with the higher temperatures being used for lead-free solder. When the solder joint between the tabbing and the cell cools, the different contraction rates of the cell and tabbing create a stress in the cell/tabbing joint. In large cells (e.g. 120 mm square), the deflection caused by this stress is negligible and is removed when the cells are laminated with a sheet of glass into a final module. However, on small cells like those used for LSCs, the deflection can be sufficient to either crack the cell or otherwise render it unusable. As an example, Fig. 2.29 (from Eikelboom *et. al.*[254]) shows the effect of different tabbing attachment processes on the bending of a silicon strip. The silicon strips were 300 μm thick and the tabbing 2 mm wide. Soldering the cell on top of a hotplate reduces the bending slightly, but it still large enough to make it impossible to attach the cell to the edge of an LSC.

An obvious solution to the problem is to attach the tabbing using a lower-temperature

Figure 2.29: Bending of 300μm thick silicon strips with attached 2 mm wide tabbing[254]. Back to front: soldering at 400°C on cold surface, soldering on 160°C hotplate, conductive adhesive cured at 160°C, conductive adhesive cured at 80°C.

process, for example by the use of conductive adhesive[254, 255, 256, 257, 258]. These consist of a resin base, such as epoxy or acrylic, loaded with a conductive metal powder such as silver or gold. Curing temperatures can be as low as 80°C. The nearest two strips in Fig. 2.29 used conductive epoxy to bond the tabbing. Clearly, there is greatly reduced bending. Eikelboom *et. al.*[254] studied the effect of temperature cycling on the contact resistance of a conductive adhesive joint and found it to be equal to or better than a conventional soldered joint. A benefit of conductive adhesives in the construction of conventional laminated modules is that the adhesive curing can be carried out during the lamination phase, as temperatures used to melt the lamination material (e.g. EVA) are also sufficient to cure the adhesive[254].

Although conductive adhesives offer many advantages, there are several drawbacks. Firstly, although the amount of adhesive required is small, they are still expensive compared with normal soldering. In addition, the surfaces of the cell and tabbing may require additional treatment to ensure a good bond with the adhesive. For example, screen-printed aluminium electrodes, which are slightly porous, absorb the adhesive and reduce the strength of the bond[254]. Finally, as conventional soldering is currently the standard technique in industry, it is unlikely that the use of a conductive adhesive would gain widespread acceptance should LSCs become commercialised.

It is possible, however, to use normal soldering techniques and avoid bending of the cell. This can be done by *simultaneously* soldering tabbing in corresponding locations

on the front and rear of the cell. The joints cool equally and the front and rear stresses cancel each other out. The result is a perfectly flat cell. Obviously, both joints cannot be made manually, so a jig was designed by the author to achieve this.

Two pieces of tabbing, cut slightly shorter than the length of the cell, are clamped on the front and rear of the cell by a jig with spring-loaded fingers. The tabbing is not clamped along its entire length. Rather, five individual clamps are used. This results in five soldering locations along the tabbing and reduces stresses further by leaving the tabbing between the joints free to expand or contract.

Fig. 2.30 shows several views of the soldering jig. The five fingers are pressed on the cell using springs under the retaining screws. The jig is made from aluminium, which provides a non-stick surface should excess solder from the tabbing contact the jig.

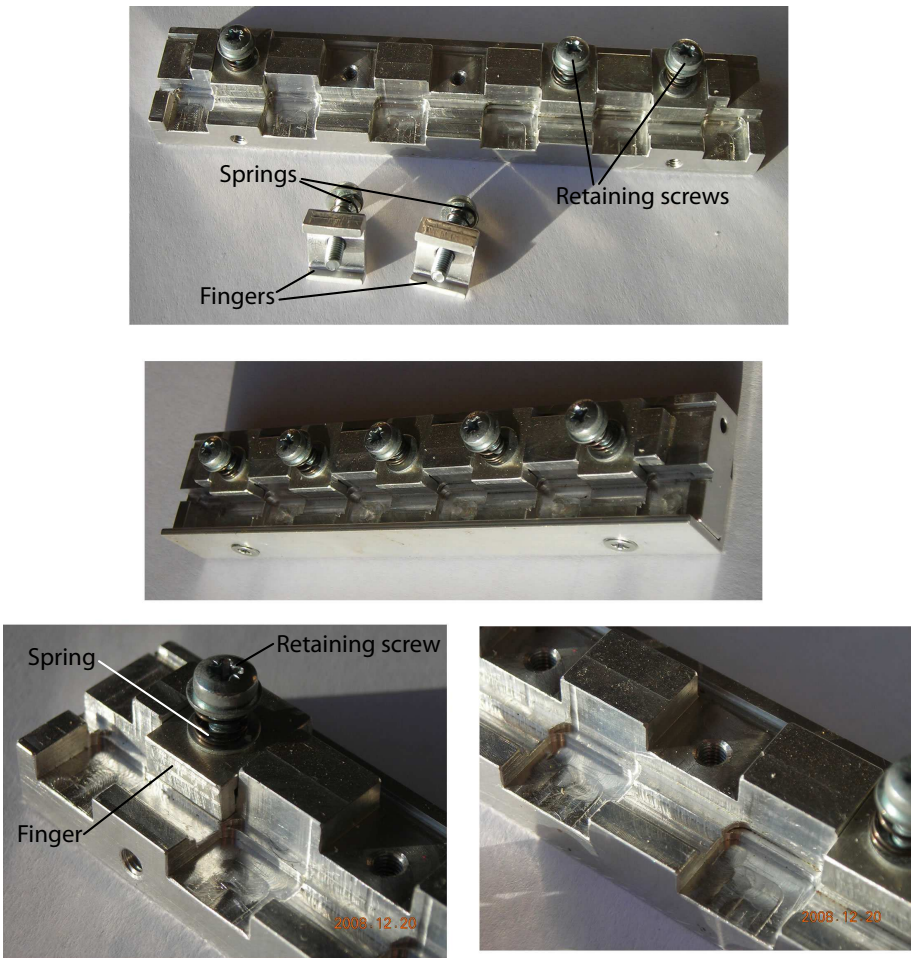

Figure 2.30: Double-sided soldering jig

The choice of the type of tabbing is important. Two kinds are available, differing in

the tinning process and the resulting thickness of the solder plating[259]. Both are manufactured from thin copper sheet. In the first kind, the sheet is electroplated with a thin layer of tin solder and then cut into thin strips. Because the tin has been electroplated, the coating is extremely thin (0.5-2 μm). It was found that this type of tabbing had insufficient solder on it to form a good joint with the busbar. The second type of tabbing is also made from thin copper sheet, but the sheet is cut into strip form first and then dipped in a bath of molten tin solder. This results in a much thicker coating (10-18 μm), and gave a much stronger joint with the busbar.

To ensure a perfectly straight and flat piece of tabbing which achieves good contact with the surface of the cell and busbar, short lengths of tabbing are held in a vice and manually stretched slightly beyond the elastic limit. The resulting deformation straightens the material. Fig. 2.31 shows the solar cell and tabbing assembled in the jig, ready for heating. One piece of tabbing is hidden behind the cell. A K-type thermocouple monitors the temperature. A liquid flux pen is used to coat both the cells and tabbing with flux.

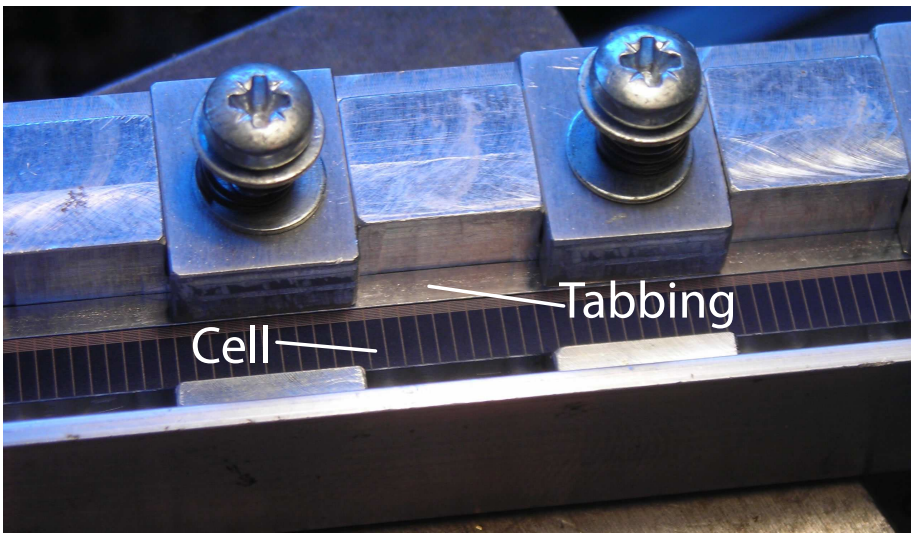

Figure 2.31: Cell and tabbing in jig

It was found that, during the gluing process used to attach the cells to the edges of the sheet (Section 2.6.2), it was advantageous to have a slight curve in the cell, such that the concave side faced the edge of the LSC. As a result, the ends of the cell made contact with the edge first when the cell was pressed into place against the edge. This resulted in fewer air gaps between the cell and the LSC sheet. To obtain a suitable

bend in the cell, the tabbing strip used for the front contact is stretched further before it is soldered to the cell. During the cooling period after soldering, the front tabbing exerts a greater contractive force than the rear tabbing, bending the cell slightly in the desired direction.

The entire jig was supported over the jaws of a vice and heated from below to 200°C using a propane torch (Fig. 2.32), just above the melting point of the lead-based solder used on the tabbing. A gas torch was the only source of heat which could raise the temperature of the jig quickly enough to avoid the flux evaporating and the busbar oxidising. Induction heating would be ideally suited to this purpose. Once the solder had flowed, the jig was cooled rapidly to about 120°C with an electric fan. The cell was removed whilst still hot (at ∼150°C), as it was found that the jig contracted on the cell if it was allowed to cool to room temperature.

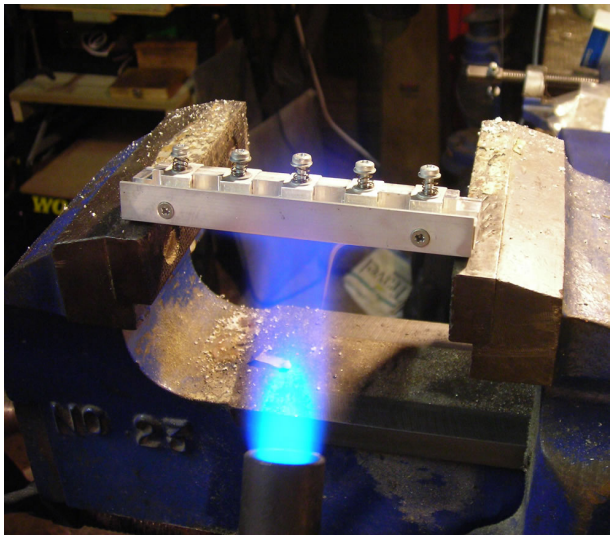

Figure 2.32: Heating soldering jig

Fig. 2.33 shows some examples of LSC cells with tabbing attached along the busbar. Connections to external circuitry can easily be made by soldering additional pieces of tabbing on at right-angles to those already attached to the cell. In the edge clips (Section 2.6.2), these additional pieces of tabbing were used to locate the cell in the clip.

Although there is now no bending stress perpendicular to the plane of the cell, there is a slight bend in the plane of the cell as both the front and rear tabbing are at the same edge of the cell. This is approximately 0.5 mm over the 10 cm length of the cell.

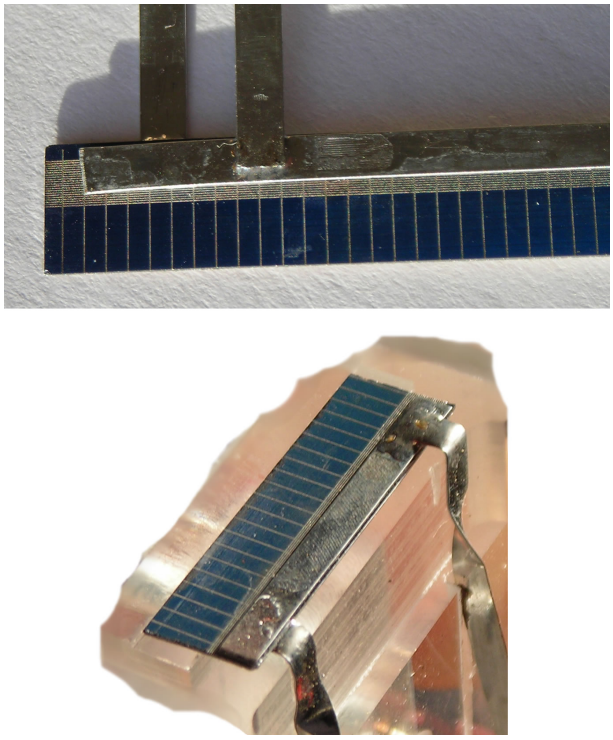

Figure 2.33: Example of double-sided soldering

This is not a great problem, as the active area of the cell can be made slightly wider to compensate. Thinner tabbing could also be used to reduce the stress.

When this soldering technique is used on LSC cells, fill factors equal to or greater than those of a full-wafer cell can be obtained as will be shown in Section 7.1.3.

2.6.2 Edge attachment of cells

Solar cells must be optically coupled to the edges of the LSC sheet they are attached to. They must also be securely held and should preferably be encapsulated to protect them from contact oxidation and moisture damage.

The best means of providing both optical coupling and mechanical support for the cells is to glue then permanently to the edges of the sheet. The refractive index of most adhesives is a close match to that of the LSC sheet (most polymers have an index in the range 1.4-1.6). When an LSC module is exposed to sunlight, it will naturally heat up and the components will expand. The different expansion rates of the LSC sheet and the solar cell will create a stress in the adhesive joint and the adhesive must be

able to withstand this. A good choice of adhesive would appear to be cyanoacrylate, which provides a good bond to both PMMA and to silicon. However, it was found later (Section 7.1) that cyanoacrylate is extremely brittle and cells had a tendency to separate from the edge when the module heated up. A better choice is two-part epoxy resin, such as Araldite. Modules constructed using this adhesive showed no problems with cell separation (Section 7.1.3).

The adhesive layer is extremely thin (<50μm) so the optical quality of the adhesive is not that important and more consideration can be given to obtaining a good mechanical joint. Araldite epoxy, while slightly opaque in bulk form, has negligible absorption in the thin layer between the solar cell and the sheet edge. This was confirmed by measuring the transmission of a pair of microscope slides which were glued and pressed together to simulate the joint between the cell and the LSC. The transmission over the range 300-1200 nm was >99 % (corrections were made for the absorption of the microscope slides themselves).

If adhesive is applied to the cell and the cell then placed on the edge of the sheet, excess adhesive will invariably spread out and form a fillet between the cell and the surface of the sheet. This can lead to a large fraction of the trapped fluorescence being lost via optical coupling into the glue, as shown in Fig. 2.34.

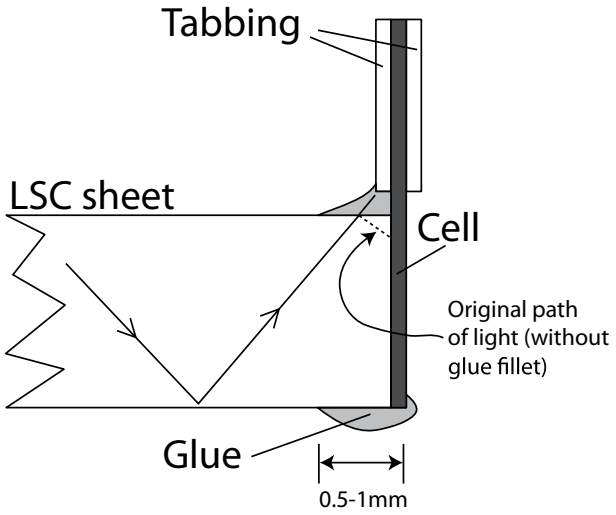

Figure 2.34: Losses in glue fillet. Dotted line indicates original path of light ray (without glue fillet).

The light ray indicated in Fig. 2.34 demonstrates the effect that the presence of

a glue fillet has on trapped light. The light ray would have originally reflected off the top surface of the sheet and struck the solar cell (indicated by the dotted line). However, because the glue fillet extends a short distance out on to the sheet's surface and overlaps the reflection point, TIR no longer occurs and the light ray continues on into the glue where it may be absorbed by the glue, strike the tabbing, or otherwise be lost.

Because the active region of the cell is only the thickness of the sheet (e.g. 3 mm), glue can severely affect the amount of light reaching the cell even if it only extends a short distance on to the sheet. As an example, if the glue overlaps the sheet by, for example, 0.2 mm on both the front and rear surfaces, this would reduce the illuminated region of the cell to approximately 2.6 mm (the distance the glue extends is mirrored on to the surface of the cell), a reduction of ∼13 %.

Although the amount of adhesive used can be controlled, it is impossible to use the exact amount to avoid glue spreading out from the joint. Besides, if encapsulation of the entire cell is desired, this must extend over the surface of the sheet to provide a hermetic seal. A possible solution to this problem is to deposit a mirror coating on the top and bottom surfaces of the sheet, confined to a narrow strip at the edges. The mirror could consist of an aluminium thin film, applied by a vacuum coating technique such as thermal evaporation or sputtering. Metallisation of plastic surfaces to create reflectors is a standard process and stable coatings with good adhesion to the underlying plastic can easily be achieved.

Fig. 2.35a shows the effect of such a mirrored strip on the path of light inside the sheet. Instead of being transmitted into and lost in the glue fillet, the ray is reflected from the mirrored strip and strikes the cell, even though glue is present on top of the mirrored strip. Although comments were made earlier (Section 1.5.3) on the problems of applying coatings that are not 100 % reflective to the rear surfaces of LSC modules to reduce losses and it was concluded that these actually led to a reduction in efficiency because of a loss on each of the many reflections, the mirrored strip at the edge is acceptable because it can be made narrow enough (∼1 mm) that light only makes a single reflection from the mirror. All other reflections are total internal reflections from the LSC surfaces. The reduction in the illuminated area of the LSC sheet by

the mirrored strips is negligible - a 1 mm-wide mirrored strip around the edge of a 30 cm x 30 cm LSC results in only a ∼1 % reduction in total illuminated area.

Fig. 2.35b demonstrates how the entire cell and tabbing could be encapsulated. Although the encapsulant has to extend over the surface of the sheet, the mirrored strip prevents any losses. The cell and tabbing are completely enclosed, preventing any damage from oxidation or moisture.

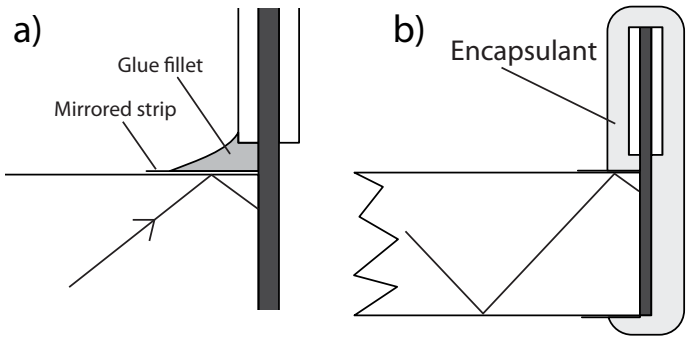

Figure 2.35: Use of a mirrored strip to prevent glue losses. a) Close-up of mirrored strip. b) Encapsulation of entire cell.

As the bare cells are quite fragile, it would be advantageous during the attachment process if the cells were mounted in a holder or clip which provided mechanical support and/or encapsulation. Ideally, the clip would also provide alignment of the cell with the edge of the sheet to ensure the cell covered the entire edge. It would also protect the cells from the external mounting frame used to hold the LSC sheet, coverglass and rear reflector together.

A prototype was designed consisting of a two-part plastic clip which held the cells securely and provided a locating slot which the edge of the LSC sheet fitted into. Fig. 2.36 shows a drawing of the clip with a cell in place.

The widths of the cells are uniform as they are cut with a computer-controlled laser. The groove in the bottom part of the clip is slightly larger than the width of the cell and allows it to fit neatly. An additional, smaller groove provides clearance for the thickness of the tabbing soldered to the back surface of the cell. The top part is attached to the bottom either with glue or (in the prototype) by pinning. When both parts are assembled, a space is left into which the edge of the LSC sheet can fit.

The prototype was machined from PMMA, but extrusion or injection-moulding would

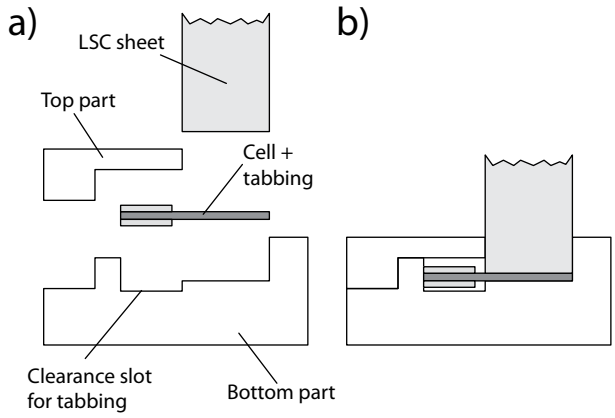

Figure 2.36: Two-part cell edge clip showing (a) separate parts (b) complete

be ideally suited to manufacture this shape of clip. Both parts could be moulded in one piece and then pressed together once the cell was in place.

Electrical connections to the cell are made by soldering tabbing at right-angles to the length of the cell. This tabbing passes through grooves cut in the clip. If a jig is used (Fig. 2.37) to attach the tabbing connections at specific distances relative to one end of the cell, the tabbing can then be used to accurately position the cell in the clip and prevent its movement lengthwise. This is important, for example, in constructing a clip with mitred ends, where it is important to prevent the cell from protruding from one end of the clip.

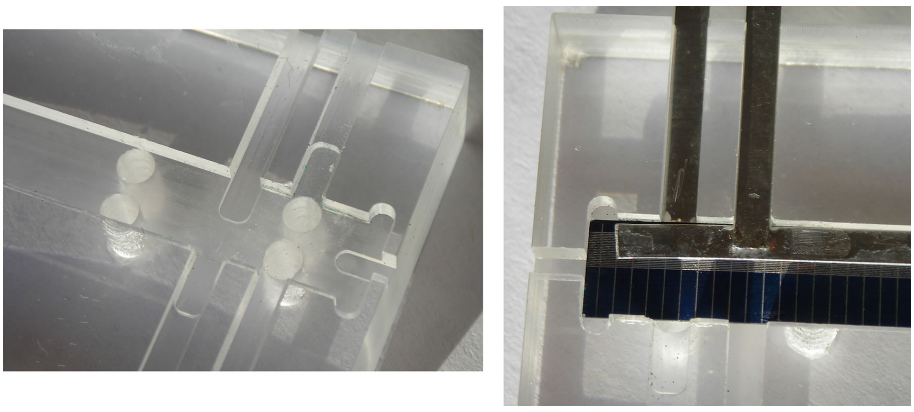

Figure 2.37: Jig for attaching tabbing connections

In Fig. 2.37, the cell is placed in a slot cut in a piece of plastic and moved against a stop at one end. Short lengths of tabbing are then laid in additional grooves at right-angles to the cell and soldered by hand.

Fig. 2.38 shows the assembly stages of the prototype clip. As this was a prototype, it was assembled without using any glue. The cell is placed between the two halves of the clip which are then pinned together. The ends of the clip (shown in Fig. 2.38d) have been mitred with a fly-cutter to provide a mating surface with the corresponding clip on the next edge of the sheet. The clip is slightly longer than the cell, as can be seen from the small space between the cell end and the end of the clip in Fig. 2.38d.

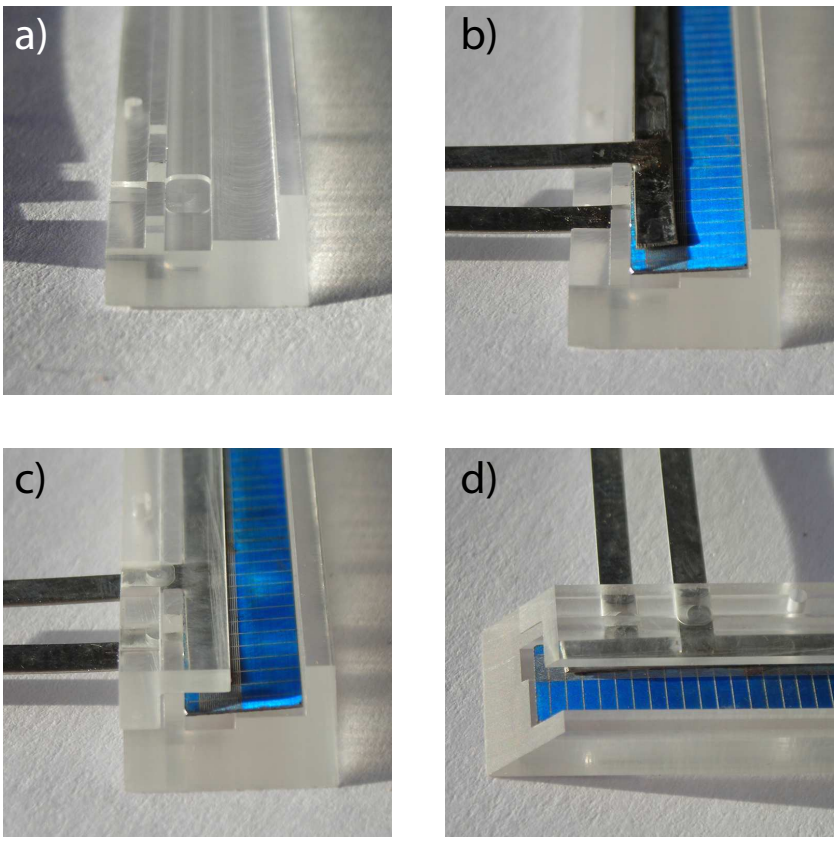

Figure 2.38: Prototype edge clip. a) Bottom part. b) Cell placed in bottom part - note grooves for tabbing. c) Top part in place. d) Final assembly. End has been mitered at 45° to mate with another clip. Note clearance between end of cell and end of clip.

Several edge clips like this were constructed. Fig. 2.39 shows the corner of an LSC sheet with two edge clips attached to the edges. The clips are held in contact with the edges using sprung plungers. The ends of the clips are mitred at 45° and form a close fit. The tabbing connections of each cell come out clear of the sheet and can be connected externally. The copper pins shown hold both parts of the clip together.

Although the two-part clip results in a strong holder for the cell, it still requires assembly. A better solution would be a one-piece clip moulded directly around the cell. This may be possible using the injection-moulding technique of "overmoulding".

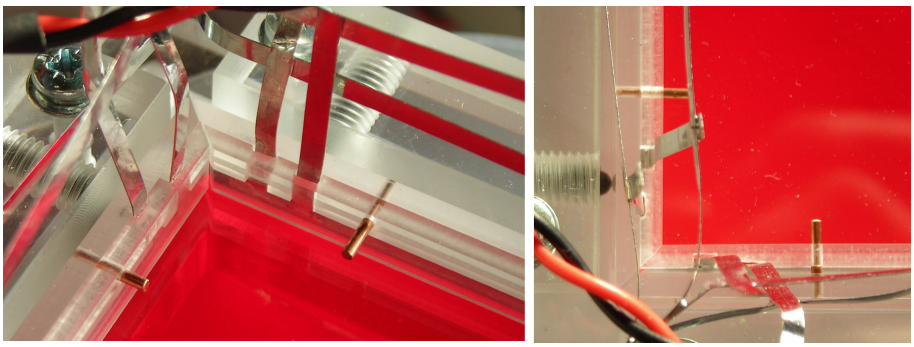

Figure 2.39: Two edge clips mounted on an LSC sheet

This is used, for example, to form a tool handle around a metal tool, or to add a rubber grip to a plastic part. The piece to be overmoulded is placed in the injection mould first and molten plastic or rubber is then injected around the piece. Once cool, the piece is embedded in the resulting plastic or rubber part. Material would be prevented from coating the cell's surface so the cell can still be glued to the edge of the LSC sheet.

A proposed system for moulding and gluing a one-piece clip is shown in Fig. 2.40. The cell, with tabbing connections already made, is retained in the injection mould by either the use of a vacuum hold-down (shown) or by mechanically clamping the tabbing. This is neccessary to prevent the cell moving when molten plastic is injected. The mould is closed and filled. The surface of the cell is held in close contact with the internal mould surface to prevent plastic covering the surface. Once removed from the mould, the cell would be completely encapsulated, with flying tabbing leads for electrical connection and a slot into which the edge of the LSC can be fitted and glued.

Instead of using an opaque material for the clip, a transparent plastic such as polycarbonate could be used. This would have the benefit that, if the plastic did leak past the mould and cover the surface of the cell slightly, it would not affect performance any because, once glued to the edge of the LSC sheet, light rays would pass straight through any excess plastic present on the front of the cell.

The author believes that the combination of a mirrored strip and pre-encapsulated cell can provide a simple, robust means of constructing LSC modules and is well suited to mass production. The use of the mirrored strip and pre-encapsulated cell can be

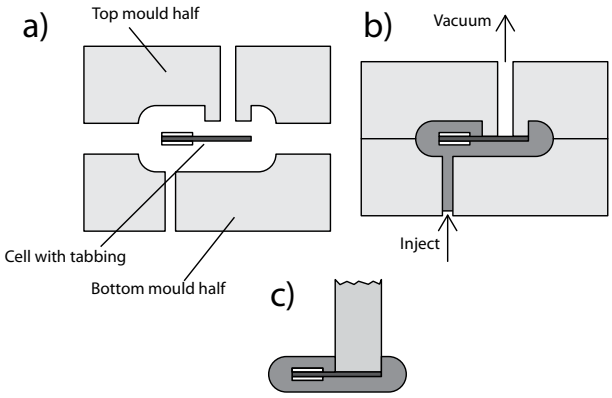

Figure 2.40: Overmoulding technique for cell encapsulation. (a) Mould separated. (b) Mould closed and plastic injected. (c) Completed clip attached to edge of LSC.

applied to any cell type, as the problems of encapsulation, electrical connection and cell attachement are common to all. The prototpye clips constructed show it is a feasible technique. With proper design, clips could be moulded that interlocked with each other when in place on the edges of a sheet.

Although the edge clip technique is suitable for a production module, it was deemed uneccessary for the experimental modules constructed here. Instead, bare cells were simply glued to the edges using the minimum amount of glue required for a good joint. The first (Section 2.6.3) and second (Section 2.6.4) LSC modules suffered from an excess of glue in the joint. However, a better gluing technique was perfected and this was used in the construction of the third set of modules (Section 2.6.5) and is described in that section.

Individual constructional details of each module will now be discussed.

2.6.3 First module

This module used a 10 cm x 10 cm square sheet, 0.3 cm thick, containing four of the Lumogen dyes. Details of the dye mixture and concentrations are given later in Section 7.1.1.

Because the optimum solar cells were not yet available, the module was constructed using non-optimum cells. This resulted in a greater shading loss from the smaller spacing of the fingers. Electrical contact to the cells was made by soldering tabbing

to only one location on the cell's busbar, as the double-sided soldering jig had not yet been developed. This led to a higher series resistance and correspondingly lower fill factor in the results. In addition, the one-sided soldering resulted in a small bend in the cell near the end which made it harder to achieve a good glue joint between the cell and the edge.

Cells were attached to the edges using cyanoacrylate glue. This provided a good mechanical joint, but this was subject to thermal stress when the module was illuminated in the solar simulator and several of the cells were damaged because of this.

Fig. 2.41 shows several views of the first module. A close-up of the connections to the solar cells is shown.

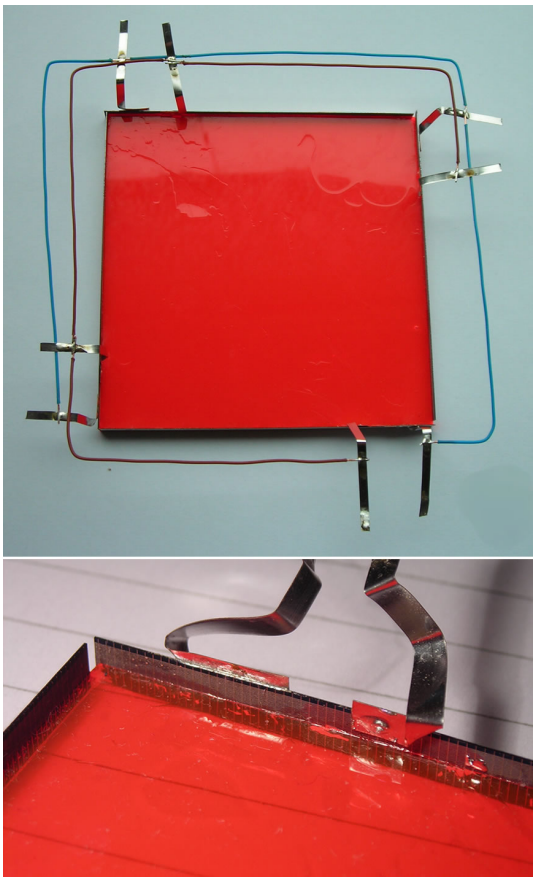

Figure 2.41: First LSC module

Note how the tabbing only makes contact with one part of the busbar - the series resistance from the opposite end of the busbar reduces the efficiency and fill factor. The surface of the sheet is not perfectly flat, as the sheet separated from the glass-plate mould during the casting process. These "separated" areas still have an optically

smooth surface which is flat and parallel to the main surface of the sheet, but is lower by approximately 0.5 mm. As the surface is parallel, the effect of these separated areas on the path of trapped fluorescence photons is minimal. No increased losses were visible from these regions. Note also the areas where there is an airspace between then cell and the sheet edge where glue has not flowed. These appear bright in the bottom photo and increased in size and frequency after the module was illuminated because of thermal stress.

2.6.4 Second module

The second module improved on the design of the first and also used a 10 cm x 10 cm x 0.3 cm sheet. Before the optimisation simulations presented in Chapter 6 were performed, preliminary simulations had also indicated that a mixture of Violett 570 and Rot 305 dyes would result in the highest efficiency. It was decided to produce an LSC sheet containing concentrations of 300 ppm Violett 570 and 900 ppm Rot 305, although the later optimisation simulations showed that these concentrations were unnecessarily high and did not result in any improvement in efficiency.

A mirrored strip (as described in Section 2.6.2) was deposited on the faces of the sheet. An electron-beam evaporator was used to deposit a thin aluminium layer. Masking was provided by two squares of aluminium placed on both faces of the sheet and clamped together with rare-earth magnets on either side. The edge of the sheet was protected with a layer of Kapton tape. Although the aluminium deposit initially appeared bright, it slowly turned brown on exposure to the atmosphere. The reason for this is unknown. It also turned brown in proximity to the epoxy adhesive used to attach the cells. This problem could be solved by use of a better coating technique and better control of the process.

Optimised cells were used (Section 2.5). They were glued to the edges of the sheet first, before electrical connections were attached. Araldite epoxy was used to attach the cells. Instead of soldering connections, an attempt was made to use conductive silver paint instead. Thin wires were secured in place over the busbar and rear contact using spots of epoxy. Conductive paint was then applied to make a connection between the

wire and the underlying contact. The fumes from the solvent in the conductive paint appeared to affect the aluminium mirror coating and turned it brown.

Fig. 2.42 shows several views of the module. Fig. 2.42c shows how excess glue can extend over the surface of the sheet, yet not affect internal reflection of light from the surface. The long coiled wire connections shown contributed to the series resistance losses and were later removed.

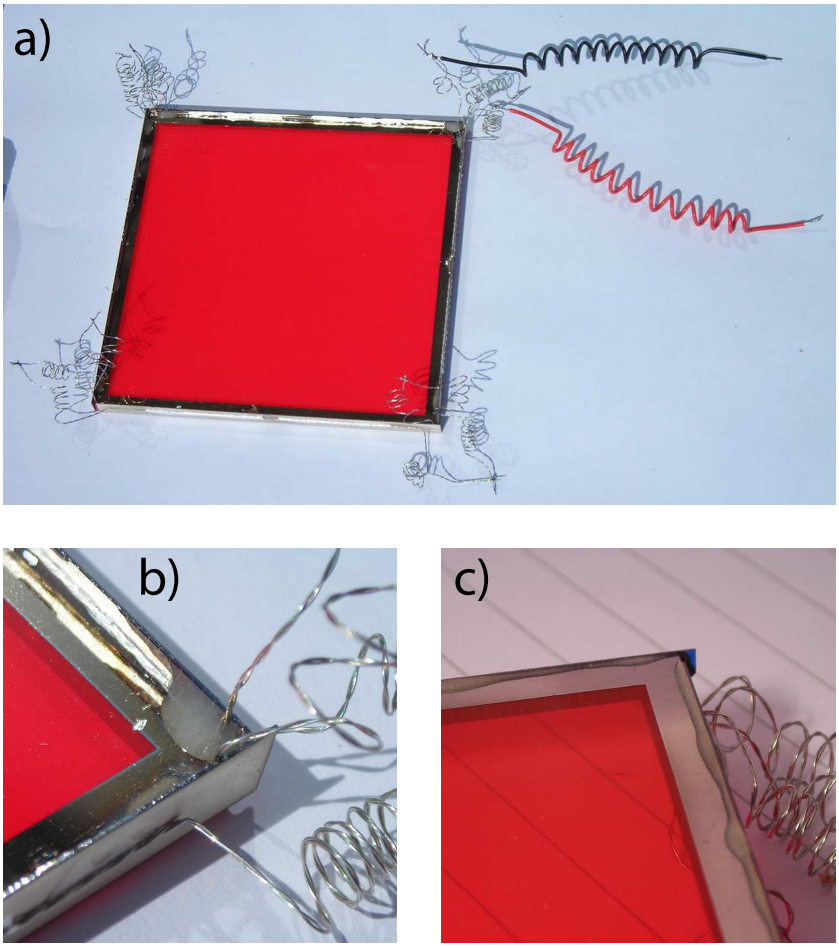

Figure 2.42: Second LSC module. a) Entire module. b) Front view, showing cell connections. c) Rear view. Note glue covering the mirrored strip.

2.6.5 Third, fourth and fifth modules

Concentrations for these modules were chosen based on the optimisation simulations performed in Section 6.1.1. Full details of the dye concentrations used are given in Section 7.1.3.

Optimised cells with tabbing attached using the double-sided soldering jig were used. External tabbing connections were attached to the middle of the tabbing on the busbar and rear surface of the cell. Because of the problems of the aluminium coating experienced with the second module (Section 2.6.4), it was decided not to apply a mirrored strip to these sheets. Instead, the cells were simply glued using the bare minimum of adhesive required to achieve a good bond. A jig was designed and constructed by the author to hold the cells in place while gluing and this is described below.

The LSC sheet, which had its edges cut and machined (Section 2.3.5), was clamped to a thick piece of flat aluminium plate. A spacer is used underneath the sheet to raise it off the surface of the plate and to protect its surface (wood, covered with paper masking tape, is ideal). Another wooden protective pad is used on top of the sheet. This clamping arrangement is shown in Fig. 2.43. The length of the protective pads is less than the length of the sheet edge so they can clear other cells already attached to the other edges of the sheet.

The entire jig was clamped so that the LSC sheet was vertical, with the edge to be glued facing upwards. Epoxy adhesive was mixed and loaded into a disposable syringe. A narrow bead of glue, approximately 1 mm wide by 0.5 mm thick, was deposited along the middle of the upturned edge using a 2.5 cm^3 disposable syringe with an 18-gauge blunt drawing-up needle. 5-minute Araldite epoxy was used. The jig was then turned upside down so the sheet was still vertical but the glue-coated edge now faced downwards.

The solar cell, with tabbing attached, was then placed in a machined PTFE holder which located it against the edge of the sheet. This holder is shown in Fig. 2.44a. PTFE was chosen as it is non-stick and will prevent excess glue sticking to it. It is also slightly flexible, which allows even pressure to be applied along the entire length of the cell. The top surface of the holder is machined flat except for two small protruding locating pegs (indicated). The cell is placed on the top surface and slid against the pegs as shown. The length of the pegs is such that they fit between the LSC sheet and the aluminium plate when the holder is in place.

The holder is now placed against the aluminum plate and slid upwards so the cell

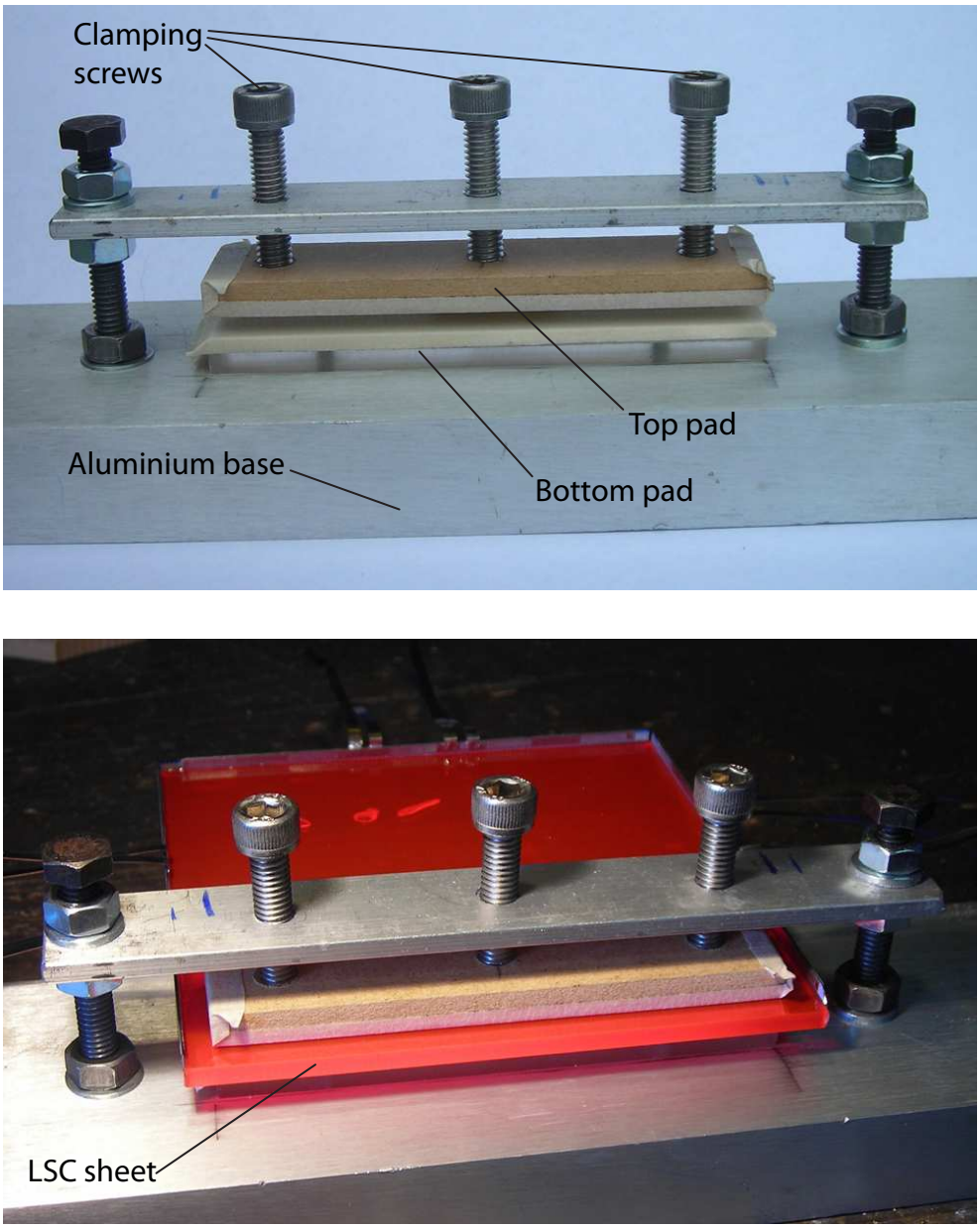

Figure 2.43: Clamp for gluing jig

contacts the glue on the edge of the sheet. Upwards pressure is then applied until the glue has set and the cell is attached. Pressure is also applied to keep the holder in contact with the aluminium plate. The process of bringing the holder up to the edge of the sheet is shown in Fig. 2.44b. Although some glue will come out the edges of the joint, it does not flow on to the surfaces of the sheet because the sheet is positioned above the cell and gravity keeps the glue away. Any that flows on to the PTFE holder simply releases once set. The two locating pegs leave slight marks on the surface of the sheet, but as the pegs are only $\sim$0.5 mm wide, the effect is negligible

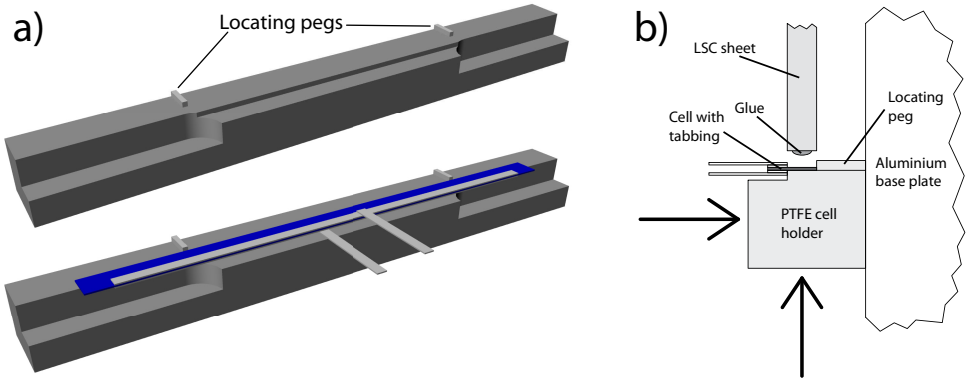

Figure 2.44: (a) PTFE holder for cell. (b) Method of applying cell to edge of sheet.

Fig. 2.45 shows both the holder in place and with it removed once the glue has set. The cell can be seen attached to the edge. The holder was kept in place by hand pressure for approximately 30 min to ensure the glue had set completely and the joint was left a further hour before removing the sheet and proceeding to the next cell.

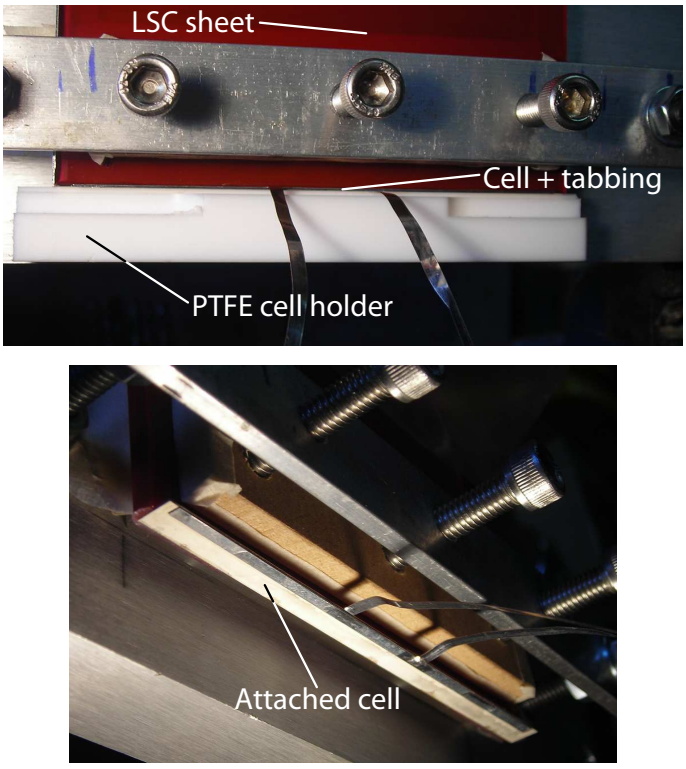

Figure 2.45: Cell in position and attached

Once all cells had been attached to the edges of the sheet, it was removed and mounted

in a plastic frame. The frame protects the cells and sheet from mechanical damage. Four pieces of copper-clad PCB were glued around the edges of the frame and the tabbing from each cell soldered to these. External connections could then be soldered to the pieces of circuit board, rather than directly to the tabbing leads from the cell. This prevented any damage to the cell during soldering/desoldering connections. The sheet was held in place on the frame with four V-shaped adjustable clamps at each corner, screwed to the frame. Both the frame and clamps were laser-cut from 2 mm acrylic sheet. A hole in the frame is left behind the LSC sheet to allow light to be transmitted through the sheet and interact with any back reflector present without interference from the material of the frame.

Fig. 2.46 shows one of the completed modules (module 3, Violett 570 + Rot 305 mixture). The tabbing connections between the cells and circuit board pieces are bent slightly to avoid straining the cells. Note the presence of three bubbles in the cast LSC sheet. Although the presence of these bubbles will cause some trapped light to be scattered out of the LSC and lost, the effect is minimal. The total area of the regions affected by the bubbles is $\sim$0.5 cm^2. To try and determine the magnitude of the loss introduced by the bubbles, the simulation program was modified by adding a 0.5 cm^2 region to the LSC where photons had a certain probability of being scattered and lost. With a probability of 0.5, the predicted efficiency decreased by only 2 % relative. Therefore, the bubbles, although not desirable, do not result in any significant reduction in the overall efficiency of the module.

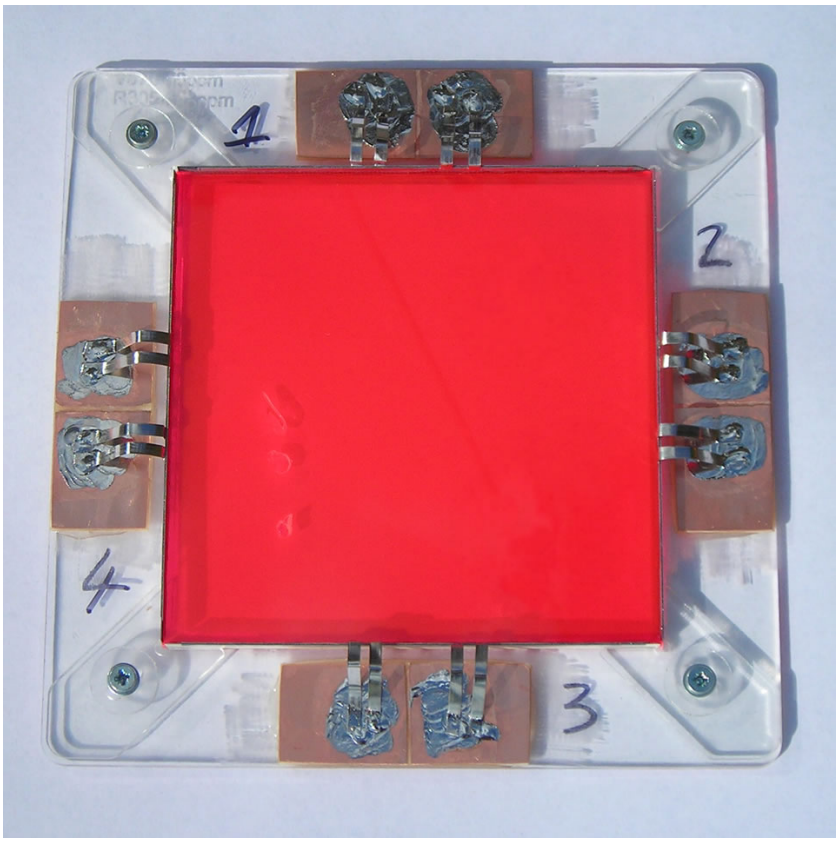

Figure 2.46: Module 3 completed

2.6.6 Sixth module

The sixth module was based on a 60 cm x 60 cm x 0.3 cm sheet containing 400 ppm of Rot 305 dye. An important feature of this module is the attempt to vary the lengths of the cells attached to the edges in order to achieve current-matching. The lengths chosen, and the procedure used to determine them, are described in detail later in Section 7.2. Optimised cells were again used (designed for 5x concentration, Section 2.5) and were cut to length using a diamond disc saw mounted in a Dremel tool. As shown in 2.47, the diamond saw was used to cut a line through the back contact of the cell into the silicon, but not as deep as the junction itself, to prevent damage. The cell was then snapped by hand at the cut line. It was possible to achieve a length tolerance of ±0.5 mm with this method.

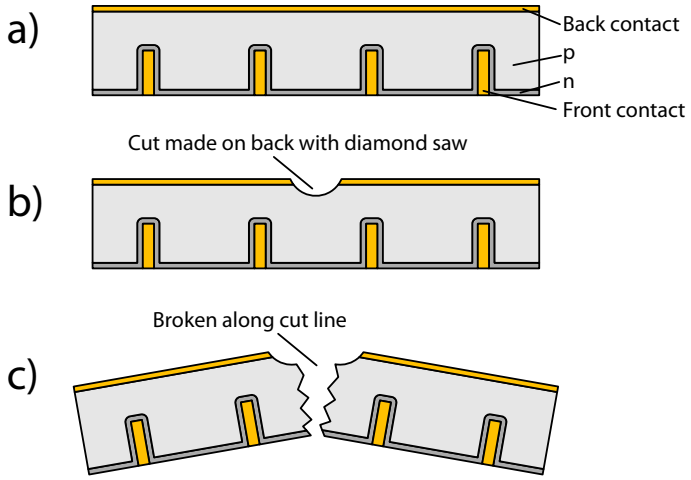

Figure 2.47: Cutting of LGBC cells. Original cell shown in a). Shallow cut made on rear of cell with diamond saw, b). Cell snapped at cut line, c).

To assist with gluing the cells to the edges of the LSC sheet, a larger version of the jig described in Section 2.6.5 was built by the author, capable of clamping the entire 60 cm edge of the sheet. The construction is similar to that shown in Fig. 2.43; the LSC sheet is held between a top and bottom pad with clamping screws, and the cell is brought into contact with the edge using the same PTFE holder.

Fig. 2.48 shows an overall view of the gluing jig. The main body is constructed from 50 mm-square steel box section. Another piece of box section is bolted to the bench top and contains a pivot, which allows the entire LSC sheet to be rotated (while

still clamped) and locked into either an "edge-up" or "edge-down" position. Glue is applied to the sheet edge in the "edge-up" position, then the sheet is rotated and the cell attached in the "edge-down" position, similar to the procedure described in Section 2.6.5.

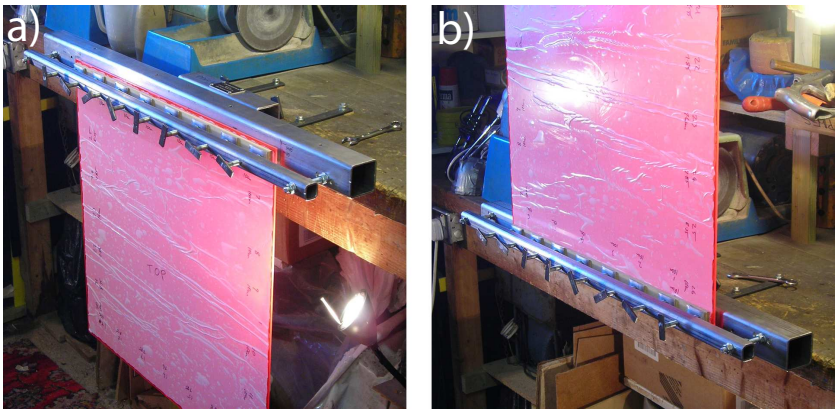

Figure 2.48: Overall view of gluing jig for large module. Sheet shown rotated into a) edge-up position and b) edge-down position.

Fig. 2.49 shows a detail of the clamping arrangement, which is similar to that in Fig. 2.43. The LSC sheet is clamped between a paper-tape-covered acrylic bottom pad (attached to the steel box section) and a wooden (MDF) top pad. The thickness of the bottom pad is again such that the locating pegs of the PTFE cell holder (Fig. 2.44) can fit underneath the LSC sheet. A total of eight clamping screws were used along the length of the edge to apply a uniform force to the pads. Note that the surface of the sheet is protected with film to prevent scratches - this is only removed once the entire LSC module is completed.

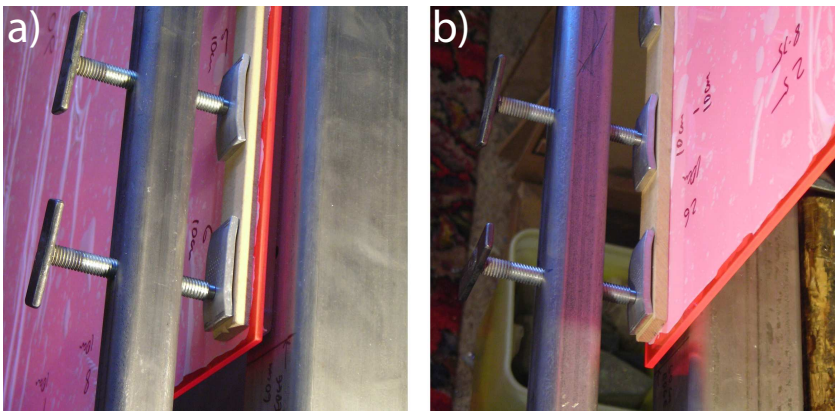

Figure 2.49: LSC sheet clamped in gluing jig. Shown in a) edge-up and b) edge-down positions.

Finally, Fig. 2.50 shows a complete line of cells attached to one edge of the sheet. Care was taken to ensure a slight space between adjacent cells to prevent any electrical contact, as the cells will later be connected in series.

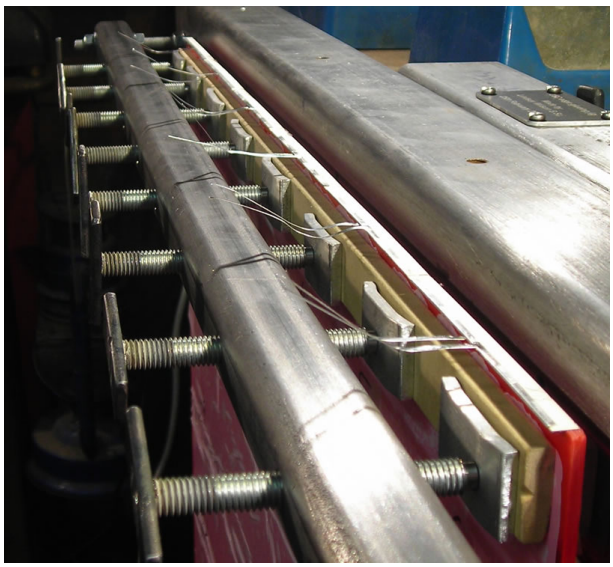

Figure 2.50: Cells attached to edge of sheet

The completed LSC module is shown in Fig. 2.51. The LSC sheet is mounted on a wooden base (made from 6 mm MDF) attached to a steel angle-iron frame. A clamp is used at each corner to prevent the LSC sheet moving. Small pieces of sheet foam padding are placed under each corner and at the midpoint of each edge to prevent the cells from striking the wooden base. Foam is also used on the corner clamps. A nylon retaining screw is used at each corner to hold the sheet down and prevent it from falling out during transport, should the module be inverted.

The tabbing connections from each cell are soldered to small pieces of PCB material which are glued to the wooden base. This provides a solid connection point for external electrical connections and prevents the tabbing contacts from being disturbed. Interconnections are made between cells using 1.5 mm-diameter solid copper wire soldered to the PCB contacts. Care is taken to ensure that the interconnections are flexible (by making a "U"-bend in the middle of the wire) to allow for expansion/contraction. The overall frame dimensions are 86 cm x 86 cm square.

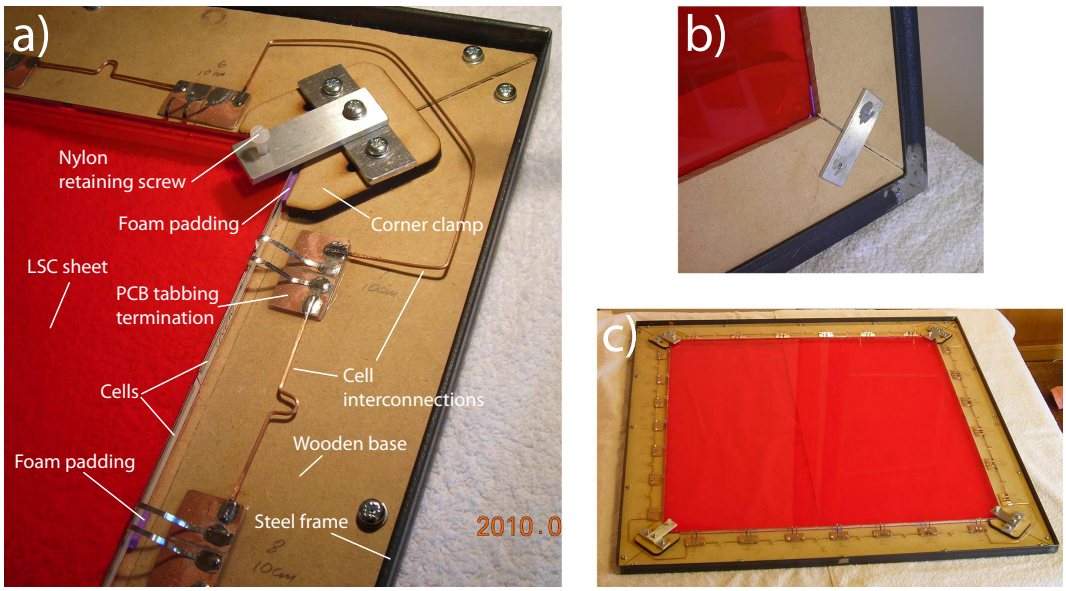

Figure 2.51: Sixth module finished. a) Detail of LSC sheet mounting and cell interconnections. b) Rear of module, showing frame and base. c) Overall view of module.

2.7 LSC characterisation

Several pieces of equipment were used for measuring the performance of LSC modules after construction. Two different solar simulators were used for measuring the overall solar-to-electric efficiencies of LSC modules. A custom-built sourcemeter was also used to measure the I-V curve of a module and its maximum power output. This was used in angular dependence and sunny/cloudy comparative measurements.

2.7.1 Oriel solar simulator

Access to this was provided courtesy of NaREC. The simulator is shown in Fig. 2.52. Light from an Oriel xenon arc lamp is collimated and filtered to provide an approximation of an AM1.5g solar spectrum. It is directed downwards on to a water-cooled brass vacuum chuck. This is important when measuring bare cells, as it keeps the cell temperature constant. It is less important for LSC modules, as the cells on the edges of an LSC do not heat up appreciably. The poor thermal conductivity of the PMMA makes it difficult to control the sheet temperature. The light source provides uniform illumination across the entire area of the chuck (12 cm x 12 cm square). LSC modules tested on this machine are usually 10 cm x 10 cm square.

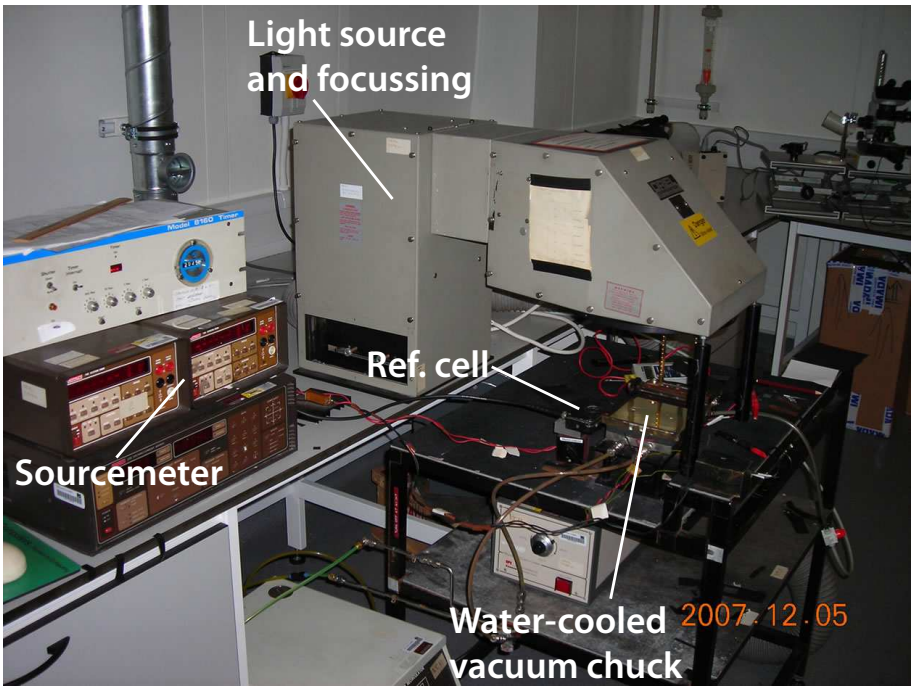

Figure 2.52: Solar simulator at NaREC

Spring-loaded busbars are provided which can be used for making contact with the busbars of bare cells, instead of soldering connections to them. Again, these cannot be used with LSC modules. Connections are instead made by flying leads of tabbing.

A small reference solar cell is placed near the vacuum chuck. This monitors the illumination intensity and the arclamp current is adjusted to keep this constant.

The I-V curve of the solar cell or module under test is measured with a computer-controlled Keithley sourcemeter. Fill factor, short-circuit current, open-circuit voltage, maximum power point etc. are automatically calculated.

Before performing measurements on an actual module, the solar simulator must first be calibrated by measuring a secondary reference cell (calibrated against a primary reference cell, which in turn has been calibrated by the Fraunhöfer Institute for Solar Energy Systems, Germany) of known short-circuit current under 1-sun illumination. The intensity of the simulator lamp is adjusted to obtain the same short-circuit current. The intensity in the simulator is then also one-sun, or $1000\,\mathrm{W/m^2}$.

2.7.2 Spire flash tester

To test the large 60 cm x 60 cm LSC module constructed at the end of the project (Section 2.6.6), a SPI-SUN Simulator 240A flash tester[260] was used, also at NaREC[246]. Instead of the continuous xenon arc lamp used in the Oriel simulator (Section 2.7.1), this uses a constant-intensity, long-duration xenon flashlamp to illuminate the module under test. Illumination time during the flash is on the order of ∼30 ms and is uniform to ±3 % over an area of 61 cm x 122 cm[260]. The module is exposed to the flashlamp at a range of different voltages and the current produced measured at each voltage to plot the I-V curve. The module is placed in a drawer which is lined with black anodised aluminium to prevent reflections of illumination light or stray light inside the machine. Electrical connection is made to the module with crocodile clips. Fig. 2.53 shows the machine and an LSC module in place.

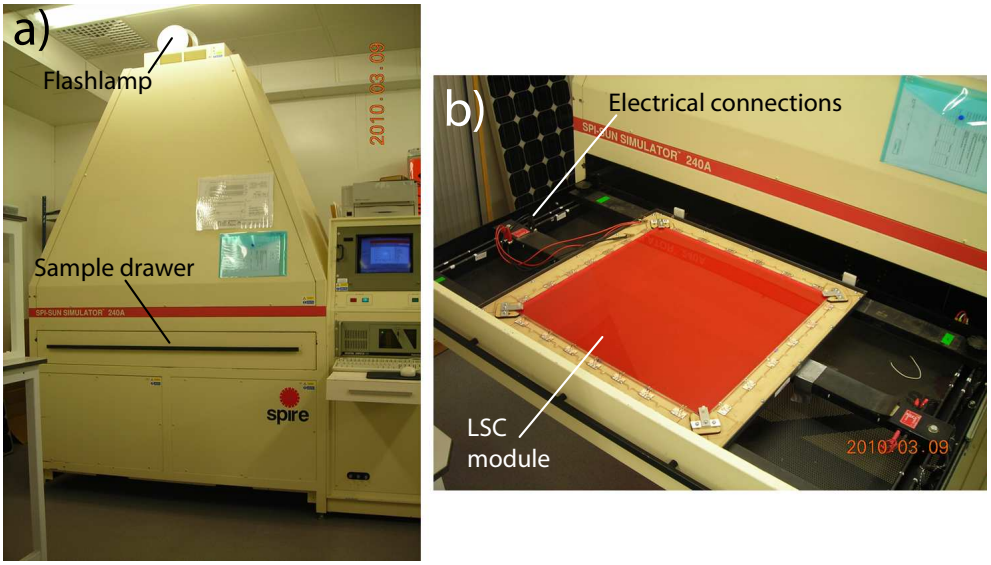

Figure 2.53: SPI-SUN Simulator 240A showing a) overall machine and b) sample compartment, with an LSC module under test.

To calibrate the machine, measurements are first made of the I-V characteristics of a BP Solar sc-Si module which has previously been calibrated at Fraunhöfer. The intensity of the flashlamp is adjusted (by altering the firing voltage) until the measured short-circuit current matches that obtained from Fraunhöfer (to within 0.5 %).

As shown in Fig. 2.54, the simulator spectrum matches the AM1.5g solar spectrum closely, except at wavelengths below ∼380 nm, where the light from the simulator is of

lower intensity or absent entirely. This presents a problem, since, as shown later (Fig. 6.14 of Chapter 6), the LSC containing Rot 305 dye still responds well to light with λ <380 nm because of the high absorption coefficient of the dye in the UV region. The measured efficiency of such an LSC exposed to illumination from the SPI-SUN will therefore be less than under actual AM1.5g solar radiation.

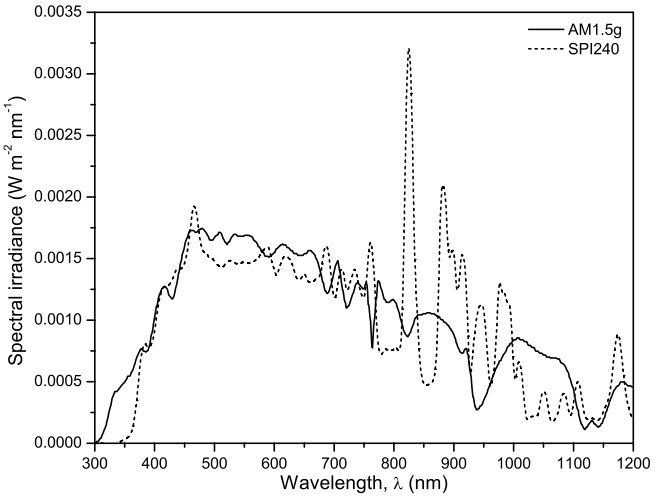

Figure 2.54: Illumination spectrum of SPI-SUN, compared with AM1.5g. Note absence of light at wavelengths <380 nm.

However, it is a simple matter to determine a correction factor to account for the difference in illumination spectra when presenting results of the efficiency. Such a correction factor can be obtained in several different ways, namely:

- use the Raytracer simulation program (Section 2.4.2) to calculate the efficiency of the LSC under both SPI-SUN and AM1.5g illumination;
- manually integrate the total photons in the SPI-SUN and AM1.5g spectra at all wavelengths <650 nm, which is the maximum wavelength to which the red-dyed LSC responds;
- measure the efficiency of a small red-dyed LSC module using both the Oriel and SPI-SUN simulators.

All three of these methods were tried, and all showed that the efficiency of the Rot 305-containing LSC under AM1.5g illumination was 5.5±1 % greater than under the

illumination from the SPI-SUN. This factor of 1.055 (corresponding to 5.5 %) can be applied to efficiency measurements from the SPI-SUN system to obtain a corrected efficiency under AM1.5g illumination, a technique which has been described previously[253]. Note that this correction factor only applies for the particular dye mixture and concentration used (400 ppm of Rot 305).

2.7.3 A simple sourcemeter

This was originally designed by the author for use in angular dependence measurements (Section 7.4). A simple means of measuring the I-V curve of a solar cells or LSC module was needed in order to calculate the maximum power produced.

Sourcemeters are based on the principle of applying a fixed (but adjustable) voltage to the device under test and then measuring the current which flows[261]. The applied voltage is then swept through a range of values to obtain the I-V curve. The voltage is usually microprocessor-controlled in the more advanced instruments. However, for the experiments performed here, nothing so complex is needed and the voltage ramp is taken from the output of a function generator. The ramp is buffered and fed to a series combination of the cell under test and a current-sensing resistor. The circuit diagram is shown in Fig. 2.55.

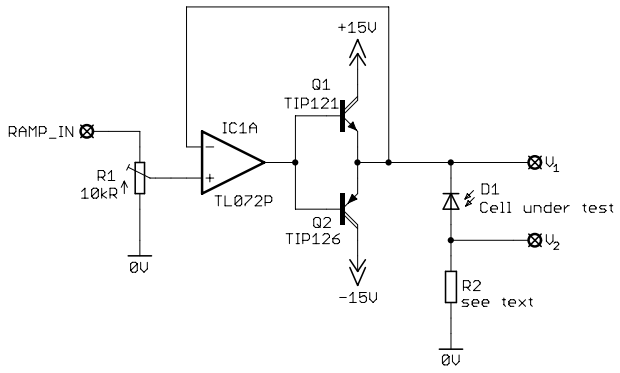

Figure 2.55: Simple sourcemeter circuit

The function generator is connected to RAMP_IN. R1 allows the amplitude of the ramp to be adjusted. The ramp voltage is buffered by the unity-gain follower formed by IC1A, Q1 & Q2 and is applied to the top end of solar cell D1. R2 is chosen to give a large enough signal for measurement of the current flowing. Voltages V_1 &

V_2 are measured at opposite ends of the cell with a dual-channel USB oscilloscope (Picoscope 2202). The cell voltage and current are calculated from $V_{cell} = (V_1 - V_2)$ and $I_{cell} = -V_2/R2$ respectively. To give an example, Fig. 2.56 shows the two voltage waveforms measured for a device under test and the calculated I-V curve. The two points indicated correspond to when the cell is operating at short-circuit (zero cell voltage, $V_1 = V_2$) or at open-circuit (zero cell current, $V_2 = 0$). The offset and amplitude of the applied voltage ramp are adjusted to ensure the cell operates between these two limits.

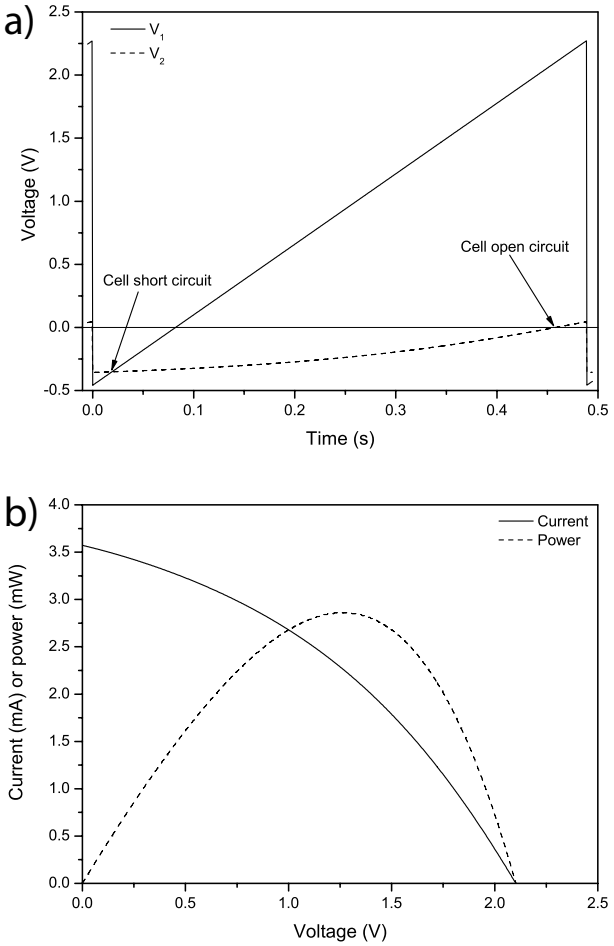

Figure 2.56: Sourcemeter example results a) voltage waveforms b) calculated I-V curve

2.8 Accelerated weathering

To determine the photostability of the organic dyes, samples of PMMA containing the dyes were exposed to UV radiation from a QUV weathering machine[262] at Lucite International's labs. This machine not only illuminates the samples with UV light but also exposes them to heat and humidity. The exposure cycle consisted of 4 hours UV exposure at 50°C with no humidity and then 4 hours in darkness at 50°C with a water spray. The lamp, type UVA-340, is designed to simulate the UV region of the solar spectrum from 300 nm to 365 nm, as this is the region most likely to cause photodegradation[263, 264, 265]. Fig. 2.57 shows the illumination spectrum measured at the sample position, compared with an AM1.5g solar spectrum. The weathering machine normally accepts samples of dimensions 50 x 75 mm. However, because of the large number of samples which required exposure, holders were made which held four 20 x 33 mm samples. The holder is shown in Fig. 2.58.

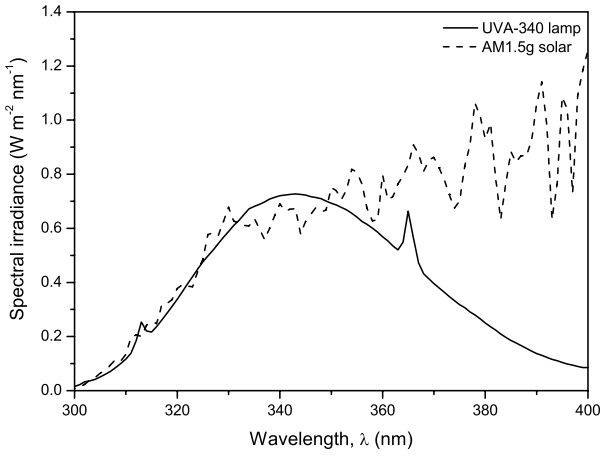

Figure 2.57: Spectrum of UVA-340 lamp used in QUV machine

To measure the progress of photodegradation, the absorption coefficient of the sheet was measured both before weathering and at 1 week intervals up to a maximum of 5 weeks. Although it is difficult to make a comparison between QUV weathering and real-world weathering because of unavoidable differences in experimental conditions such as illumination spectrum, temperature and humidity[266, 267], it was found (Section 7.3) that a sample exposed for 4 months in California showed the same

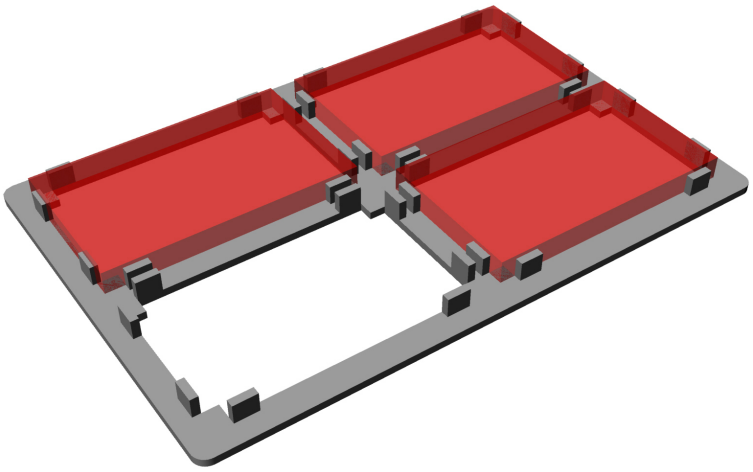

Figure 2.58: Holder for multiple weathering samples

degradation as did a sample exposed for 7.2 weeks in the QUV machine.

2.9 Conclusions

Several different fluorophores have been described which appear to be suitable for use in LSCs, including organic dyes and rare-earth compounds. Their absorption spectra can be determined in PMMA using a spectrophotometer and their emission spectra and quantum yields using a spectrofluorometer and integrating sphere. The results of these optical measurements are presented in Chapter 4.

PMMA is highly appropriate for use in LSC modules, as it can easily be doped with a range of fluorophores and can be cast into sheet or bulk form using either the waterbath or autoclave casting techniques. Its high transparency in the visible spectral region makes it most suitable for visible-emitting fluorophores, since its absorption in the near infrared limits the usable range of wavelengths to $<800\,\text{nm}$. Above this, host absorption losses become large enough to reduce the module efficiency.

The development of the Monte-Carlo simulation program "Raytracer" allows a wide range of possible LSC designs to be evaluated and the effect of module parameters, such as size and dye concentration/ratio, on the module efficiency and embodied energy to be studied. The results of these simulations are presented in Chapter 6. Once an optimum LSC design has been chosen, modules can then be constructed to

test their performance and these are studied in Chapter 7.

LGBC solar cells were chosen for use in LSCs because of the ease of fabricating cells of suitable aspect ratios. They have high operating efficiency and low reflectance when optically coupled to the edge of the LSC sheet.

Several novel constructional techniques have been developed to aid LSC module construction. The double-sided soldering jig eliminates bending stresses in the solar cells, while still ensuring good electrical contact with the tabbing. A proposed design for an edge "clip" to hold the solar cell in place has been presented and a protoype shows the feasibility of the idea. The technique of mirroring a strip on the surfaces of the sheet would enable the entire edge to be encapsulated without affecting optical performance.

The next chapter describes the study of the thermal-lens technique for measuring quantum yields and its associated difficulties.

Chapter 3

Thermal-lens spectrometry

It was initially thought that the thermal-lens (TL) technique, which was introduced in Section 1.7, would provide a more accurate means of measuring quantum yields than the integrating sphere, based on the reported accuracies in the literature. Therefore, the TL technique was studied in detail and an experimental system constructed to test its suitability. Unfortunately, it was found impossible to obtain either accurate or repeatable results from the apparatus, as is described in this chapter. No reasons for this were found and it was deemed wiser to move to the integrating-sphere technique instead.

3.1 Introduction

Gordon[205] was the first to observe a laser-induced photothermal effect by placing a cuvette containing a light-absorbing solution within the resonator cavity of a He-Ne gas laser. The observed effects included bistability of laser operation and temporal variation of both laser output power and beam diameter. The lifetime of these effects was on the order of seconds, indicating that they were due to thermal effects. This was confirmed by the observation of convection in the cuvette when the laser was running. It was also observed that the beam diameters at the cavity mirrors were different when the cuvette was inserted. This suggested the formation of a lens inside the cuvette and this was explained by the formation of a refractive index gradient

inside the sample due to the heating effect of the laser beam[205].

The first observation of a TL formed outside a laser cavity was by Rieckhoff[268]. A He-Ne laser beam was passed through a 20 cm-pathlength cell containing a variety of different solvents such as water, benzene, hexane and acetone. After turning the laser on, the beam after the sample cell was seen to slowly diverge over a period of several seconds, indicating the formation of a TL.

In 1973, Hu & Whinnery[204] were the first to suggest using the behaviour of the TL inside a fluorescent dye-doped sample as a means of measuring the quantum yield of the dye. They argued that the rate of formation or decay of the TL was proportional to the amount of heat deposited in the sample by the excitation beam. Heat is deposited in the sample by both non-radiative decay of the dye molecules and also by the Stokes shift in energy between absorption and emission. By comparing the magnitude of the TL formed in the dyed sample to that in a non-fluorescent reference sample with zero quantum yield, where all absorbed excitation light is converted to heat, it was possible to calculate the quantum yield of the dyed sample.

Instead of using the same laser beam to both excite the sample and to probe the TL formed, it is possible to use a separate "probe" laser of a different wavelength to detect the TL. This is used in the dual-beam TL technique[269]. While more complex than the single-beam method, it results in a greater sensitivity and a lower noise figure[206] and is the technique most commonly used.

Since its invention, the TL technique has been used in both single-beam[270, 271, 272, 205, 204, 273] and dual-beam[274, 275, 276, 277, 278, 279, 280, 281, 282, 212, 211, 109, 269, 283, 213, 284] configurations to determine the optical properties of a variety of both solid and liquid samples. Perhaps of most interest is the study by Lesiecki & Drake[284] where the dual-beam TL technique was used to measure the quantum yields of organic dyes in PMMA for application in luminescent solar concentrators.

The theory of TL formation and decay in both single-beam and dual-beam systems is described next.

3.2 Theory

Consider a Gaussian laser beam focussed on to a sample of transparent material, for example PMMA, doped with a fluorophore (Fig. 3.1). The laser wavelength is such that it is absorbed by the fluorophore.

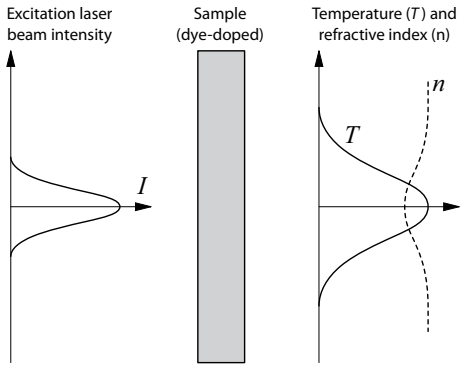

Figure 3.1: Gaussian laser beam passing through absorbing sample, showing temperature and refractive-index variations

A fraction of the laser beam's energy is absorbed on its passage through the sample by the fluorophore molecules, exciting them. They can then decay either by emitting a photon (radiative decay) or by dissipating the energy as heat in the host material (non-radiative decay). The excitation process and two decay processes are shown in Eqns. (3.1) to (3.3)

$$\text{Excitation :} \qquad h\nu_{excitation} + F \rightarrow F^* \tag{3.1}$$

$$\text{Radiative decay :} \qquad F^* \rightarrow F + h\nu_{emission} + heat_{Stokes} \tag{3.2}$$

$$\text{Non} - \text{radiative decay :} \qquad F^* \rightarrow F + heat_{Non-radiative} \tag{3.3}$$

where

$h\nu_{excitation}$	is an excitation photon (from the laser beam)
F	is an unexcited fluorophore
F^*	is an excited fluorophore
$h\nu_{emission}$	is a fluorescence photon

$heat_{Stokes}$	is the heat produced in the sample due to the difference in absorbed and emitted photon energies
$heat_{Non-radiative}$	is the heat produced by non-radiative decay of the excited fluorophore.

Decay processes other than the above are possible (for example, photochemical reactions of the fluorophores or energy transfer to another molecule) but it is assumed that the probability of these occurring is low compared with the two shown above[204].

The total amount of laser energy which is absorbed by the sample can be determined by measuring the intensity of the excitation laser beam both before and after the sample. This is the energy turned into both fluorescence emission and heat by the fluorophores. In order to calculate the quantum yield of the dye, we need to calculate the fraction of absorbed laser energy which is turned into heat alone. This can be determined from the TL.

The Gaussian profile of the excitation laser beam causes different amounts of energy to be deposited in the sample across the excitation beam front. As this energy is turned into heat inside the sample, a temperature gradient forms. Because of the temperature dependence of the refractive index of the host material[285, 203], this gives rise to a gradient in refractive index as shown in Fig. 3.1. The temperature rise is greatest on the axis of the excitation beam. Likewise, the change in refractive index is also greatest on axis. Most materials[285, 203], including PMMA, have a negative dn/dT, as the refractive index change is mainly due to physical expansion of the material.

The extent of the temperature gradient can be as much as one order of magnitude[274] larger then the diameter of the excitation beam, as heat is conducted away from the excitation region by the bulk of the sample. The resulting refractive index profile has the same effect on the passage of the excitation laser beam (or, for that matter, any light passing through this region of the sample) as does a conventional concave lens (if $dn/dT < 0$). This gives rise to the use of the term "thermal lens" to denote the refractive index profile within the sample.

The TL does not form instantly when the excitation laser beam is turned on because

it depends on achieving an equilibirium heat flow within the material. The rate of formation or decay of the TL is an indication of how much heat is being deposited within the sample.

The formation of the TL can be measured by monitoring the remnant of the excitation beam which passes through the sample - as the lens forms, the laser beam after the sample will slowly diverge. However, in highly absorbing samples there may be insufficient excitation light transmitted through the sample to give a measurable signal. Instead, it is possible to use a second, "probe", laser to detect the TL[269]. The wavelength of the probe laser beam is chosen such that it is not absorbed by either the fluorophore or the host material, since any absorption of the probe beam would alter the TL.

The shape of the refractive index profile within the sample is complex and this has resulted in two different theoretical treatments of the lens - the "parabolic"[205, 204] and "aberrant"[286, 207] models.

The parabolic model was the first to be used in the field of TL spectrometry and was originally developed by Gordon[205] and Hu[204]. To simplify calculations, the refractive index variation with distance from the beam axis was approximated by a parabolic curve. This approximation is valid for distances up to one beam radius from the axis[205], with an error of less than 1 %. The parabolic variation of refractive index, n, with radial distance from the axis, r, was of the form shown in Eqn. (3.4), where n_0 is the refractive index on-axis, δ is a constant and ω is the radius of the excitation beam in the sample.

$$n = n_0[1 + \delta(r/\omega)^2] \tag{3.4}$$

To ensure validity of this equation when using a dual-beam TL method, the diameter of the probe beam within the sample must be less than or equal to the diameter of the excitation beam. This ensures that all of the probe beam passes through the region of the TL where the parabolic approximation holds. There seems to be some confusion in the literature over whether excitation and probe beams should have exactly the same radius inside the sample[206] or whether it is sufficient to ensure the probe is

smaller than the excitation[269]. Since the only restricting criterion is the limit of accuracy of the parabolic fit, the second option (probe smaller than excitation) would appear to be a better choice.

The aberrant model[286, 207] instead treats the TL by using diffraction integral theory and integrating the small phase shifts introduced by the change in refractive index across the beam front[207]. Although applicable to a wider range of experimental situations, as there is no restriction on the relative sizes of the excitation and probe beams in a dual-beam system, the analysis is more complex and also requires knowledge of the thermooptical properties (dn/dT, thermal conductivity and diffusivity) of the host material. The parabolic model, by contrast, can be used in such a way that the need for the thermooptical properties is eliminated[204]. We use the parabolic method throughout the rest of this chapter.

Although placing the sample at the focus of the excitation beam would result in the maximum strength of TL formed, the effect of this lens on the passage of the laser beam is a minimum because the wavefronts of the beam are parallel at the focus[204]. It can be shown that, to maximise the effect of the TL on the laser beam, the sample should be placed one confocal distance from the focus[204]. The confocal distance, z_c, is calculated from Eqn. (3.5)

$$z_c = \frac{\pi\omega_0^2}{\lambda} \tag{3.5}$$

where ω_0 is the radius of the laser beam at the focus (at the beam waist). Since measuring the beam parameters (spot size, confocal distance) introduces additional errors, the ideal position for the sample is usually found by moving the sample until the maximum TL signal is obtained.

Fig. 3.2 summarises the sample positions and relative beam diameters for both single-beam and dual-beam TL systems. In a single-beam (also called thermal blooming) system, Fig. 3.2a, the sample should be placed one confocal distance after the beam waist. This maximises the TL signal. In a dual-beam system, Fig. 3.2b, the sample should be placed one confocal distance after the waist of the probe beam. Its position relative to the waist of the excitation beam is less critical, but it is usually placed

at the beam waist to achieve greatest excitation intensity at the sample. The probe beam diameter is made less than or equal to the excitation beam diameter inside the sample. This may require the use of beam expanders/compressors to achieve a suitable waist diameter.

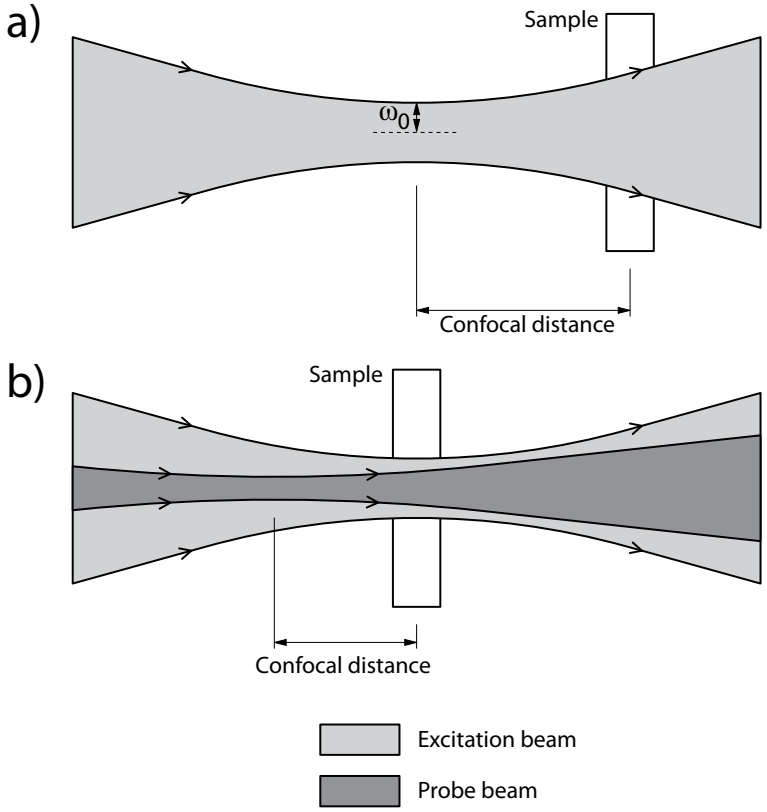

Figure 3.2: Thermal-lens systems using (a) single beam and (b) dual beams

The steady-state focal length, f_∞, of the TL is governed by the equilibrium balance between heating from the excitation beam and conduction by the host matrix and can be calculated from Eqn. (3.6)[204]

$$f_\infty = \frac{\pi k \omega^2}{PA(dn/dT)} \tag{3.6}$$

where k is the thermal conductivity of the host material, P is the incident laser power, ω is the beam radius within the sample, A is the fraction of incident laser power converted to heat alone within the sample and dn/dT is the change in refractive index with temperature. If the excitation beam is turned on at time $t = 0$, the buildup of the focal length in the approach to steady-state is given by Eqn. (3.7)

$$f(t) = f_\infty(1 + t_c/2t) \tag{3.7}$$

where t_c is the time constant of the TL and is given by $t_c = \rho c\omega^2/4k$, where ρ is the host material density and c is the heat capacity.

The simplest means of detecting the formation of the TL is to monitor the time variation of the far-field on-axis intensity of the laser beam after the sample (which is the excitation beam in a single-beam system and the probe beam in a dual-beam system). This is done using a pinhole/photodiode combination[204, 284]. The intensity measured at the centre of the far-field beam varies according to Eqn. (3.8)

$$I(t) = \frac{I(0)}{1 - \frac{\theta}{1+\frac{t_c}{2t}} + \frac{\theta^2}{2\left(1+\frac{t_c}{2t}\right)^2}} \tag{3.8}$$

where

$I(t)$	is the intensity at a time t after the excitation beam has been turned on
$I(0)$	is the equilibrium far-field intensity at the centre of the beam
$\theta = \frac{PA\frac{dn}{dT}}{\lambda k}$	is called the thermal-lens coefficient
$t_c = \rho c\omega^2/4k$	is the time constant of the thermal lens (s)
A	is the fraction of incident laser power which is degraded to heat either by non-radiative decay or by the Stokes shift in fluorescence emission
P	is the power of the excitation beam (W)
$\frac{dn}{dT}$	is the variation of host refractive index with temperature (K^{-1})
λ	is the excitation wavelength (m)
k	is the thermal conductivity of the host (W m^{-1} K^{-1})
ω	is the radius of the excitation beam in the sample (m)
ρ	is the density of the host (kg m$^-$3)
c	is the specific heat capacity of the host (J kg^{-1} K^{-1})

The experimental parameter of interest is θ, the TL coefficient. This can be obtained by a least-squares fitting of Eqn. (3.8) to experimental data for the intensity variation with time. From this we can determine A, the fraction of incident laser power which is converted to heat alone within the sample.

If the sample has a non-zero luminescent quantum yield, a photometric measurement of the fraction of incident laser power absorbed by the sample, A_p, will be greater than A and related to the quantum yield, η_{PLQY}, by Eqn. (3.9)

$$\eta_{PLQY} = \frac{\nu_{ex}}{\langle \nu_{em} \rangle} \left[1 - \frac{A}{A_p} \right] \tag{3.9}$$

where

ν_{ex}	is the excitation laser frequency (Hz)
$\langle \nu_{em} \rangle = \frac{\int \nu E(\nu) d\nu}{\int E(\nu) d\nu}$	is the average fluorescence emission frequency (Hz)
$E(\nu)$	is the fluorescence emission spectrum of the fluorophore in units of photon counts

The ratio $\nu_{ex}/\langle \nu_{em} \rangle$ accounts for the heat generated in the sample by the Stokes shift of the fluorescence emission. For example, although a fluorophore may have 100 % quantum yield, heat is still generated in the sample because of the lower energy of the emitted photons.

We can use Eqn. (3.9) to calculate the quantum yield of the fluorophore. However, this approach lacks precision because of the need to know both dn/dT and k exactly for the host material of the sample under study. These parameters can vary depending on the methods used to prepare the sample. For example, dn/dT of PMMA was shown to vary between -1.1x10^{-4} K^{-1} and -2.5x10^{-4} K^{-1} depending on the method of manufacture[203].

It is possible to avoid this problem by comparing the TL coefficients obtained from the fluorescent sample with those from a non-fluorescent reference containing a fluorophore with zero quantum yield. In such a reference, all absorbed excitation energy is converted to heat[271, 270]. If identical host materials are used for both sample and reference (both are manufactured using identical techniques) and the reference has zero quantum yield, the quantum yield of the fluorescent sample can be calculated

from Eqn. (3.10)

$$\eta_{PLQY} = \frac{\nu_{ex}}{\langle \nu_{em} \rangle} \left[1 - \frac{A_p^{ref} \theta^{sample}}{A_p^{sample} \theta^{ref}} \right] \tag{3.10}$$

where the superscripts denote the A_p and θ values for the sample and reference. The A_p values for the sample and reference can be measured with a spectrophotometer and the TL coefficients are obtained from fits of Eqn. (3.8) to experimental data. At no point is knowledge of the thermooptical properties of the host material required.

The theoretical derivation used thus far places several constraints on the experimental system[284]. These are as follows:

1. Both excitation and probe beam (if used) must have a TEM_{00} Gaussian profile.
2. The excitation power absorbed within the sample must be small enough to avoid spherical aberration and convection effects in the TL, which requires $\theta \leq 1$.
3. Sample and reference must be positioned at the same location relative to the waists of the laser beams
4. The sample thickness (along the optical axis) should be short compared to the confocal distance to ensure a constant beam diameter throughout the sample[207]. For the current experimental system, this places an upper limit of about 1 cm on the thickness.
5. However, the sample thickness should be long compared with the diameter of the excitation beam to avoid end effects - for example, at least five times the beam diameter[204, 284]. The lower limit on sample thickness is about 0.15 cm for the current system.
6. Finally, when sampling the far-field beam with a photodiode and pinhole, the sampled area of the beam must be small compared with its diameter - for example, less than 5 %.

We now look at the experimental TL system constructed by the author.

3.3 Experimental

Fig. 3.3 shows a schematic diagram of the TL system. It is a dual-beam system, using a visible excitation laser and an infrared probe laser. Each component of the system is described below.

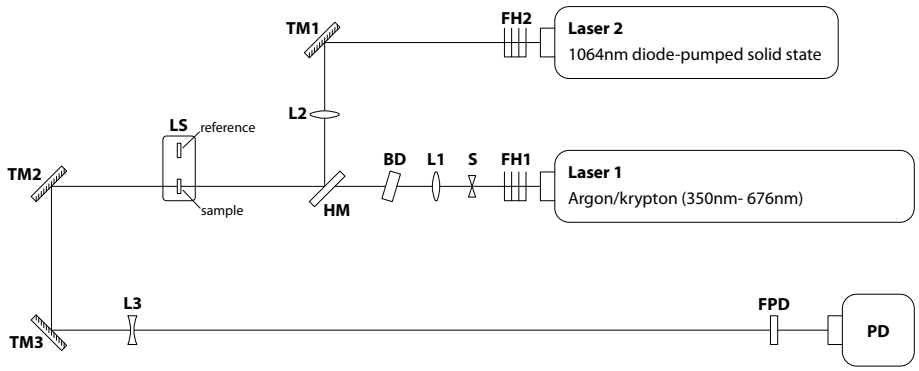

Figure 3.3: Dual-beam thermal-lens system. *FH1, FH2* - neutral-density filter holders. *S* - mechanical shutter. *L1* - convex focussing lens for excitation beam. *BD* - beam displacer. *HM* - hot mirror for combining beams. *L2* - convex focussing lens for probe beam. *LS* - linear slide for mounting sample and reference. *L3* - concave expanding lens. *FPD* - photodiode filter. *PD* - photodiode with pinhole. *TM1, TM2, TM3* - turning mirrors.

3.3.1 Lasers

The laser used for sample excitation (Laser 1 in Fig. 3.3) was a mixed-gas argon/krypton ion laser (Spectra Physics model 265). By using several different pairs of front and rear optics, it was possible to generate wavelengths in the range 350-676 nm. With UV front and rear optics, the 350 nm line is generated. A white-light (broadband) front optic and a blue-green reflective rear prism generate lines from 457 nm to 531 nm - these are the argon lines. By substituting the rear prism with a red-reflective prism, the 647 nm and 676 nm krypton lines are generated. This range of wavelenghs allows a wide range of fluorophores to be studied.

The output from this laser is, unfortunately, not steady, but has a 100 Hz ripple of around 5 % magnitude superimposed on it. This is because of poor smoothing in the power supply. It does not affect the formation of the TL, as the time constant of formation and decay is on the order of seconds. By choosing a sampling period which is not a multiple of 100 Hz, it is possible to average this ripple out in the oscilloscope

measurements later. The output beam is 95 % Gaussian, determined from a least-squares fit to the profile. Single-line powers up to several hundred mW are available. The laser tube is usually operated at its maximum current and the light intensity controlled by inserting neutral density (ND) filters into the beam path.

A probe laser wavelength of 1064 nm was chosen, as this is not absorbed appreciably by either the host material (in this case PMMA) or by any of the fluorophores studied. A diode-pumped solid state (DPSS) laser (Elforlight I4-300-1064) was used to generate the probe beam. It had a fixed output power of 300 mW and beam power was again controlled by inserting ND filters. The probe laser beam is also 95 % Gaussian.

3.3.2 Individual optics

The filter holders FH1 and FH2 accept ND filters which are used to control the intensity of both the excitation and probe beams. Since the ND filters used were of the absorptive type (as opposed to reflective), it was important to place holder FH1 *before* the shutter S. If the filters were placed after the shutter, the time-varying TL formed within the glass of the filter results in a varying beam intensity after the filter. By placing the filter before the shutter, the TL can stabilise and the transmitted intensity through the filter remains constant.

It was found that air currents in the lab had an effect on the intensity of the probe beam as measured with the photodiode. It emerged that these draughts were affecting the TL formed within the ND filters in holder FH2 and causing the intensity to vary. A shield of black card was used to exclude draughts from the area around FH2.

The shutter S consists of a small, blackened aluminium vane attached to a solenoid. The solenoid is actuated by a MOSFET driven from the squarewave output of a function generator. The duty cycle and period of the squarewave can be adjusted serparately to vary the fraction of time for which the sample is illuminated by the excitation beam. The shutter had 7.4 ms response time (off→on) and a 0.6 ms switching time (10 % - 90 % levels). A trigger signal for the oscilloscope was taken from the function generator.

Immediately after the shutter is the lens L1 which is used to focus the excitation

beam on to the sample. This was a 50 cm focal length, 2.5 cm diameter lens of BK7 glass.

In order to accurately align the excitation and probe laser beams so they are co-axial, a beam displacer BD is used to shift the focussed excitation beam. It consists of a fused silica window, 5 cm diameter and 1 cm thick, mounted in a two-axis gimbal with micrometer adjusters. When the window is tilted, the excitation laser beam passing through is displaced perpendicular to its direction of propagation as shown in Fig. 3.4, but remains travelling parallel to its original direction. The laser beam can be shifted without distorting the profile at the focus.

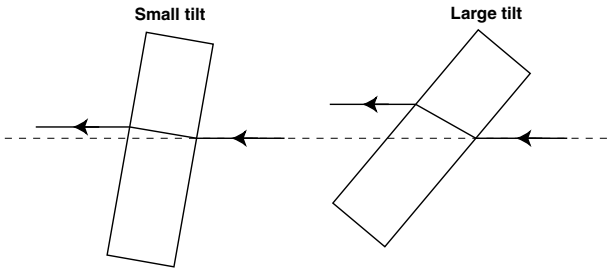

Figure 3.4: Beam displacer showing lateral displacement of the laser beam

Both the excitation and probe beams need to be superimposed coaxially on each other. This is achieved with a hot mirror (HM) (Melles Griot type 03-MHG-009). The transmission spectrum for both 0° & 45° incident angles is shown in Fig. 3.5. When used at 45°, it transmits 350-800 nm and reflects 800-1200 nm, which are ideal wavelength ranges for combining the excitation and probe beams. The hot mirror is held in a kinematic mirror mount to allow the direction of the reflected probe beam to be adjusted.

The probe beam is also focussed using a concave lens L2 which also has a focal length of 50 cm. The diameters of the beams from the lasers were such that it was possible to ensure the probe beam was smaller than the excitation beam at the sample position. Turning mirror TM1 is used to direct the probe beam on to the hot mirror.

The sample holder is described in greater detail in the next subsection.

After the sample, the laser beams are folded back along the optical table with turning mirrors TM2 and TM3. A convex lens L3 is used to expand the laser beam before reaching the photodiode detector. This ensures that the detector samples only a small

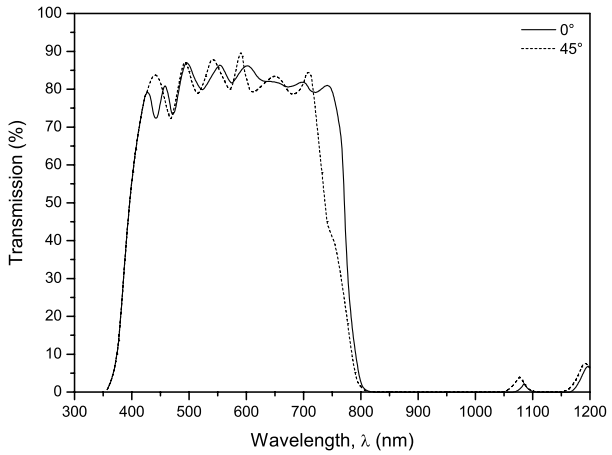

Figure 3.5: Transmission spectrum of hot mirror

part of the beam near the axis. A 1064 nm laser-line filter, FPD, is used to block the excitation laser from falling on the photodiode. The total pathlength between the sample position and the photodiode is 2-3 m. The diameter of the expanded probe beam at the photodiode is 5-10 cm. Since the diameter of the photodiode is only 0.1 cm, this ensures that only the centre of the beam is sampled.

3.3.3 Samples

PMMA sheets containing the fluorophores to be studied were cast using the waterbath technique (Section 2.3.1). These samples are 3 mm thick and have parallel, optically-flat surfaces.

The black dye Makrolex X70 was used as a non-fluorescent reference. This is an organic dye which can be doped into PMMA and absorbs all wavelengths <800 nm. It is therefore transparent to the 1064 nm wavelength of the probe beam, which is one of the requirements. Both sample and reference had the same thickness.

It is unclear from the literature if the absorbances of the sample and reference should be matched by adjusting the dye concentration (as is mentioned in Terazima[212]), whether it is sufficient that they are close (within 20 %, Lesiecki[284]), or whether it is the TL coefficients of sample and reference that should be comparable[270]. If sample and reference must have exactly the same absorbance, then each sample

would require its own reference. Since the fluorescent PMMA samples had already been manfactured, this would have requried a large number of reference samples to be cast. Instead, a single range of reference sample concentrations was cast, and it was possible to always choose a reference sample with an absorbance within 10 % of that of the fluorescent sample. Matching the TL coefficients would seem to be more suitable, as the strengths of the thermal lenses in sample and reference are then comparable. The range of reference concentrations allowed this to be achieved as well.

In order to position the sample and reference successively in the excitation beam, a two-position linear slide was used. This is shown in Fig. 3.6. A standard 25 mm travel linear slide with micrometer adjustment (Thorlabs PT1/M) was modified by removing the spring return and mounting a second micrometer adjuster to the end opposite the existing adjuster. The tip of each adjuster bears on a hard steel stop to limit the travel. The attractive force of small rare-earth magnets glued to both the slide and the base holds the slide in position at each end of its travel. The sample and reference were mounted in two plate holders (Thorlabs FP01) mounted on top of the slide.

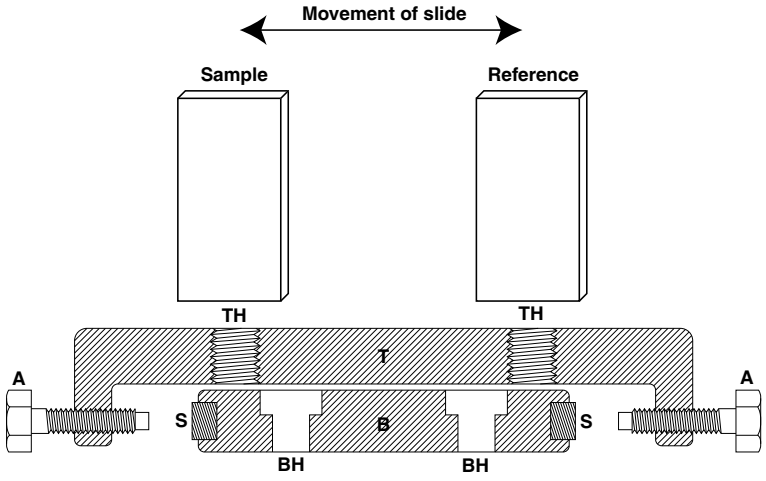

Figure 3.6: Two-position linear slide for holding samples. *T* - top (movable). *B* - bottom (fixed to optical table). *TH* - threaded holes for attaching sample holders. *BH* - holes for fixing slide to optical table. *A* - adjustment screws. *S* - hardened steel stops. Slide movement is perpendicular to direction of laser beam.

Using this arrangement, either the sample or reference may be moved into the excitation beam and can be returned to exactly the same position each time, enabling successive measurements to be made at the same point on the sample and reference.

3.3.4 Detection and analysis

The probe beam intensity after passing through the sample was measured with an amplified InGaAs photodiode (Thorlabs PDA10CS). The filtering pinhole (100 μm) was usually attached directly to the front of the photodiode mount. Although specified to be sensitive in the range 700 nm - 1800 nm, it was found that it had sufficient sensitivity to be used in the visible spectrum as well. This enabled it to be used in thermal blooming (single-beam) measurements, where the photodiode samples the excitation beam. The photodiode is mounted on an X-Y linear stage which allows it to be positioned accurately in the centre of the probe beam.

The output from the detection photodiode was recorded with a USB oscilloscope (Picoscope model ADC-212). A feature of this model is its high resolution (12-bit) which is essential when recording small thermal-lens signals, which may consist of a small change in a large voltage. Triggering for the oscilloscope was taken from the outuput of the function generator which drives the shutter.

The oscilloscope software has a number of different operating modes which are useful for setting up the TL experiment. When recording actual TL data, the successive averaging mode is used to reduce the effect of the ripple in the excitation beam. Another mode can display both the current waveform and the historical maximum and minimum waveforms - this is useful for aligning the beams to obtain maximum TL signal, as described in the procedure below.

Data are saved from the software in text format and imported into Microcal Origin. Eqn. (3.8) is fitted to the experimental data to determine both the TL coefficient, θ, and the time constant of the TL, t_c.

3.3.5 Procedure

The excitation laser was first tuned to a wavelength where the fluorophore under study absorbed and the power adjusted using ND filters to obtain a measurable TL signal but without the aberrations which occur at higher laser powers. Excitation powers are typically 5-20 mW.

The fractional absorbances (A_p) of the samples and references need to be measured for use in later calculations. This can be done using a conventional spectrophotometer. However, it is usually more convenient to use the excitation laser beam itself in conjunction with a laser power meter (Newport 818-UV). This also avoids any possibility of wavelength mismatch between the excitation laser and a spectrophotometer.

The method used for this is shown in Fig. 3.7. To obtain a beam from the excitation laser suitable for this measurement, the turning mirror is inserted between the filter holder FH1 and shutter S (Fig. 3.3) to deflect the beam at 90° to its original direction.

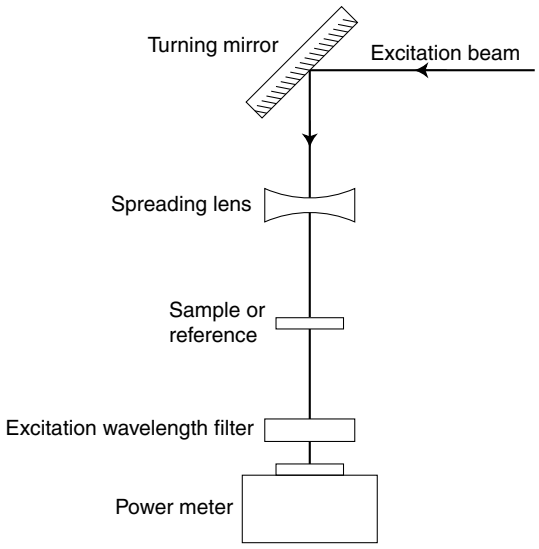

Figure 3.7: Method for measuring sample or reference absorbance

A concave lens (-10 cm focal length) is used to spread the excitation beam out to a diameter of about 4 mm when it strikes the sample or reference. This reduces the effect that scratches or other defects on the surface of the sample have on the amount of light detected by the power meter. For example, if a narrow beam were used and happened to strike a scratch, a larger proportion of the light would be scattered (and therefore not reach the power meter) than if a wider beam were used. For the same reason, the power meter is placed close to the sample (5 cm separation).

When measuring fluorescent samples with high absorbances, the intensity of the transmitted excitation beam may be comparable to the intensity of the fluorescence emission from the sample falling on the power meter. This will result in a lower-than-actual absorbance value. To eliminate this problem, a laser-line filter is attached to the front

of the power meter to block any fluorescence emission, which is always at a longer wavelength than the excitation.

Because of the 100 Hz ripple in the excitation beam intensity, a reading could not be taken directly from the power meter display. Instead, the analog output of the power meter was measured with the USB oscilloscope in averaging mode. An RC low-pass filter (-3 dB point at 20 Hz) was used to reduce the amount of ripple.

Firstly, the signal from the power meter with a piece of clear, undoped PMMA in position, P_{clear}, is recorded. The purpose of this is to correct for Fresnel reflection from the front and rear surfaces. Next, the signal with the sample or reference in position, P_{dyed}, is recorded. The fractional absorbance of the sample, A_p, can then be calculated from Eqn. (3.11).

$$A_p = \frac{P_{clear} - P_{dyed}}{P_{clear}} \tag{3.11}$$

The correct position for mounting the sample and reference must now be found (one confocal distance from the waist of the probe beam). This is done using the laser power meter with a pinhole mounted on the front. The power meter is moved along the length of the probe beam on an optical rail and measurements of the on-axis power taken at successive positions. The pinhole is centred on the beam each time with a two-axis linear stage. The recorded power is greatest when positioned at the beam waist and decreases on either side. The measured power is related to the distance from the beam waist by Eqn. (3.12)[224]

$$P = \frac{k}{1 + \left[\frac{z - z_0}{z_c}\right]^2} \tag{3.12}$$

where

- k is a constant
- z is the position of the pinhole (cm)
- z_0 is the position of the beam waist (cm)
- z_c is the confocal distance (cm)

The correct position could also be found by measuring the TL signal at different sample positions but this would require the entire system to be re-aligned for each position. As will be seen in the results section, the actual position is not critical ($\pm 10\,\%$ of the confocal distance affects the TL signal by less than $1\,\%$).

The excitation and probe beams must now be aligned so that they pass through exactly the same spot on the sample or reference under study.

First, the beam displacer is set at the midpoint of its travel using the adjusters. Next, a laser viewing card is used to align the beams roughly. The card is placed immediately after the hot mirror and TM1 is adjusted to centre the probe beam on the excitation beam. The card is then moved to a position just before TM2 and this time the hot mirror is adjusted to centre the pump beam on the excitation beam. This procedure is repeated several times to align the beams to within several millimeters.

The beams are now aligned more accurately using a combination of the laser power meter and a $100\,\mu$m pinhole. The pinhole is attached to the front of the power meter which is mounted on a two-axis translation stage. Since both laser beams are Gaussian, we can detect the centre of the beam when a maximum signal is obtained from the power meter. The procedure is similar to that using the laser viewing card. First, the probe beam is blocked and the power meter is placed immediately after the hot mirror. It is centred on the excitation beam by using the translation stage. The excitation beam is now blocked and the probe beam unblocked. Using TM1, the probe beam is centred on the pinhole/power meter. As before, the power meter is now moved to immediately before TM2, probe beam blocked, pinhole centred on excitation beam, excitation beam blocked and probe beam unblocked. The probe beam is now centred on the pinhole by adjusting the hot mirror. This procedure is repeated up to ten times, alternating between the two positions of the power meter, until the beams are aligned.

The final alignment procedure involes using the beam displacer to shift the excitation beam until a maximum TL signal is obtained. The excitation beam is first blocked and a piece of reference material with a high absorbance (to give an easily-detected signal) is placed in the holder on the linear slide LS. Mirror TM3 is used to centre the probe beam on the photodiode, with final adjustment made using the translation

stage of the photodiode. The excitation beam is now unblocked and the shutter started. A fast shutter speed (∼200 ms on-time) enables the photodiode signal to respond quickly to movement of the beam displacer.

The oscilloscope is set to display both current and historical maximum and minimum waveforms of the photodiode signal. A screenshot of the oscilloscope software is shown in Fig. 3.8. Because the chopping period of the shutter is much less than the time constant of the TL, the lens does not completely disappear after the excitation beam is turned off and before it is turned on again. The shaded region of the top trace indicates the historical limits of the waveform.

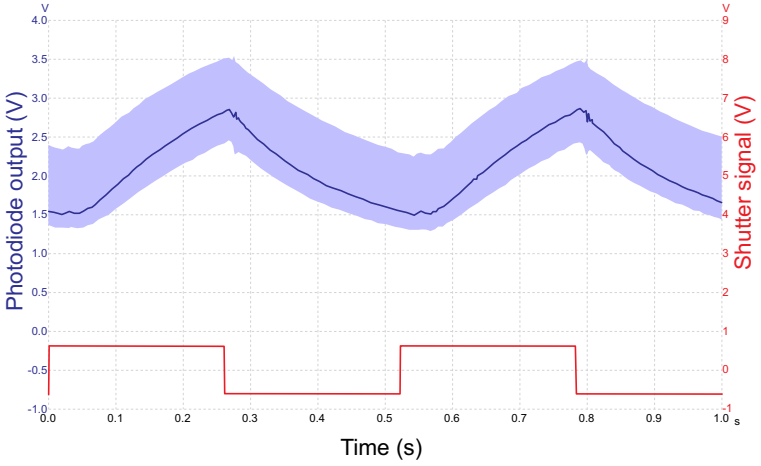

Figure 3.8: Maximising the TL signal. Top - photodiode signal. Bottom - shutter signal (low=on).

As the beam displacer is adjusted (and the position of the excitation varied), the magnitude of the TL signal varies. When the TL signal is greatest, the minimum limit of the photodiode waveform has its lowest value (greatest strength of TL formed, hence greatest divergence of probe beam, hence lowest recorded intensity by photodiode). The beam displacer is slowly adjusted through the optimum position and the minimum limit of the waveform is recorded in the software. The beam displacer is then adjusted back until the current photodiode waveform coincides with the lowest recorded waveform (shown by the lower boundary of the shaded region of the top trace in Fig. 3.8). This procedure is repeated several times in both the horizontal and vertical adjustment directions of the beam displacer.

Both the excitation and probe beams now pass through exactly the same point on the

sample or reference and are aligned so that the TL signal is maximised. Unfortunately, this alignment procedure had to be repeated every time the excitation laser was switched on or re-tuned because of the poor alignment stability of the Ar/Kr laser.

A sample and reference to be studied are now mounted in their respective holders on the linear slide. This has previously been positioned correctly relative to the waist of the probe beam. Sample and reference are mounted so the laser beams pass through them at a point at least 0.5 cm from the edge. It was found that when the samples were cut from a larger sheet and/or edge polished, an optical distortion was sometimes observed within several millimeters of the cut edge. This is caused by the release of thermal streses in the material (which originated during the cooling of the sheet after post-curing) and is a common occurrence when machining cast materials, even metals. If the laser beams passed through this location, the TL would distort and make measurements impossible.

The sample and reference were also positioned so the beams did not strike any surface defects such as scratches, as this would scatter excitation and probe light and make measurements inaccurate. This was determined by placing a white screen 1 m after the sample and observing the excitation beam on the screen. If no scattering is occurring, a single central spot is seen. If, however, the beam is striking a scratch, a line is seen passing through the central spot. The sample and reference are simply moved until only the central spot is seen.

The probe beam must be realigned on the photodiode when switching between sample and reference, as there will be small differences in the orientation of the front and rear surfaces of the sample and reference. This cannot be avoided. With the excitation beam blocked, mirror TM3 is used to centre the probe beam on the photodiode and final adjustment made by moving the photodiode on its translation stage. When the maximum output from the photodiode is obtained, the beam is centred.

The TL signals from the sample and reference can now be measured. With the probe beam centred on the photodiode, the excitation beam is unblocked and the shutter started. The oscilloscope records the photodiode output as the TL forms and decays. An example of the waveform (obtained from a sample with a large absorbance to make the effects clearly visible) is shown in Fig. 3.9. Before the excitation beam is

switched on at time 0 s, the photodiode output is steady - there is no TL present in the sample and it is in equilibrium with the surroundings. When the excitation beam is turned on at 0 s, the photodiode signal drops sharply as the TL forms and the probe beam diverges. It is this part of the curve to which we fit Eqn. (3.8) to determine θ and t_c.

The excitation beam is switched off at time 1 s and the TL gradually disappears as heat is conducted to the bulk of the sample from the region that was under illumiation. The intensity rises to its steady-state value. We must ensure that the lens disappears completely before the next time the excitation beam is switched on. This is done by choosing a suitable duty cycle for the shutter. A 10 % duty cycle (for example, on for 1 second and off for 9 seconds) is sufficient. Illumination times are usually 1-2 s. Successive cycles are averaged with the oscilloscope to reduce noise.

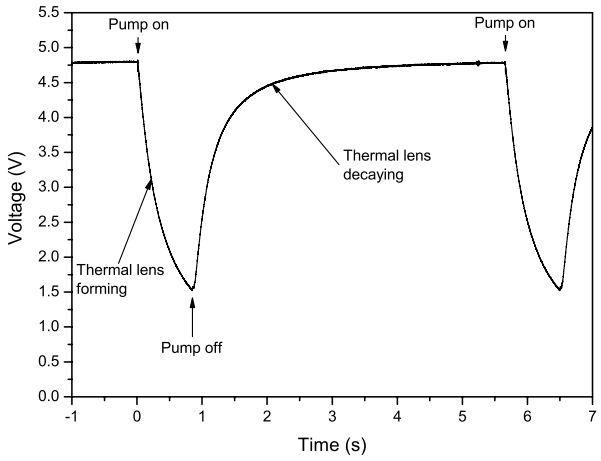

Figure 3.9: Example of photodiode waveform, showing formation and decay of thermal lens.

Fig. 3.10 shows an example of fitting Eqn. (3.8) to the decay of the photodiode signal. The photodiode output has been normalised to a steady-state value of 1 unit, so that $I(0) = 1$ in Eqn. (3.8). The oscilloscope is triggered from the function generator output at 0 s, but the TL does not start forming until a short time later because of the response time of the shutter. To enable Eqn. (3.8) to be fitted, t was replaced with $t - t_0$ where t_0 is the shutter response time. t_0 is in the range 7-8 ms.

An excellent fit is obtained, with R^2 values greater than 0.999. If it is found that the curve does not fit the data points exactly, then this is most likely an indication of

too high an excitation beam power causing aberrations in the TL. It was possible to demonstrate this, but required excitation powers in the region of 100-200 mW before any measurable aberrations started to occur.

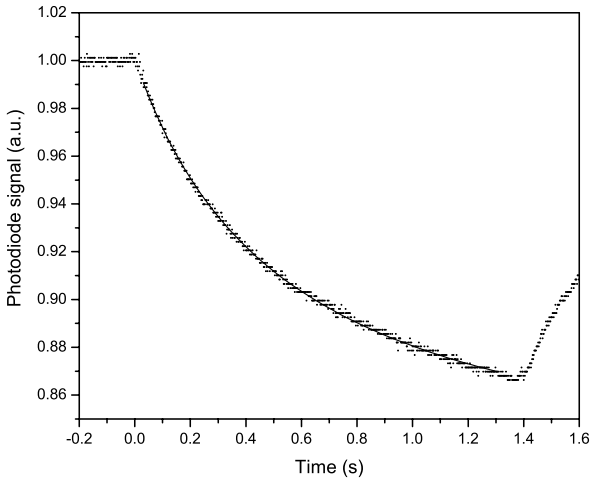

Figure 3.10: Fitting theoretical equation (line) to experimental decay data (points).

From the fitted curve, we can obtain values for θ which can then be used in Eqn. (3.10) to determine the quantum yield of the fluorescent sample.

3.4 Results

Over the year or so spent constructing and developing the TL system, the chief problem encountered was the inability to obtain consistent and repeatable results. Measurements made at different times on exactly the same samples with the same experimental configuration often gave totally different results. In addition to being non-repeatable, they also did not agree with values for quantum yield obtained by other methods, for example using an integrating sphere.

Presented below are the results obtained from the final few months of investigating the TL method, before it was dropped in favour of the integrating sphere. They clearly demonstrate the problem of non-repeatability, despite correct experimental parameters. Prior to these measurements, the TL system had been used in a variety of different configurations on a wide range of different samples and host materials in

attempts to try and find reasons for the variation in the results to no avail.

3.4.1 Double-beam TL on Orange 240

Presented below is a complete double-beam TL measurement of a sample of Lumogen F Orange 240 dye in PMMA. Sample and reference concentrations are shown in Table 3.1. The fractional absorbances, A_p, at the excitation laser wavelength are also shown.

Table 3.1: Sample and reference details

	Dye	Concentration (ppm)	A_p
Sample	Lumogen F Orange 240	73	0.843
Reference	Makrolex X70	40	0.181

The first task is to determine the correct sample position relative to the waist of the probe beam. This is done by performing a longitudinal scan of the on-axis probe beam intensity, measured using a 100 μm pinhole and laser power meter. The intensity is plotted in Fig. 3.11 with the curve showing a fit of Eqn. (3.12).

From Eqn. (3.12) we can see that, at the confocal distance, the on-axis intensity falls to half of its value at the waist. From Fig. 3.11, the distance which corresponds to half the maximum intensity is $z_c = 7.8$ cm - this is the confocal distance. The sample and reference should be placed at this position.

Next, the transverse profiles of the excitation and probe beams were measured at the sample position and are shown in Fig. 3.12. They were measured using a 100 μm pinhole in combination with the laser power meter. A Gaussian profile was fitted to the experimental data to determine the beam radii. The variation of intensity with radial position in a Gaussian beam is given by Eqn. (3.13)

$$I = I_0 e^{-2\left(\frac{r}{\omega}\right)^2} \tag{3.13}$$

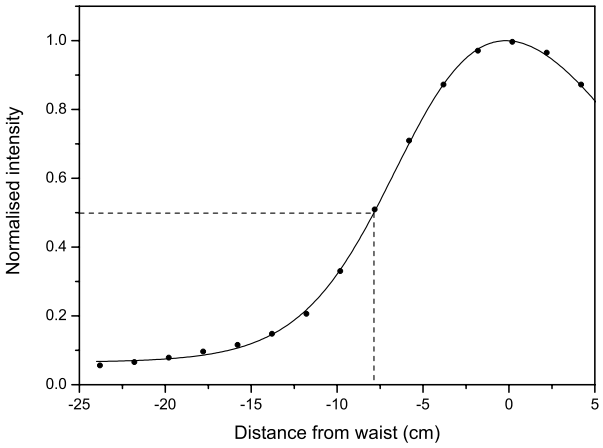

Figure 3.11: On-axis intensity of probe beam. Dashed line indicates confocal distance.

where

I_0 is the intensity at the centre of the beam

I is the intensity at a distance r from the centre of the beam

r is the radial distance from the centre of the beam (m)

ω is the radius of the beam (m), where the intensity falls to $\frac{1}{e^2}$ of its value in the centre

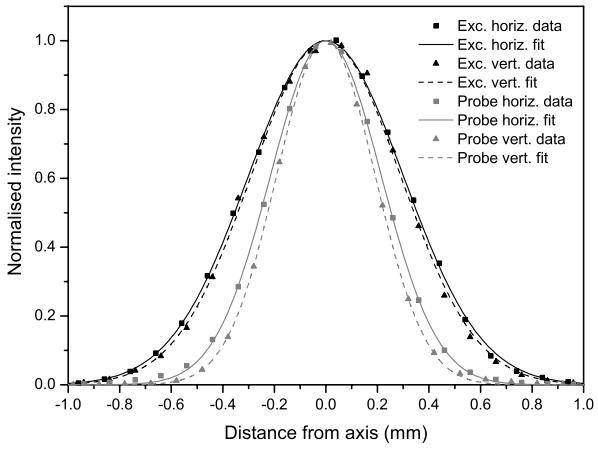

Figure 3.12: Horizontal and vertical profiles of both excitation (black) and probe (light gray) laser beams. Fitted Gaussian curves shown.

The parameters of the excitation and probe beams (wavelength, power and radii) are listed in Table 3.2. The beams are slightly elliptical in profile, the probe beam more

so, but it is not expected this will affect the results as they still have Gaussian profiles. A spatial filter was tried, unsuccessfully, in an attempt to improve the circularity of the probe beam.

Table 3.2: Excitation and probe-beam parameters

			Beam radius (mm)	
	λ (nm)	P (mW)	Horizontal	Vertical
Excitation	457	10	0.60	0.58
Probe	1064	3	0.43	0.38

The TL coefficients were now measured and were repeated once to check the variation. Fig. 3.13 shows the measured TL decay curves for the sample and reference. Even without fitting the decay equation, we can see that there is a large difference between successive measurements. This is not due to any variation in excitation laser power, since it was monitored throughout and remained constant.

When Eqn. (3.8) is fitted to the experimental data, we obtain the TL coefficients (θ) shown in Table 3.3. There is clearly a large variation - around 10 % - in the TL coefficients of both the sample and reference. The only possible explanation for this is an error in aligning the probe beam on the photodiode, as this is the only part of the system which was changed between measurements (when switching between sample and reference, the probe beam must be realigned). No bleaching or photodegradation is occurring, as shown later (Table 3.6). This is surprising, as great care was taken to ensure that the probe beam was exactly centred on the photodiode (by finding the position which gave the maximum signal).

Table 3.3: Double-beam TL coefficients

	TL coefficient (θ)	
	1^{st} meas.	2^{nd} meas.
Sample	-0.203	-0.187
Reference	-0.108	-0.124

To calculate the quantum yields, Eqn. (3.10) was used with values for the absorbances and TL coefficients. The excitation laser frequency, ν_{ex}, is 6.56x10^{14} Hz. The average fluorescence emission frequency was determined from the fluorescence spectrum to be

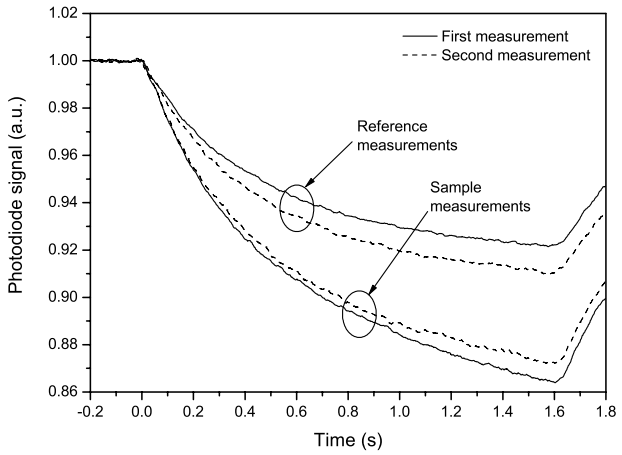

Figure 3.13: TL decay curves for sample (bottom pair of curves) and reference (top pair of curves)

$\langle \nu_{em} \rangle$ =5.34x10^{14} Hz. The quantum yields calculated from the sucessive measurements are **73 %** and **83 %**. Clearly these do not agree with each other. They also do not agree with the actual quantum yield of the Orange 240 dye, which was measured later using the integrating sphere to be 100 % (Chapter 4).

3.4.2 Single beam measurements

In an attempt to simplify the system and find the cause for the variation in results, the experimental system in Fig. 3.3 was converted to a single-beam (thermal blooming) system by removing the 1064 nm laser and positioning the sample and reference one confocal distance from the waist of the excitation beam. The photodiode was then used to detect the excitation beam divergence as the lens formed.

First, single-beam measurements were made on the same 73 ppm Orange 240 sample with the 40 ppm X70 reference. The excitation laser power was 13 mW and the wavelength again 457 nm. Table 3.4 shows the results.

Table 3.4: Single-beam TL results

Experiment	θ_{sample}	θ_{ref}	η_{PLQY} (%)
1	-0.625	-0.505	86
2	-1.413	-0.469	34

The large difference in coefficients may have been due to scattering from scratches on the surface of the sample, despite careful efforts to ensure that scratches were avoided.

We will now look at the variation of TL coefficient both at different sample positions and as various elements of the system are realigned. A freshly-cast reference was used in all these measurements, which contained 20 ppm of X70 dye. Extreme care was taken to avoid any scratches on the surfaces of the sample.

Fig. 3.14 shows the variation of TL signal with reference position (relative to the waist of the excitation beam). When the reference is placed at the beam waist, θ is zero. When moved away from the waist, θ increases and reaches a maximum negative value at a distance of 19 cm, shown by the dashed line. This corresponds to the confocal distance. The behaviour of the TL signal with position is exactly in agreement with theory (see, for example, Hu[204] who obtains a similar graph).

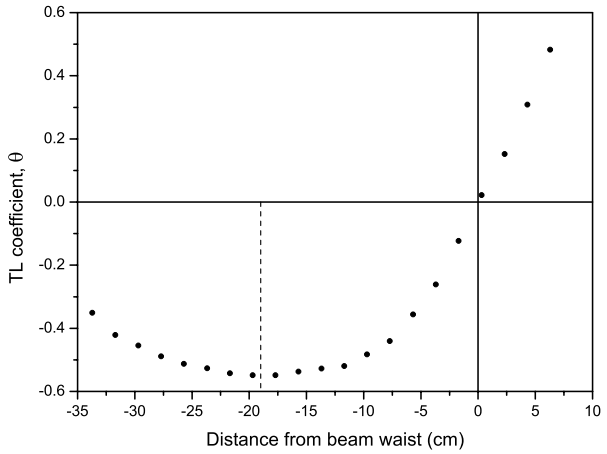

Figure 3.14: TL coefficient versus distance from beam waist. Negative distances are towards the photodiode, positive distances are towards the excitation laser.

Note that the reference does not have to be positioned at exactly the confocal distance - a variation of a few centimeters either side does not affect the TL signal appreciably.

Having found the confocal distance, we now perform quantum yield measurements on a fluorescent sample. This time, the Rot 305 dye was used in a concentration of 70 ppm. The 20 ppm X70 reference is again used. Table 3.5 lists the results.

There is around 20 % variation in the TL coefficients of both sample and reference.

Table 3.5: Single-beam TL results on Rot 305 sample

Experiment	θ_{sample}	θ_{ref}	η_{PLQY} (%)
1	-0.535	-0.504	104.8
2	-0.674	-0.453	92.4
3	-0.572	-0.451	98.9
4	-0.690	-0.423	88.3
5	-0.577	-0.474	100.4

This can only be due to variations in beam alignment when centring the beam on the photodiode between successive measurements. It would appear that the cause of the variation is related to beam alignment. To test this, the TL coefficients were recorded several times using different alignment procedures. The 20 ppm X70 reference was used in all cases.

First, no alignment changes were made and six successive measurements taken of the TL signal. Nothing was changed or moved between measurements. The time between measurements was 2 minutes. Results are shown in Table 3.6. There is little variation in the TL coefficient. This is expected, as the only parameter which could affect the coefficient is a variation in the power of the excitation laser beam, which was around 1 % over the course of the readings. In addition, this shows there is no bleaching or photodegradation occurring, since this would lead to a steady decrease in TL coefficient over time.

Table 3.6: Consecutive TL coefficients, no changes

Experiment	θ_{ref}
1	-0.364
2	-0.364
3	-0.362
4	-0.366
5	-0.367
6	-0.363

Next, the beam was re-aligned on the photodiode between measurements. The sample remained in its holder. Alignment consisted of turning the excitation beam on continuously and adjusting the turning mirror TM3 and photodiode to achieve a maximum intensity. Results are shown in Table 3.7. There is a large random variation (nearly

20 %) in the TL coefficient. This suggests that beam alignment on the photodiode is the main cause of error in the TL coefficient. A similar variation was also observed when the reference was removed and re-mounted in its holder between measurements.

Table 3.7: Consecutive TL coefficients, with re-alignment

Experiment	θ_{ref}
1	-0.362
2	-0.371
3	-0.327
4	-0.328
5	-0.372
6	-0.393
7	-0.344
8	-0.335
9	-0.312
10	-0.369

To study the effect of the relative alignment of the photodiode and the excitation beam, a linear stage was used to move the photodiode across the excitation beam and the TL coefficient recorded at several positions. The intensity at the start of the TL decay curve was also recorded. The results are shown in Fig. 3.15.

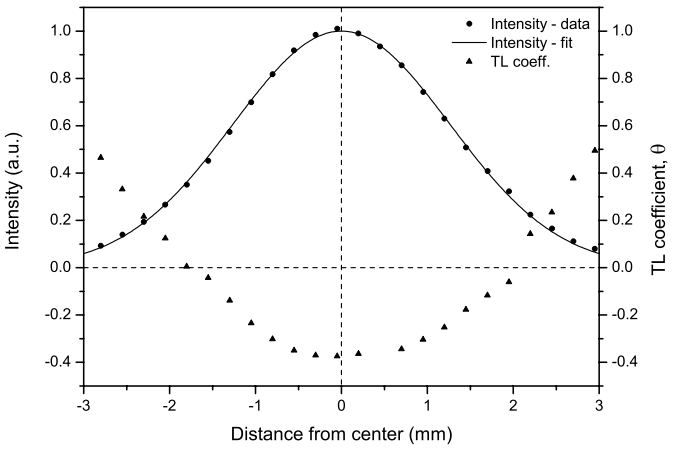

Figure 3.15: Initial intensity and TL coefficient versus distance from centre of excitation beam

The initial intensity shows a Gaussian profile across the beam. This is expected, since the original excitation laser beam also had a Gaussian profile and is simply enlarged by the presence of the TL. The TL coefficient has a maximum negative value at the

centre of the beam and reduces in magnitude moving away from the centre. The photodiode should be located at the centre of the beam to maximise the TL signal.

Although the maximum signal does occur at the centre of the beam, the exact position does not appear to be critical. There is little change in the signal up to ±0.2 mm away from the centre. Considering that it is possible to position the photodiode to within 0.002 mm using the linear slide, it should be perfectly possible to align the photodiode exactly in the centre of the beam.

Instead of merely adjusting the photodiode until the maximum intensity is achieved, we instead record the intensity at several points either side of the centre, fit a Gaussian and determine the exact centre position from the curve. This technique was tried when making single-beam quantum yield measurements on the Rot 305 sample. The values obtained are shown in Table 3.8.

Table 3.8: Single-beam TL results on Rot 305 sample, better alignment procedure

Experiment	θ_{sample}	θ_{ref}	η_{PLQY} (%)
1	-0.462	-0.332	94.9
2	-0.506	-0.355	94.1

There is around 10 % variation in θ between the measurements. Although the calculated quantum yield is constant, this is purely coincidental since the TL coefficients of both sample and reference happen to increase by the same amount. Although a much-improved alignment technique was used, the TL coefficients obtained are still not repeatable.

3.4.3 Double beam on Rot 305

Finally, the experiment was changed back to a dual-beam system and the quantum yield of the 70 ppm Rot 305 sample measured again. The photodiode was aligned using the improved procedure of plotting the variation with position and fitting a Gaussian curve. Results are shown in Table 3.9.

Neither the TL coefficients nor the calculated quantum yield is repeatable. They also do not agree with the values obtained from the single-beam measurement. This

Table 3.9: Dual-beam results on Rot 305 with better alignment procedure

Experiment	θ_{sample}	θ_{ref}	η_{PLQY} (%)
1	-0.165	-0.279	102.2
2	-0.164	-0.205	90.4

is despite optimum experimental conditions - excellent sample and reference surface quality, correct positioning of sample and reference relative to the beam waist, correct relative excitation and probe beam diameters at sample, concentric alignment of excitation and probe beams at the sample position and exact alignment of the probe beam on the photodiode by using a Gaussian fit. The quantum yield does not agree with that measured using the integrating sphere (100 % for Rot 305).

Results of measurements on quantum yield standards also do not agree with accepted values. Rhodamine 101 in acidified (HCl) methanol solution in a 0.2 cm cuvette gave random quantum yield values between 50-110 % upon successive measurements. The accepted value is 98 %[287, 38, 288].

Although the values obtained do not agree with values measured with other methods, the most important observation is the non-repeatability. Even if there was some experimental parameter which was incorrect and resulted in incorrect values for the TL coefficient and quantum yield, the measurements should still at least be repeatable. This is not the case.

3.5 Conclusions

In summary, it was not possible to construct a working TL system for measuring quantum yields. Despite this being a theoretically sound method capable of great accuracy, it was impossible to obtain repeatable results and no explanations for this were ever found.

The method is also severely limited by the need for samples with optical-quality, flat, parallel surfaces. By contrast, the integrating-sphere technique can accept a wide range of samples, including solids, liquids and scattering samples. Although apparently less accurate than the TL method, this is outweighed by the benefits of

the ease of measurment and the wide choice of samples.

Another disadvantage of the TL method is that there is no standard TL system available. All authors have constructed their own systems, with the inevitable differences between them. This makes it difficult to compare results. By contrast, the integrating sphere method uses standard equipment (an integrating sphere manufactured by Labsphere and a commercial spectrofluorometers from, for example, Horiba Jobin-Yvon or Edinburgh Instruments) which enables the results to be easily repeated by any researcher.

The integrating-sphere technique is used in the next chapter to measure the quantum yield of a range of different fluorophores.

Chapter 4

Optical properties of visible- and NIR-emitting fluorophores

Polymethylmethacrylate (PMMA) is a prime candidate for LSC construction because of its high optical clarity and photostability[227, 289]. In order to correctly model and predict the performance of different fluorophores in an LSC, the optical properties of the fluorophore must be measured. Since the absorption spectrum, emission spectrum and quantum yield of a fluorescent species generally depend on the host material (Lakowicz[38] Ch. 7, and Sah et. al.[53]), these properties must be measured when the fluorophore is incorporated into the actual host material used in the LSC, which in this case is PMMA. The majority of previous measurements of optical properties have been done in solution[48], because of the convenience of producing samples. In this chapter, the optical properties of both visible- and NIR-emitting fluorophores are measured. This includes a section detailing the use of an integrating sphere to measure quantum yield.

4.1 Absorption and emission of visible-emitting organic dyes in PMMA

For measurement of the dye absorption spectra, sheet samples of PMMA containing a known concentration of dye were cast using the waterbath technique described

previously in Section 2.3.1. The samples had optically flat surfaces, since they separated from the glass mould plates. The dye concentrations were calculated to provide approximately 80 % absorption at the peak, which was found to be a good balance between having sufficient absorption to enable the absorption coefficient to be measured accurately while transmitting enough light for the spectrophotometer detector to record it successfully. All samples were post-cured, as it had previously been found by the author that post-curing had no detrimental effect on the dye efficiency and improved the optical quality of the PMMA. Because of the thickness variation of the sheet from edge to edge, four measurements were taken at each corner and the results were averaged.

In order to make accurate measurements of the molecular emission spectrum, free from the effects of re-absorption, samples with an extremely weak concentration of dye were used (Section 2.2.2). These typically had approximately 3 % peak absorption, but still gave sufficient signal for accurate detection of the emission spectrum. The samples were excited near the edge to minimise re-absorption effects, as described previously (Section 2.2.2). The different sample concentrations used for absorption and emission measurements are shown in Table 4.1. The excitation wavelength used for each dye is also shown.

Table 4.1: Sample concentrations and excitation wavelengths

	Conc. (ppm) used to measure		
Dye	absorption	emission	Excitation wavelength (nm)
Violett 570	32.6	3.5	360
Gelb 083	13.3	1.7	440
Gelb 170	22.1	1.8	460
Orange 240	12.4	1.2	470
Rot 305	30.2	3.5	530

The absorption and emission spectra for each of the dyes is shown in Fig. 4.1. Emission is in units of photon counts. Both absorption and emission spectra have been normalised to a peak value of unity for ease of viewing. The spectral features of each dye are shown in Table 4.2. The approximate error in the peak absorption coefficient is ±2 %, based on the corner-to-corner variation across one sheet sample. Both the peak and average emission wavelengths shown in Table 4.2 were obtained from the

emission spectra of the low-concentration samples in Table 4.1, where re-absorption effects are absent.

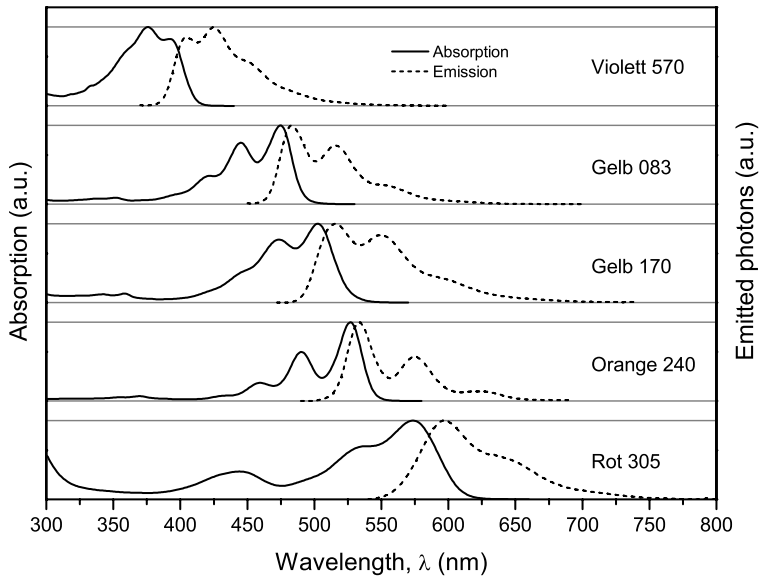

Figure 4.1: Visible dye absorption and emission spectra (normalised)

Table 4.2: Visible dye spectral features

Dye	Peak abs. wavelength (nm)	Peak abs. coefficient (ppm^{-1} cm^{-1})	Peak em. wavelength (nm)	Average em. wavelength (nm)
Violett 570	375	0.123	425	434
Gelb 083	474	0.233	483	513
Gelb 170	502	0.165	516	551
Orange 240	526	0.289	534	561
Rot 305	573	0.102	597	622

4.2 PLQY of visible-emitting organic dyes using an integrating sphere

The photoluminescent quantum yield (PLQY) of each of the individual dyes and of dye mixtures was measured using the integrating sphere described in Section 2.2.3. The measurement technique and calculation procedure for PLQY determination are

described below. Fig. 4.2 shows the integrating-sphere system, with the sample holder, filter positions and re-absorption processes indicated.

The excitation wavelength was chosen based on the absorption spectrum of the dye and is the same as that listed in Table 4.1. Enough light should be absorbed by the sample to give a measurable signal - this typically results with samples which have an absorbance greater than 0.1.

Excitation and emission spectra are recorded both with a sample present in the sphere and with an empty sphere or reference sample. The excitation and emission spectra recorded when the sphere is empty give a measure of both the intensity of excitation light and the strength of any background emission from the sphere (for example, contamination or fluorescence from the sphere material itself when excited in the ultraviolet[290]). Instead of a totally empty sphere, a sample of clear (undoped) PMMA is sometimes used when it is neccessary to correct for the absorption of the PMMA itself, for example in the ultraviolet. The differences in the areas of the excitation and emission spectra recorded with an empty sphere and with a sample present give an indication of how many photons are absorbed and emitted by the sample, respectively. A simple calculation from this leads to the PLQY.

When the excitation spectrum is recorded, a neutral density (ND) filter (typically 0.5 % transmission) is inserted between the sphere and the detection monochromator because the higher intensity of the excitation light would damage the photomultiplier detector if it were not reduced. The transmittance of the filter is measured as follows with the sphere in place and is used to scale the excitation spectrum used in the calculations. The detection monochromator is set to detect the peak excitation wavelength. Another ND filter, of the same transmission or higher, is inserted in the excitation beam (before the sphere). Measurements are then taken of the detector signal both with and without the emission ND filter in place. After subtracting the detector background, the ratio of these gives a correction factor which can be applied to the excitation spectra. The locations of these excitation and emission filters are shown in Fig. 4.2.

If there is a risk of detecting second-order excitation light, a long-pass filter is placed between the sphere exit port and the detection monochromator. Corrections are made

for the transmission spectrum of the filter.

The four recorded spectra (after correction for monochromator, sphere, detector and ND filter response) are designated as follows.

1. E_C - emission spectrum, sample in sphere
2. L_C - excitation spectrum, sample in sphere
3. L_A - excitation spectrum, empty sphere
4. E_A - emission spectrum, empty sphere

The quantum yield is calculated from Eqn. (4.1)

$$PLQY = \frac{E_C - E_A}{L_A - L_C}, \tag{4.1}$$

where E_C, L_C, L_A, E_A are the areas under the respective spectra. The areas are calculated from the raw spectral data by summing the product of photon count-rate and wavelength over the entire spectrum. For example, the area of the emission spectrum with the sample in the sphere is $E_C = \sum E_C(\lambda)\,\Delta\lambda$ where E_C is the area of the emission spectrum and $E_C(\lambda)$ is the photon count-rate at a particular wavelength.

When the fluorophore has a small Stokes shift, as is the case with the Lumogen F dyes, there is a high probability that the emitted photon will be re-absorbed by the sample. The same PLQY will apply to re-absorption/re-emission events. This will lead to an apparent reduction in the measured PLQY of the sample, especially of samples containing dyes with low quantum yields. Two different kinds of re-absorption can occur. Firstly, emitted photons which are trapped within the integrating sphere (but outside the sample) can pass through the sample multiple times and be re-absorbed by another dye molecule in the sample. Secondly, emitted photons from within the sample can be re-absorbed before they have a chance to reach the sample's surface. The second process is more important in highly concentrated samples while the first dominates at low concentrations. Although the two processes are different, the effects they have on the measured PLQY can be treated similarly.

The different absorption/emission processes are shown in Fig. 4.2. Ray (1) represents the excitation light. Ray (2) denotes emission which has left the sample and is inside the sphere but which passes back through the sample and becomes re-absorbed. Ray (3) shows emission being absorbed inside the sample, before the primary emission reaches the surface of the sample and escapes.

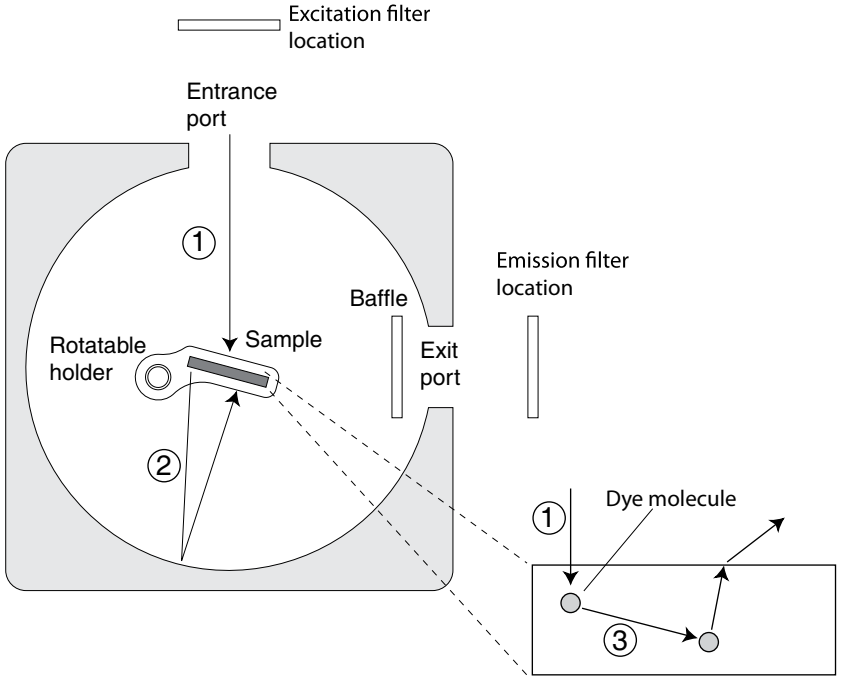

Figure 4.2: Integrating-sphere system showing different re-absorption processes

As re-absorption (RA) increases, the observed emission spectrum will be increasingly red-shifted. However, the shape of the emission spectrum in the long-wavelength regime, where the dye absorption is negligible, will show minimal difference compared with the molecular emission spectrum. It has been shown that there can be an absorption "tail" of extremely low absorption coefficient which extends several hundred nanometers beyond the bulk of the dye absorption spectrum [70, 61], however the effect of this only becomes significant over the long pathlengths (greater than $\sim$0.5 m) experienced in actual LSC sheets. For re-absorption occurring in the integrating sphere, this tail is not a significant problem.

The RA correction technique used here is based on that described by Ahn *et. al.* [291]. Using this technique, the molecular emission spectrum (measured outside the sphere from a weakly concentrated sample which is not affected by re-absorption,

typically a concentration of a few ppm) is scaled to match the observed emission spectrum at long wavelengths. An example of this is shown in Fig. 4.3 for the Gelb 083 dye, where the molecular emission has been scaled to match the observed emission at wavelengths greater than ∼575nm where re-absorption is negligible.

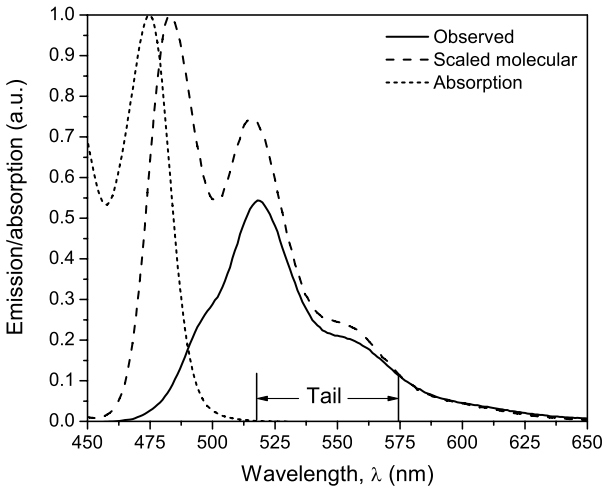

Figure 4.3: Example of RA correction procedure

It can be seen in Fig. 4.3 that, although the absorption spectrum appears only to extend to around 520 nm, there is still a difference in the molecular emission and observed emission spectrum up to 575nm, an indication of an absorption tail extending at least to 575nm.

Denoting the molecular emission spectrum by $F'(\lambda)$ and the observed emission spectrum by $F_{obs}(\lambda)$, a re-absorption coefficient (RA coefficient), a, can be calculated from Eqn. (4.2).

$$a = 1 - \frac{\sum F_{obs}(\lambda)\, d\lambda}{\sum F'(\lambda)\, d\lambda} \tag{4.2}$$

Both $F'(\lambda)$ and $F_{obs}(\lambda)$ are measured in terms of photon count rate as before. a can take values ranging from 0 (zero re-absorption) to 1 (maximum re-absorption, total overlap). The corrected PLQY can then be calculated from the observed PLQY by using Eqn. (4.3).

$$PLQY_{corr} = \frac{PLQY_{obs}}{1 - a + (a \times PLQY_{obs})} \tag{4.3}$$

As can be seen from the equation, if the real quantum yield is 1.0 then re-absorption will have no effect on the measured value.

The PLQY can, in theory, be determined from a single measurement and re-absorption correction. However, when the PLQY is near 100 %, an additional technique can be used to verify the actual PLQY. If there is no quenching present in the sample at higher concentrations, then any decrease in measured PLQY must be due entirely to non-unity PLQY and the effects of re-absorption. The presence or absence of quenching in the sample can be determined by looking at the progression of corrected PLQY values as the dye concentration increases, where a decrease in corrected PLQY indicates quenching. We can determine how much of a decrease in measured PLQY would be expected for a particular increase in re-absorption coefficient. For example, if a dye has an actual PLQY of 99 % and a re-absorption coefficient of 0.7 is measured, the observed PLQY will drop to 96.5 %, a decrease of 2.5 %. If the observed decrease in measured PLQY is less than this, we can be confident that the actual PLQY lies between 99 % and 100 %. Since the repeatability of the integrating-sphere technique is of the order of 2 %, we can then achieve an accuracy of around 1 % when the PLQY lies near 100 %.

The repeatability of the integrating-sphere technique was checked by running ten experiments on exactly the same sample. Measurements were split over two days. The sample holder was also rotated slightly ($\sim 5^\circ$) half-way through measurements to see if the angular position of the sample had any effect on the measured PLQY. The spread of measured PLQY values was no greater than 2 % over all the readings, therefore 1 % error bars are shown on the PLQY graphs. Additionally, the change in orientation of the sample holder had no effect on the readings.

Results for both single and mixed dyes are now presented.

4.2.1 Single dyes

The PLQY of each of the Lumogen F dyes were measured in PMMA. Disc samples were made for the sphere as described in Section 2.3.5. Because of the large amount of re-absorption of fluorescence with increasing sample concentration, the re-absorption correction described previously was used. The uncorrected PLQY, re-absorption coefficient and corrected PLQY are presented separately for each dye. The re-absorption correction only has significance when the dye has a PLQY less than 100 %. For this reason the corrected PLQY is only shown for those dyes with non-unity PLQY.

Violett 570. Results shown in Fig. 4.4. Although the excitation wavelength of 360nm effectively excites the dye, it is also absorbed by the PMMA host material. To compensate for this, a sample of clear (undoped) PMMA was used in the sphere when the "empty sphere" spectra were recorded. Because the undoped reference sample had exactly the same dimensions as the dyed sample, the absorption of the PMMA is effectively corrected for . Referring to the figure, as the dye concentration is increased, the amount of re-absorption (as measured by the re-absorption coefficient) also increases, as expected. However, there is no apparent decrease in the measured PLQY, despite this re-absorption. Because there is no decrease, there is no quenching occurring at the higher concentrations. Additionally, the dye PLQY must lie between 99-100 %, as a lower value would lead to a reduction in the measured PLQY as re-absorption increases.

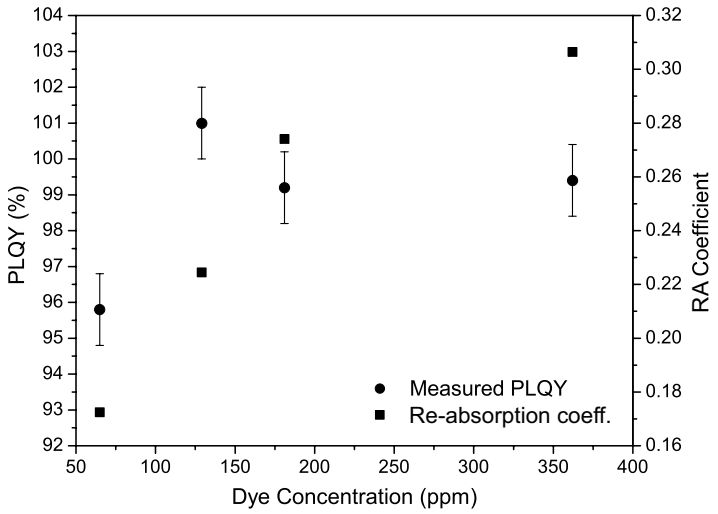

Figure 4.4: PLQY and re-absorption coefficient of Violett 570

Gelb 083. Results shown in Fig. 4.5. The measured PLQY shows a decrease with increasing concentration, however this is purely due to the effects of re-absorption, as the corrected PLQY does not change with increasing concentration. No quenching occurs. The PLQY is 96 %±1 %.

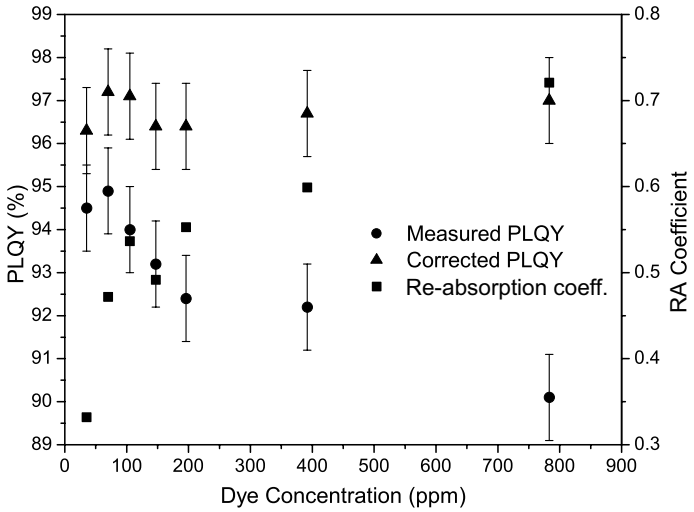

Figure 4.5: PLQY and re-absorption coefficient of Gelb 083

Gelb 170. Results shown in Fig. 4.6. The PLQY is 98 %±1 % at low concentrations and shows a slight (2 %) drop as the concentration is increased to 790 ppm. This is evidence of quenching at higher concentrations.

Orange 240. Results shown in Fig. 4.7. There is no detectable decrease in the

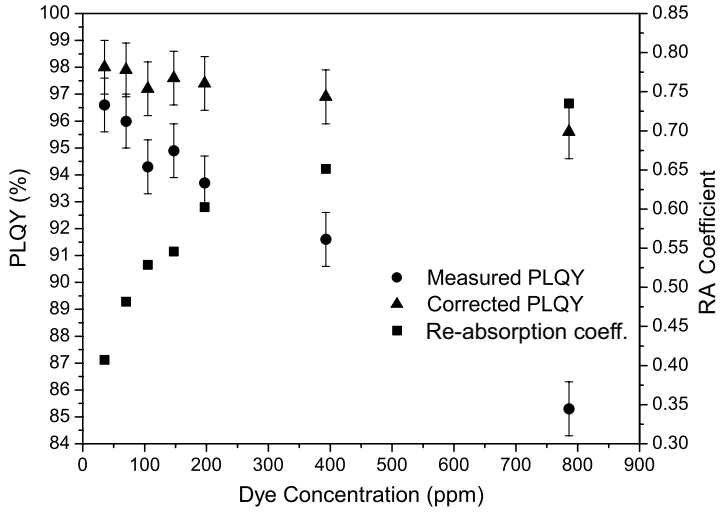

Figure 4.6: PLQY and re-absorption coefficient of Gelb 170

measured PLQY as the concentration increases, similar to the case for Violett 570. By the same argument, the PLQY must be 100 %, as a lower value would again lead to a drop as re-absorption increased.

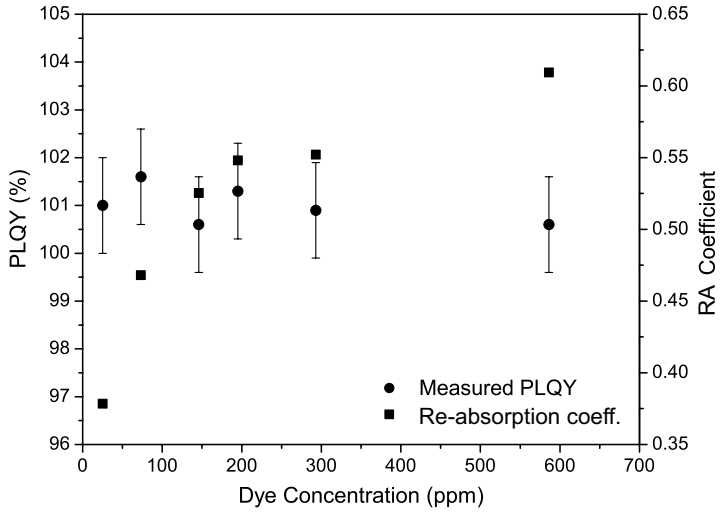

Figure 4.7: PLQY and re-absorption coefficient of Orange 240

Rot 305. Results shown in Fig. 4.8. Once again, no decrease in measured PLQY is observed. The PLQY is 100 %.

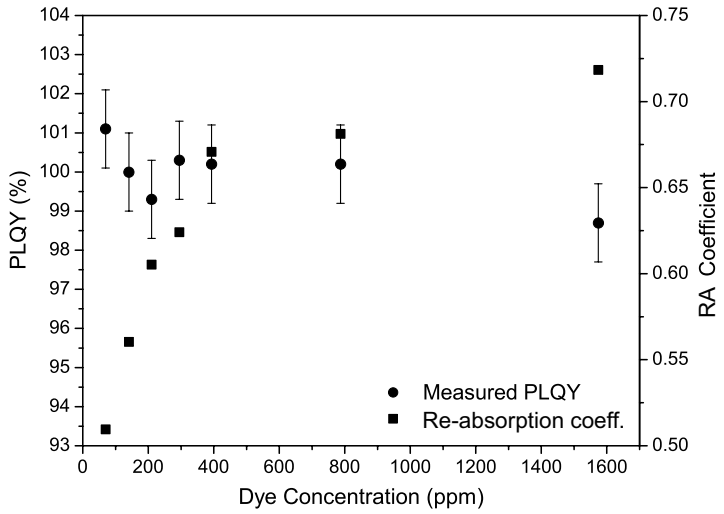

Figure 4.8: PLQY and re-absorption coefficient of Rot 305

4.2.2 Mixed dyes

The emission spectra and quantum yields of several dye mixtures were measured. Both a three-dye and a four-dye mixture were studied. The concentrations of the dyes in each of the samples are shown in Table 4.3 and were chosen to achieve an optical density of at least four over the absorption range of the dye mixture. This ensured that all of the excitation light was absorbed and that the emission spectrum measured was primarily due to the longest-wavelength dye since it absorbed the emission from all of the shorter-wavelength dyes.

Table 4.3: Mixed-Dye Concentrations

Dye	Three-dye concentrations (ppm)	Four-dye concentrations (ppm)
Violett 570	362	362
Gelb 083	196	196
Orange 240	146	146
Rot 305	0	394

The emission spectra of the dye mixtures were obtained from the spectra taken from the integrating-sphere PLQY measurements. Because of the high absorption that occurs inside the sphere and inside the sample, the observed emission spectra were identical to the spectra from the individual dye with the longest emission wavelength

(Orange 240 for the three-dye mix, Rot 305 for the four-dye), even when the mixture is excited at a short wavelength. For example, when the sample is excited with 380nm light, only the Violett 570 dye will initially be excited. However, its emission will subsequently be absorbed by the Gelb 083, Orange 240 and Rot 305 dyes. The spectrum which is actually observed is no different from the Rot 305 emission spectrum. Since some of the dyes have non-unity PLQY, the observed PLQY of the mixture is expected to decrease with shorter excitation wavelengths as more dye interactions will occur. This is observed in practice.

The PLQY of the mixtures is shown in Table 4.4 at different excitation wavelengths. The re-absorption correction has not been applied to the dye mixture results because, unlike for a single dye, the "molecular" emission spectrum (i.e. that observed at low concentrations of the dye mixture) depends on the excitation wavelength. An average of five separate measurements were taken.

Table 4.4: Mixed-Dye PLQY

Dye mixture	Excitation wavelength (nm)	Measured PLQY (%)
Three-dye	480	101
Three-dye	430	97
Three-dye	380	104
Three-dye	350	103
Four-dye	530	99
Four-dye	490	96
Four-dye	440	92
Four-dye	400	91
Four-dye	350	93

The three-dye mixture shows an unusual progression in PLQY as the excitation wavelength is decreased. The high PLQY when excited at 480 nm is easily explained: only the Orange 240 dye is excited at this wavelength and this has unity quantum yield as described previously. The drop to 97 % when excited at 430 nm is because the Gelb 083 dye is now being excited. Since this dye only has a 96 % PLQY, the measured PLQY of the mixture drops. The rise in PLQY when the excitation wavelength drops to 380 nm is not easily explained. In theory, it should stay at around 97 % since the Violett 570 dye has 100 % PLQY. The increase is explained by the emission from the

Violett 570 dye directly exciting the Orange 240 dye, rather than being absorbed by the Gelb 083. Since both Violett 570 and Orange 240 have near 100 % PLQYs, the measured PLQY will also be near 100 %. This is confirmed by the PLQY measured at an excitation wavelength of 350 nm. Only Violett 570 is directly excited at this wavelength and the measured PLQY of 103 % implies that Violett 570 is exciting Orange 240 directly.

The progression of measured PLQY for the four-dye mixture is as expected. As the excitation wavelength is decreased, the fluorescence emission is absorbed and re-emitted by an increasing number of dyes in the mixture. Since some have less than unity PLQY, the overall PLQY decreases as the excitation wavelength is decreased. At excitation wavelengths below 440 nm, the PLQY remains reasonably constant since Violett 570 is being excited first and it has 100 % PLQY.

Although a mixture of these visible dyes can absorb a wide range of wavelengths, the PLQY is non-unity at shorter excitation wavelengths, leading to a reduced efficiency. Instead, it may be possible to use a high concentration of only the Rot 305 dye, since it exhibits a wide absorption range. The feasibility of this is studied next.

4.3 Effect of excitation wavelength on the optical properties of Rot 305

Rot 305 is unique in that it exhibits a wide absorption bandwidth of 200-300 nm, compared with only ∼100 nm for the other Lumogen dyes, and shows significant absorption at all wavelengths <600 nm. Because it shows no signs of fluorescence quenching even at relatively high concentrations, it is suggested that a high concentration of Rot 305 could be used to absorb a wide range of the solar spectrum, instead of using a mixture of several different dyes. To determine its suitability for this, both the emission spectrum and PLQY of Rot 305 in PMMA were measured as the excitation wavelength was varied from 310 nm to 620 nm in 20 nm steps.

Fig. 4.9 shows the emission spectra measured from a sample of concentration 5 ppm. This concentration was sufficiently low that re-absorption effects were minimised. In

addition, excitation and detection were performed at the edge of the sample as before (Section 2.2.2), which also reduced the effects of re-absorption. The results have been separated into two groups (Fig. 4.9a and 4.9b) depending on the excitation wavelengths chosen and whether any change in the spectral profile was observed. All spectra have been normalized to a peak value of 1.

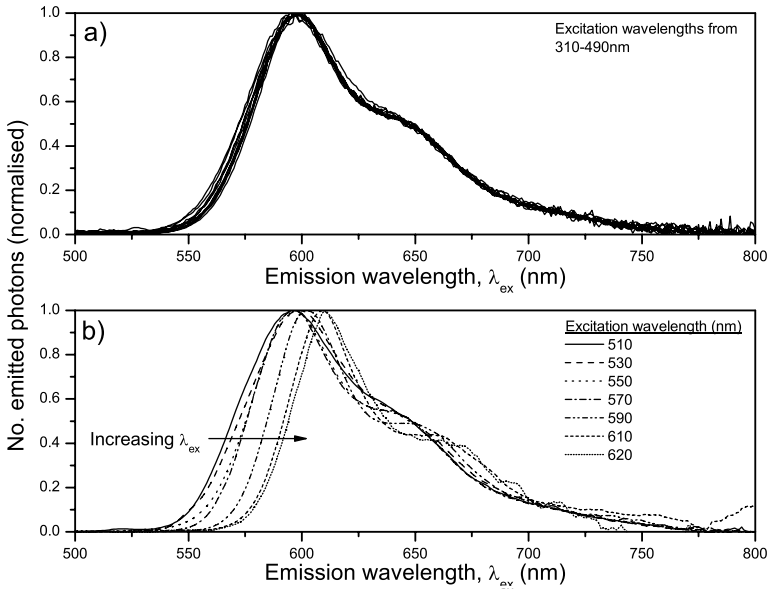

Figure 4.9: Rot 305 emission at different excitation wavelengths. a) 310-490 nm. b) 510-620 nm.

As the excitation wavelength was increased from 320-490 nm (Fig. 4.9a), there was no significant change observed in the shape or wavelength of the emission spectrum. The peak emission wavelength remained fixed at 597 nm. At excitation wavelengths above 490 nm, however, the spectra showed a shift towards progressively longer wavelengths as the excitation wavelength was increased. The peak emission wavelength increased from 597 nm at λ_{ex} =510 nm to 611 nm at λ_{ex} =620 nm.

Fig. 4.10 shows the measured quantum yield at different excitation wavelengths. The sample concentration in this case was 98 ppm, since a higher concentration was required to achieve a detectable signal using the integrating sphere. Within the error limits (2 %), there is no detectable change in the PLQY as the excitation wavelength is varied.

The intrinsic emission spectrum of the Rot 305 dye molecule must be independent of excitation wavelength, as can be seen from the energy-level diagram in Fig. 1.3,

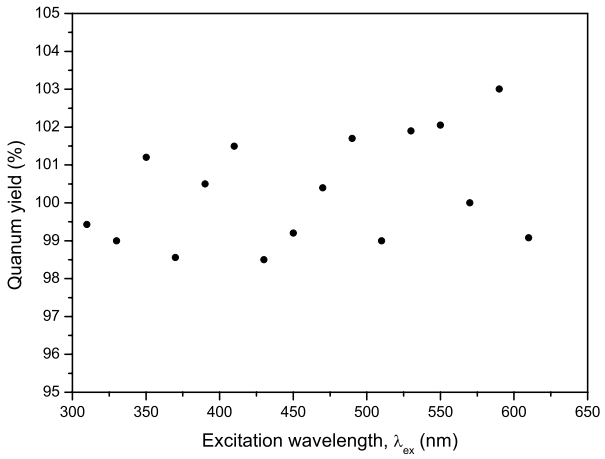

Figure 4.10: Rot 305 PLQY at different excitation wavelengths

Chapter 1. Regardless of the energy of the excitation photon, the excited molecule always relaxes to the lowest vibrational level of S_1 before decaying to a vibrational level of S_0 by emitting a fluorescence photon, resulting in the same emission wavelengths. This is borne out by the invariance of the emission spectrum with excitation wavelength in the range 310-490 nm. Likewise, the PLQY also remains constant since the emission process is the same.

The change in the emission spectrum which occurs at excitation wavelengths greater than 490 nm can be explained by the presence of aggregated dye molecules, such as dimers or trimers, which have longer emission and absorption wavelengths than the individual (monomer) molecules. As the excitation wavelength is increased, the contribution to the emission spectrum from these aggregates becomes progressively larger, resulting in a red-shift of the composite spectrum, until at an excitation wavelength of 620 nm, the observed emission is due entirely to aggregates.

The invariance of PLQY with excitation wavelength indicates that aggregation does not appreciably reduce the PLQY, with the value remaining near unity over the entire range of excitation wavelengths. The features of red-shifted emission and high PLQY are characteristic of so-called "J-aggregates" where the molecules are stacked with their planes parallel but displaced from a perfect sandwich structure by a longitudinal offset between adjacent molecules. Rot 305 is a perylene bisimde dye and J-aggregate formation in non-polar solvents (such as methylcyclohexane) has previ-

ously been observed for perylene bisimide dyes which are similar to Rot 305 in having phenoxy substituents in the "bay area" of the perylene core[292]. By contrast, perylene bisimides with no bulky substituents (such as phenoxy groups) in the bay area tend to form sandwich-type H-aggregates which show blue-shifted absorption spectra and greatly reduced quantum yields relative to the monomer[293].

These results are significant, because they suggest that the re-absorption losses in an LSC sheet containing Rot 305 will be less than expected from assuming the emission spectrum is independent of excitation wavelength. Re-absorption of monomer emission at wavelengths on the red edge of the absorption spectrum will result in excitation of red-shifted aggregate emission. The emission spectrum resulting from each re-absorption event is thus progressively red-shifted, which decreases the probability of subsequent re-absorption.

4.4 NIR emitters

We will now apply the techniques used in measuring the properties of the visible-emitting organic dyes to a range of NIR-emitting fluorophores (organic dyes, rare-earth nanoparticles and rare-earth complexes).

Where possible, their properties (absorption, emission and PLQY) were measured in PMMA hosts. This was not possible for all of the NIR emitters. The NIR organic dyes dissolved in MMA monomer and were easily doped into PMMA samples. However, the rare-earth nanoparticles required such a high concentration (around 7000 ppm, due to their low absorption coefficient) that it was impossible to make PMMA samples. In addition, several of the rare-earth complexes did not dissolve well in either MMA or DCM, making their incorporation difficult. It is indicated when the properties were measured in a solvent instead of in PMMA.

Because some of the NIR-emitting compounds have emission wavelengths in the 900-1100 nm range, there was some concern that their emission would be absorbed by the PMMA host and that this problem would be increased by the multiple passes that light makes through a sample inside the integrating sphere. To check whether

this would be a problem, a synchronous scan (setting both excitation and emission monochromators to the same wavelength and moving them together) was performed with both an empty sphere and with a sample of undoped PMMA present in the sphere, but located out of the direct excitation beam. The sample was a disc of 11 mm diameter and 2 mm thickness. If the sample is absorbing some of the light trapped inside the sphere, then the detected intensity at that wavelength will be lower than with an empty sphere. By taking the ratio of the synchronous scan with the sample present to the scan with an empty sphere, we obtain a transmission value which is an indication of how much light the sample is absorbing. This is shown in Fig. 4.11.

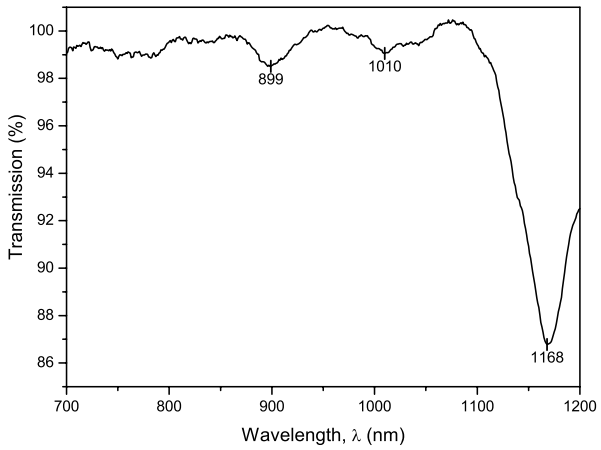

Figure 4.11: Transmission of sphere containing 2 mm thick PMMA sample

Troughs appear in the transmission spectrum, corresponding to the absorption peaks of PMMA (Section 2.3.4). They are visible at 899, 1010 and 1168 nm in Fig. 4.11. However, at the emission wavelengths of the complexes under study (around 1000 nm), the magnitude of the absorption of the PMMA is extremely small (at most 1 %) and can be ignored.

Results are now presented for the three different types of emitters.

4.4.1 NIR organic dyes

As before, different sample concentrations are used for measuring the absorption and emission spectra - a high concentration for measuring the absorption spectrum (to ensure enough light is absorbed to give an accurate signal) and a low concentration for measuring the emission spectrum (low enough that re-absorption effects are minimised). Emission was measured from the edge of the disc samples made for the sphere, with excitation also at the edge (Section 2.2.2). The different sample concentrations used are shown in Table 4.5. The excitation wavelengths used when measuring the emission spectra are also shown. All samples are in PMMA hosts.

Table 4.5: NIR organic sample concentrations and excitation wavelengths

	Conc. (ppm) used to measure		
Dye	absorption	emission	Excitation wavelength (nm)
KF402	30	3	560
NIR1	30	3	600
NIR3	30	3	600

Fig. 4.12 shows the absorption and emission spectra of the samples of the three NIR dyes. Their spectral features (absorption and emission wavelengths and absorption coefficients) are shown in Table 4.6.

All three dyes have very similar emission ranges, with the separation in peak emission between the lowest and highest only 60 nm. The maximum absorption wavelength achievable with the NIR dyes is around 750 nm, compared with only 625 nm for the visible dyes (limited by Rot 305). This will allow a greater part of the solar spectrum to be absorbed by an LSC sheet. The peak absorption coefficients of KF402 and NIR3 are comparable to those of the visible organic dyes, while that of NIR1 is nearly double.

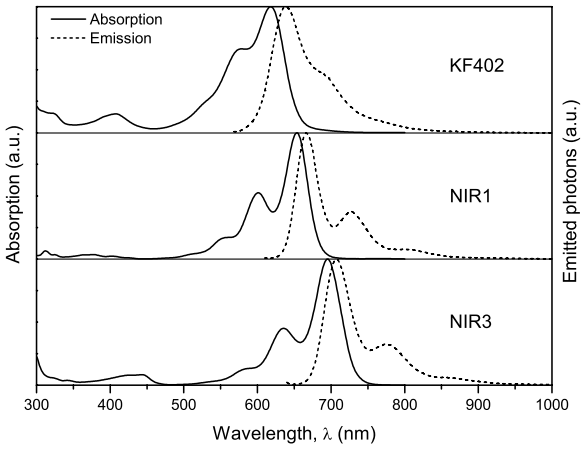

Figure 4.12: Absorption and emission of NIR organic dyes (normalised)

Table 4.6: NIR organic dye spectral features

Dye	Peak abs. wavelength (nm)	Peak abs. coefficient (ppm^{-1} cm^{-1})	Peak em. wavelength (nm)	Average em. wavelength (nm)
KF402	618	0.194	640	669
NIR1	654	0.346	666	703
NIR3	695	0.225	707	743

The quantum yields of the three organic dyes are shown in Figs. 4.13-4.15. There was difficulty in preparing clear samples of KF402 and NIR1 at concentrations above 200 ppm, as this seemed to be the limit of solubility of the dye. At concentrations higher than this, the samples appeared to contain undissolved dye and were cloudy.

KF402 (Fig. 4.13) exhibits the highest PLQY of the three dyes, with 80 % quantum yield at low concentrations. The PLQY does decrease at higher concentrations, indicating the presence of concentration quenching. Although the 375 ppm sample contained undissolved dye, the quantum yield was still 58 %. Despite the measured PLQY being lower than that measured by Seybold *et. al.*[48] of 92±10 %, this is perhaps explained by the lower concentration used by him (around 1 ppm). A minimum concentration of 25 ppm was required while using the integrating sphere in the measurements presented here to achieve a detectable emission signal level. Since concentration quenching does appear to occur, a lower concentration will result in a higher PLQY. In addition, he measured the PLQY in chloroform solution and, since the PLQY depends on the solvent[53], this also explains the difference.

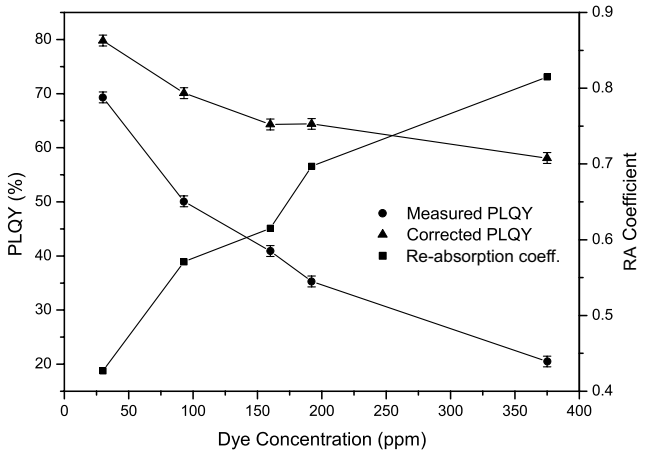

Figure 4.13: PLQY and re-absorption coefficient of KF402

NIR1 (Fig. 4.14) has a quantum yield of 65-70 %, showing a slight drop as concentration is increased. The low PLQY of the 330 ppm sample is due to undissolved dye (the maximum dissolved concentration achievable was 200 ppm). By comparison, Holtrup *et. al.*[46] measured a PLQY of 90±10 % at a concentration of 1 ppm in methylcyclohexane. The large difference could be explained, again, by the different solvents

used and the lower concentration. In addition, the dye may be subject to thermal degradation during the PMMA curing process (a decrease in sample absorption was often observed) or it may react with the initiator used in the reaction. Both will lead to a reduction in the amount of active dye molecules present and a corresponding reduction in the PLQY.

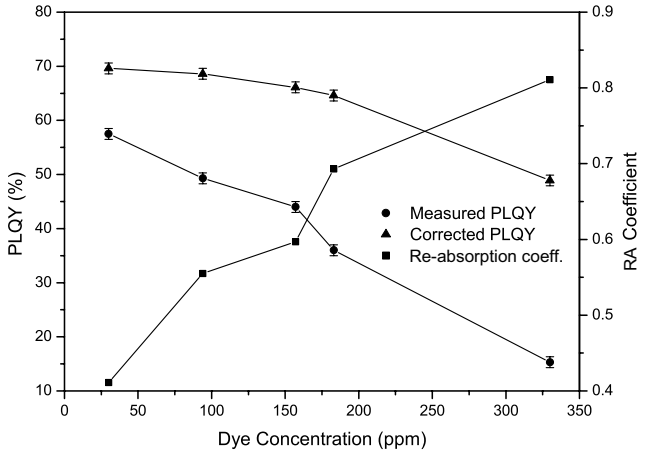

Figure 4.14: PLQY and re-absorption coefficient of NIR1

The last dye, NIR3 (Fig. 4.15), has a PLQY of 60-65 % even at the highest sample concentration of 392 ppm. A small amount of concentration quenching is present, as the PLQY decreases by around 5 % over the range of concentrations studied. The PLQY is in agreement with that obtained by Nolde *et. al.*[47] of 53±10 %, which was again measured a lower concentration (1 ppm) and in a liquid solvent (toluene).

Although the quantum yields of the three organic dyes may seem high, it must be remembered that any non-unity quantum yield will drastically increase the losses from re-absorption which occur in an LSC. If these NIR-emitting organic dyes were combined with the visible dyes (for example, Rot 305) in the same sheet, photons from the visible dye which would have reached the edges will be absorbed by the NIR dyes and there is a high probability (the complement of the PLQY) of their being lost. To balance these increased losses, there will be an increased number of solar photons absorbed because the addition of the NIR dyes extends the absorption range. However, this is not enough to overcome the additional losses and it has been shown that the only solution is to incorporate the NIR dyes in a totally separate LSC

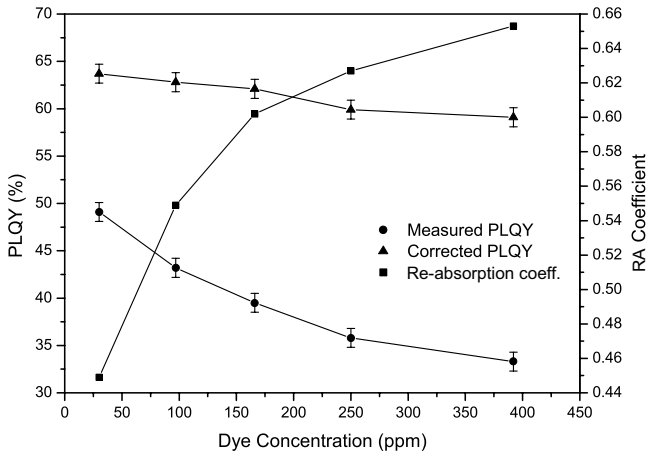

Figure 4.15: PLQY and re-absorption coefficient of NIR3

sheet to create a stacked module[34]. This is demonstrated both theoretically and experimentally in Chapter 6 and Chapter 7, respectively.

4.4.2 Rare-earth nanoparticles

Although each of the four different nanoparticle compositions (Section 2.1.3) was studied, the only one which showed any detectable emission was pure NdF_3.

Because of the extremely small absorption coefficient, it was impossible to make a PMMA sample containing sufficient nanoparticles to provide a detectable absorption. Therefore, the absorption spectrum was measured using a solution of the nanoparticles in THF. For the same reason, fluorescence emission was recorded from solid nanoparticle powder, instead of from a PMMA sample.

Fig. 4.16 shows the absorption and emission spectra for NdF_3 nanoparticles. The solution concentration used for the absorption spectrum measurement was 6980 ppm by weight in THF and was measured in a 10 mm silica cuvette. The absorption coefficient shown in Fig. 4.16 is corrected to be valid in PMMA.

The sharp absorption peaks of the Nd^{3+} ion can clearly be seen, but are superimposed on top of an exponentially rising background absorption. This is most likely caused by scattering from un-dissolved or aggregated nanoparticles in solution. Although the

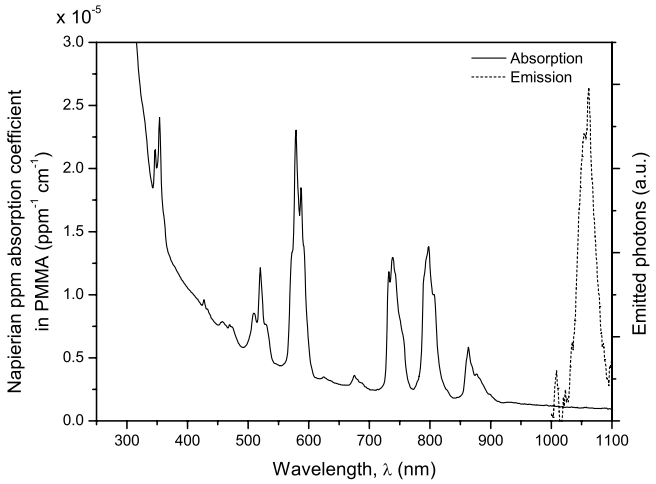

Figure 4.16: Absorption (solid) and emission (dashed) of NdF_3

solution was sonicated for several hours, no reduction in this background was seen.

The absorption coefficient of the nanoparticles is extremely low, approximately four orders of magnitude less than a typical absorption coefficient for an organic dye. This makes their incorporation into LSCs impractical because of the extremely high concentrations required. To achieve an optical density at the peak absorption equal to a sheet containing 300 ppm of an organic dye, an LSC sheet containing nanoparticles would require a concentration of several million ppm, in other words it would consist of solid nanoparticles and no host.

Upon excitation at 581 nm, weak emission was only observed at the Nd peak at 1064 nm. The quantum yield was measured to be 0.005 %. Emission at the other neodymium wavelengths of 890 nm and 1320 nm was either absent or too weak to be measured.

Although rare-earth nanoparticles display emission wavelengths ideally suited to LSC use (close to the bandgap of silicon solar cells), their low absorption coefficients and PLQY make them unsuitable. The final type of NIR emitter to be studied in this section overcomes the problem of low absorption coefficient by using an organic ligand to absorb radiation and transfer the energy to a rare-earth ion.

4.4.3 Rare-earth complexes

The optical properties of the MO49 europium-containing complex described in Section 2.1.4 were measured. Due to the strong absorption of PMMA below 300 nm (Fig. 2.14), it was impossible to measure the absorption spectra in that host material. Since the main purpose of measuring the absorption spectrum is simply to determine a suitable excitation wavelength, the complex was instead dissolved in DCM and the absorption spectrum measured in solution. An absorption coefficient in PMMA was obtained from the value measured in DCM and the relative densities of the two materials, as described in Section 2.2.1. Emission and PLQY measurements were, however, made on samples of the complex doped into PMMA. Although MO49 contains a europium ion which emits in the visible, it is studied in this section as an example of the possible performance of the rare-earth complexes.

As before, different sample concentrations were used for measuring the absorption and emission spectra. The absorption spectrum was measured from a 7.3 ppm concentration of the complex in DCM solution, while the emission spectrum was measured from a 110 ppm concentration in PMMA, the higher concentration being used to obtain a good emission signal strength. The absorption and emission spectra are shown in Fig. 4.17. Its absorption spectrum shows a peak centred at 300 nm with a magnitude comparable to that of the organic dyes. The emission spectrum consists of a collection of five peaks in the range 575-700 nm, with the most intense peak at 613 nm. These are attributable to the transitions from the $^5D_0$ state to the $^7F_{J=0,1,2,3,4}$ states[136].

The Stokes shift is ∼300 nm - extremely large when compared with the 30-50 nm shifts of the organic dyes. As a result, there is zero overlap of the absorption and emission spectra and hence there will be zero re-absorption losses in an LSC sheet containing such complexes.

The PLQY was measured in PMMA at four different sample concentrations (110, 133, 146 and 240 ppm) and is shown in Fig. 4.18. It decreases from around 91 % to 84 % at higher concentrations. Although the quantum yield is certainly not as high as that of the visible organic dyes, the absence of any re-absorption can actually result in a greater fraction of photons being trapped in an LSC sheet when compared

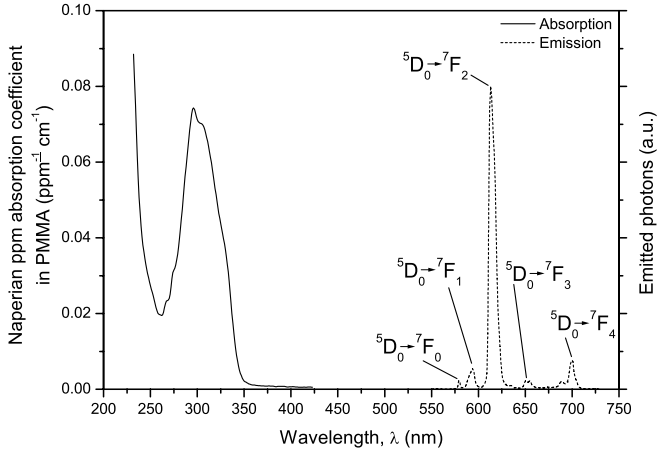

Figure 4.17: Absorption (solid) and emission (dashed) spectra of MO49. Absorption measured from 7.3 ppm concentration in DCM solution. Emission measured from 110 ppm concentration in PMMA at excitation wavelength of 320 nm.

with the organic dyes, as studied later in Chapter 5. The measured PLQY value is in agreement with that obtained by Moudam *et. al.*[140] of 85±10 %, measured at a concentration of 240 ppm.

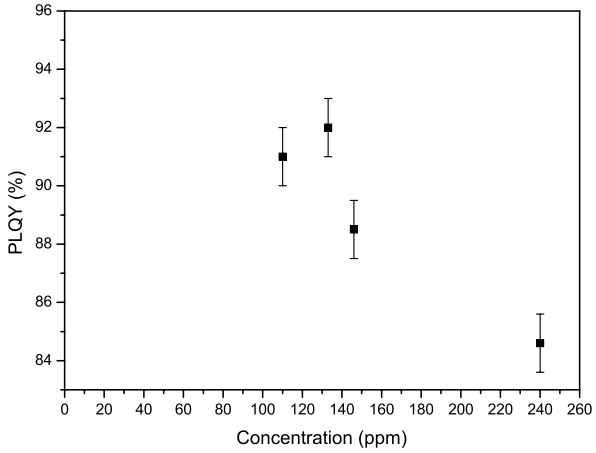

Figure 4.18: PLQY of MO49 complex in PMMA

NIR-emitting rare-earth complexes using the same ligands as MO49 have recently been produced by substituting the europium ion with ytterbium or neodymium ions[153, 154]. As an example, the absorption and emission spectra of an ytterbium-containing complex, MO65, are shown in Fig. 4.19 (adapted from Rowan *et. al.*[153]). Similar to MO49, the complex exhibits absorption around 300 nm and has a well-

separated emission peak centred at 980 nm, corresponding to emission from the ytterbium ion. However, unlike the high PLQY of the MO49 europium-containing complex, the PLQY of these ytterbium- and neodymium-containing complexes is extremely low, at most 1-2 %[153, 154]. The PLQY of the MO65 ytterbium complex shown in Fig. 4.19 is 1.9 % in DCM solution[154].

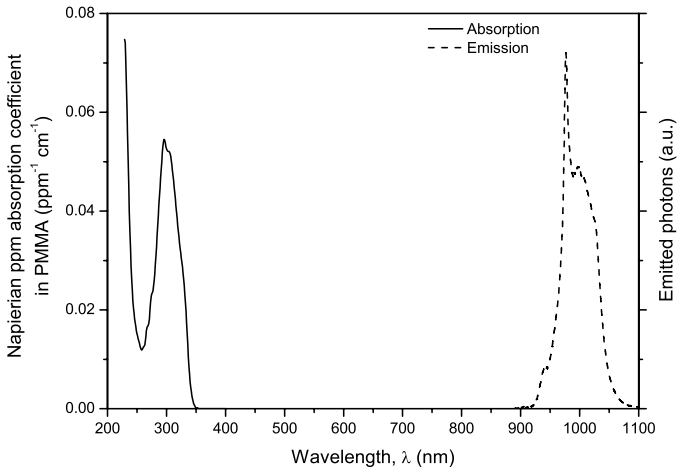

Figure 4.19: Absorption and emission of MO65 ytterbium complex in PMMA (after Rowan *et. al.*[153])

4.5 Discussion

The Lumogen F visible-emitting organic dyes exhibit near-unity quantum yields and high solubilities. There is the possibility of absorbing all wavelengths below 650 nm using a combination of several of the dyes. Their quantum yields remain near-unity even at high concentrations or in mixtures with other dyes, suggesting that these dyes could provide a solution to two major problems in LSC development - those of high quantum yields and a wide absorption bandwidth[6].

By comparison, the dyes which were used in the initial development of LSCs were widely-available organic laser dyes, which did not have as good PLQY as the Lumogen F range. Batchelder[16] analysed a range of such dyes, both experimentally and theoretically, and showed that, because of the effects of re-absorption, the quantum yields of the dyes needed to ideally be close to unity to prevent a large

loss. Dyes studied included 4-dicyano-methylene-2-methyl-6-p-dimethyl amino-styrl-4H-pyran (DCM) (71 % PLQY), Rhodamine 6G (98 % PLQY) and Coumarin (71 % PLQY)[16]. However, those dyes which did have high PLQY were either difficult to dissolve in PMMA or were subject to photodegradation.

Measurements of Rot 305 showed that the PLQY was invariant with excitation wavelength, indicating that, since Rot 305 has the widest absorption bandwidth of all the dyes (around 300 nm), it may be possible to use a high concentration of Rot 305 alone to absorb a wide range of solar wavelengths, rather than using a mixture of several different dyes. As was seen, the PLQY of a mixture can be non-unity if one of the short-wavelength dyes is excited first, leading to reduced efficiency. Another benefit of Rot 305 was the progressive red-shift of the emission spectrum with increasing excitation wavelength (due to an increasing amount of emission from aggregates), which results in a decrease in re-absorption losses.

The NIR-emitting organic dyes have a much lower PLQY than the visible dyes. Although the addition of NIR dyes to an LSC sheet containing visible dyes would increase the range of wavelengths absorbed, the low PLQY (60-80 %) would introduce losses which may outweigh the benefit of the increased absorption range. As is found later (Chapter 6), this is correct, and the only solution is to place the low PLQY dye in a separate sheet to form a stacked LSC module.

All of the organic dyes exhibit an overlap of their absorption and emission spectra, which leads to emitted photons being re-absorbed by the same dye molecules. The detrimental effects of a non-unity PLQY are amplified by the multiple re-absorption events which occur in an LSC sheet containing organic dyes. For example, a 95 % PLQY will lead to approximately 77 % of photons being emitted after five re-absorption events (0.95^5).

A range of different rare-earth compounds was also analysed. These all exhibited a wide separation between their absorption and emission spectra, with a consequent absence of re-absorption losses.

Rare-earth nanoparticles showed extremely low absorption coefficients and quantum yields, making them highly unsuitable for use in LSCs because of the high concentra-

tions (greater than 50 % by weight) which would be required.

Although the rare-earth complex containing Eu^{3+} showed a high quantum yield, the PLQYs of complexes containing Nd^{3+} and Yb^{3+} are low, in the range 1-2 %[153, 154]. However, the PLQYs of these Nd^{3+} and Yb^{3+} complexes are higher than those measured by Werts *et. al.*[138] and Hebbink *et. al.*[113]. Werts *et. al.*[138] obtained PLQYs in water solution of 0.017 % for Nd^{3+} complexes and 0.09 % for Yb^{3+} complexes, while Hebbink *et. al.*[113] measured PLQYs of 0.012-0.03 % for Nd^{3+} and 0.14-0.23 % for Yb^{3+} (both in deuterated methanol). Werts obtained a similar increase of 2-5x in PLQY by using a deuterated solvent[138]. The higher PLQYs measured in PMMA can be explained by the choice of host material; in a solid host such as PMMA, the probability of non-radiative decay of the rare-earth ion (by, for example, transferring its energy to OH and CH bond vibrations in the ligands or the host) is less than in a liquid host. This results in an increased PLQY. Preliminary results from our group demonstrate the possibility of increasing the quantum yield of an Yb^{3+} complex in PMMA still further to nearly 4 % by deuteration[154]. However, the PLQY is still less than in a completely inorganic host such as YAG crystal or glass because the absence of any organic bonds eliminates non-radiative decay by this process and results in a high PLQY. Values as high as 90 % have been measured for Nd^{3+} in these inorganic hosts[108, 109].

Neodymium and ytterbium complexes have also been produced with different ligands which absorb in the visible part of the spectrum[153]. Although they currently exhibit low PLQYs (0.1-0.2 %[153]), they demonstrate that it is possible to have a ligand which absorbs in the visible and successfully transfers its energy to an emitting ion. This is important because, while the complexes with UV-absorbing ligands displayed higher quantum yields, there is little solar radiation available at 300 nm and they are of little use in actual LSCs.

4.6 Conclusions

The integrating sphere has been demonstrated to be a versatile and convenient tool for measuring the quantum yield of a wide range of different compounds. It is not

limited by the format of the samples, or by the surface or bulk properties of the host (such as scattering of excitation light), and provides a means of measuring dye quantum yields in the actual host material of the LSC in which they would be used.

Individual dyes have at most a few hundred nanometers of absorption bandwidth, therefore the amount of sunlight a single-dye LSC can absorb is limited. However, because the Lumogen dyes can be mixed without affecting their quantum yields, it is possible to absorb all of the sunlight over the range 300 nm - 650 nm using a combination of several of the dyes in the same sheet. The most important dye in the mixture is the longest-wavelength (Rot 305) which fortunately has 100 % PLQY. It is also possible to use a high concentration of the Rot 305 dye on its own.

The rare-earth complexes, by contrast, showed some excellent properties. Their absorption coefficients were high, comparable to those of the organic dyes, as a result of the ligand absorption. A complex containing the visible-emitting Eu^{3+} ion showed a quantum yield close to 90 %. In addition, the Stokes shifts were of the order of 300 nm, nearly ten times that of the organic dyes, resulting in no spectral overlap of the absorption and emission. Even though the quantum yield is lower than that of the visible organic dyes, they can still result in a higher trapping efficiency inside an LSC sheet because of the absence of re-absorption.

The main benefit of the rare-earth complexes is obviously their greatly increased Stokes shifts and zero re-absorption losses. In the next chapter, we will study the effects of re-absorption on photon transport and trapping inside LSC sheets, using both the organic dyes and rare-earth complexes as examples. We will also show the existence of tail absorption spectra present in the visible organic dyes, and demonstrate the effect of this on trapping efficiency. Later (Chapter 6), we will perform simulations of LSC performance and determine optimum dye concentrations for both visible and NIR dyes.

Chapter 5

Re-absorption in LSC sheets

The effects of re-absorption and spectral overlap on photon transport inside LSC sheets are studied in this chapter using a combination of Monte-Carlo ray-tracing simulations and experiment. Measurements of the fluorescence spectra from the end of a strip sample of LSC material under point excitation reveal how the photon transport probability varies with pathlength and can also be used to accurately determine the tail absorption spectra of the dyes. Finally, simulations of a square LSC sheet under uniform illumination show the effects of re-absorption and host absorption on photon transport and these effects are confirmed experimentally.

5.1 Introduction

A wide range of organic dyes has been developed and studied for use in LSCs[48, 43, 13], including the Lumogen F dyes characterised in the previous chapter. Although many have a near-unity quantum yield, which is one requirement for LSC use, they all suffer from the effects of re-absorption because of the overlap of their absorption and emission spectra. When a re-absorption event occurs, there is both a probability that the photon will be lost because of a non-unity dye quantum yield and also by being emitted into one of the escape cones and lost from the sheet. The probability of the escape-cone loss is 25 % for PMMA (n=1.49).

It has been reported that re-absorption is one of the major limiting factors in LSC

development[39]. Not only does the main absorption spectrum of the dye contribute to the re-absorption losses, but there also exists a low-magnitude absorption tail extending as much as several hundred nanometers beyond the end of the main absorption[61]. Although of low-magnitude, its effects are felt over the long pathlengths in LSCs. The number of photons transported to the edges of the sheet will be reduced by re-absorption.

The rare-earth complexes described in Chapter 4 would appear to offer a possible solution, as they possess large Stokes shifts (several hundred nanometers) and, therefore, exhibit little or no re-absorption. Although they have lower quantum yields than the organic dyes, they can actually result in lower losses because of the lack of re-absorption. We will choose MO49 (Eu^{3+}-containing, 86 % PLQY) as an example of a rare-earth complex and compare this with Rot 305, as both emit in the same wavelength region.

5.2 Experimental

Sheet samples of PMMA doped with a range of concentrations of the Lumogen F dyes and the MO49 complex were prepared using the waterbath casting technique described earlier (Section 2.3.1). Strip samples were cut from the as-cast sheet by hand and finished to the final size with a milling machine. Samples were 1.2 cm wide, 10 cm long and 0.3 cm thick. Both long edges and one of the short edges were roughened with sandpaper and painted with matt black acrylic paint to prevent internal reflections from these sufaces. Only the short edge where emission is detected with the optical fibre was left un-painted.

Similarly, 10 cm square sheets (for measurement of the optical efficiency) were cut from the cast sheets and machined to size. Their edges were finished with a diamond edge polisher (Section 2.3.5), leaving an optical-quality flat edge.

To measure the emission spectrum from the end of the strip samples, a setup similar to that used by Sansregret[40] and Earp[61] was used. This is shown in Fig. 5.1. For further clarity, a photograph of the setup is shown in Fig. 5.2.

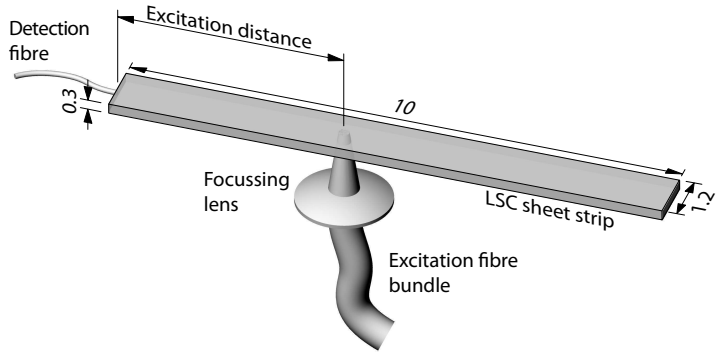

Figure 5.1: Measurement of edge spectra from strip samples (dimensions in centimeters)

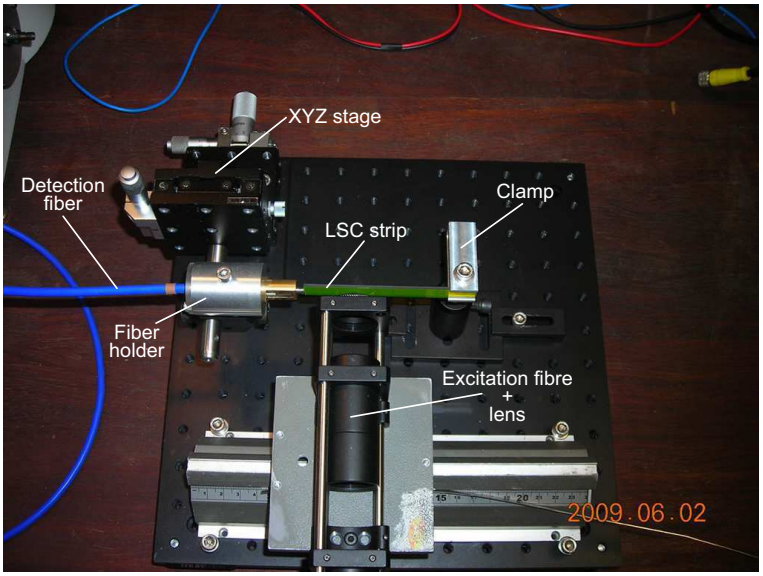

Figure 5.2: Photograph of edge-emission setup

The experiment was designed to closely approximate a point excitation source with straight-line path of the emission to the edge and minimal fluorescence from locations other than the excitation spot. This is achieved by using narrow strips with blackened edges, ensuring that any fluorescence detected arises primarily from the point of excitation with minimal contributions from edge reflections. The 10 cm x 1.2 cm strip was held at one end with a split clamp. Excitation illumination was provided by a 100 W xenon lamp and monochromator (Bentham), delivered via a 6 mm-diameter fibre bundle. A single 50 mm focal-length lens was used to focus the excitation light on to the surface of the strip. The fibre and focussing lens were mounted on an optical rail so the 2 mm-diameter illumination spot could be moved along the length of the

strip.

The excitation wavelength was chosen to match the absorption of the dye in the strip. Although it is not essential to excite the dye at exactly its peak absorption, the wavelength was chosen to be as close as possible to achieve the highest signal strength. The wavelengths used are listed in Table 5.1 for each of the dyes and the rare-earth complex.

Table 5.1: Excitation wavelengths

Fluorophore	Excitation wavelength (nm)
Violett 570	360
Gelb 083	440
Gelb 170	460
Orange 240	470
Rot 305	530
MO49	320

The detection fibre (600 μm-diameter, 0.22 NA, Ocean Optics) was mounted in a spring-loaded holder on an XYZ micrometer stage and was centred in the end of the strip. Although an optical coupling medium (glycerine) was initially tried, it was found that it had no effect on either the spectral profile or decay rate of fluorescence intensity with distance. In addition, each sample required cleaning afterwards, increasing the risk of scratching or otherwise damaging the sample. For these reasons, the use of a coupling medium was avoided. Light from the detection fibre was collected by a spectrometer (Jobin-Yvon iHR320) equipped with a UV/vis photomultiplier tube (Hamamatsu R928).

Although measurements on strip samples reveal information about the transport probability of trapped fluorescence light for a particular excitation distance, they do not directly relate to a uniformly-illuminated square LSC sheet, as there is a distribution of pathlengths inside the sheet. The percentage of photons trapped in an actual LSC sheet under uniform illumination can be determined by measuring the number of photons emitted at the edges of the sheet compared with the number absorbed. This can be done using either a solar cell[156], an integrating sphere[28] or an optical fibre[40]. While simple to use and able to collect light from the entire edge, the solar

cell gives no information on the spectral profile of the light emitted or absorbed. The integrating sphere is problematic because of sphere errors and intensity calibration. Therefore, the optical fibre approach is adopted here. The experimental setup is shown in Fig. 5.3. The 10 cm square sheets used for this were clamped vertically on an optical table. Care was taken to ensure that the clamping arrangement did not shade the fluorescent sheet from the illumination.

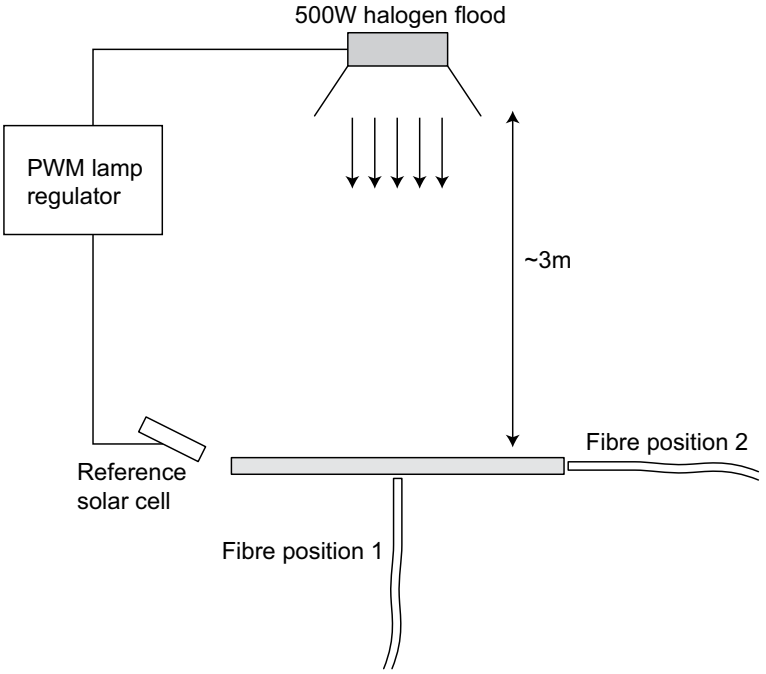

Figure 5.3: Measurement of % trapped photons. Lamp shown is used for Lumogen F sheets; replaced with xenon lamp for MO49 sheets.

Two different light sources were used to illuminate the sheet, depending on the dye under study. The organic Lumogen F dyes absorb in the visible so a tungsten-halogen lamp was used. However, the MO49 rare-earth complex only absorbs in the UV, where the output of a tungsten-halogen lamp is negligible. Therefore, for the MO49 sheets, the lamp shown in Fig. 5.3 was replaced with a Xenon lamp (150 W, Oriel). The tungsten-halogen lamp was intensity-stabilised and based on a standard 500 W outdoor floodlight with closed-loop control of the intensity (Section 2.2.4). The unfiltered output of the Xenon lamp was deliberately defocused to ensure uniform illumination across the LSC sheet under study. The output intensity was monitored with a photocell and was found to be sufficiently stable (to 0.5 %), even though the lamp is not deliberately intensity-regulated. Both lamps were placed far enough away from the

LSC sheet to ensure uniform illumination.

An optical fibre, coupled to the spectrometer (iHR320), was used to measure both the number of photons absorbed over the surface of the sheet and the number emitted at the edges. The fibre has an acceptance angle of 25.4° in air. Only those photons from the edge of the sheet which are emitted within this acceptance cone can be detected. This is approximately 2.4 %, based on the solid angle of the acceptance cone. With the fibre in position 1 (Fig. 5.3) and the LSC sheet removed, the fibre detects the light directly incident on the front surface of the LSC. The fluorescent sheet is then placed in front of the fibre. The fibre now records the light transmitted through the sheet. Once reflection is corrected for, the difference in these is a measure of the number of photons absorbed by the sheet, which was found to be in agreement with the value calculated from the Beer-Lambert law and the absorption spectrum of the dye. The fibre can then be placed in position 2 where it will measure the number of photons emitted at the edge. Corrections are then applied for the acceptance cone of the fibre, the distribution of light intensity along the edge of the sheet[12] (more intense in middle of edge), and the slight variation in sheet thickness from corner to corner. This results in values for both the number of photons absorbed over the surface and emitted at the edges. From this it is then possible to calculate the percentage of absorbed photons which are collected at the edges of the sheet.

In order to study the trapping of fluorescence photons inside the LSC sheet, several modifications were made to the Monte-Carlo simulation program (Section 2.4), as it normally calculates the electrical power output of the edge-mounted solar cells. A spectrum was recorded of the first-generation photons emitted within the sheet - those which originate from a dye molecule excited by a solar photon, rather than by a re-absorbed fluorescence photon. The program then records the spectrum of all photons which reach the edges of the sheet, thus removing the effects of solar cell response. By integrating the areas of both of these spectra, a value can be obtained for the optical efficiency of the LSC sheet, η_{OPT}, defined as the number of photons reaching the edges as a fraction of the total number of first-generation fluorescence photons emitted within the sheet, Eqn. (5.1).

$$\eta_{OPT} = \frac{\text{No. photons reaching edge}}{\text{No. initial photons emitted}} = \eta_{self} \times P_{TIR} \tag{5.1}$$

If the PLQY of the fluorophore is unity, the total number of first-generation fluorescence photons is equivalent to the total number of absorbed solar photons.

Two different sizes of LSC sheet were simulated. The smaller size, 10 cm x 10 cm x 0.3 cm, was chosen because this was a convenient size for casting and on which to perform measurements, while the larger size, 30 cm x 30 cm x 0.3 cm, was chosen as a representative size for a prototype LSC module in which re-absorption effects are more pronounced because of the longer pathlengths involved. Two million initial photons were simulated, which corresponded to a repeatability/error in the results of $\pm 0.02\,\%$.

5.3 Results

Results for the transport probability, tail absorption spectra and optical efficiency are presented below for strip and square LSC samples.

5.3.1 Transport probability

Some means is required to interpret the emission spectra obtained from the end of the strip LSC samples in order to determine the characteristics of photon transport within the strip. A logical choice would be to plot the total photon intensity obtained by integrating the measured spectra. However, problems arise in measurments on high-concentration samples because of the limited acceptance cone of the optical fibre. Fig. 5.4 shows the integrated photon intensity versus excitation distance for two different concentrations of Rot 305 dye.

The lower concentration shows a steady exponential decrease of integrated photon intensity with increasing excitation distance. However, the higher concentration shows a peak at 2 cm, with an exponential decay at larger distances. This peak is purely an artifact of the limited acceptance cone of the fibre, which is $\sim 17^\circ$ in PMMA. At

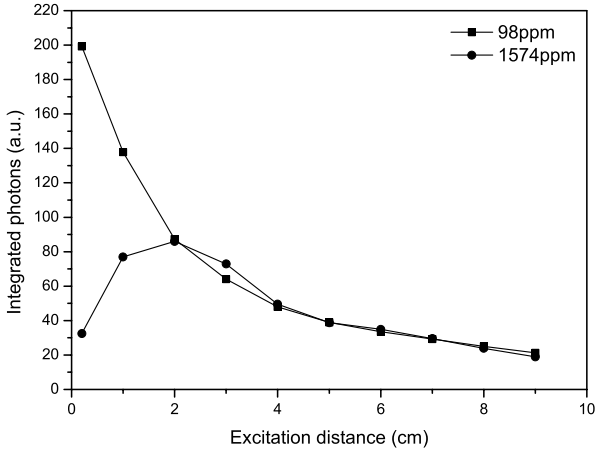

Figure 5.4: Integrated photon intensity measured at end of Rot 305-doped strip samples

high dye concentrations, the fluorescence emission originates mainly from a region near the front surface of the sheet, shown by the shaded region in Fig. 5.5. At short excitation distances, the fluorescence from this region can lie outwith the fibre's acceptance cone and can escape detection, resulting in a lower recorded intensity. As excitation distance is increased, the detected intensity initially increases as more of the fluorescence region enters the escape cone, but then decreases as re-absorption losses increase. Although this effect is present when using a fibre to detect the edge emission, it is less relevant in an actual LSC module which uses solar cells attached to the edges, as solar cells can collect light from a wide range of incident angles. In addition to this behaviour, there is the problem of normalising the intensity obtained from different samples. Different concentrations or dyes absorb different amounts of the excitation light and result in different intensities.

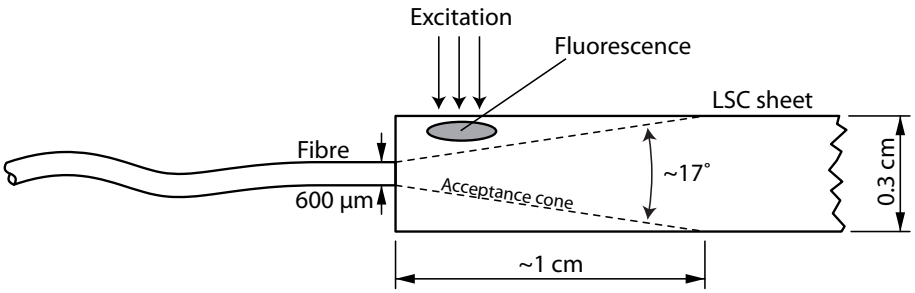

Figure 5.5: Acceptance cone of fibre, showing the limited acceptance angle of the fibre (to scale)

It can therefore be concluded that using the integrated photon intensity is not a

practical means of studying photon transport. However, the profiles of the emitted spectra can be used instead. By measuring the profiles of the fluorescence spectra emitted from the end of the strip samples at different excitation distances, it is possible to see how the probability of a fluorescence photon reaching the edge varies with excitation distance and dye concentration. The spectra can also be used to accurately determine the tail absorption spectrum of the dye in the sheet.

We define P_0 as the overall probability that a first-generation emitted photon (one emitted at the point of excitation) will reach the detection fibre without undergoing re-absorption. It is calculated from Eqn. (5.2)[40],

$$P_0 = \frac{\int E'(\lambda)d\lambda}{\int E(\lambda)d\lambda} \tag{5.2}$$

where $E(\lambda)$ is the molecular emission spectrum of the dye, when the effects of re-absorption are absent, and $E'(\lambda)$ is the spectrum measured from the end of the strip, scaled to match $E(\lambda)$ at long wavelengths where re-absorption is negligible. $E(\lambda)$ was measured from the end of a strip containing a low concentration (5 ppm) of dye, with an excitation distance of only 0.2 cm. The concentration and excitation distance are small enough that any re-absorption effects are negligible (Lakowicz[38] Sec. 2.8). The normalisation procedure used to obtain $E'(\lambda)$ is described briefly below.

Fig. 5.6 shows an example of the spectral normalisation procedure for a strip containing 98 ppm of Rot 305 dye, excited at a distance of 5 cm. The raw (unscaled) emission spectrum, $E_{raw}(\lambda)$, is divided by the molecular emission spectrum, $E(\lambda)$, to obtain the ratio $E_{raw}(\lambda)/E(\lambda)$. As can be seen in Fig. 5.6, this ratio levels out above 750 nm and is constant at $\sim$2.53. The ratio becomes constant because re-absorption is no longer occurring appreciably at these wavelengths. If $E_{raw}(\lambda)$ is then divided by this constant ratio, it is scaled so it matches $E(\lambda)$ exactly at long wavelengths, resulting in $E'(\lambda)$. Using this ratio to scale the spectra is more accurate than scaling them "manually" until they fit.

The shape of the ratio plot is indicative of how far the absorption tail extends into the emission spectrum. Once the edge-emitted spectra have been scaled as described, the probability values P_0 can be calculated from Eqn. (5.2).

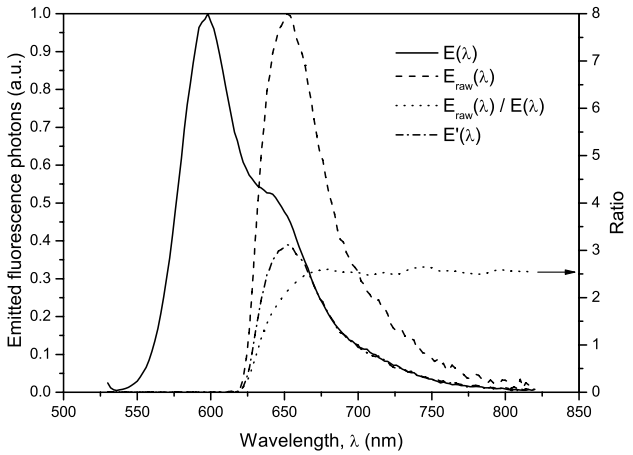

Figure 5.6: Example of scaling procedure. Shown are the molecular emission spectrum, $E(\lambda)$, the raw spectrum measured from the end of the strip, $E_{raw}(\lambda)$, the ratio $E_{raw}(\lambda)/E(\lambda)$, and the scaled emission spectrum, $E'(\lambda)$, obtained by dividing $E_{raw}(\lambda)$ by the constant ratio at long wavelengths (2.53).

The system shown in Fig. 5.1 was used to measure P_0 for strip samples containing a range of different concentrations of the Lumogen F dyes. Since the behaviour of all the dyes is similar, only results for the Rot 305 dye are discussed here. Seven different concentrations of Rot 305 (4.9, 98, 197, 295, 393, 787 and 1574 ppm) were studied at excitation distances ranging from 0.2 cm to 9 cm. The results are shown in Fig. 5.7. Since P_0 depends on both dye concentration and the excitation distance, it is plotted versus the effective optical density (OD_{eff}) of the path from the excitation point to the detector, calculated from Eqn. (5.3),

$$OD_{eff} = \varepsilon_{peak} \times c \times d \times \log(2.71828) \tag{5.3}$$

where ε_{peak} is the peak Napierian absorption coefficient of the dye ($0.102\,\mathrm{ppm}^{-1}\mathrm{cm}^{-1}$ for Rot 305 in PMMA), c is the dye concentration in ppm, and d is the excitation distance in centimeters. The logarithmic factor corrects for the different bases used in the definition of optical density and absorption coefficient. This *effective* optical density is used because the trapped fluorescence light follows a range of diagonal paths between the top and bottom surfaces of the sheet as it travels to the edge and the actual average pathlength inside the strip is unknown and different from the excitation distance, although it can be determined from ray-tracing simulations[40].

By doing this, it becomes possible to calculate a value for P_0 from the molecular emission spectrum, $E(\lambda)$, and the absorption spectrum of the dye, $\varepsilon(\lambda)$, by replacing $E'(\lambda)$ in Eqn. (5.2) with $E(\lambda)e^{-\varepsilon(\lambda)cl}$. This uses the Beer-Lambert law to predict the fluorescence spectrum transmitted through an average pathlength l of dye-doped material, where the average pathlength is obtained from ray-tracing simulations and is a factor of 1.1 to 1.3 times greater than the excitation distance, depending on the dye concentration. This calculated value, $P_{0,calculated}$, is also plotted in Fig. 5.7.

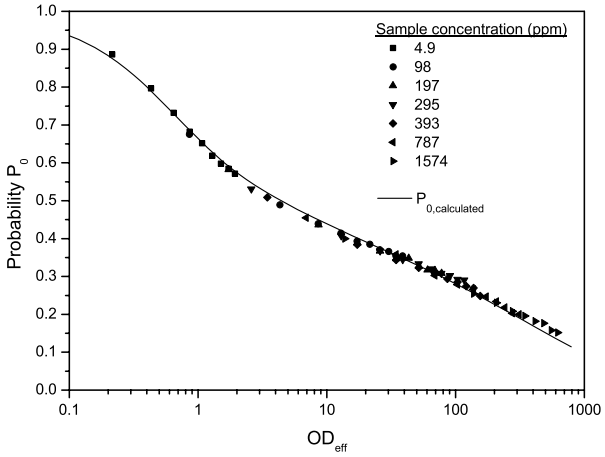

Figure 5.7: P_0 versus effective optical density for Rot 305, showing experimental data (points) and calculated curve (line)

Values measured for P_0 from the seven different sample concentrations all show good agreement with each other. For example, P_0 measured from a 393 ppm sample with an excitation distance of 3 cm is identical to that measured from a 197 ppm sample with a 6 cm excitation distance, since OD_{eff} is the same in both cases (half the concentration but twice the distance).

As either excitation distance or dye concentration is increased (both of which result in an increase in the effective optical density), the probability of the photons reaching the detector drops dramatically. At larger distances or higher concentrations, the first-generation fluorescence photons pass through a greater amount of dyed material, therefore there is an increased chance that they will be re-absorbed by the dye and lost. In addition, as the concentration is increased, the *rate* of decay of probability with excitation distance becomes *less*. The probability decreases more rapidly with,

for example, a 5 ppm sample than it does with a 393 ppm sample. This is due to increased re-absorption losses at shorter distances in highly concentrated samples. Any photons which survive more than a few centimeters will then suffer little additional re-absorption; any re-absorption that is experienced is then due primarily to the low-magnitude absorption tail. It can be seen that the decay of probability with concentration is greater at shorter excitation distances, as most re-absorption will occur within the first few centimeters.

There is good agreement between the experimental data and the calculated values obtained using the Beer-Lambert law. This is perhaps unexpected, as the Beer-Lambert law should not apply when the probability of re-emission is high, as in the case of high-PLQY fluorescent dyes. However, whereas the initially-excited fluorescence (excitation wavelength 530 nm) arises from monomer dye molecules, re-absorption tends to excite the J-aggregates so that the re-emitted fluorescence has a different, red-shifted spectrum (Section 4.3). Therefore, the attenuation of the primary, short-wavelength emission can be well approximated by simple absorption because there is little re-absorption in this short-wavelength region. The Beer-Lambert law can thus be used to model the propagation of light inside the strip.

The fraction of photons which undergo re-absorption is significant. For example, the dye concentration of 393 ppm is comparable to that which might be used in an actual LSC [a concentration high enough to absorb sufficient incident sunlight over the surface of the sheet (Section 6.1.1)]. If we consider those photons emitted 5 cm from the edge of the sheet, corresponding to an $OD_{eff} = 86$, it can be seen from Fig. 5.7 that they have only a 30 % chance of reaching a particular location on the edge, with the remaining 70 % of them undergoing re-absorption. An important fact to remember is that *average* pathlengths in an LSC of dimensions 30 cm x 30 cm, which would be considered a minimum practical size (Section 6.1.3), are around 15 cm, much larger than the pathlengths studied in Fig. 5.7.

These results show that the bulk of re-absorption occurs over the first few centimeters of the LSC, and thereafter the re-absorption is governed by the tail absorption of the dye. This is one of the reasons why many of the recently reported record LSC efficiencies[20, 19] have been measured from very small (<5 cm) mini-modules. By

constructing relatively thick modules with such small surface areas, the problems of re-absorption are reduced, but at the cost of dramatically reducing the concentration ratio.

5.3.2 Tail absorption spectra

The importance of re-absorption is clear. However, we do not yet know the extent to which the tail absorption overlaps the emission spectrum. The main part of the absorption spectrum can easily be measured with a UV/vis spectrophotometer and a sheet sample, but to measure the extremely low-magnitude absorption tail would require a much greater sample thickness - for example 10 cm. Casting samples of this thickness is not easy using the lab-scale waterbath casting technique (Section 2.3.1). However, it is possible to instead use the fluorescence spectra measured from the ends of the strip samples to determine the tail absorption spectrum[40]. If we again use $E(\lambda)$ and $E'(\lambda)$ to denote the molecular and scaled emission spectra as before, then an effective tail absorption coefficient of the dye can be calculated from Eqn. (5.4),

$$\varepsilon_{eff}(\lambda) = -\frac{1}{cl} ln \left[\frac{E'(\lambda)}{E(\lambda)} \right] \tag{5.4}$$

where the dye concentration and excitation distance are represented by c and d, both of which are known. ε_{eff} is expressed in terms of the excitation distance, rather than the average optical pathlength. Once the tail of the absorption spectrum has been calculated in terms of ε_{eff}, it is scaled to match the long-wavelength end of the main absorption spectrum, obtained from the UV/vis spectrophotometer, to give the correct value of ε corresponding to the average optical pathlength. An example of this procedure is shown in Fig. 5.8. The data from the UV/vis spectrophotometer (the main absorption spectrum) are valid below 650 nm; above this, the spectrophotometer is not sensitive enough to detect a change in the light intensity transmitted through the sample. Conversely, the data from the strip end emission are only valid *above* 650 nm, since little fluorescence is emitted at shorter wavelengths. To reduce the error, several different dye concentrations and excitation distances were used to obtain the tail absorption spectrum and the results averaged.

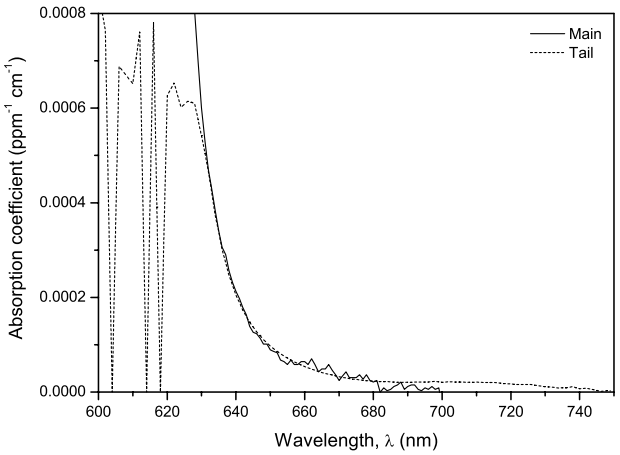

Figure 5.8: Scaling of the tail absorption spectrum (measured from the end emission of strip samples) to match the main absorption spectrum (from the UV/vis spectrophotometer) in the range 630-650 nm

To test the validity of calculating the absorption coefficient using Eqn. (5.4), it was used to calculate the absorption spectrum from fluorescence spectra measured from the end of a weakly-doped Rot 305 strip (4.9 ppm concentration and 5 cm excitation distance). The low concentration was chosen as the smaller amount of re-absorption would make it possible to obtain an absorption spectrum in a range which could then be compared with spectrophotometer measurements. The results are shown in Fig. 5.9. Data from the LSC strip show an excellent match to the spectrophotometer data over the range 550-625 nm. This confirms the validity of using Eqn. (5.4) to determine the tail absorption spectrum.

Tail absorption spectra for each of the five Lumogen F dyes were measured using the fluorescence from the ends of strip samples. The combined absorption spectra, consisting of data from both the UV/vis spectrophotometer and strip emission measurements are shown in Figs. 5.10-5.14.

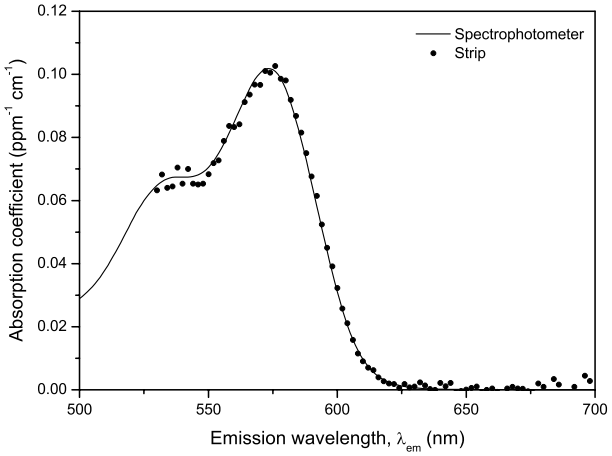

Figure 5.9: Comparison of absorption spectra obtained from both spectrophotometer and strip emission measurements

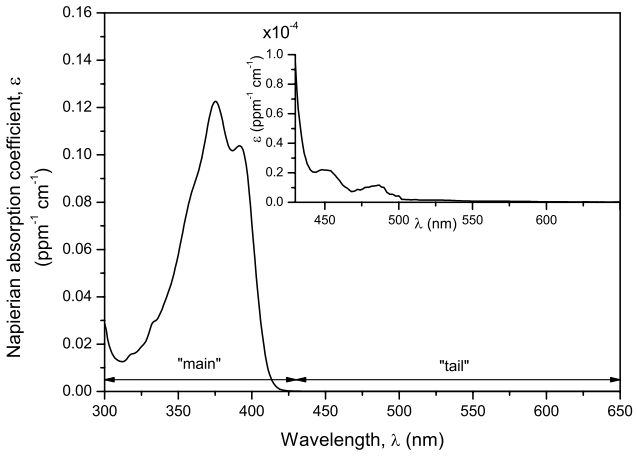

Figure 5.10: Absorption spectrum of Violett 570 in PMMA. Inset shows magnified tail absorption.

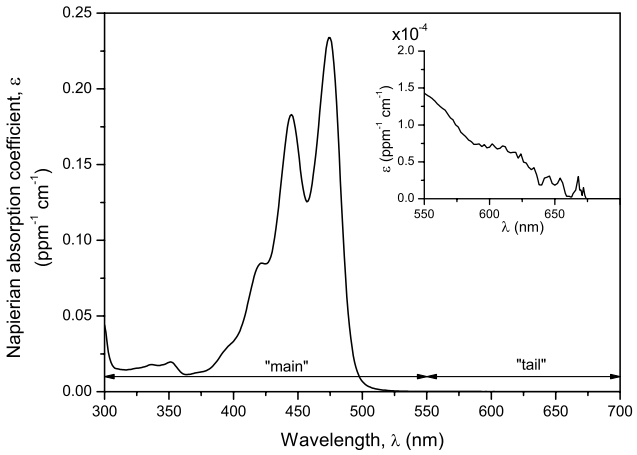

Figure 5.11: Absorption spectrum of Gelb 083 in PMMA. Inset shows magnified tail absorption.

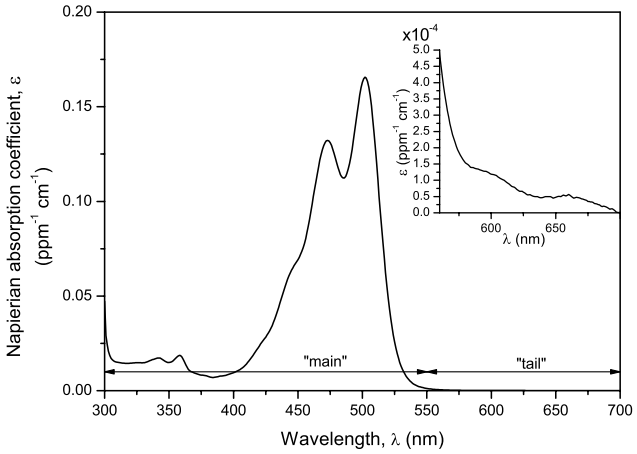

Figure 5.12: Absorption spectrum of Gelb 170 in PMMA. Inset shows magnified tail absorption.

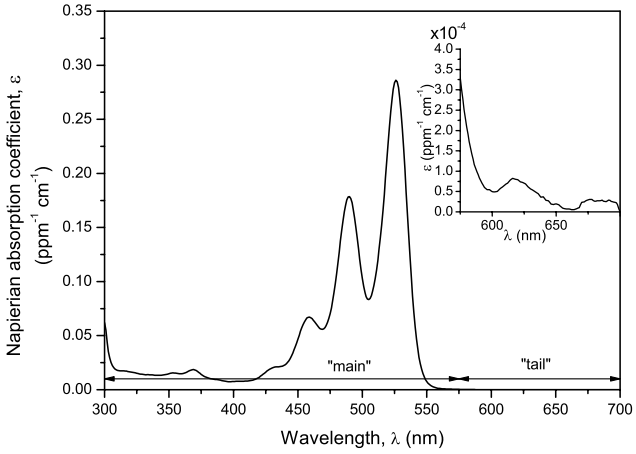

Figure 5.13: Absorption spectrum of Orange 240 in PMMA. Inset shows magnified tail absorption.

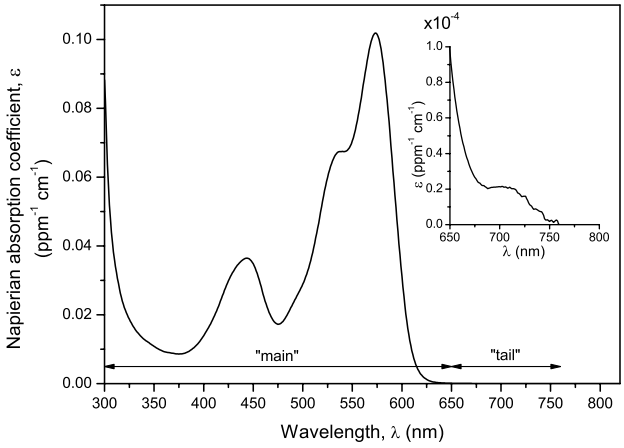

Figure 5.14: Absorption spectrum of Rot 305 in PMMA. Inset shows magnified tail absorption.

All of the dyes exhibit a low-magnitude absorption tail extending several hundred nanometers above the end of the main absorption. As a result, the dyes absorb (to some degree) over their entire range of emission wavelengths. Therefore, re-absorption will always be present, no matter how large the pathlength. The magnitude of the tail absorption is in the range 2x10^{-5} to 1x10^{-4} ppm^{-1}cm^{-1}. Although this is three to four orders of magnitude less than the peak absorption coefficient of the dye, the presence of this tail absorption becomes apparent over the long pathlengths in LSC sheets.

To give an example of the amount of absorption which the tail can contribute, consider a 60 cm x 60 cm LSC sheet containing 350 ppm of the Rot 305 dye (this is chosen based on the optimisation simulations performed in Section 6.1). The absorption coefficient in the tail region at ∼700 nm is 2x10^{-5} ppm^{-1}cm^{-1} (Fig. 5.14). Over an average pathlength of ∼34 cm, which is typical for a 60 cm x 60 cm sheet, this results in 21 % absorption of the fluorescence photons at that wavelength. The effect of the tail absorption is significant. It also demonstrates the importance of knowing the *entire* absorption spectrum, including the tail, when working with LSCs. Because of the long pathlengths involved, a tail absorption which may not be apparent on a UV/vis spectrophotometer scan can have a large impact on the photon transport in the device.

All of the above data relate to point excitation of a strip of LSC material. While this demonstrates photon transport losses at different pathlengths, it does not reproduce the performance of a real LSC, which will 1) have illumination over its entire surface and 2) have a much smaller length/breadth aspect ratio. We next look at the photon transport and losses in both 30 cm square and 10 cm square LSC devices under uniform illumination, using both simulation and experimental measurements.

5.3.3 Optical efficiency of square LSC sheets

The Monte-Carlo simulation program was used to model the photon transport inside two different sizes of square LSC sheets containing a range of hypothetical organic dyes with artificially-generated emission spectra. The object of this was to exam-

ine the effect of different Stokes shifts on the optical efficiency of the sheets. The experimentally-measured absorption spectrum of the Rot 305 dye was used in the program and remains fixed throughout. However, the *emission* spectrum was artificially shifted in wavelength to give a range of different Stokes shifts. The peak emission wavelength was varied from 574 nm to 800 nm, resulting in Stokes shifts from 0 nm to 226 nm. The results of these simulations are compared with those for LSCs doped with the MO49 rare-earth complex, which exhibits a very large Stokes shift of ∼300 nm (Section 4.4.3). First we consider the simulations of the 30 cm square sheet, which show the largest effects of re-absorption, host absorption and dye PLQY. Results are then shown for a 10 cm square sheet, along with the experimentally-measured value for Rot 305 to demonstrate the validity of the simulation.

Fig. 5.15 shows the results for a 30 cm square sheet containing 600 ppm of either the hypothetical dye or MO49. The Stokes shift of the real Rot 305 dye is 23 nm, indicated by the vertical line. The calculated η_{OPT} for a sheet containing the MO49 complex is 64 % and is shown by the horizontal line in Fig. 5.15. Since the complex exhibits zero re-absorption, this is simply the product of the probability of an emitted photon being trapped by total internal reflection, 74 % [calculated from Eqn. (1.3)], and the PLQY of the complex, 86 %.

Consider first the case where the hypothetical dye has no absorption tail (the absorption is set to zero above 650 nm), there is no host absorption and the dye has 100 % PLQY (solid curve ▬ in Fig. 5.15). At Stokes shifts above about 120 nm, η_{OPT} flattens out at 74 %. Since there is little spectral overlap and hence little re-absorption above this wavelength, this is identical to the fraction of first-generation photons which are emitted at angles outside the escape cone, calculated from Eqn. (1.3). For a refractive index of $n = 1.49$ (PMMA), this is indeed 74 %. At smaller Stokes shifts, η_{OPT} drops sharply, as re-absorption begins to occur. Even though the dye has 100 % PLQY, each re-absorption/re-emission event results in a ∼25 % chance of the emitted photon being directed out of the sheet.

If an absorption tail (from 650 nm to 750 nm) for the dye is now included in the simulation (dashed curve ▬ ▬ in Fig. 5.15), η_{OPT} drops by approximately 7 % over the range of Stokes shifts up to 100 nm. This large decrease in η_{OPT}, caused by the

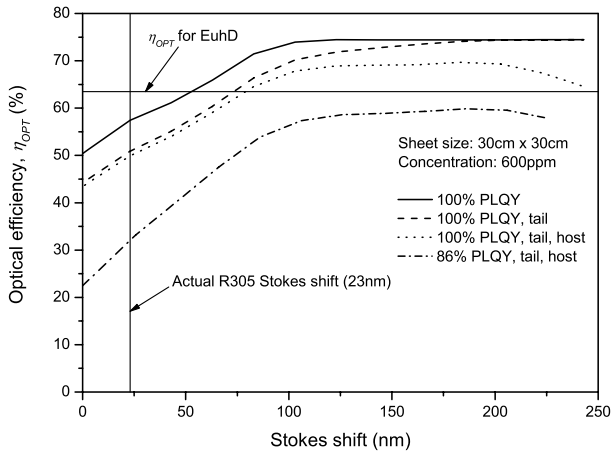

Figure 5.15: Simulated η_{OPT} for a 30 cm x 30 cm sheet containing hypothetical dyes with different Stokes shifts, showing the effects of tail absorption, host absorption and PLQY. Graphs shown are for: dye PLQY of 100 % with no tail or host absorption (solid line), dye PLQY of 100 % with tail absorption included but no host absorption (dashed line), dye PLQY of 100 % with both tail and host absorption included (dotted line), dye PLQY of 86 % with both tail and host absorption included (dash dot line). The horizontal line indicates the value of η_{OPT} for the MO49 complex. The vertical line at 23 nm denotes the Stokes shift of the real Rot 305 dye.

presence of an extremely low-magnitude tail, again demonstrates the importance of measuring the tail absorption if accurate predictions are to be made of the optical efficiency.

Inclusion of the host absorption (dotted curve ····· in Fig. 5.15) has the greatest effect at Stokes shifts above 70 nm, corresponding to peak emission wavelengths above 650 nm, where the PMMA begins to show absorption. It leads to almost a 5 % decrease in η_{OPT} at a Stokes shift of 200 nm. The two small troughs at Stokes shifts of 150 nm and 220 nm are due to the peak emission wavelength coinciding with the absorption peaks of PMMA at 730 nm and 800 nm (caused by CH and CO bond absorption[36]). However, host absorption has little effect on η_{OPT} near Stokes shifts of 23 nm, where the Rot 305 dye actually emits. This is encouraging, as it suggests that host absorption is not a concern in LSCs which use Rot 305 as the final emitter. For compounds which emit further into the red/infrared, host absorption will have a larger effect.

Under these conditions (100 % PLQY, tail and host absorption both included) which correspond to those found in an actual LSC module, η_{OPT} for the (real) Rot 305 dye is 50 %. This is less than η_{OPT} for the MO49 complex (64 %). Although the latter has

a much lower PLQY, this is compensated for by the total absence of re-absorption in the complex. The complex performs better than the organic dye for Stokes shifts up to 50 nm, above which the re-absorption losses of the dye decrease sufficiently to result in a higher η_{OPT}.

It is important to note that η_{OPT} for the Rot 305-doped 30 cm x 30 cm sheet is much higher than the P_0 value calculated from the average pathlength inside the sheet. For a 30 cm x 30 cm sheet, the average optical pathlength is approximately 15.5 cm, determined from simulations, which corresponds to an $OD_{eff} \approx 400$ at a Rot 305 concentration of 600 ppm. Referring to Fig. 5.7, the corresponding P_0 value at this OD_{eff} is $P_0 = 18\,\%$, considerably lower than the value of $\eta_{OPT} = 50\,\%$. η_{OPT}, however, describes the percentage of photons detected at *any* location on *any* edge. This is in contrast to the point excitation/detection method used to determine P_0 where photons from secondary and subsequent emission events lack a direct path to the detector and will not generally contribute.

To demonstrate how critical a high PLQY is for the organic dyes, we now consider the effect of reducing the quantum yield to 86 %, the same as the MO49 complex (dash-dot curve **-·-** in Fig. 5.15). The effect this has on η_{OPT} is dramatic; at a Stokes shift of 23 nm, it decreases to only 32 %. Thus, a small change in PLQY is magnified by the multiple re-absorption/re-emission events which occur in the sheet.

Fig. 5.16 shows the same simulations as in Fig. 5.15 but performed on a 10 cm square sheet containing 210 ppm of either hypothetical organic dye or MO49 complex. The effects of re-absorption, host absorption and PLQY are less pronounced because of the lower dye concentration and shorter pathlengths, but they still exist. MO49 still performs better than Rot 305.

The experimental system shown in Fig. 5.3 was used to measure the values of η_{OPT} for 10 cm square sheets containing Rot 305 or MO49. The measured value of 60±3 % obtained for a sheet containing Rot 305 is shown in Fig. 5.16 and is in good agreement with the calculated value. The value of η_{OPT} for the MO49 sheet was 65±3 %, which is also in good agreement with the calculated value of 64 %.

The error bars on the experimental measurement are due to both the difficulty in

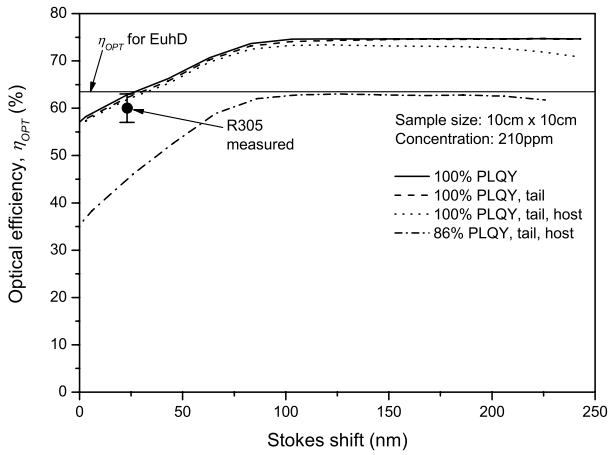

Figure 5.16: Simulated (lines) and measured (black circles) η_{OPT} for a 10 cm x 10 cm sheet. For description of each curve, see caption of Fig. 5.15

correcting for the slight non-uniform thickness of the sheet (∼5 % corner-corner) and the noise in the low signal level from the spectrometer (the spectrometer slits had to be set very narrow when the fibre was measuring the incident light and these slit settings must be kept for the edge measurements as well). Although not shown, four other concentrations of sheets (70 ppm, 197 ppm of Rot 305 and 110 ppm, 146 ppm of MO49) were also measured and they, too, exhibited good agreement with simulated values (within 2 %).

5.4 Conclusions

Studies of the fluorescence spectra measured from the end of strip samples of LSC material containing organic dyes show the presence of re-absorption. Most re-absorption occurs over the first few centimeters of pathlength, with subsequent re-absorption mainly caused by the low-magnitude absorption tail of the dye. The losses from re-absorption are significant - only 30 % of initial photons survive a pathlength of 5 cm through a 393 ppm Rot 305 sample.

The end-emitted fluorescence spectra were also used to determine the tail absorption spectra for each of the Lumogen F organic dyes. All dyes show the presence of a tail extending several hundred nanometers beyond the end of the main absorption.

When combined with the long pathlengths present in LSC modules, the absorption tail makes a significant contribution to the loss of photons by re-absorption (as much as 15 % relative loss). Because of the many re-absorption events which occur with an organic dye, the PLQY has a large effect on the optical efficiency. Decreasing the Rot 305 dye quantum yield from 100 % to 86 % results in *halving* the optical efficiency. By contrast, rare-earth complexes such as MO49 can outperform the organic dye even though their PLQY is lower, due to the lack of re-absorption. If the absorption wavelengths of rare-earth complexes can be extended into the visible part of the spectrum, then they will be ideally suited for use in LSCs.

We are now in a position to try and determine the optimum dye mixtures and combinations which result in the highest possible module efficiency. This is studied in the next chapter.

Chapter 6

LSC design

Previous chapters have detailed the properties of a range of fluorophores and their behaviour when incorporated into an LSC module. However, it is not yet known how the efficiency of an LSC module depends on its various parameters (dye mixture & concentration, thickness, size, aspect ratio). In this chapter, we use the Monte-Carlo simulation program to study the effects of the module parameters on the efficiency. The effects of changing parameters are all highly inter-dependent. For example, the variation of efficiency with dye concentration changes depending on the module size and the variation of efficiency with aspect ratio changes with different sheet thicknesses. It is, therefore, difficult to cover all possible variations. However, the author believes that the most important dependencies have been covered here.

Althought the cost performance of LSCs has been studied before and it was concluded that they offered the possibility of generating electricity at 30-50 % of the cost of conventional PV modules[21], no detailed analysis of the cost and energy of building-integrated LSCs has been performed. The results from the ray-tracing efficiency simulations were used to calculate the cost and embodied energy at a range of different module parameters. The results suggest that it is difficult to achieve a lower cost or embodied energy than conventional PV.

6.1 Module simulations

The Monte-Carlo ray-tracing program (Section 2.4.2) was used to simulate the module efficiency, average dye interactions and average pathlength for a range of different module parameters including thickness, size and aspect ratio. The host material used throughout this section is PMMA. In addition, it is assumed that no scattering occurs within the host material.

6.1.1 Dye mixture

The first task is to determine an optimum dye mixture for the LSC sheet. The simulation program was used to calculate the efficiency of three different types of LSC modules using a wide range of different dye concentrations. The three types simulated were

- Single-sheet module using only Lumogen fluorescent dyes
- Single-sheet module with both Lumogen and NIR fluorescent dyes
- Two-sheet module with only Lumogen dyes in first sheet and only NIR dyes in second sheet

All modules were simulated without a back reflector (light transmitted by the sheet and rear escape-cone emission is lost). The effect of different types of back reflector is studied later in Section 6.1.2. Gelb 170 was not simulated, as its absorption and emission spectra are close to that of Orange 240 but has a lower quantum yield.

Table 6.1 lists the concentrations of dyes simulated for the single-sheet, Lumogen-only module. Combinations of each of these dye concentrations were taken by the program, resulting in a total of 2401 different simulated mixtures. Obviously, some of these will result in a low efficiency (for example, those with a low concentration of dyes), but it was simpler to simulate all possible combinations rather than trying to restrict the program to likely combinations. The upper limit of each dye's concentration is equivalent to an optical density of 5 in a 0.3 cm thick sheet. This is sufficient to

absorb all incident sunlight over the dye's absorption range, and there is no need to go to higher concentrations.

Table 6.1: Simulated dye concentrations for single-sheet, Lumogen-only module

Dye concentration in ppm (OD for a 0.3 cm sheet in brackets)							
Violett 570		Gelb 083		Orange 240		Rot 305	
0	(0)	0	(0)	0	(0)	0	(0)
9	(0.15)	5	(0.15)	4	(0.15)	11	(0.15)
19	(0.3)	10	(0.3)	8	(0.3)	23	(0.3)
38	(0.6)	20	(0.6)	16	(0.6)	45	(0.6)
78	(1.25)	41	(1.25)	34	(1.25)	94	(1.25)
157	(2.5)	82	(2.5)	67	(2.5)	188	(2.5)
313	(5)	164	(5)	134	(5)	377	(5)

Table 6.2 shows a portion of the simulation results for a 10cm x 10cm, 0.3 cm thick module. The results have been sorted in decreasing order of module efficiency.

The highest efficiencies are obtained from dye mixtures containing high concentrations of Rot 305 and Violett 570 dyes - addition of the other two dyes does not improve efficiency. This is because of the wide absorption range of Rot 305. At high concentrations, it can absorb sunlight over the range of wavelengths covered by the Gelb 083 and Orange 240 dyes. There is therefore no need to use them. The addition of a small amount (50-100 ppm) of Violett 570 improves the efficiency as the absorption of Rot 305 is low in the region around 370 nm and Violett 570 boosts absorption at this wavelength.

The four-dye mixture also results in an increased number of dye interactions per photon travelling inside the sheet, as short-wavelength photons must cascade through more dyes before they are emitted from the longest-wavelength dye. Therefore, there is a greater probability that photons will be re-emitted out of the sheet and lost.

The same simulations were also performed on a larger LSC sheet (60 cm x 60 cm) to see if the size of the sheet affects the optimum dye mixture. However, the results showed that the best dye mixture is still one with a high concentration of only Rot 305 and Violett 570 dyes.

Table 6.2: Simulation results for single-sheet, Lumogen-only module

	Dye concentration (ppm)				
Row #	V570	G083	O240	R305	**Efficiency (%)**
1	157	20	8	377	3.86
2	78	20	16	377	3.85
3	78	20	67	377	3.85
4	157	41	8	377	3.84
5	313	10	16	377	3.84
6	157	41	16	377	3.84
7	313	20	4	377	3.84
8	78	0	16	377	3.84
9	157	10	8	377	3.83
10	78	5	16	377	3.83
11	157	41	0	377	3.83
12	157	10	16	377	3.83
13	78	5	67	377	3.83
14	157	20	34	377	3.83
15	78	10	4	377	3.83
16	157	0	34	377	3.83
17	78	82	8	377	3.83
18	313	0	34	377	3.83
19	78	41	34	377	3.83
20	157	20	4	377	3.83
21	38	82	8	377	3.82
22	313	10	67	377	3.82
23	78	0	0	377	3.82
24	313	5	4	377	3.82
25	78	10	34	377	3.82
26	313	20	8	377	3.82
27	313	41	16	377	3.82
28	313	0	67	377	3.82
29	157	82	0	377	3.82
30	78	20	34	377	3.82
31	313	20	0	377	3.82
⋮	⋮	⋮	**Data omitted**	⋮	⋮
342	0	10	34	377	3.69
343	0	0	0	377	3.68
344	157	41	67	188	3.67
⋮	⋮	⋮	**Data omitted**	⋮	⋮
2397	0	0	4	0	0.25
2398	0	5	0	0	0.23
2399	19	0	0	0	0.16
2400	9	0	0	0	0.09
2401	0	0	0	0	0.00

The results of simulations to determine the optimum Rot 305 concentration in a Rot 305/Violett 570 mix are shown in Fig. 6.1. The sheet thickness was 0.3 cm throughout. Fig. 6.1a shows the total number of solar photons absorbed by the sheet and was obtained by applying the Beer-Lambert law to the incident solar spectrum and integrating. Results for three different Violett 570 concentrations (0, 50 & 200 ppm) are shown. Fig. 6.1b shows the variation of module efficiency with Rot 305 concentration. Results for two different module sizes, 10 cm x 10 cm and 60 cm x 60 cm, are shown to demonstrate the differences between them. Again, the results are plotted

for three different Violett 570 concentrations.

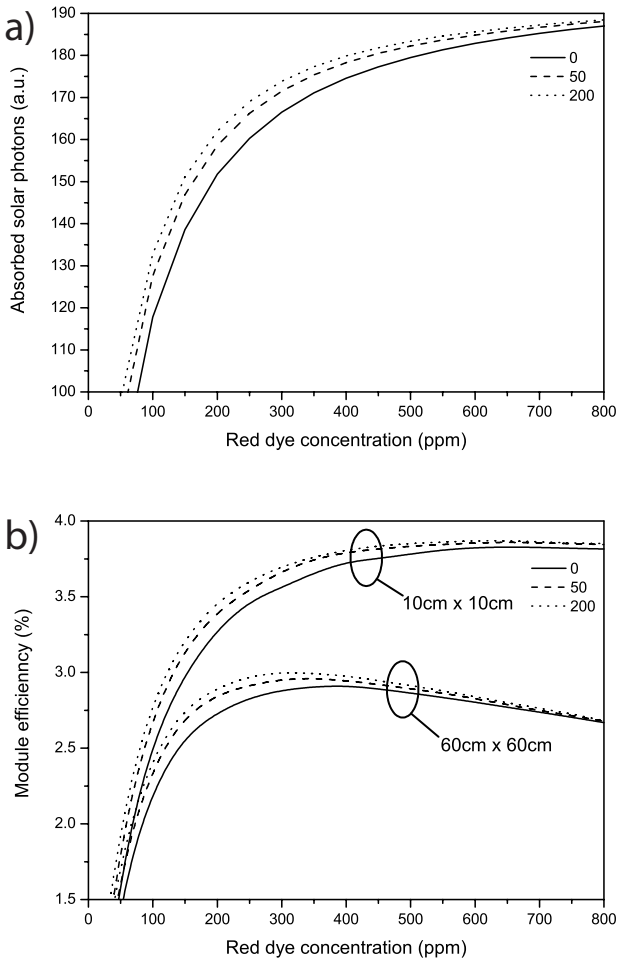

Figure 6.1: Effect of Rot 305 dye concentration on a) total absorbed solar photons b) module efficiency. Shown at three different Violett 570 concentrations.

As Rot 305 concentration is increased, the sheet absorbs a steadily increasing number of incident solar photons, as seen from the upwards slope of the curves in Fig. 6.1a. However, the module efficiencies do not show a correspondingly steady increase, despite the increasing light absorbed. The efficiencies of the 10 cm x 10 cm module show a shallow peak at ∼650 ppm and those of the 60 cm x 60 cm module peak at 300-400 ppm. Above these peaks, the efficiencies steadily decrease.

The peaking of the efficiency is a result of the balance between the number of solar photons absorbed and the re-absorption losses. Below the peak, the efficiency increases with increasing dye concentration because more solar photons are being absorbed by the sheet. Above the peak, however, the high dye concentration results in

greater re-absorption losses and these outweigh any benefit gained from absorbing a small additional number of solar photons. The efficiency then decreases with increasing concentration. Re-absorption losses are greater for larger module sizes because of the longer pathlength. The concentration which results in maximum efficiency moves to lower values as the module size is increased. This is evident from Fig. 6.1b. The effects of module size are studied in more detail later (Section 6.1.3).

The addition of Violett 570 improves the efficiency slightly, but mainly at lower concentrations of Rot 305. 50 ppm of Violett 570 is sufficient to maximise the efficiency - greater concentrations do not produce a significant improvement.

Based on these results, the Rot 305 concentration which results in the maximum efficiency over a range of module sizes would appear to be in the range 300-500 ppm. We will choose 350 ppm as a compromise between the amount of dye required and the efficiency achieved. Although there is a shift in optimum concentration with module size, 350 ppm still results in an efficiency which is close to the peak. The optimum dye mixture for a 3 mm thick sheet is then 50 ppm of Violett 570 and 350 ppm of Rot 305, resulting in an efficiency of 3.75 % for a 10 cm x 10 module. This compares favourably with the results of Slooff *et. al.*[19], who predicted an efficiency of ∼2.9 % for an LSC sheet containing 100 ppm of Rot 305. From Fig. 6.1b, we can see that the efficiency predicted here for a concentration of 100 ppm is around 2.7 %, which is a close match.

Fig. 6.2 shows the effect of the Rot 305 quantum yield on module efficiency. Three different sizes of modules were simulated (20 cm x 20 cm, 60 cm x 60 cm and 100 cm x 100 cm), all containing 350 ppm of Rot 305. The efficiency is clearly not linearly proportional to the quantum yield. The effects of a non-unity PLQY are magnified by the multiple re-absorption/re-emission events which occur within the LSC sheet. This demonstrates how important it is for a dye to have a high quantum yield if it is to perform well in an LSC. The rate of decrease is greater at higher module sizes because of the increased number of dye interactions.

Fig. 6.3 shows both the incident and transmitted solar photons for a 3mm thick sheet containing this optimum mixture of dyes. The sheet absorbs nearly all incident solar photons up to 600 nm. Some transmission occurs in the region 400-500 nm,

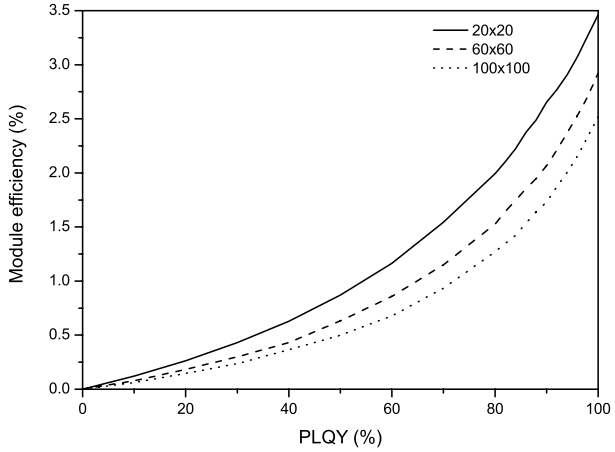

Figure 6.2: Efficiency versus Rot 305 PLQY

where absorption of Rot 305 is least. As explained before, greater dye concentrations cannot be used to increase absorption in this range because of increased re-absorption. The only ways of absorbing more solar photons are to either use a thicker sheet with the same concentration of dye, or to use a back reflector. A thicker sheet absorbs more light, but does increase re-absorption losses as both the dye concentration and pathlength are the same. A back reflector will direct unabsorbed solar photons back towards the sheet and give them a second chance to be absorbed. Both of these techniques are studied later.

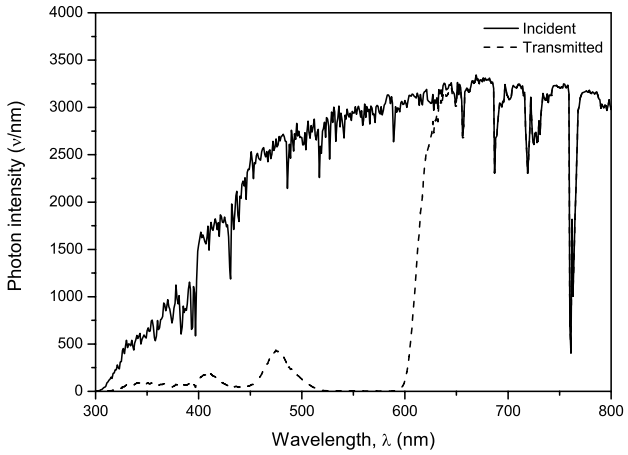

Figure 6.3: Incident and transmitted solar photons for a 0.3 cm-thick sheet containing 50 ppm of Violett 570 and 350 ppm of Rot 305.

We now look at the effect of combining one or several of the NIR-emitting organic dyes with the Violett 570 and Rot 305 dyes in the same sheet. As explained in Section 1.5.4, the motivation for this is the possibility of using the second sheet to absorb both the escape-cone losses from the first sheet and unabsorbed sunlight.

Different concentrations of the three NIR-emitting organic dyes (KF402, NIR1 & NIR3) were mixed with the optimum visible dye concentration (50 ppm Violett + 350 ppm Rot 305) in the same sheet. Sheet thickness was 0.3 cm and module size was 10 cm x 10 cm. The concentrations of the NIR dyes are listed in Table 6.3. This resulted in 216 simulations. The maximum concentrations were limited by the solubility of each dye.

Table 6.3: NIR dye concentrations for single-sheet, visible + NIR dye module

Dye concentration in ppm (OD for a 0.3 cm sheet in brackets)		
KF402	NIR1	NIR3
0 (0)	0 (0)	0 (0)
15 (0.4)	12 (0.5)	20 (0.6)
30 (0.8)	24 (1.1)	42 (1.2)
60 (1.5)	48 (2.2)	88 (2.6)
120 (3)	96 (4.3)	186 (5.4)
200 (5)	192 (8.6)	390 (11.4)

A portion of the simulation results is shown in Table 6.4. The results have again been sorted by decreasing order of module efficiency.

Perhaps surprisingly, the highest efficiency is obtained without any NIR dye present in the sheet. Even the addition of a small amount is sufficient to reduce the efficiency drastically (e.g. 15 ppm of KF402 reduces efficiency from 3.75 % to 2.31 %, a 38 % relative decrease). All of the NIR dyes strongly absorb the emission from the Rot 305 visible dye and, as a result of their poor quantum yield (even the best, KF402, is only 78 %), this strongly reduces the amount of light reaching the cells. Re-absorption losses are also greater with the NIR dyes because of their low quantum yield. A sheet was later cast with a concentration of 30 ppm of NIR3 to demonstrate this decrease.

Clearly, trying to combine a low-quantum yield NIR dye with the visible dyes in the same sheet is not a route to success. Although the NIR dye increases the amount of

sunlight absorbed by extending the absorption range of the sheet, this is not enough to overcome the effects of low-quantum yield and re-absorption.

Table 6.4: Simulation results for single-sheet, visible + NIR dye module

	Dye concentration (ppm)			
Row #	KF402	NIR1	NIR3	**Efficiency (%)**
1	0	0	0	3.75
2	15	0	0	2.31
3	0	24	0	2.15
4	0	12	0	2.13
5	0	48	0	2.09
6	15	12	0	2.01
7	30	0	0	2.01
8	15	24	0	2.01
9	15	48	0	1.95
10	30	24	0	1.91
11	0	96	0	1.90
12	30	12	0	1.89
13	0	0	88	1.87
14	30	48	0	1.87
15	0	0	186	1.86
16	0	12	88	1.84
17	15	96	0	1.82
18	15	0	88	1.82
19	0	0	42	1.81
20	15	0	186	1.80
21	0	12	186	1.79
22	0	12	42	1.77
23	0	24	88	1.77
24	30	0	88	1.77
25	15	12	88	1.77
26	0	0	20	1.75
27	30	96	0	1.75
28	0	0	390	1.75
⋮	⋮	**Data omitted**		⋮
212	200	192	186	1.18
213	200	0	0	1.16
214	200	192	0	1.16
215	200	192	42	1.14
216	200	192	20	1.10

Instead of combining the NIR and visible dyes in the same sheet, a two-sheet stacked module can be constructed with the NIR dye in a separate sheet. This has the advantage of separating the two dyes and preventing the NIR dye from affecting the emission from the Rot 305 dye.

The simulaton program was modified to model two sheets. The top sheet contained only the optimum visible mixture of Violett 570 and Rot 305 dyes. The bottom sheet contained a range of different concentrations of NIR dyes only. The concentrations are listed in Table 6.5. Sunlight strikes the top sheet first, since if it struck the bottom sheet, a large fraction would be lost because of the low-PLQY NIR dye. Both sheets

are 0.3 cm thick and 10 cm x 10 cm square, as before. The total number of simulations was 800.

Table 6.5: NIR dye concentrations for bottom sheet in a two-sheet module

Dye concentration in ppm (OD for a 0.3 cm sheet in brackets)					
KF402		NIR1		NIR3	
0	(0)	0	(0)	0	(0)
5	(0.13)	5	(0.22)	5	(0.15)
8	(0.2)	8	(0.4)	10	(0.3)
13	(0.33)	13	(0.6)	20	(0.6)
21	(0.5)	21	(0.9)	40	(1.2)
34	(0.9)	34	(1.5)	80	(2.4)
54	(1.4)	54	(2.4)	150	(4.4)
86	(2.2)	86	(3.9)	300	(8.8)
140	(3.5)	140	(6.3)		
220	(5.5)	220	(10)		

Results are shown in Table 6.6. The highest efficiency is obtained from a mixture containing a high concentration of only NIR3 dye. Addition of the other two NIR dyes does not improve the efficiency. The NIR sheet will only be illuminated with light of wavelengths above ∼600 nm, as the light below 600 nm has already been absorbed by the top sheet (see Fig. 6.3). NIR3 has the longest-wavelength absorption of the three dyes and will absorb more incident photons than either of the others. Therefore, it will result in the highest efficiency, even though its quantum yield is the lowest of the three (63 %). A concentration of 80 ppm of NIR3 would appear to be sufficient to achieve maximum efficiency.

The bottom sheet absorbs both solar photons which have been transmitted through the top sheet, and also rear escape-cone photons from the top sheet. The relative contributions of these to the increase in efficiency were determined using the simulation program by selectively choosing what "kind" of photons are absorbed by the bottom sheet - either solar photons or rear escape-cone photons. If neither kind is absorbed, the calculated efficiency is 3.75 %, identical to that of the single-sheet module, since the bottom sheet is not illuminated. If only escape-cone photons are absorbed, the efficiency is 3.91 %, a rise of 0.16 %. If only solar photons are absorbed, the efficiency is 4.46 %, a rise of 0.71 %. Finally, if both solar *and* escape-cone photons are ab-

sorbed, the efficiency is 4.62 %, a total rise of 0.87 %. This also corresponds to the values obtained in Table 6.6. From these figures, we can calculate that, of the 0.87 % total rise, 0.71 % was due to absorbed solar photons and 0.16 % was due to absorbed escape-cone photons. In relative terms, approximately 80 % of the rise came from absorbed solar photons and 20 % from absorbed escape-cone photons.

Table 6.6: Simulation results for two-sheet module

	Dye concentration (ppm)			
Row #	KF402	NIR1	NIR3	**Efficiency (%)**
1	5	8	150	4.64
2	0	0	150	4.64
3	8	8	150	4.63
4	5	0	150	4.63
5	13	0	300	4.63
6	34	0	150	4.63
7	0	21	150	4.62
8	5	0	80	4.62
9	5	0	300	4.62
10	0	13	80	4.62
11	13	8	150	4.62
12	5	5	80	4.62
13	8	5	80	4.62
14	8	0	150	4.62
15	5	5	150	4.61
16	13	13	150	4.61
17	13	0	80	4.61
18	0	13	150	4.61
19	8	5	150	4.61
20	13	0	150	4.61
21	0	13	300	4.61
22	0	5	150	4.61
23	8	0	80	4.61
24	21	13	80	4.61
25	5	5	300	4.61
26	8	0	300	4.61
27	13	5	300	4.60
28	8	5	300	4.60
29	21	0	150	4.60
⋮	⋮	**Data omitted**		⋮
796	13	0	0	4.01
797	0	0	5	3.99
798	8	0	0	3.96
799	5	0	0	3.92
800	0	0	0	3.75

To conclude, the dyes and concentrations chosen for the three module types are listed in Table 6.7, along with the predicted module efficiencies. Later (Section 2.6), these modules are constructed and their performance measured under solar illumination.

Next, the effects of different types of back reflector on the module performance are studied.

Table 6.7: Chosen concentrations and predicted efficiencies for 10 cm x 10 cm modules

				Two-sheet	
		Single sheet, visible only	Single sheet, visible + NIR	Visible sheet	NIR sheet
Conc. (ppm)	Violett 570	50	50	50	-
	Rot 305	350	350	350	-
	NIR3	-	30	-	80
Predicted efficiency		3.75 %	1.85 %	4.62 % (combined)	

6.1.2 Back reflector

It was mentioned in Section 6.1.1 that a planar back reflector placed behind the LSC sheet could be used to improve the efficiency. A back reflector achieves two goals. First, it directs unabsorbed sunlight back towards the sheet, effectively doubling the pathlength over which the light can be absorbed. Second, it also directs rear escape-cone fluorescence losses back into the sheet where they can be re-absorbed.

Two different kinds of back reflector are studied here and their relative effects on module performance explained. We will first consider a specular reflector, where light is reflected back at the same incident angle. Later we study a diffuse reflector. All LSC sheets are 0.3 cm thick and are 10 cm x 10 cm square and contain 50 ppm Violett 570 + 350 ppm Rot 305.

A feature of the simulation program is that it can distinguish between different types of photon - whether a particular photon is a fluorescence photon emitted by a dye, or whether it is an incident solar photon. This enables the creation of selective back reflectors which can, for example, reflect solar photons but not fluorescence photons. This allows the individual contributions of each to the relative efficiency to be studied.

We first show the simulation results of various reflectors that selectively reflect different types of photons. These are shown in Table 6.8. Data for a module without a back reflector are shown for comparison. "Detected photons" is the total number of photons absorbed by the solar cells attached to the edges of the sheet. "Relative photons" are again the total detected photons, but normalised to the sheet with no back reflector. The total number of initial solar photons simulated was 2,000,000. Because the efficiency of the module is not linearly proportional to the amount of light absorbed by the sheet (cells operate more efficiently at higher intensities), the number of detected photons is a more useful indication of the amount of photons absorbed by the sheet.

The reflector "New escape cone only" was created to reflect only those rear escape-cone photons which have not *already* been reflected by the back reflector. When a rear escape-cone fluorescence photon is reflected back into the sheet, it is possible that it is re-absorbed and then re-emitted back out the rear escape cone and strikes the rear

Table 6.8: Simulation of specular back reflectors

	Reflector	Efficiency (%)	Detected photons	Relative photons
1)	None	3.75	344,716	1.000
2)	New escape cone only	3.89	354,712	1.029
3)	All escape cone only	3.88	357,126	1.036
4)	Solar only	3.99	366,088	1.062
5)	All photons	4.17	380,566	1.104

reflector again. The number of times this happens cannot be calculated analytically. In order to compare the simulation with values obtained from the Beer-Lambert law and the rear escape-cone spectrum, we must look only at these "new" escape-cone losses.

The efficiency is clearly increased by the presence of a back reflector. When the contributions from both solar and fluorescence photons are combined (multiplying 1.036 by 1.062) we obtain a value (1.100) which is very to close to the simulated number, 1.104, as would be expected. It is not exactly equal, since the improvement that results from reflecting fluorescence photons is greater when solar photons are also reflected (more absorbed solar photons result in greater escape-cone losses). A better approximation can be obtained by first calculating the relative increase obtained from fluorescence photons when solar photons are also reflected as follows. The *absolute* increase obtained from fluorescence photons is 0.036. Therefore, the *absolute* increase from fluorescence photons when solar photons are also reflected is $0.036 \times 1.062 = 0.038$. The corresponding relative increase is $1 + 0.038 = 1.038$. Finally, the relative increase when both fluorescence and solar photons are reflected is $1.038 \times 1.062 = 1.103$, which is much closer to the simulated value of 1.104.

The only two mechanisms which result in an improvement in the number of detected photons when a back reflector is used are therefore reflection of unabsorbed solar photons and rear escape-cone photons. To demonstrate the validity of these figures, we will now use a combination of Beer-Lambert law and the spectra from the simulation program to obtain the same results.

The number of detected photons is directly proportional to the number of photons

(either solar or fluorescence) absorbed by the dye in the sheet. In the simulation, 2,000,000 initial solar photons were simulated incident on the surface of the LSC sheet. The number of photons absorbed by the sheet at a particular wavelength can be calculated from Eqn. (6.1). α is the combined absorption coefficient of the sheet. This accounts for surface reflection and also includes absorption of light reflected from the rear surface.

$$\nu_{absorbed} = \nu_{incident}(1 - R)(1 - e^{-\alpha x})(1 + Re^{-\alpha x}) \tag{6.1}$$

The number of transmitted photons is calculated from Eqn. (6.2)

$$\nu_{transmitted} = \nu_{incident}(1 - R)^2 e^{-\alpha x} \tag{6.2}$$

Fig. 6.4 shows both the incident, absorbed and transmitted photon spectra for a 3 mm thick sheet. The total number of solar photons absorbed by the sheet, obtained by integrating the spectrum of absorbed photons, is 563,976 (the actual magnitude is arbitrary). It is worth noting that the ratio of detected photons to absorbed photons (344,716/563,976 = 61.1 %) agrees exactly with the values of % trapped photons obtained previously in Fig. 5.16, Chapter 5.

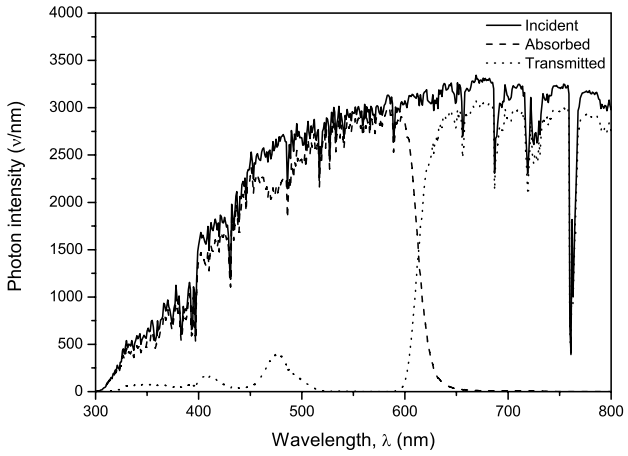

Figure 6.4: Incident, absorbed and transmitted solar photons for a 0.3 cm-thick sheet.

First, we will calculate the increase in detected photons by reflecting only the unab-

sorbed solar photons. We take the transmitted spectrum from Fig. 6.4 and calculate the number of absorbed photons when it is passed back through the 3 mm sheet. Fig. 6.5 shows the incident, absorbed and transmitted spectra for the second pass through the sheet. By integrating the curves again, we can calculate that a total of 34,893 additional photons are absorbed. This brings the total number of absorbed photons to 598,869.

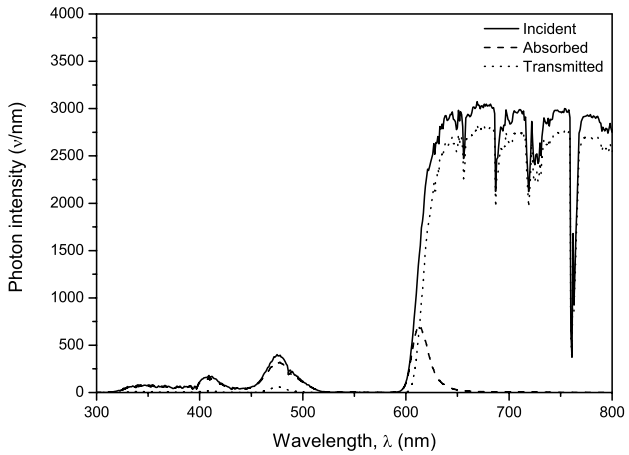

Figure 6.5: Incident, absorbed and transmitted solar photons on second pass through 0.3 cm sheet.

The spectrum of rear escape-cone losses can now be used to calculate the number of photons absorbed when they are reflected back through the sheet. In order to calculate the absorbed photons, we need to know the pathlength through the sheet. It will not be 3 mm, as the photons will be distributed at random angles within the escape cone. The greatest pathlength possible is $3 \times cos(\theta_C) \approx 4$ mm. As an average value, we will use 3.5 mm.

Fig. 6.6 shows the incident, absorbed and transmitted photons for rear escape-cone losses directed back towards the sheet. The pathlength chosen is 3.5 mm. Integrating again, we obtain the additional number of photons absorbed to be 16,338. We obtain the total number of photons absorbed by the sheet when only escape-cone photons are reflected to be $16,338 + 563,976 = 580,314$.

A summary of the total absorbed photon numbers calculated for the different back reflectors is shown in Table 6.9.

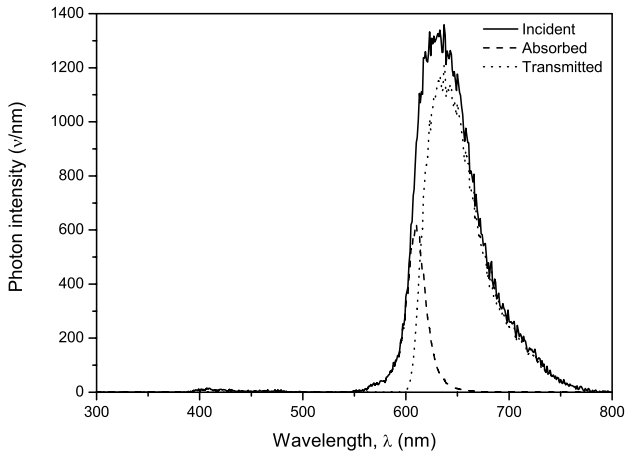

Figure 6.6: Incident, absorbed and transmitted escape-cone photons. Pathlength 3.5 mm.

Table 6.9: Calculated absorbed photons for specular reflectors

	Reflector	Absorbed photons	Relative photons
1)	None	563,976	1.000
2)	New escape cone only	580,314	1.029
3)	Solar only	598,869	1.062

If we compare the relative photon ratios in Table 6.9 with those in Table 6.8, we can see that there is exact agreement between corresponding values. We have thus demonstrated the causes of the improvements in efficiency obtained when using a specular back reflector.

We now turn our attention to a diffuse back reflector, where photons are reflected in a totally random direction, distributed evenly over a hemisphere. A diffuse reflector should, in theory, increase the amount of solar photons absorbed (compared with a specular reflector) because the reflected photons will experience longer pathlengths inside the sheet. It will not improve the re-absorption of reflected escape-cone losses, as these were already directed at random angles.

Table 6.10, in the same format as Table 6.8, shows the simulated number of detected photons for different selective diffuse back reflectors. Note that, as a diffuse reflector will reflect solar photons directly on to the cell and give a spuriously high number, only fluorescence photons have been detected here.

Table 6.10: Simulation of diffuse back reflectors (only fluorescence photons detected)

	Reflector	Efficiency (%)	Detected photons	Relative photons
1)	None	3.75	344,716	1.000
2)	New escape cone only	3.85	354,712	1.029
3)	All escape cone only	3.88	357,125	1.036
4)	Solar only	3.99	366,778	1.064
5)	All photons	4.15	380,221	1.105

If we compare the relative improvements with those in Table 6.8, we can see that there is hardly any change in the values. There is no change in the improvement obtained when escape-cone photons are reflected. This is expected - as explained above, the escape-cone photons are already randomly directed so a diffuse reflector has no effect on their average pathlength inside the sheet. There is a slight increase in the improvement when solar photons are reflected (1.064 instead of 1.062). This is also expected - although a diffuse reflector increases the pathlength that solar photons will experience when travelling back through the sheet, the increase is small (from 3 mm to ∼3.5 mm). In addition, larger incident angles on the back surface will also result in a higher reflection loss, which counterbalances the larger pathlength achieved in the sheet. The Fresnel reflectance averaged over all incident angles is around 15 %, compared with 4 % for normal incidence.

Therefore, as far as the number of detected fluorescence photons is concerned, there is no benefit in using a diffuse reflector instead of a specular one.

The relative increase obtained when all photons are reflected, 10 %, is in exact agreement with the results obtained by Debije *et. al.* when studying the effect of a diffuse reflector on photon transport inside a strip LSC sample[28].

However, if diffuse and specular back reflectors are compared in practice, it is found that the diffuse reflector does result in a greater module efficiency than the specular (by about 10 %, Section 7.1). This is not due to any greater number of solar photons absorbed by the LSC sheet, but arises from incident solar photons being reflected directly on to the cells by the diffuse reflector. The light path is shown in Fig. 6.7.

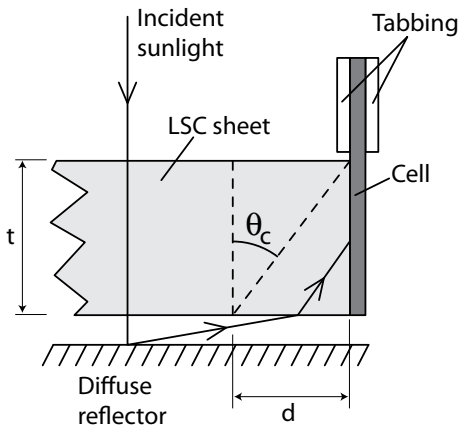

Figure 6.7: Incident solar photons directly reflected on to edge cell.

If *all* photons incident on the cells are detected, i.e. both solar and fluorescence photons, the simulated efficiency is 4.45 %. When the dye is removed from the sheet (i.e. a clear piece of PMMA), the efficiency is still 0.44 %. This efficiency is due entirely to solar photons which were scattered from the diffuse back reflector on to the cells. This effect has been used by previous reserachers to create "non-luminescent" concentrators[294, 295, 296].

Although this effect is certainly desirable, it should not be relied upon to create a high module efficiency. The reflected solar photons which contribute to this must originate from a narrow strip near the edge of the sheet, as shown in Fig. 6.7. Photons must strike the sheet within the distance d of the edge. d is related to the critical angle and the thickness of the sheet by $d = t \times tan\theta_c$, where t is the thickness of the sheet. For a 3 mm thick PMMA sheet, this is about 2.7 mm. Because of the narrow width of the originating region, the presence of any object over this region (for example, a solar cell mounting clip, Section 2.6.2, or a mirroring strip, Section 2.6.2) can almost totally block this light from reaching the cells. This was observed in practice (Section 2.6.4) on a module which had 4 mm wide mirrored strips on the surfaces of the sheet near the edges. The benefit of a diffuse reflector was greatly reduced.

When the planar dimensions of the LSC sheet are comparable to this distance d, a diffuse reflector will result in an extraordinarily high efficiency, possibly giving the false impression of the LSC sheet having a high optical efficiency. Care must be taken to distinguish between the effects. The relative contribution of such directly-detected

solar photons to the overall efficiency is shown in Fig. 6.8 where it is plotted against sheet size for three different thicknesses. As the size of the LSC sheet is decreased, the contribution from solar photons rises sharply. The contribution is also larger for thicker sheets, since d is correspondingly larger. The size of the contribution is significant at small dimensions. For example, Goldschmidt *et. al.*[20] published data on a LSC with dimensions 2 cm x 2 cm square and 0.6 cm thick. In this size, the contribution from solar photons is nearly 40 %. Therefore, although they measured an overall module efficiency of 6.7 %, the actual efficiency due to proper "LSC action" alone (i.e. fluorescence) is only around 4 % (60 % of 6.7 %). Similarly, in the device studied by Slooff *et. al.*[19], which had dimensions 5 cm x 5 cm square by 0.5 cm thick, around 20 % of the total efficiency is due to directly-detected solar photons. This is in agreement with the authors' figures of 25-30 %[19], although this includes a contribution from the addition fluorescence photons generated by the second pass of sunlight through the dyed sheet.

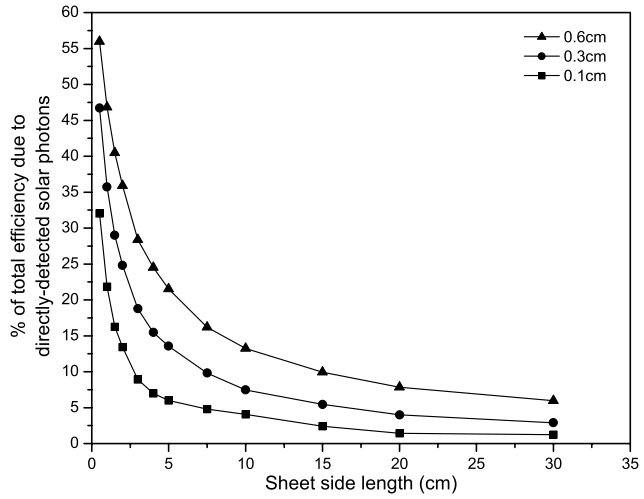

Figure 6.8: Contribution to total module efficiency from solar radiation reflected from the back reflector directly on to the solar cells. Square sheet, data shown at three different sheet thicknesses. Dye mixture: 50 ppm Violett 570 + 350 ppm Rot 305.

In practice, it may actually be more convenient to use a diffuse reflector rather than a specular one. For example, a specular reflector would require a sheet of mirror-coated plastic or glass, with the associated processing costs of the mirroring. By contrast, a diffuse reflector could consist of any matt white plastic sheet, for example uPVC or white foam-PVC board, both of which are less expensive than a specular reflector.

Nothing is lost by using a diffuse reflector, and there may be a gain if there are still reflected solar photons reaching the cells directly.

We now turn our attention to the effects of module size, shape and thickness on overall efficiency.

6.1.3 Module size and shape

The physical dimensions of the module will obviously have an effect on the efficiency. Larger modules generally lead to an increase in re-absorption losses and a corresponding reduction in efficiency. Host absorption losses also increase with size, although they remain small in the visible region (around 0.5 % of the incident power for a 60 cm x 60 cm sheet, shown later in Fig. 6.18). The effects of thickness, sheet size and aspect ratio on efficiency, average dye interactions and average pathlength are studied.

Effect of thickness

It was mentioned earlier (Section 6.1.1) that a thicker sheet could be used to absorb more incident sunlight and hence improve efficiency. The thickness of the sheet affects both the amount of sunlight absorbed and also the concentration of dye required to achieve a certain optical density.

Two different sizes of square modules were simulated - 10 cm x 10 cm and 60 cm x 60 cm. Dye concentrations were either kept constant at 50 ppm Violett 570 + 350 ppm Rot 305 or were varied inversely with the sheet thickness to maintain a constant OD. In the latter case, the concentrations were chosen to achieve 50 ppm Violett570 + 350 ppm Rot 305 at a sheet thickness of 0.3 cm. For example, a 0.6 cm thick sheet would then contain 25 ppm Violett 570 + 175 ppm Rot 305. No back reflectors were used. Sheet thicknesses ranged from 0.05-1.5 cm. Figs. 6.9, 6.10 & 6.11 show the variation of module efficiency, average dye interactions and average pathlength with sheet thickness, respectively.

We first consider the case of constant dye concentration. As the thickness is increased, module efficiency similarly increases. Although the absolute magnitudes of the effi-

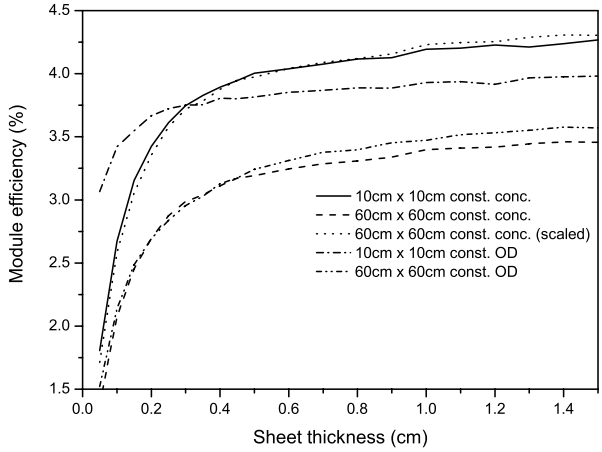

Figure 6.9: Module efficiency versus sheet thickness.

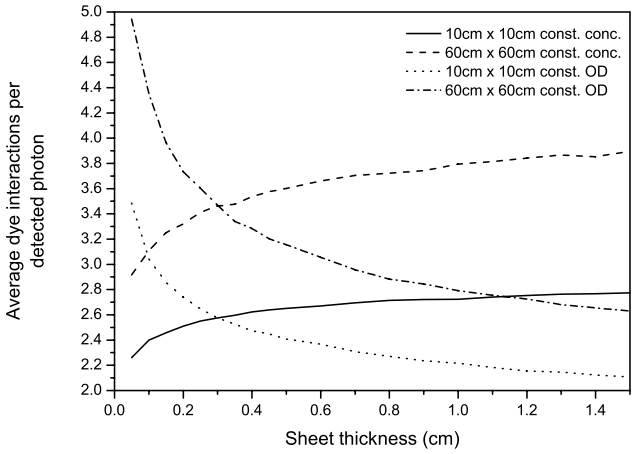

Figure 6.10: Average dye interactions versus sheet thickness.

ciencies of the two different sheet sizes are different, the relative improvements with increased thickness are the same, as can be seen by scaling the efficiency of the 60 cm x 60 cm module to match that of the 10 cm x 10 cm module. The curves shown in Fig. 6.9 are nearly identical (compare ▬ with ▪▪▪▪▪). This increase in efficiency is due to the sheet absorbing an increased number of solar photons - since the dye concentration is constant, the optical density of the sheet will increase at greater thicknesses.

As the thickness is increased, both the average dye interactions per photon and average pathlength remain relatively unchanged, as would be expected (Figs. 6.10 & 6.11). Although larger thicknesses result in a greater distance along the ray's path between

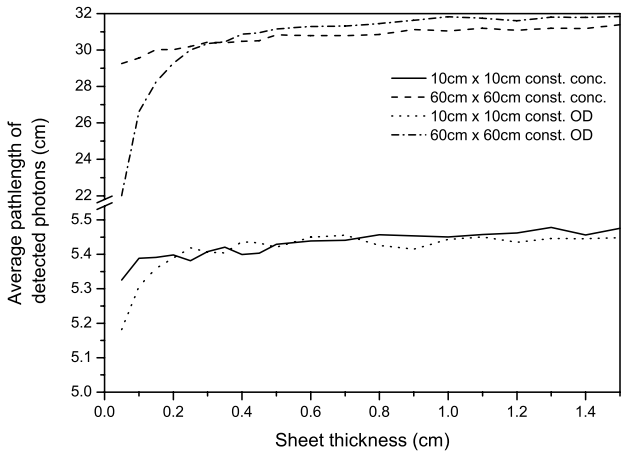

Figure 6.11: Average pathlength versus sheet thickness. Note split in vertical axis.

reflections, the number of reflections decreases to keep the total pathlength constant. Therefore, the amount of re-absorption losses is independent of the thickness.

If the concentration is now adjusted along with the thickness to maintain a constant optical density, we can see that the efficiency again increases at greater thicknesses, but now the average dye interactions drop rapidly. The pathlength remains relatively constant (Fig. 6.11). At larger thicknesses, dye concentrations are lower. Since pathlength is the same, the probability of a re-absorption event occuring drops, reducing the number of dye interactions. In the case of the 10 cm x 10 cm module, the efficiency increase obtained with constant OD is less than that with constant concentration. For the 60 cm x 60 cm module, they are roughly the same. Average pathlengths are again constant, except for small thicknesses. This is because the extremely high dye concentration required at these thicknesses results in greater re-absorption losses. Photons are therefore more likely to be detected with shorter pathlengths. This effect is more pronounced in the larger module because of the larger pathlength.

The improvement achieved by using a thicker sheet is not great. For example, the efficiency of the 60 cm x 60 cm module increases from 2.95 % at 0.3 cm thick to 3.31 % at 1 cm thick. The same improvement can be achieved by using the thinner sheet and adding a back reflector. Using thick sheets (∼1 cm) in a module is impractical because of the weight of the LSC sheet and the high cost and embodied energy. These results are in agreement with those obtained by Roncali *et. al.*[297] and Heidler[298]

who both observed an increase in efficiency with thicker LSC sheets.

Effect of size

We can now study the effects of module size on performance. We confine ourselves to square modules for the present - the effects of aspect ratio on rectangular modules are studied later. All sheets, unless stated otherwise, are 0.3 cm thick and contain the optimum mixture of 50 ppm Violett 570 + 350 ppm Rot 305. No back reflectors were simulated.

The first graph, Fig. 6.12, is a more detailed version of Fig. 6.1. It shows the dependence of module efficiency on Rot 305 concentration at a range of different module dimensions, from 10 cm x 10 cm to 140 cm x 140 cm. The progression of the optimum dye concentration to lower values at larger dimensions is clearly shown. This is a result of achieving a balance between absorbing sufficient solar photons and minimising the re-absorption losses. The decay of efficiency above the peak is faster at larger module dimensions, again a result of increased re-absorption loss. Although there is a shift in the optimum concentration, the peaks are shallow and the optimum concentration chosen (350 ppm) results in near-peak efficiency for all module sizes.

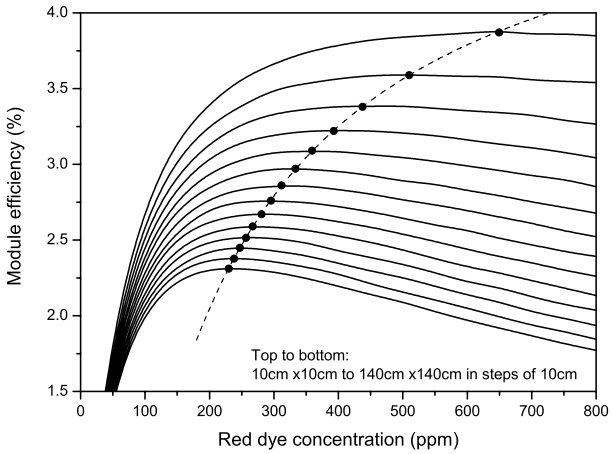

Figure 6.12: Efficiency versus Rot 305 concentration at different module sizes.

Fig. 6.13 shows both the module efficiency and average dye interactions as size is increased. Over the range of sizes simulated, the efficiency decreases from 3.85 %

at 5 cm x 5 cm to 2.25 % at 140 cm x 140 cm, while the dye interactions increase by roughly the same fraction. The drop in efficiency is due to the increased pathlength and re-absorption losses at larger module sizes. Although larger sizes are less efficient, they may result in a lower embodied energy because of the proportionately reduced amount of solar cells used (perimeter-to-area ratio is larger). This is investigated later (Section 6.2).

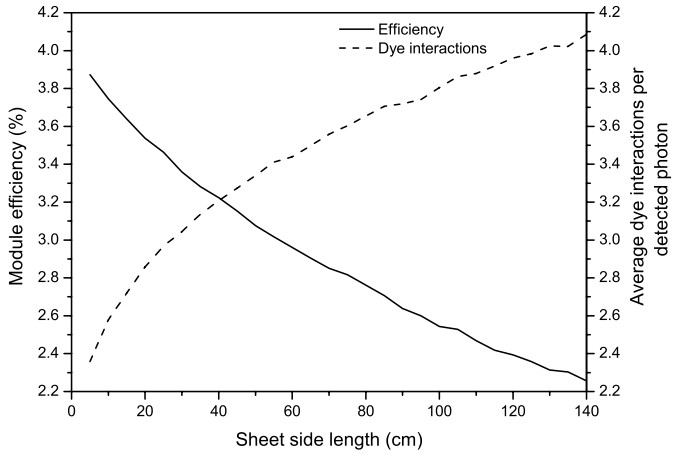

Figure 6.13: Efficiency and average dye interactions versus module size.

Module external quantum efficiency (EQE) is plotted in Fig. 6.14 for four different module sizes. This is the probability that a solar photon incident on the module generates an electron-hole pair in the solar cells. It is approximately constant over the range 300-600 nm, the absorption range of the sheet, and decreases with increasing module size in proportion to the efficiency. The troughs visible in the spectra at ∼410 nm and ∼475 nm correspond to the wavelengths where the absorption of the dye is a minimum (compare with the Rot 305 absorption spectrum in Fig. 4.1, Chapter 4 which also shows corresponding troughs). The magnitude of the EQE is comparable to that obtained by Goldschmidt *et. al.*[20] and Slooff *et. al.*[19], although their results were obtained from LSCs with a much smaller size/thickness ratio (smaller and thicker).

The concentration ratio, defined as the ratio of the short-circuit current density measured in the edge-mounted cells to that measured from a cell under 1-sun illumination, is plotted versus module size in Fig. 6.15. It is shown for four different sheet thick-

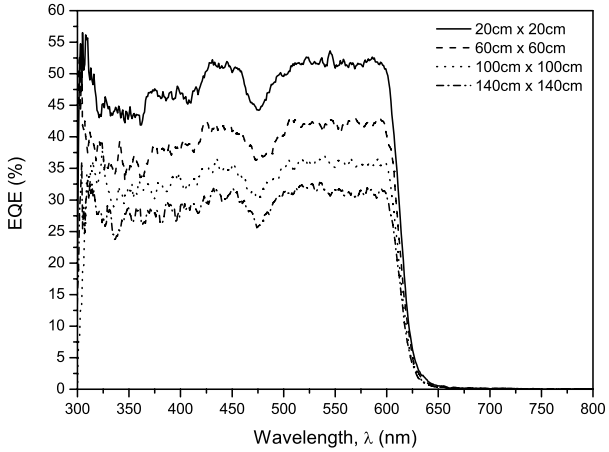

Figure 6.14: External quantum efficiency of module at four different sizes.

nesses (0.1, 0.3, 0.5 & 1.0 cm) and both with and without a back reflector. The concentration ratio increases with increasing module size and decreases with increasing module thickness. The concentration of the short-circuit current is less than the geometric concentration (ratio of surface/edge areas) because the sheet is not absorbing the entire solar spectrum and there are losses from both re-absorption and, to a lesser extent, host absorption. The large 60 cm x 60 cm LSC module described later (Section 7.2), exhibited a concentration ratio of ∼5x, close to the predicted ratio of ∼7x in Fig. 6.15.

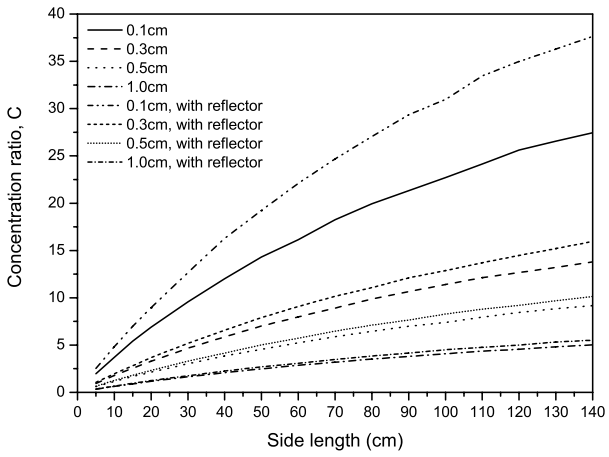

Figure 6.15: Concentration ratio (I_{SC} ratio) versus module size. Four different thicknesses shown.

At larger module sizes, cells will have to be designed to handle the higher current

density and the finger spacing on the front of the cells will decrease. This will result in higher shading losses and reduced power output. This effect needs to be balanced against the increased power available from larger modules.

Since the module is square, there will be a variation in intensity along the edges of the sheet, with a higher intensity in the middle of the edge. This is because those photons which strike the edge at a location near the corners have a longer average pathlength than those striking the middle of the edge and therefore experience higher losses from re-absorption and host absorption. Fig. 6.16 shows a two-dimensional histogram of the photon intensity at the edges of both 10 cm x 10 cm and 140 cm x 140 cm sheets. The sheet thickness was 0.3 cm. Only half of the edge length is shown, since the distribution is symmetrical about the middle of the edge. The intensity decreases at the ends of the edge to approximately 60 % of its value in the middle. Fig. 6.17 shows a cross-sectional plot of the 2D plots in Fig. 6.16 and shows the variation to be largely independent of the sheet size, although the larger sheet does exhibit a slightly lower intensity ($\sim$5 %) at the ends of the edge because of greater host absorption losses in the larger sheet. Friedman[12, 13] and Sidrach de Cardona *et. al.*[166] obtained similar results for the intensity variation along the sheet edge.

Fig. 6.16a shows a slightly increased intensity towards the front side of the sheet edge. Because of the exponential decay of the intensity of the incident sunlight as it travels through the sheet and is absorbed (a consequence of the Beer-Lambert law), more solar photons are absorbed near to the front surface. Similarly, a greater proportion of fluorescence is emitted from near the front surface. As a result, the photon intensity measured at the edge is also greater near the front surface. However, this effect is much lower with the larger sheet because the greater pathlength and number of reflections randomise the distribution of light trapped inside the LSC.

Non-uniform edge illumination can reduce the efficiency of the edge-connected solar cells[166, 167, 168], especially in a series-connected set of cells where the maximum current is limited by the cell with the lowest illumination. However, a series-connected combination is required in order to operate at a higher voltage and reduce resistive losses in the tabbing interconnections[166]. The uniformity of the edge illumination can be improved by using a polygonal sheet with a greater number of sides[170, 12, 13],

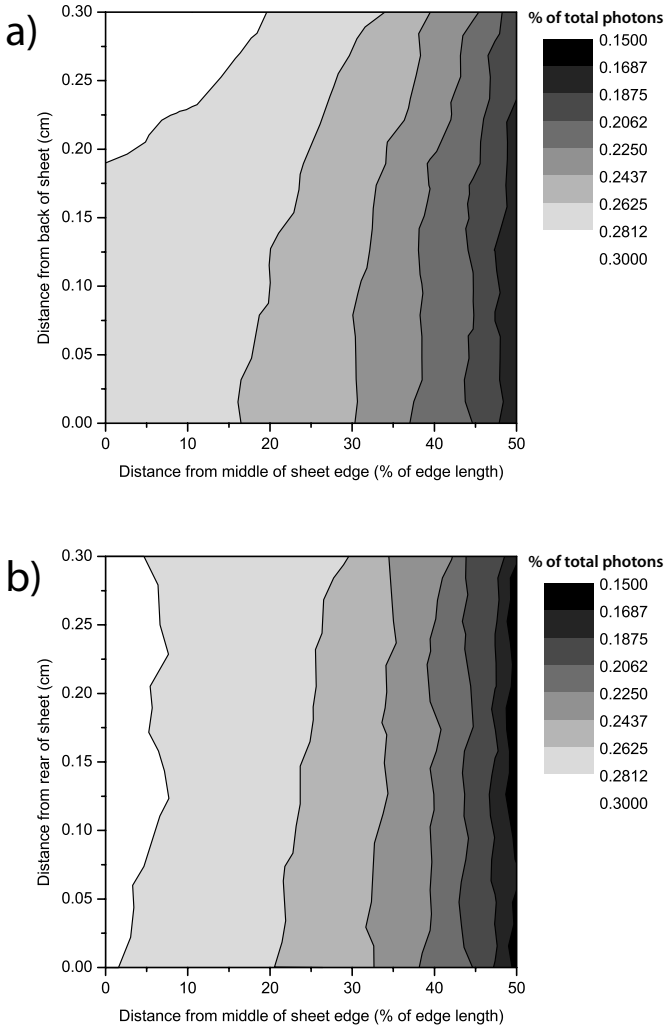

Figure 6.16: Distribution of photons at the sheet edge. Results for both a) 10 cm x 10 cm and b) 140 cm x 140 cm modules are shown. The figure, which represents half of the sheet edge, is divided into a grid of 400 squares, 20 squares on a side. The greyscale value corresponds to the percentage of the total photons which fall in that particular square.

for example hexagonal. Alternatively, as demonstrated later (Section 7.2), the cells can be current-matched by adjusting their lengths.

We now calculate a power breakdown analysis for different sizes of module. This shows the contribution each loss mechanism (for example, host absorption, escape-cone loss) makes to the total. There are, in total, seven different loss types in the module and these are described below. They are designated by their abbreviations.

RX sol. Reflected solar radiation. Because of Fresnel reflection, a portion of the incident sunlight is reflected from the front and rear surfaces of the sheet.

TX sol. Transmitted (unabsorbed) solar radiation. The absorption range of the

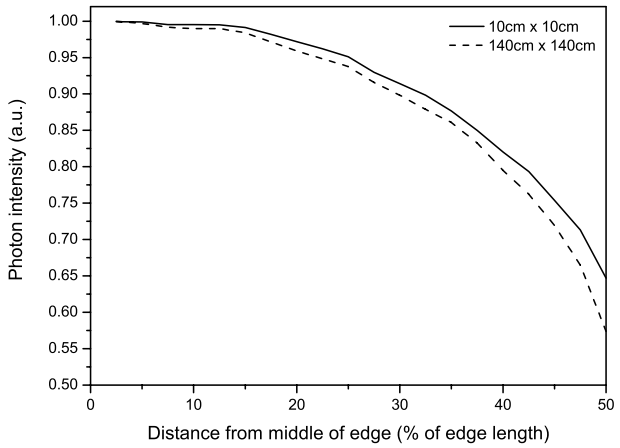

Figure 6.17: Intensity variation along length of cell. Intensity has been normalised to that at the middle of the edge.

Lumogen dyes only extends to ∼625 nm and all incident light above this is mostly transmitted (the remainder is either reflected from the sheet or absorbed by the host).

Sol. abs. host. Incident solar radiation absorbed by the host material of the LSC sheet. While not significant in the visible, it does occur in the infrared part of the incident spectrum because of the high absorption of the PMMA host at wavelengths above ∼1000 nm (see Fig. 2.14, Chapter 2). This contributes to heating of the sheet, which can in turn reduce the operating efficiency of the edge-mounted cells.

Fluor. abs. host. Trapped fluorescence absorbed by the host. Once fluorescence has been emitted by the dye and is travelling to the edges of the sheet via successive total internal reflections, some is absorbed by the host. Although the absorption coefficient of the host is small ($\sim 0.001\,\mathrm{cm}^{-1}$) at the emission wavelength, the long pathlengths can lead to several percent absorption as explained previously in Section 2.3.4.

Front esc. Front escape-cone loss. There is a ∼13 % probability (calculated geometrically from Eqn. (1.3), Chapter 1) that an emitted photon is lost into the front escape cone, and a similar probability for the rear escape cone. The magnitude of the escape-cone losses is an indication of the amount of re-absorption

occurring in the sheet.

Rear esc. Rear escape-cone loss. This is of similar magnitude to the front escape-cone loss.

Stokes. Power lost in Stokes shift of photons. Fluorescence photons are emitted at a longer wavelength (lower energy) than the corresponding absorbed photon. This fraction accounts for the energy lost in the shift in wavelength.

If the sheet contained dyes with less than 100 % quantum yield, there would be an additional loss from photons being absorbed by the dye but not emitted. However, as both the Violett 570 and Rot 305 dyes have near-unity quantum yield, this loss mechanism is absent.

All of the remaining power is absorbed by the cells and this fraction is designated by **Abs. cells**. Of the power absorbed by the cells, around 27 % is converted to electricity (calculated from the emission spectrum and the EQE spectrum of the cell). This remains constant over the size range studied, although it depends on the emission spectrum and the type of cell used.

Fig. 6.18 shows a power breakdown for a 60 cm x 60 cm, 0.3 cm-thick module with no back reflector, both as a function of the incident solar wavelength (Fig. 6.18a) and as a total, integrated over the entire solar spectrum (Fig. 6.18b).

Transmitted solar radiation contributes the largest loss of 58.7 %. Although at first glance this may seem poor, a large fraction of this comes from solar wavelengths which cannot be utilised by the dye or the cells. Referring back to Fig. 6.3, we can see that the maximum absorption wavelength of the dyed sheet is ∼620 nm. Of the 1000 W/m^2 incident on the LSC, ∼635 W/m^2 lie above 620 nm (obtained by integrating the AM1.5g spectrum) and cannot be absorbed by the dye. After the combined loss due to both reflection and absorption by the host (6.1 %+2.25 %=8.35 %), this leaves 582 W/m^2 which is transmitted by the sheet. This is in close agreement with the percentage (58.7 %) calculated by the model in Fig. 6.18. Since silicon cells can only operate efficiently with wavelengths up to about 1000 nm and there is around a 100 nm red-shift in a dye absorption/emission process, it is difficult to utilise solar wavelengths above 900 nm. If it were possible to absorb all wavelengths below 900 nm

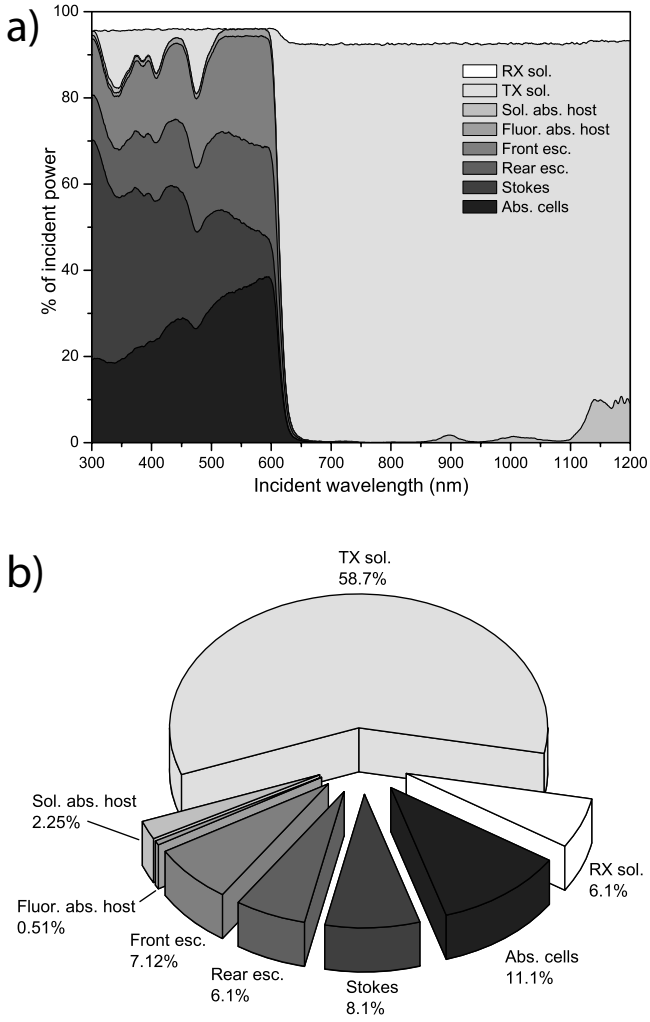

Figure 6.18: Power loss breakdown of 60 cm x 60 cm module. a) shows the breakdown per incident solar wavelength, while b) shows the total loss breakdown integrated over the AM1.5g solar spectrum.

with the sheet, the transmission loss would decrease to around 30 % (again obtained by integrating the AM1.5g spectrum). There is room for improvement in the absorption in the range 600-900 nm, but this is hampered by the poor quantum yield of dyes absorbing in this region (Section 1.5.4).

Similarly, the loss from solar radiation directly absorbed by the host material of the LSC (2.25 %) comes entirely from solar wavelengths above 900 nm where the absorption of the PMMA is strongest. This loss contributes to heating of the LSC sheet.

Little can be done to improve the reflection loss, as any coating applied to the surfaces

of the sheet interferes with the transport of fluorescence light inside.

The loss from host absorption of the fluorescence is present, but not greatly significant. It is about 5 % of the total power absorbed by the cells.

The main effect of the Stokes loss is heating of the LSC sheet. For a 1 m^2 module, this is about 80 W of heating power. When the LSC sheet is enclosed in a module with front and rear covers (to provide mechanical and environmental protection for the LSC sheet), this could cause the temperature of the sheet to rise significantly, affecting the performance of the cells. The temperature rise may have a greater effect than in a conventional PV panel, since the LSC sheet (where the heat is generated) is insulated from the atmosphere by the air spaces between it and the covers, unlike in a conventional PV panel where the glass laminate is in direct contact with the atmosphere and can be cooled by air currents. The Stokes loss cannot be reduced as it is an inherent feature of the dye emission process.

The front escape-cone loss is approximately 16 % larger than the rear escape-cone loss, which was also observed by Debije *et. al.*[67] who measured a 10-30 % greater front loss. The reasons for this are evident when the escape-cone spectra are plotted (Fig. 6.19). The main feature of the spectra is the Rot 305 emission from 550-800 nm. There is also a small amount of Violet 570 emission, shown in the enlarged inset. Comparing the two spectra, we can see that the Violet 570 emission spectrum in the rear escape cone is approximately half that in the front. In addition, the Rot 305 fluorescence in the rear spectrum shows signs of increased re-absorption as the low-wavelength end of the spectrum is reduced in intensity. First-generation fluorescence (absorption of a solar photon and emission of a fluorescence photon) is distributed more towards the front surface of the sheet, as this is where most of the incident sunlight is absorbed. Photons directed towards the rear surface therefore have a greater chance of being re-absorbed by the dye compared with photons directed towards the front. This explains both the different magnitudes and spectral shapes of the escape-cone losses[67].

The power breakdown is calculated for a range of square modules of thickness 0.3 cm ranging in size from 5 cm x 5 cm to 140 cm x 140 cm and is shown in Fig. 6.20. The losses from reflected solar, transmitted solar and host absorption of solar remain constant throughout the size range as expected. Both front and rear escape-cone losses in-

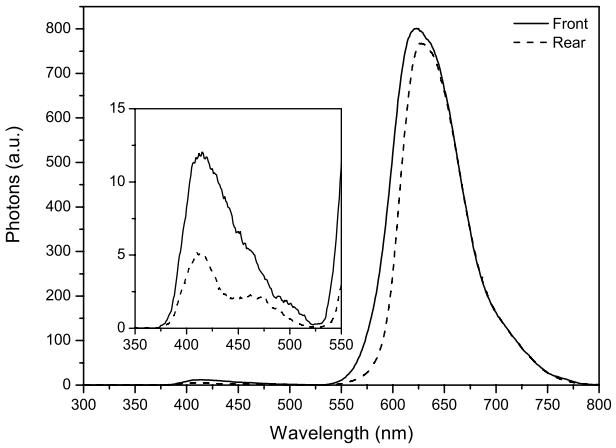

Figure 6.19: Front and rear escape-cone spectra, showing fluorescence emission from Rot 305. Inset shows Violet 570 fluorescence.

crease because of greater re-absorption losses caused by the longer pathlength. Stokes losses remain constant as they are predominantly influenced by the first-generation absorption/emission process where the energy difference between emitted and absorbed photons is greatest. Subsequent re-absorption events have a much smaller energy difference and do not contribute as much to the Stokes loss. The remaining power absorbed by the cells decreases steadily, in line with the decreasing module efficiency shown in Fig. 6.12.

Figs. 6.21 & 6.22 show the variation in both module output power and average pathlength with size. At small sizes (side lengths below about 60 cm), the output power is proportional to the square of the side length, as shown by the parabolic fit in Fig. 6.21. Also, the average pathlength scales linearly with side length, as shown by the linear fit in Fig. 6.22. Pathlength is approximately half the side length for square modules. However, at larger side lengths, neither the output power nor the pathlength follows the same progression as at small side lengths. Output power now scales linearly with side length. Pathlength still increases with increasing side length, but at a decreasing rate.

We can attribute both of these effects to the formation of a "dead area" in the centre of the LSC sheet. Photons which are generated within this dead area are farther from the edge cells, suffer greater re-absorption and host absorption losses and are less

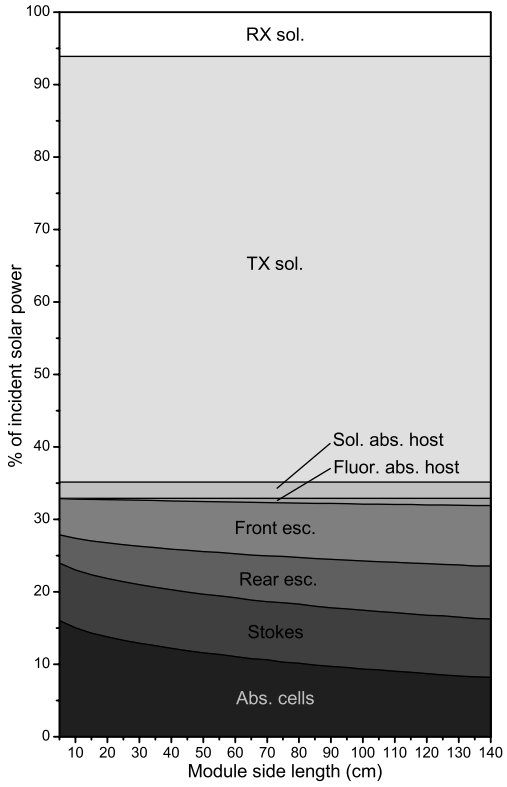

Figure 6.20: Power loss breakdown versus square module size. LSC sheet contains 50 ppm Violett 570 + 350 ppm Rot 305 and has a constant thickness of 0.3 cm.

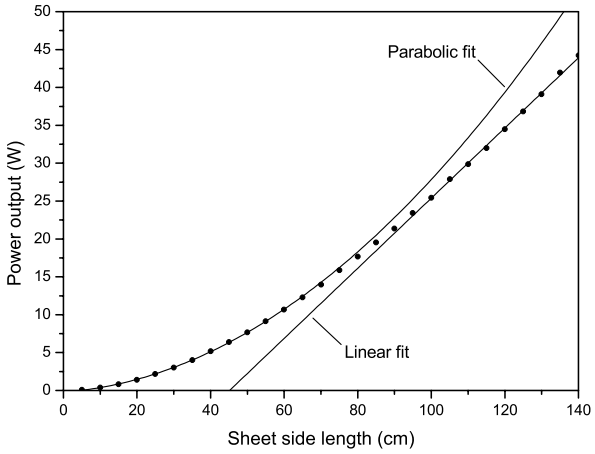

Figure 6.21: Module output power versus size.

likely to reach the edges. This is apparent from the pathlength - it is proportionately shorter than at smaller side lengths, indicating that detected photons originate from nearer the edges. Output power scales linearly with side length as it will increasingly be proportional to the sheet perimeter rather than area.

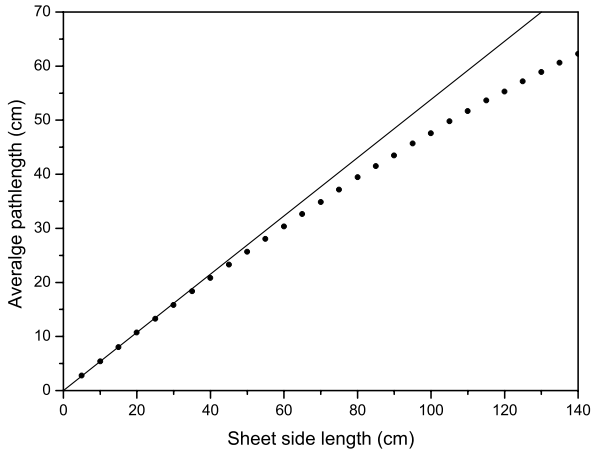

Figure 6.22: Average pathlength versus size.

To show the presence of such a dead area, we can plot a 2D histogram of the locations on the LSC's surface which result in a photon being detected at the edge. Because the LSC is four-fold symmetrical, only one-quarter of the sheet is considered. The surface of the quarter is divided into a grid of 400 squares, 20 squares on a side. Therefore, the dimension of each square is $1/40^{\text{th}}$ of the side length of the LSC. The simulation program records, for each square, the percentage of the total edge-detected photons which were generated by solar photons striking that particular square, and converts this to a greyscale value. This is a measure of how sensitive the module is to solar photons striking that particular square. Fig. 6.23 shows such a histogram for both 10 cm x 10 cm and 140 cm x 140 cm modules.

The 10 cm x 10 cm sheet (Fig. 6.23a) shows excellent uniformity across the sheet, with the sensitivity at the centre of the sheet only perhaps 5 % less than that at the edges. However, the 140 cm x 140 cm sheet (Fig. 6.23b) shows almost half the sensitivity at the centre.

Although it is obviously desirable to have as large a sheet as possible to obtain a high power output per module, the presence of a dead area becomes a significant problem at larger sizes. A possible way to reduce the pathlengths experienced by the trapped fluorescence while keeping module area (and hence collected solar power) the same is to use a rectangular sheet, as originally proposed by Weber & Lambe[8]. By making the sheet in the form of a long, narrow strip, it is possible to bring the edge cells

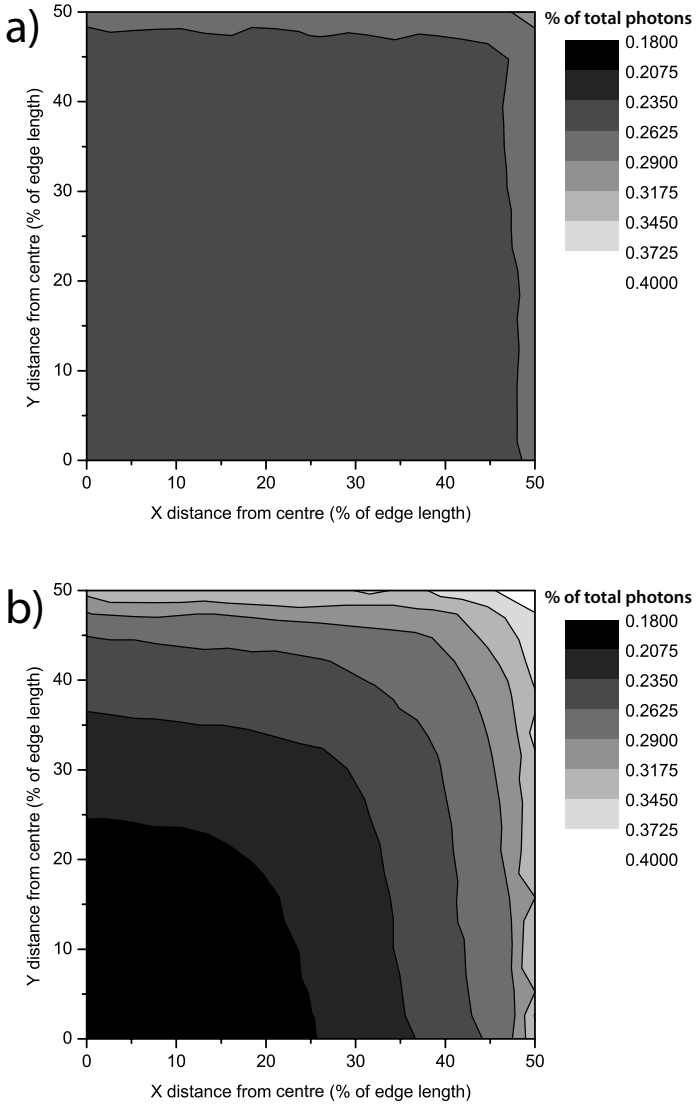

Figure 6.23: Distribution of initial photons which are detected at edge. Results for both a) 10 cm x 10 cm module and b) 140 cm x 140 cm module are shown. The figure, which represents one quarter of the LSC surface, is divided into a grid of 400 squares, 20 squares on a side. The greyscale value corresponds to the percentage of the total detected photons which originated from solar photons striking that particular square.

closer to the source of fluorescence and reduce the pathlength. We will now look at the effect of aspect ratio on module performance.

Effect of aspect ratio

We define the aspect ratio of a sheet, a, as the ratio of its length to breadth as shown in Eqn. (6.3). Given a particular sheet area, A, the length and breadth can be calculated from Eqns. (6.4) & (6.5).

$$a = \frac{l_x}{l_y} \tag{6.3}$$

$$l_x = \sqrt{aA} \tag{6.4}$$

$$l_y = \sqrt{\frac{A}{a}} \tag{6.5}$$

Five different module areas were simulated - 100, 400, 3600, 10000 & 19600 cm^2, corresponding to square module side lengths of 10, 20, 60, 100 & 140 cm respectively. The aspect ratio was varied from 0.01 to 1. Sheet thickness was constant throughout at 0.3 cm.

The variation of module efficiency, average dye interactions and average pathlength with aspect ratio are shown in Figs. 6.24, 6.25 & 6.26 respectively. Normalised versions of each of the data sets are also shown for comparison.

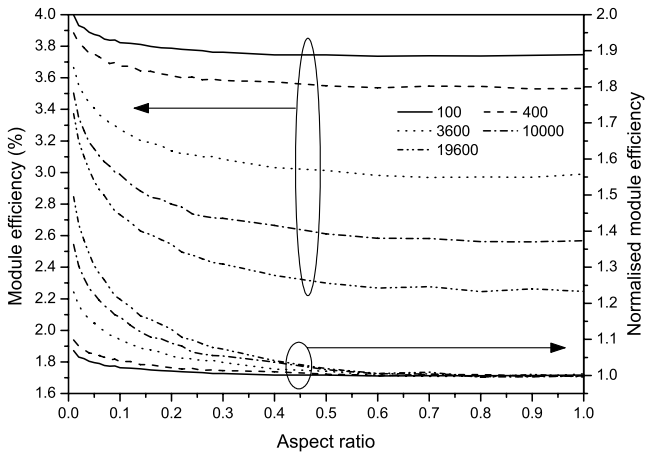

Figure 6.24: Module efficiency versus aspect ratio, shown for five different module areas. Lower set of curves is normalised to values at aspect ratio 1.

Module efficiency increases as the aspect ratio is decreased (moving towards a more rectangular sheet). The increase is greater for larger module sizes, as might be expected. However, it does not become significant until aspect ratios of less than 0.1-0.2. For example, there is only a 16 % improvement in the efficiency of a 1 m^2 sheet in going from an aspect ratio of 1 to 0.1. At this aspect ratio, the sheet has dimensions of approximately 0.32 m x 3.2 m. This is an impractical shape and size for, as an

example, a windowpane (if the LSC is to be building-integrated), because the narrow width requires a greater amount of window framing to be used to cover the same area. In addition, there is a 65 % increase in perimeter in moving to the smaller aspect ratio and a corresponding increase in the amount of silicon used in the cells around the edges. This can lead to an *increase* in the embodied energy, as studied later in Section 6.2.

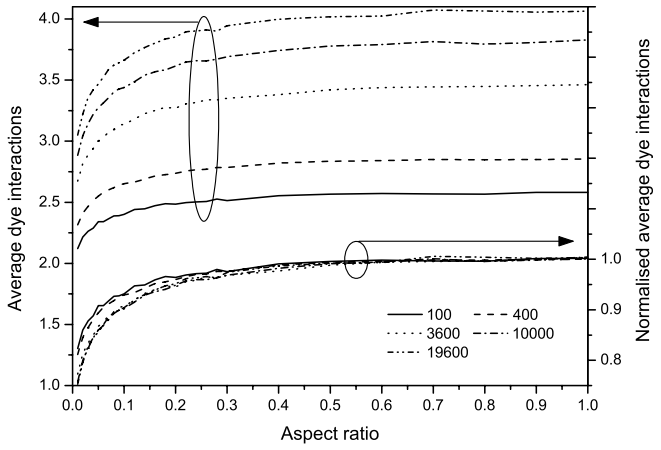

Figure 6.25: Average dye interactions versus aspect ratio, shown for five different module areas. Lower set of curves is normalised to values at aspect ratio 1.

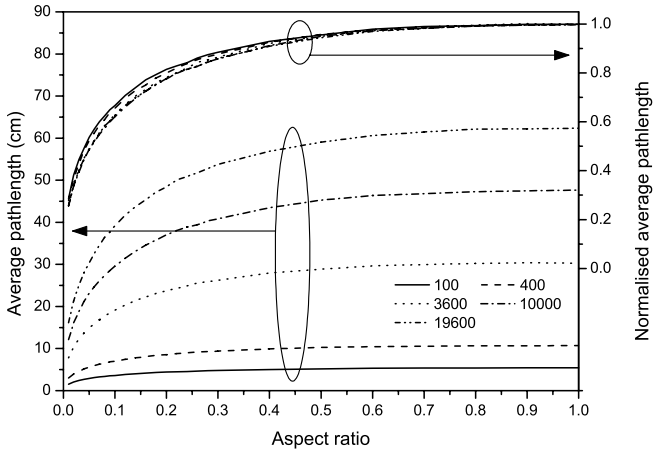

Figure 6.26: Average pathlength versus aspect ratio, shown for five different module areas. Upper set of curves is normalised to values at aspect ratio 1.

Average dye interactions and average pathlength both also decrease with smaller aspect ratios. The relative magnitude of the decrease is similar for all module sizes,

as seen from the normalised curves in Figs. 6.25 & 6.26. Although the average pathlength shows a large decrease at smaller aspect ratios, the relative decrease in dye interactions is similar to the increase in module efficiency and again does not become significant until aspect ratios below 0.1-0.2. It would appear that, although a small aspect ratio is capable of reducing the pathlength and increasing the efficiency slightly, the benefit is outweighed by the larger physical dimensions of the panel. In addition, as shown later, there is no improvement in embodied energy at small aspect ratios.

6.1.4 Minimum required PLQY of a rare-earth complex

As was seen in Chapter 5, rare-earth complexes would appear to offer the possibility of reducing the re-absorption losses within LSC sheets. However, the quantum yields of complexes which absorb in the visible and emit in the NIR (such as those containing Nd^{3+} or Yb^{3+} ions) are currently extremely low[153, 154]. It is of interest to determine the minimum quantum yield for a rare-earth complex before it achieves parity with, for example, the Rot 305 organic dye.

To determine this, a hypothetical rare-earth complex was created for use in the simulation program. Its absorption and emission spectra are shown in Fig. 6.27. The absorption spectrum has been set equal to that of the Rot 305 dye. The emission spectrum is that of the Yb^{3+} ion, from Rowan *et. al.*[154].

Simulations were then performed of three different sizes (20 cm x 20 cm, 60 cm x 60 cm and 100 cm x 100 cm) of LSC sheets containing a constant concentration (350 ppm) of the complex. The quantum yield of the complex was varied from 0 % to 100 %. The overall solar-to-electric efficiency of the module cannot be used to compare the performances of the complex and the Rot 305 dye, as the solar cell performs poorly (50 % IQE) at the emission wavelength of the complex and would give an apparently low result. Instead, the total number of fluorescence photons emitted at the edges was measured as a percentage of the total incident solar photons, thus removing the response of the solar cell. This is equivalent to assuming that the cell has 100 % EQE at all wavelengths and then recording the short-circuit current. In addition,

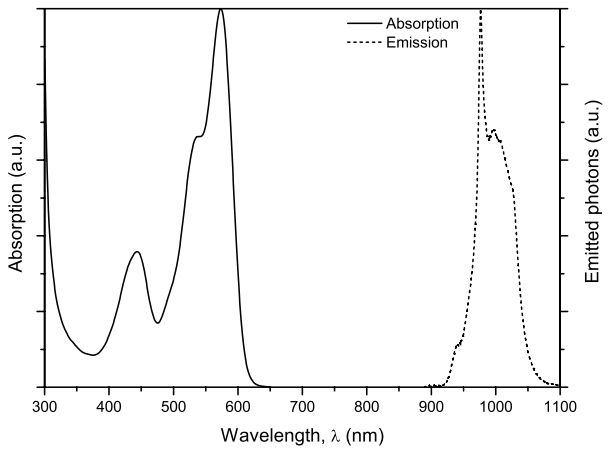

Figure 6.27: Absorption and emission spectra of artificial complex

simulations were run both with and without host absorption included. No back reflector was used in any of the simulations.

Fig. 6.28 shows the results. The percentage of photons which are emitted at the edge is plotted against the PLQY of the complex for the three different module sizes. When host absorption is not included (indicated by the line ▬), the percentage is independent of module size. However, when host absorption is included, the percentage drops significantly with increasing size (shown by the lines ▬▬, ▪▪▪▪ and ▬▪▬). The three arrows on the right-hand axis at 10.5 %, 8.5 % and 7.3 % represent the percentage of edge-emitted photons for modules containing the real Rot 305 dye of dimensions 20 cm x 20 cm, 60 cm x 60 cm and 100 cm x 100 cm, respectively.

We can see that, when host absorption is present, the complex can never perform better than the Rot 305 dye, even though its quantum yield is 100 %. This is because of the extremely strong absorption of the PMMA host in the wavelength region where the complex emits.

If host absorption is disregarded then the complex can perform better than Rot 305, but only if its PLQY is greater than a certain value. These minimum quantum yields are indicated by the dots in Fig. 6.28 and are 77 % for a 20 cm x 20 cm sheet, 62 % for a 60 cm x 60 cm sheet and 53 % for a 100 cm x 100 cm sheet.

Disregarding host absorption is a somewhat artificial case. The effects of host absorp-

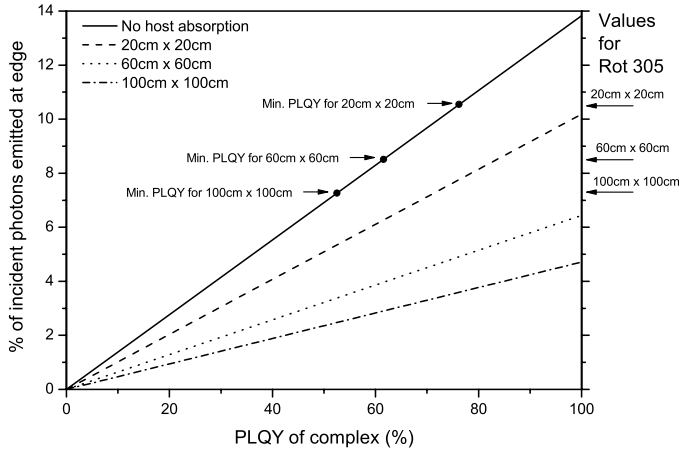

Figure 6.28: Percentage of incident solar photons emitted at the edges versus PLQY of rare-earth complex. The arrows on the right-hand axis indicate the percentages for Rot 305-doped modules.

tion could perhaps be minimised in practice by using a thin-film LSC with a substrate made from low-iron soda-lime glass, borosilicate glass or fused silica. However, this creates the problem of requiring a much higher dye concentration in the thin film and the possibility of concentration quenching, although recent results suggest that LSCs containing the Rot 305 dye still perform well at concentrations as high as 10,000 ppm, retaining around 70 % of their efficiency at low (∼300 ppm) concentrations[299]. Either way, NIR-emitting rare-earth complexes will need to exhibit quantum yields of at least ∼50 % if they are to show promise for use in LSCs.

We next look at the maximum efficiency which is achievable with an LSC using silicon solar cells.

6.1.5 Efficiency limit

Consider a hypothetical "best" dye that is capable of absorbing all solar photons below a certain wavelength, λ_{MAX}, and emitting these with 100 % PLQY at a wavelength $\lambda_{MAX} + 100$ (i.e. 100 nm separation between the maximum absorption wavelength and the emission wavelength). There is therefore zero re-absorption. This 100 nm offset was chosen as a compromise between simulating an organic dye (where the average emission wavelength occurs nearly at the same wavelength as the maximum

absorption) and a rare-earth complex (where several hundred nanometers of difference is required to achieve the necessary energy transfer)[137, 134, 113, 23, 136, 138].

Simulations were performed of the module efficiency as λ_{MAX} was increased from 300 nm to 1100 nm. Three different sizes of module (20 cm x 20 cm, 60 cm x 60 cm and 100 cm x 100 cm) were again simulated. The results are shown in Fig. 6.29 for situations both with and without host absorption included.

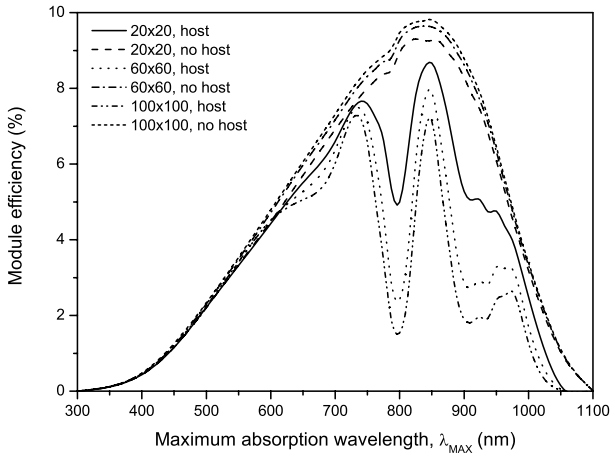

Figure 6.29: Module efficiency versus maximum absorption wavelength

When host absorption is disregarded, the maximum efficiency achieveable is 9-10 %, with a slight increase at larger module sizes. The maximum occurs at λ_{MAX}=850 nm. The decrease above this is due to the lower IQE of the LGBC silicon cell at these wavelengths. When host absorption is included, troughs appear in the efficiency at 800 nm & 900 nm, corresponding to the presence of PMMA absorption peaks at thes wavelengths. The magnitude of the troughs is large because of the extremely narrow emission bandwidth of our artificial dye (1 nm). A maximum again occurs at λ_{MAX}=850 nm, but only of 8 %. Given that the effects of re-absorption and non-unity dye PLQY will also be present in a practial LSC, a more reasonable upper limit to the efficiency would appear to be in the region of 6 %. These results are in agreement with Galluzzi *et. al.*[300], who found that an emission wavelength of 900-950 nm was optimum, and with data from General Electric[299] which also indicate that the maximum efficiency for a silicon-based LSC is in the range 6-8 %.

It should be noted that the values predicted here are much lower than those from

the thermodyanmic model of LSC operation[301, 296] since they did not account for the additional losses caused by re-absorption. Although the results expressed here are limited by the performance of the cells used, they do express a *practical* limit on the device efficiency which can be achieved with silicon cells and a PMMA host. As explained before, although other cell technologies (for example, gallium arsenide) can result in a higher efficiency, this benefit is outweighed by the extra cost of the cells themselves.

We next look at the effects of various module parameters on the cost and embodied energy, with a view to finding a configuration which minimises these values.

6.2 Cost and embodied energy

LSC devices are well-suited to use in building-integrated photovoltaics (BIPV)[57]. They can be mounted in a standard window curtain walling system, providing both light to the interior and generating electricity. Other, conventional, technologies which can also be used as windows (i.e. which are semi-transparent) are thin-film amorphous silicon modules[302, 303, 304] and glass/glass laminates[305, 306, 307, 308]. In the latter, standard full-wafer cells are laminated between glass sheets with the spaces between the cells allowing light to pass through. To determine whether LSCs are a cost-effective or energy-effective alternative to these other technologies, a comparison can be made between the cost and embodied energy of each, measured either per unit module area or per peak watt produced. Although it has been suggested recently that LSC modules can produce electricity at 30-50 % of the cost of conventional PV modules[21], there has been little analysis done specifically on building-integrated LSC modules. In this section, the cost and energy content of a range of different types of LSC modules, both bulk and thin-film, will be studied and compared to those of a glass/glass laminate. In a similar fashion to the efficiency simulations performed in Section (6.1.3), the effects of module size and aspect ratio on cost and energy will be analysed.

Only the costs and embodied energies of the material components of the modules are studied, since processing, manufacturing and labour costs are unknown and will

vary greatly between countries, especially for LSCs for which there is obviously no established manufacturing technique. It is also difficult to compare costs with amorphous silicon or other thin-film modules, as a large fraction of the cost and energy of these comes from manufacturing and processing, rather than from raw materials. However, it is possible to calculate material costs and energies for both LSC modules and glass/glass laminates and perform a comparison.

Although previous sections have focussed on LSCs based on a sheet of bulk-doped PMMA host material, we will include several additional technologies here for comparison on cost and energy grounds. In addition to PMMA, another material used for bulk-doped LSCs is polycarbonate (PC)[28]. A major advantage of PC is its greatly reduced flammability compared with PMMA[183]. Thin-film (TF) devices are also included, as they may have advantages in terms of embodied energy. We will consider here TF devices based on a layer of dyed PMMA on a glass substrate, which may be either borosilicate glass (e.g. Schott BF33[309]) or a low-iron soda-lime glass (e.g. Saint-Gobain Diamant[310] or Pilkington Optiwhite[311]), both of which have low absorption.

Although thin films can also be applied to substrates of clear PMMA or PC, they do not affect the initial cost or energy of the resulting module, since the TF can be of the same material as the substrate and has the same cost and energy density. However, they do have an effect when considering the costs of replacing the dyed sheet at the end of its life - replacing a TF costs less than a bulk sheet. Therefore, in the later analysis of the effect of dye lifetime (Section 6.2.3), thin films on PMMA and PC substrates are included.

Fig. 6.30 shows both the absorption coefficients and refractive indices of the four different host materials studied. The edge-emission spectrum of a Rot 305-doped sheet is also shown, to indicate the range over which host absorption is important. In the region of interest (600-800 nm), PMMA has the lowest absorption coefficient, followed by PC with around 5x greater absorption, and the two glasses (BF33 and low-iron) having the highest. It is therefore expected that the module efficiency will be highest with PMMA and lowest with glass substrates.

The structures of both LSC and glass/glass laminate modules used for cost and energy

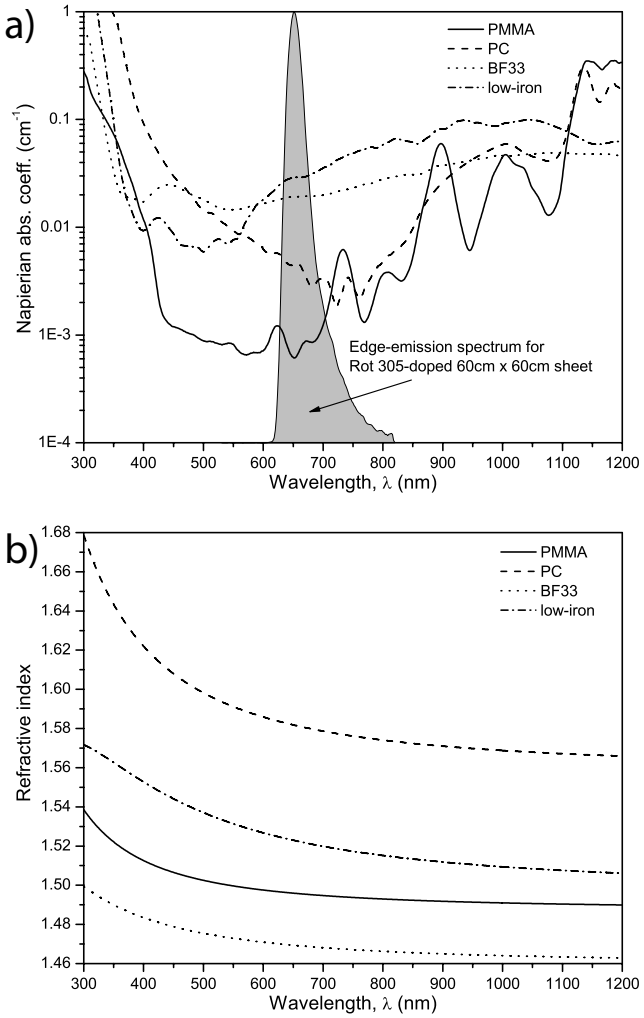

Figure 6.30: Absorption coefficient (a) and refractive index (b) for polymethylmethacrylate (PMMA), polycarbonate (PC), Schott "borofloat 33" glass (BF33) and low-iron soda-lime glass. The edge-emission spectrum of a Rot 305-doped sheet is shown for comparison.

analysis are shown in Fig. 6.31. They are described briefly below.

Both bulk and TF LSC structures (Fig. 6.31a and b) use a 6 mm-thick front cover made from low-iron soda-lime glass to achieve the highest light transmission to the LSC sheet. This cover is required to protect the LSC sheet from external weather, and also to provide structural support against wind loading. The thickness of 6 mm was chosen as this is a common thickness for curtain wall windows[312]. The front cover must be separated from the LSC sheet by an air gap; if it were directly coupled, trapped light could be lost into the front cover.

The thickness of the LSC sheet in bulk LSCs was chosen to be 3 mm, a standard

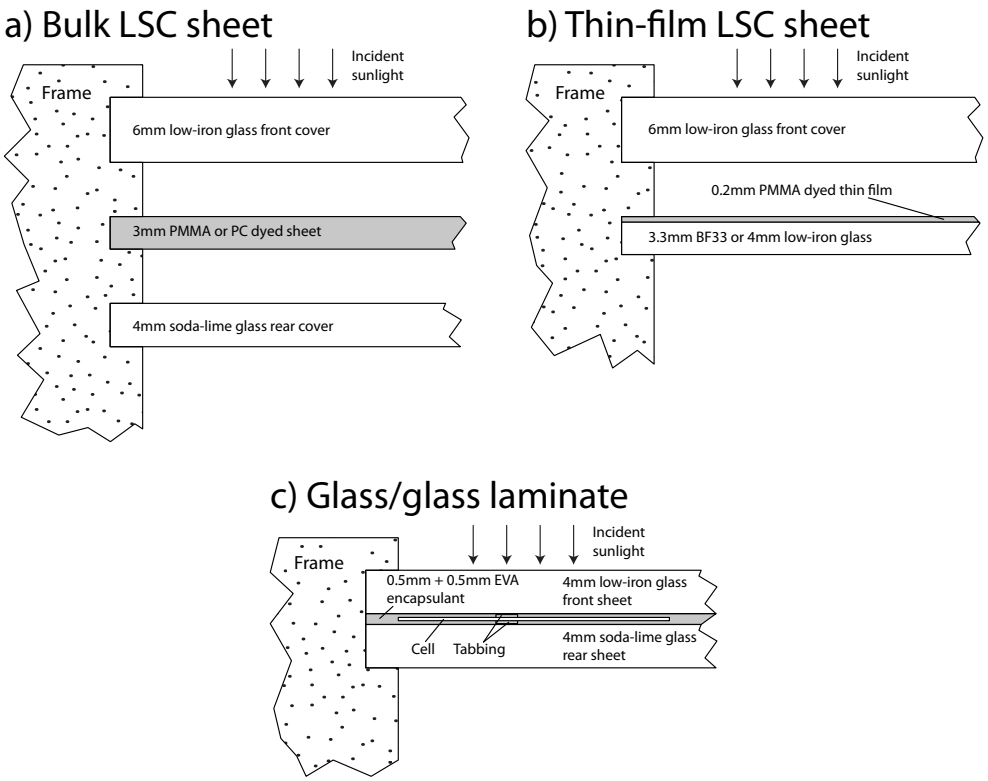

Figure 6.31: Chosen module structures and materials for a) bulk-doped LSC, b) thin-film LSC, and c) glass/glass laminate.

commercial thickness. Thicker sheets result in a needlessly high usage of material, while thinner sheets lack structural support during handling and processing. Although the optimum dye mixture was found to contain both Violett 570 and Rot 305 dyes (Section 6.1.1), it was found later (Section 7.3) that the Violett 570 dye showed poor photostability, and it was decided not to include it in the dye mixture. The Rot 305 concentration was increased to 400 ppm to compensate, resulting in an optical density of OD5.3. This dye has been shown to perform well in LSCs at concentrations as high as 10,000 ppm[299]. Therefore, for TF sheets, a PMMA film thickness of 0.2 mm was chosen, resulting in a dye concentration in the film of $(3/0.2) \times 400 = 6000$ ppm. TF substrates are either 3.3 mm-thick BF33 borosilicate or 4 mm-thick low-iron glass, both of which are commercially-available standard thicknesses.

A back cover is used to protect the rear (inside) surface of the bulk-doped LSC sheet from damage from either cleaning or dust/dirt. Since this does not need a high optical transparency (sunlight has already been absorbed by the LSC sheet), it is made from standard soda-lime window glass. The thickness is 4 mm - thinner than the front

cover since it experiences less loading stress. If the surface of the LSC sheet can be protected without affecting the transport of trapped light, for example by applying a hard coating, it is possible to dispense with a rear cover. Therefore, in the analysis of bulk-doped LSCs, modules both with and without a rear cover will be considered. TF modules do not suffer from this problem, since the LSC sheet can be oriented with the TF layer facing the front cover glass. The exposed surface on the inside is then a glass surface which is less prone to damage.

The structure of the glass/glass laminate (Fig. 6.31c) is based on the specifications for Suntech Power's "Light-Thru" module[305], although other manufacturers' designs are similar (for example, Romag's "PowerGlaz" modules[313]). Cells are laminated between front and rear cover glass. The front glass is 4 mm-thick low-iron, since it must have a high optical transparency, but the rear glass is 4 mm-thick soda-lime window glass since it does not require a high transparency. A total EVA film thickness of 1 mm (two sheets of 0.5 mm placed front and behind the cells) is chosen. By varying the spacing between the cells in the laminate, the transparency of the module can be varied, although higher transparencies will obviously result in a lower efficiency. This is shown in Fig. 6.32, where the module efficiency of a Suntech Light-Thru module is plotted versus the transparency. As expected, there is a linear variation between efficiency and transparency. It is important to note that, unlike the LSC, the glass/glass laminate has an efficiency that is independent of module size or shape.

The framing, which is common to both LSCs and glass/glass laminates, is standard extruded-aluminium curtain walling. For the analysis performed here, the "MX" range from Technal Ltd. was chosen[314]. Depending on the particular model, this can be used for both single- and double-glazing, which is relevant for LSCs.

For the purposes of calculating the cost and embodied energy of different sizes and aspect ratios, it is most convenient to determine the material costs and energies in units relevant to the particular component of the module. For example, the amount of front cover material is determined by the module area, and cost and energy should be expressed as £/m^2 and MJ/m^2. However, the number of edge cells used in the LSC is proportional to the perimeter length, therefore cost and energy for them should be expressed as £/m and MJ/m. Given a particular module size and aspect ratio,

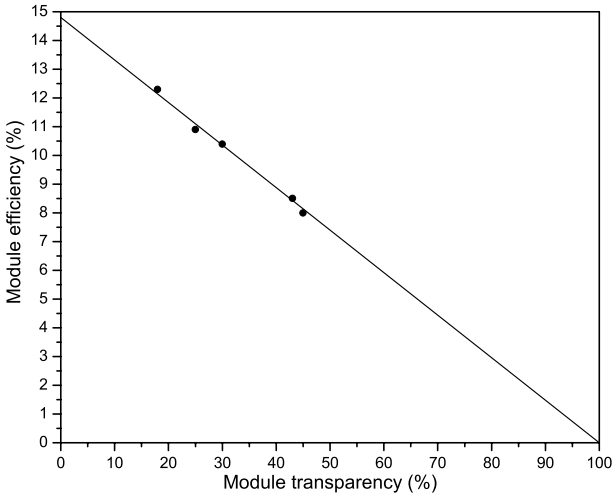

Figure 6.32: Variation of efficiency of a glass/glass laminate module with percentage transparency. Data for a Suntech "Light-Thru" module[305]. Points shown are from sample designs given in the datasheet.

it is then simple to calculate the total cost and energy by adding up those of the components. A brief description of the calculation of per-area and per-length costs and energies for all the module components is given below.

Low-iron glass Cost based on Saint-Gobain Diamant[312] (Pilkington Optiwhite is similar). Bulk prices for a 3.2 m x 2.5 m sheet: £190 for 6 mm thickness, £145 for 4 mm thickness. Costs per area are £24/m^2 for 6 mm-thick and £18/m^2 for 4 mm-thick. Glass density is ∼2.5g/cm^3 and embodied energy is 20 MJ/kg[177, 179]. Therefore, energies per area are 300MJ/m^2 for 6 mm and 200MJ/m^2 for 4 mm.

PMMA Cost based on bulk data from Lucite[315]. £2.5k/ton for bulk material. Density is 1.2g/cm^3. Costs per area are £9/m^2 for 3 mm sheet and £0.6/m^2 for a 0.2 mm thin film. Bulk embodied energy is 131 MJ/kg[180, 181]. Therefore, energies per area are 472MJ/m^2 for 3 mm sheet and 31MJ/m^2 for 0.2 mm thin film.

Polycarbonate Cost data from Gilbert Curry[316]. £3.3k/ton for bulk material. Density 1.2g/cm^3. Cost per area is £12/m^2 for a 3 mm sheet. Bulk embodied energy is 113 MJ/kg[177]. Energy per area is then 407 MJ/m^2.

BF33 borosilicate glass Data from Schott[317]. Cost per area is £53/m^2. Density 2.2g/cm^3. Bulk embodied energy is 20MJ/kg[177, 179]. Energy per area is then 145 MJ/m^2.

Rot 305 dye Based on a concentration of 400 ppm in a 3 mm sheet, we require 1.4 g/m^2 of dye. At a cost of around £10/g[81], this corresponds to £14/m^2. No figures are available for the embodied energy, but it can be assumed to be small since only 1.4 g is used per square meter.

Soda-lime glass Cost based on Saint-Gobain Planilux[312]. Bulk price for a 3.2 m x 2.5 m sheet is £110 for 4 mm thickness. Density is 2.5 g/cm^3. Cost per area is £14/m^2. Bulk embodied energy is again 20 MJ/kg[177, 179]. Embodied energy per area is then 200 MJ/m^2 for 4 mm thick.

Cells Data from NaREC[318]. Per wafer (5-inch semi-square) bulk cost is £6, which translates to £2.6/W. For LSC edge cells, we can cut twenty 10 cm-long, 0.5 cm-wide cells from a single wafer. Cost per cell is then £0.30, so cost per meter of perimeter is £3/m. Embodied energy of sc-Si cells is 2800 MJ/m^2[319], including production, purification, zone refining, wafering and cell processing. Area of 1 meter of edge cells is 0.005 m^2. Therefore energy per meter of perimeter is 14 MJ/m. For full-wafer cells, which are 12.7 cm square, energy per cell is 45 MJ.

Tabbing Data from Ulbrich[259]. Cost around £0.50/m. Embodied energy of copper is 70 MJ/kg[177] and its density is 8.6 g/cm^3. Tabbing dimensions are 0.25 mm x 2 mm. Therefore embodied energy is 0.3 MJ/m.

Framing Data from Technal[320]. Cost of framing *including* glazing is approximately £350-400/m^2, although this varies with the exact specification. The framing on its own is £250-300/m^2[320]. As an average value we will take £280/m^2. Embodied energy needs to be per length of framing. The mass per length is ∼4 kg/m. Bulk embodied energy for extruded aluminium is 153 MJ/kg[177] (assuming a 33 % recycled content). Therefore, embodied energy per meter is 612 MJ/m.

EVA film A common thickness used is 0.5 mm. Cost of this thickness of "Vistasolar" film from Etimex is £3.4/m^2[321]. However, in a laminate module, two sheets

are used front and back of the cell. Therefore total EVA cost per area of module is £6.8/m^2. Embodied energy is 200-300 MJ/m^2[319, 322, 323]. We will take 250MJ/m^2 as a average figure.

Table 6.11 summarises these cost and energy values. Clearly, the largest contributor to the cost is the aluminium framing. Where possible, a comparison will be made of the costs and energies of a module both with and without framing.

Table 6.11: Material costs and embodied energies of LSC and laminate module components. For derivation and sources of values, see text p.254

Component	Cost	Embodied energy
LSC module		
6 mm low-iron glass front cover	£24/m^2	300 MJ/m^2
3 mm PMMA clear sheet	£9/m^2	472 MJ/m^2
3 mm PC clear sheet	£12/m^2	407 MJ/m^2
0.2 mm PMMA thin film	£0.6/m^2	31 MJ/m^2
3.3 mm BF33 glass	£53/m^2	145 MJ/m^2
4 mm low-iron glass	£18/m^2	200 MJ/m^2
Rot 305 dye (OD5.3)	£14/m^2	-
4 mm soda-lime glass rear cover	£14/m^2	200 MJ/m^2
Edge cells (per meter of perimeter)	£3/m	14 MJ/m
Tabbing	£0.5/m	0.3 MJ/m
Framing	£280/m^2	612 MJ/m
Laminate module		
4 mm low-iron glass front sheet	£18/m^2	200 MJ/m^2
0.5 mm + 0.5 mm EVA lamination film	£6.8/m^2	250 MJ/m^2
Full-wafer cells (127 mm square)	£6/cell	45 MJ/cell
Tabbing	£0.5/m	0.3 MJ/m
4 mm soda-lime glass rear sheet	£14/m^2	200 MJ/m^2
Framing	£280/m^2	612 MJ/m

In order for the cost and energy figures obtained for LSC modules to be compared with those of glass/glass laminates, a suitable transparency for the laminate must be chosen. The transparency can either be chosen to achieve a comparable amount of light transmitted to the building interior, or to achieve a comparable module efficiency. Calculations of both are described below.

The total amount of light transmitted by the LSC can be determined from the absorption spectrum of the dye and the glass covers. However, we must also account for the non-uniform response of the human eye across the visible spectrum, which

extends from 400 nm to 700 nm and peaks at 550 nm. This is represented by the CIE photopic luminosity function, $\overline{y}(\lambda)$[324]. The "brightness" of light falling on a surface *as perceived by the human eye* is called the illuminance, E_v, and has units of lumens/m^2 or lux. It can be determined from a given spectral irradiance function $E_\lambda(\lambda)$ (in W m^{-2} nm^{-1}) using Eqn. 6.6[224].

$$E_v = 638 \int_0^\infty \overline{y}(\lambda) E_\lambda(\lambda)\, d\lambda \tag{6.6}$$

where

E_v	is the illuminance (lm/m^2 or lux)
$\overline{y}(\lambda)$	[sometimes called $V(\lambda)$] is the standard 2° photopic luminosity function (dimensionless)[324]
$E_\lambda(\lambda)$	is the spectral irradiance (W m^{-2} nm^{-1})

Fig. 6.33 shows the spectra (in units of spectral irradiance) incident on and transmitted through an LSC module. The transmitted spectrum is shown both with and without a rear cover present, since this adds an additional ∼9 % reflection loss. The CIE luminosity function is shown for comparison.

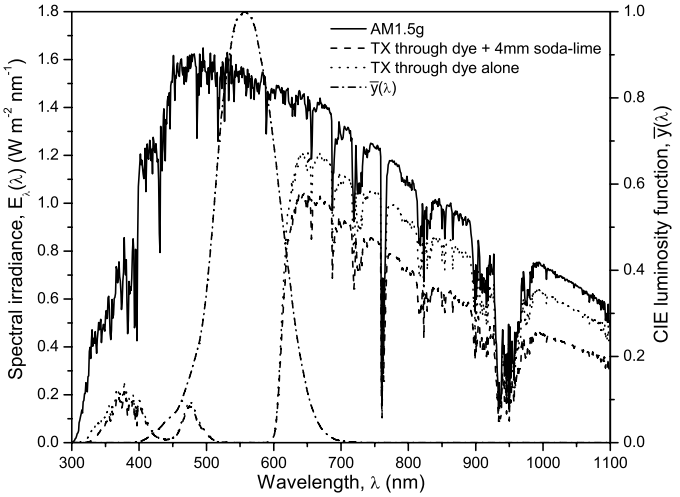

Figure 6.33: Sunlight (AM1.5g) incident on and transmitted through a dyed LSC module with either no back cover or a 4 mm soda-lime glass sheet. CIE luminosity function is shown to enable calculation of illuminance.

When Eqn. 6.6 is applied to the transmitted spectra, the illuminances obtained are

8,800 lux and 10,100 lux for modules with and without a back cover, respectively. The illuminance of the AM1.5g spectrum is 106,000 lux. The transmitted illuminance is therefore ∼10 % of the incident illuminance. Consequently, a glass/glass laminate module with a 10 % area transparency would transmit the same illuminance as the LSC module. From Fig. 6.32, the corresponding efficiency is 13.4 %.

The transparency can also be chosen to achieve a comparable module efficiency. As shown later in the results, bulk LSC modules based on PMMA and PC result in the lowest cost and energy. Therefore, it is sensible to match the laminate efficiency to them. A 1 m x 1 m LSC using either PMMA or PC has an efficiency of ∼2.3 % (Fig. 6.35). Referring back to Fig. 6.32, the corresponding module transparency is 85 %.

These transparency values can be used to calculate the dimensions of a "unit square" of glass/glass laminate. Costs and energies can be calculated for this unit square and then extrapolated to a value per square meter. Fig. 6.34 shows the resulting unit squares for both matched illuminance and matched efficiency. The cells used are based on standard 12.7 cm (5-inch) semi-square wafers. Two lengths of tabbing are used, extending completely over the front of one cell and the rear of the next cell in the string.

Table 6.12 summarises the properties of the two different types of laminate module. The cost and energy are first calculated per unit square, then per square meter.

We now have all the data required to calculate and study the costs and energies of LSC and laminate modules.

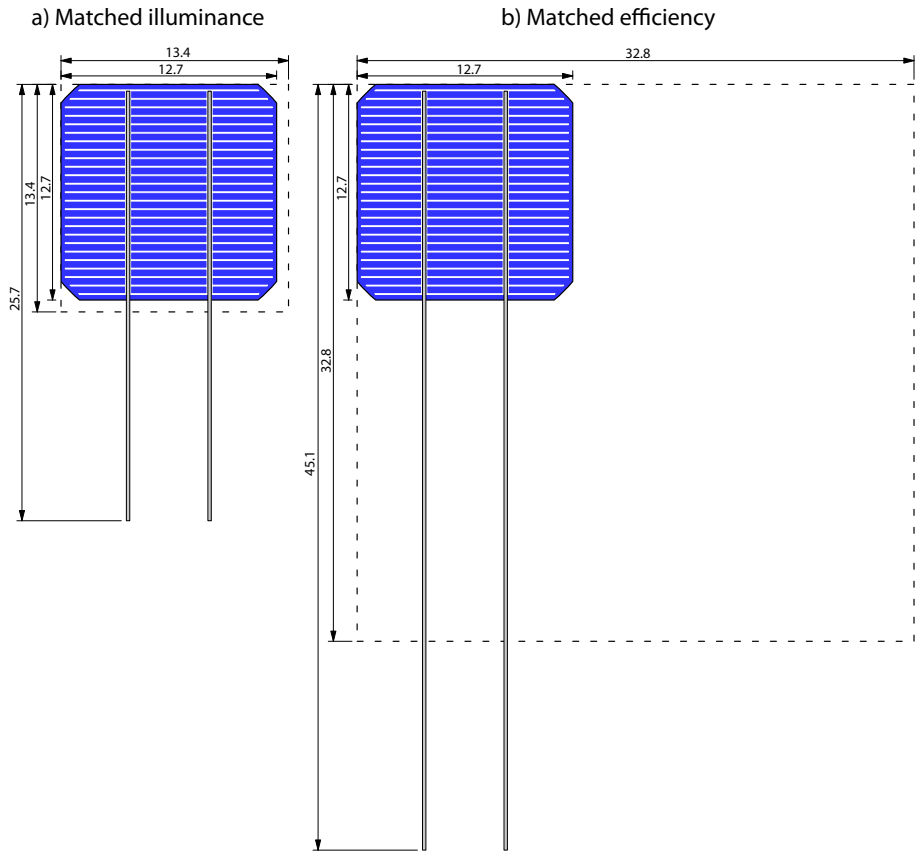

Figure 6.34: Unit squares of a glass/glass laminate module used for the calculation of cost and energy. Shown for modules with both a) matched illuminance and b) matched efficiency. All dimensions are in centimeters.

Table 6.12: Characteristics of glass/glass laminate modules under conditions of both matched illuminance and matched efficiency.

	Matched illuminance		Matched efficiency	
Module characteristics				
Transmission	10 %		85 %	
Efficiency (Fig. 6.32)	13.4 %		2.3 %	
Unit square area (Fig. 6.34)	0.0179 m^2		0.1076 m^2	
Cost and energy per unit square area, excluding frame				
Front glass	£0.323	3.59 MJ	£1.94	21.5 MJ
EVA lamination	£0.122	4.49 MJ	£0.732	26.9 MJ
Cell	£6.00	45.0 MJ	£6.00	45.0 MJ
Tabbing	£0.267	0.154 MJ	£0.451	0.271 MJ
Rear glass	£0.251	3.59 MJ	£1.51	21.5 MJ
Total	£6.95	56.8 MJ	£10.6	115 MJ
Cost and energy per m^2 of module area, excluding frame				
	£387	3160 MJ	£98	1070 MJ

6.2.1 Effect of size

Fig. 6.35 shows the predicted efficiencies versus size for square LSC modules. As expected, the BF33 and low-iron TF modules have the lowest efficiency because of the high absorption coefficient of the host material. PMMA and PC are comparable. Note that PC has a higher efficiency than PMMA at small sizes (<40 cm). Despite the larger absorption coefficient of PC, the higher refractive index results in a greater fraction of fluorescence light being trapped inside the LSC sheet. At larger sizes (>40 cm), the effect of higher absorption becomes more significant and PC has a lower efficiency than PMMA.

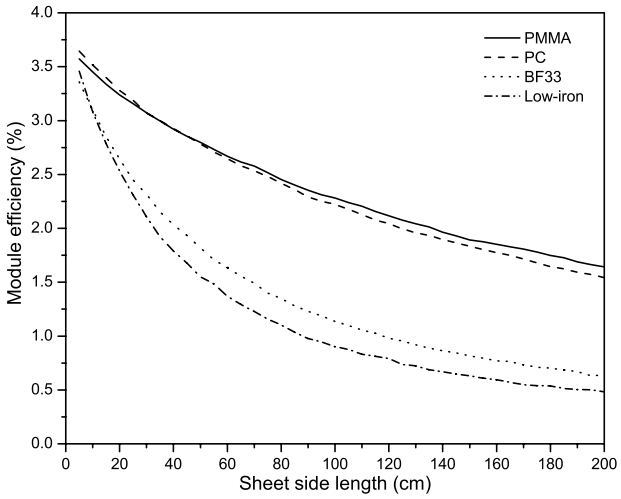

Figure 6.35: Variation of LSC module efficiency with square side length, shown for four different host materials.

Fig. 6.36 shows £/Wp versus module size. There is little difference between the £/Wp of PMMA and PC LSCs, a result of their similar efficiencies. The addition of a back cover also has little effect. However, the BF33 and low-iron TF LSCs show a much higher £/Wp than any of the polymeric LSCs. This is a result of their lower efficiency, as was seen in Fig. 6.35. When a frame is included, the £/Wp of PMMA and PC shows a minimum at ∼20 cm. The £/Wp of both laminate modules is constant over all sizes, since their efficiencies are constant. A matched-illuminance laminate results in a £/Wp that is less than half that of the LSCs, while the matched-efficiency laminate has an equal or slightly greater £/Wp.

Without a frame, the minimum £/Wp of LSCs occurs at ∼60-100 cm. The laminates

again show a constant £/Wp over all sizes, but this time they are comparable to the LSCs.

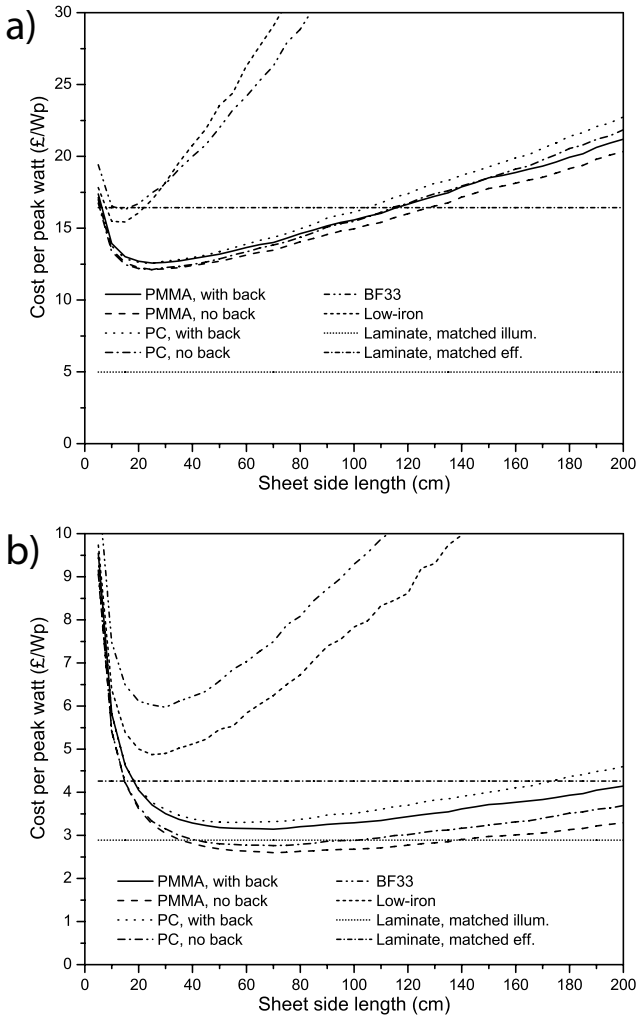

Figure 6.36: Cost per peak watt of LSC and glass/glass laminate modules plotted against square module size, shown both a) with and b) without a frame.

Fig. 6.37 shows the dependence of the cost per area on module size. Note that this excludes the framing cost, which adds a uniform £280/m^2 to all values. The £/m^2 of the PMMA, PC and low-iron LSCs are all similar, but BF33 is higher because of the higher per-area cost of the substrate material. There is no minimum or optimum size - £/m^2 shows a monotonic decrease with increasing size. The laminate modules exhibit a higher £/m^2, although that of the matched-efficiency laminate is only ∼25 % higher than the LSCs.

Finally, the dependence of MJ/Wp on size is shown in Fig. 6.38, again both with

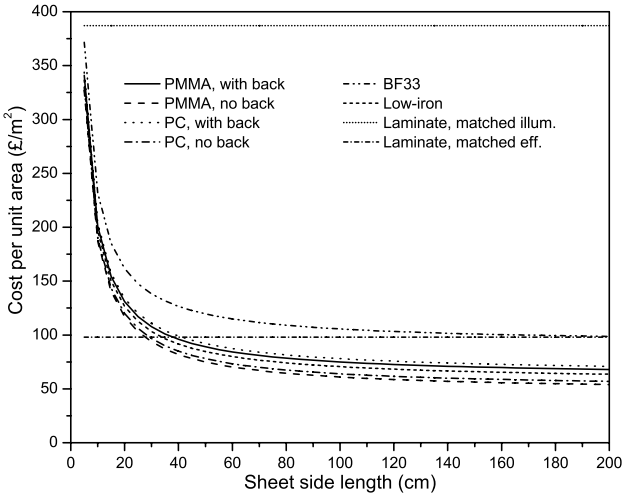

Figure 6.37: Cost per area of LSC and glass/glass laminate modules plotted against square module size. Figures exclude the cost of framing, which adds a uniform £280/m^2 to all values.

and without a frame. The BF33 and low-iron LSCs again show a higher MJ/Wp than PMMA and PC. With framing, the matched efficiency laminate shows a similar MJ/Wp to the LSCs and the matched illuminance laminate a greatly reduced MJ/Wp, around 60 %. With no framing, the MJ/Wp of PMMA and PC LSCs lie between that of the two different laminates.

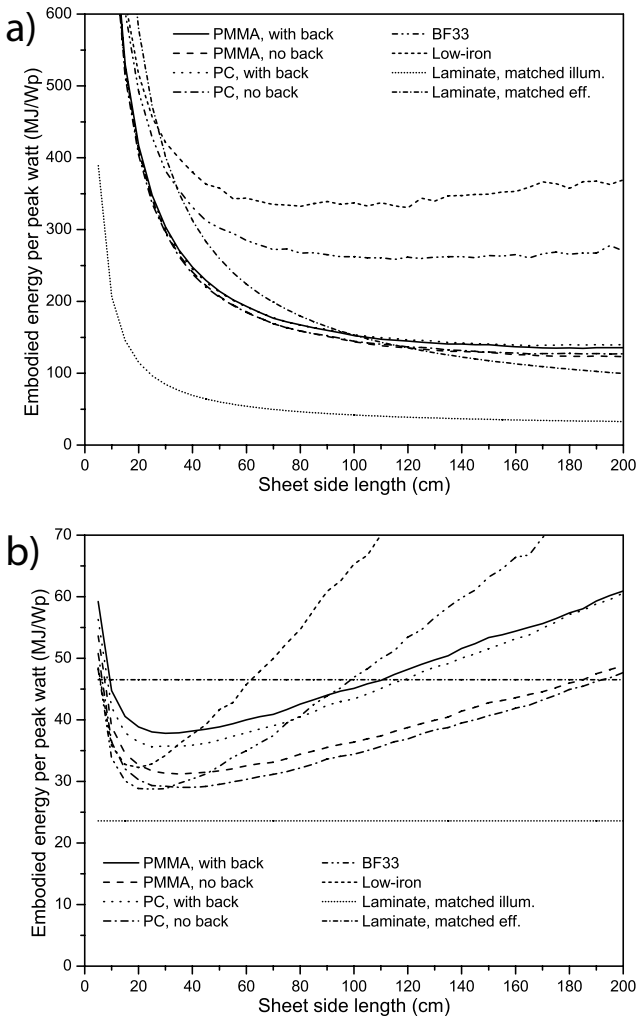

Figure 6.38: Embodied energy per peak watt of LSC and glass/glass laminate modules plotted against square module size, shown both a) with and b) without a frame.

6.2.2 Effect of aspect ratio

The effect of aspect ratio on cost and energy was studied at several different module areas (0.36, 1, 1.96 and 4 m^2). However, since the visible trends were identical for all sizes, only the results for the module area of 1 m^2 are presented here.

Fig. 6.39 shows £/Wp versus aspect ratio. Although the BF33 and low-iron LSCs show a large decrease in £/Wp at small aspect ratios, they still remain higher than PMMA and PC. The reason for the larger change in BF33 and low-iron is once again the higher host absorption; as the aspect ratio decreases, the corresponding reduction in average pathlength results in a proportionately larger reduction in the losses in BF33 and low-iron. Interestingly, there is hardly any change in £/Wp of PMMA and PC LSCs until aspect ratios <0.2, and even then the change is slight. Although the module area remains constant and small aspect ratios result in a higher efficiency, there is an increase in the perimeter length and a corresponding increase in the cost and energy due to cells, tabbing and framing which offsets the effects of the increased efficiency. There is little or no benefit from using small aspect ratios, especially when one considers that the aspect ratios of most glazing units lie above ∼0.5 (for example, where the height is twice the width). Smaller aspect ratios result in dimensions that are impractical to handle and process.

Figs. 6.40 and 6.41 show the effect of aspect ratio on £/m2 and MJ/Wp, respecively. Fig. 6.40 excludes the cost of the frame, which adds a uniform £280/m^2 to all values. At small aspect ratios, the £/m2 and MJ/Wp with a frame increase - a result of the proportionately greater perimeter length. However, these changes are again only significant for aspect ratios of <0.2.

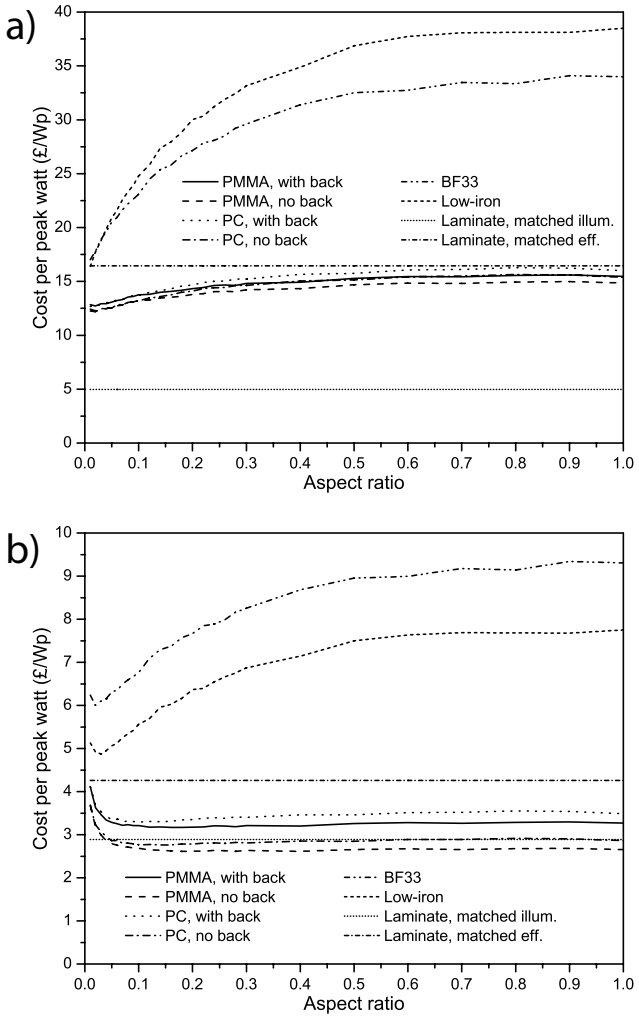

Figure 6.39: Cost per peak watt of LSC and glass/glass laminate modules plotted against aspect ratio, shown for a $1\,m^2$ area and both a) with and b) without a frame.

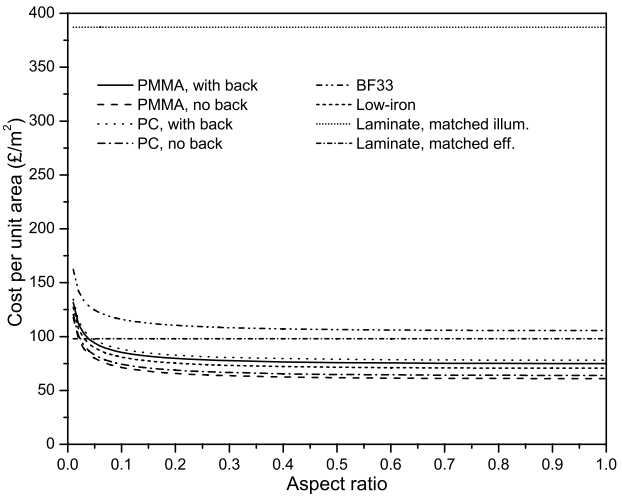

Figure 6.40: Cost per area of LSC and glass/glass laminate modules plotted against aspect ratio. Shown for a 1 m^2 area. Figures exclude the cost of framing, which adds a uniform £280/m^2 to all values.

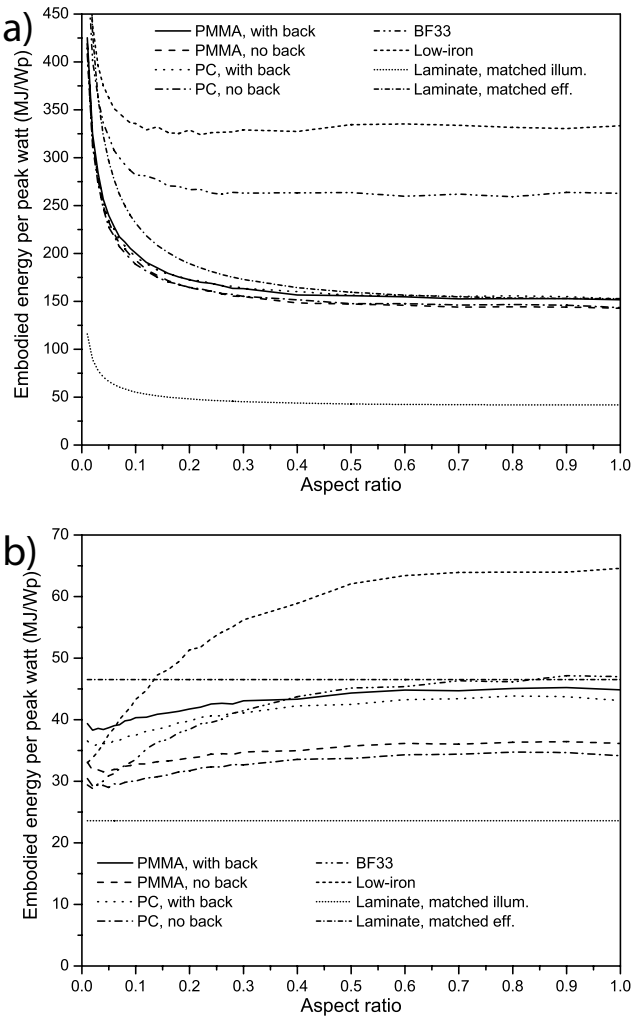

Figure 6.41: Embodied energy per peak watt of LSC and glass/glass laminate modules plotted against square module size. Shown for a $1\,m^2$ area and both a) with and b) without a frame.

6.2.3 Effect of dye lifetime

The figures for £/Wp, £/m^2 and MJ/Wp presented thus far are based on the assumption that the dye used in the LSC lasts indefinitely and does not degrade. This is obviously not true - dyes photodegrade and have a limited lifetime. Studies of the Violett 570 dye have shown that the emission intensity of dyed PMMA samples is reduced to ∼50 % of its initial value after two years' exposure[62], although this is strongly dependent on the host polymer and the exposure conditions[48, 62, 71, 325]. Although the Rot 305 dye does exhibit the highest photostability of the Lumogen dyes, it also suffers from photodegradation. Van Sark *et. al.*[62] found that the emission from a Rot 305-doped PMMA sample decreased by 3-14 % over 1.5 years' exposure, depending on the type of PMMA used. Clearly, the lifetime of organic dyes is much less than the 20-25 years over which conventional silicon PV modules are typically guaranteed to operate. If the dye in the LSC reaches the end of its useful lifespan, then both the dye and the host material must be replaced. This results in a recurring consumables cost which must be accounted for in a proper comparison of LSCs with laminate modules.

We will assume that it is possible to separate the dyed material component from the rest of the module for replacement, to avoid the need to replace, for example, the edge-mounted solar cells, or the substrate in a thin-film module. While this may be difficult in practice, the LSC is disadvantaged further if these components also have to be replaced. Table 6.13 lists both the "baseline" and "consumable" costs and energies for a range of different LSC technologies. Note the inclusion of PMMA thin-film and PC thin-film LSCs; as described previously, the use of a TF significantly reduces the consumable costs, since only the TF is replaced, rather than the entire sheet. These use a 0.2 mm-thick film of dyed PMMA or PC, respectively. For simplicity, the use of a rear cover is avoided on all the modules. As seen previously, it does not affect the cost or energy significantly.

Baseline components are those which remain in place throughout the module's entire lifetime. For example, baseline components for a PMMA bulk module would comprise the front cover glass, solar cells, tabbing, and framing (if used). The consumable components for the same module comprise the PMMA sheet and the dye, since the

dye is doped into the PMMA sheet.

Table 6.13: Baseline and consumable costs and energies of a 1 m^2 module. PMMA and PC modules do not use a back cover.

Technology	Baseline with frame		Baseline no frame		Consumable	
PMMA bulk	£318	2805 MJ	£38	357 MJ	£23	472 MJ
PMMA T-F	£327	3277 MJ	£47	829 MJ	£14.6	31 MJ
PC bulk	£318	2805 MJ	£38	357 MJ	£26	407 MJ
PC T-F	£330	3212 MJ	£50	764 MJ	£14.8	27 MJ
BF33	£371	2950 MJ	£91	502 MJ	£14.6	31 MJ
Low-iron	£336	3005 MJ	£56	557 MJ	£14.6	31 MJ

The number of times the consumable components require replacement can be determined simply from the dye lifetime and the desired lifetime of the entire module (e.g. for a module lifetime of 20 years and a dye lifetime of 5 years, the consumables would have to be replaced four times). Although the total embodied energy can be calculated easily from the sum of the baseline energy and the product of the consumable energy with the number of replacements, this same technique cannot be used to determine total cost, because of the effects of inflation and interest.

However, it is possible to calculate the total cost of the module, called the net present value or NPV, by using inflation and discount/interest rates to translate future consumable costs into present-day levels. The NPV can be obtained from Eqn. (6.7) below.

$$NPV = P_{base} + \sum_{n=0}^{N} P_{consum} \times \left[\frac{1+g}{1+d}\right]^{n \times l} \tag{6.7}$$

where

NPV	is the Net Present Value of the module, including all future consumable costs referenced to today's values
P_{base}	is the baseline cost of the module excluding all consumables
N	is the total number of times the consumables must be replaced, plus 1 to include the initial consumables
P_{consum}	is the cost of consumables at today's values

g is the yearly inflation rate, assumed to be 0.03 (3 %)

d is the yearly discount/interest rate, assumed to be 0.06 (6 %)

l is the lifetime of the consumables

The inflation rate, g, is simply the rate at which consumable costs increase over time, relative to present levels. The discount/interest rate, d, is the rate of interest received on funds which are invested at present to pay for consumable costs in the future. Therefore, at some future time, although the consumable cost will have increased, the value of funds available will also have increased (by a larger amount).

Figs. 6.42, 6.43 and 6.44 show the effect of dye lifetime (and hence the interval between consumable replacements) on £/Wp, £/m^2 and MJ/Wp, respectively. The number of replacements required has been calculated based on a desired maximum module lifetime of 20 years, which is the minimum lifetime of a conventional laminate module. Because of the discrete number of replacements required, there are steps in the graphs at 10, 6.66, 5, 4 years etc. For reference, the values of £/Wp, £/m^2 and MJ/Wp for the two laminate modules are also shown.

At shorter dye lifetimes, the cost and energy increase sharply as the number of consumable replacements increases. Lifetimes <5 years result in both £/Wp and MJ/Wp for the LSC exceeding those of the laminate modules. The benefit of the PMMA and PC thin-film LSCs can be seen in Fig. 6.44 - at short dye lifetimes, the TF modules result in a greatly reduced embodied energy. At a dye lifetime of 5 years, a PMMA thin-film module (with frame) results in ∼30 % lower MJ/Wp than a PMMA bulk module. It would appear that, if LSC modules are to compete with laminate modules on the basis of either cost or energy, the dyes used must exhibit lifetimes greater than 5-10 years.

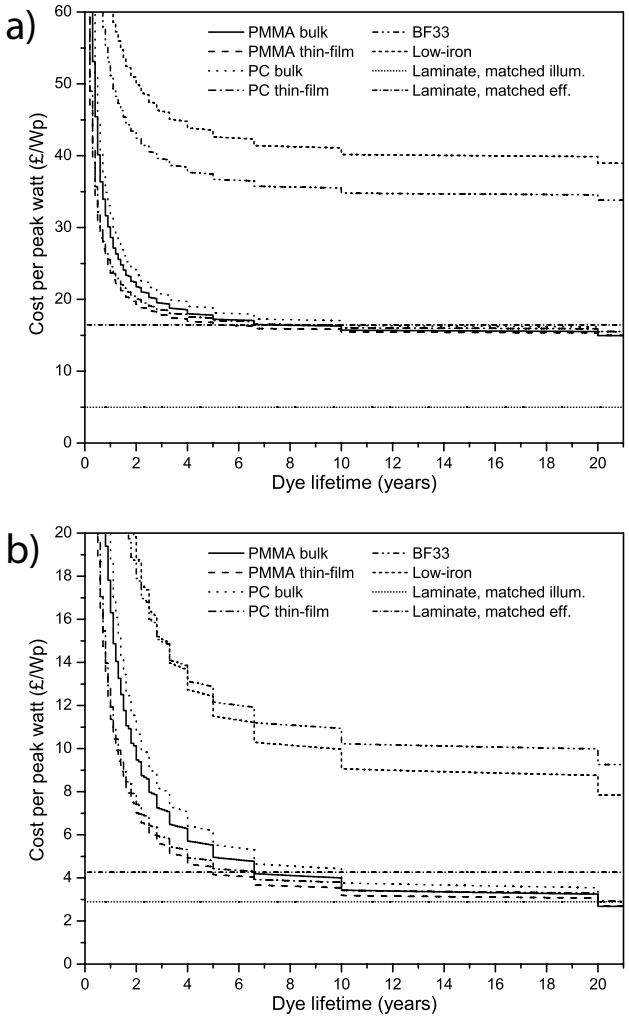

Figure 6.42: Cost per peak watt of LSC and glass/glass laminate modules plotted against dye lifetime. Shown for a $1\,m^2$ area and both a) with and b) without a frame.

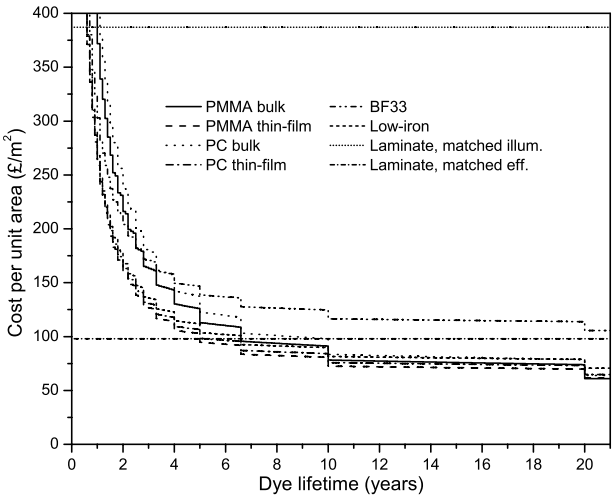

Figure 6.43: Cost per area of LSC and glass/glass laminate modules plotted against dye lifetime. Shown for a 1 m^2 area. Figures exclude the cost of framing, which adds a uniform £280/m^2 to all values.

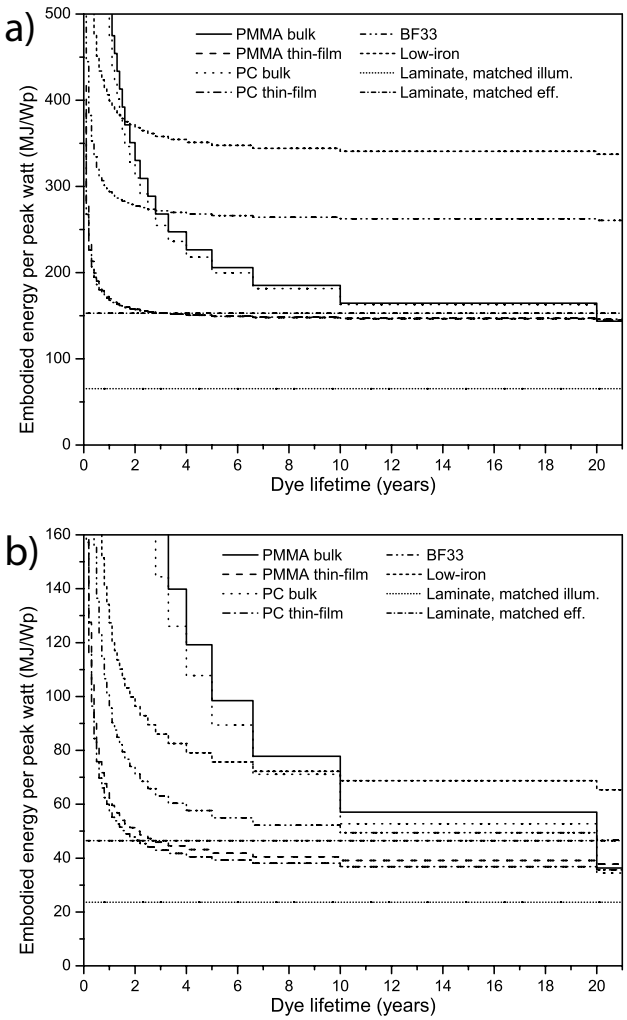

Figure 6.44: Embodied energy per peak watt of LSC and glass/glass laminate modules plotted against dye lifetime. Shown for a $1\,m^2$ area and both a) with and b) without a frame.

6.3 Discussion

In this chapter, we have studied the effects of dye mixture, sheet thickness, size & aspect ratio on both the overall solar-to-electric efficiency and the cost and energy content of LSC modules, with a view to optimising all of these parameters.

Based on achieving a balance between absorbing as large a fraction as possible of the incident solar radiation and keeping re-absorption losses within the sheet to a minimum, an optimum dye mixture for a single-sheet LSC module of 50 ppm Violett 570 + 350 ppm Rot 305 was obtained. This agrees well with recent results from General Electric[299] which also show that the optimum Rot 305 concentration is in the range 300-400 ppm. This resulted in an efficiency of 3.75 % for a 10 cm x 10 cm square, 0.3 cm thick module. Addition of further dyes to the same sheet resulted in a decrease in efficiency.

For a two-sheet module, with separate visible and NIR sheets, the optimum dye for the NIR sheet was found to be 80 ppm of NIR3. When combined with a sheet containing the optimum visible mixture of Violett 570 and Rot 305, this resulted in a total module efficiency of around 4.6 %.

The effects of back reflectors were studied and explained. A back reflector was found to increase efficiency by reflecting back unabsorbed solar radiation and rear escape-cone fluorescence loss back into the sheet, giving them a chance to be re-absorbed. The predicted increase for a 10 cm x 10 cm single-sheet module by using a back reflector was from 3.75 % to 4.15 %. Diffuse and specular back reflectors result in the same improvement when only fluorescence photons are considered, although a diffuse reflector can reflect incident sunlight directly on to the cells.

Module efficiency was found to decrease at larger module sizes as a result of increased re-absorption losses. To avoid this, different aspect ratios were studied and it was found that smaller aspect ratios led to higher efficiencies, although the increase was not large. Thicker sheets, containing the same dye concentration, also resulted in higher efficiencies since they absorbed more solar radiation.

The cost and embodied energy of both LSC and glass/glass laminate modules were

studied at a range of different module sizes, aspect ratios and dye lifetimes. The results highlight several important points. The cost and energy of LSCs using thin film on glass substrates (both BF33 borosilicate and low-iron soda-lime) were uniformly greater than with PMMA or PC substrates, regardless of size or aspect ratio. This is a result of the higher absorption coefficient of the glass, and indicates that such materials should not be used in LSCs.

It was found that a square LSC module size of 20-60 cm results in a minimum cost for both PMMA and PC LSCs and also a minimum MJ/Wp when the frame is excluded. Although a reduction in the aspect ratio resulted in a slight reduction in the £/Wp with a frame, the effects are only significant at aspect ratios <0.2. A rectangular module can therefore be used if desired, but it does not result in any appreciable increase or decrease in cost or embodied energy.

The relatively short lifetime of the organic dyes (compared with the lifetime of a convetional silicon PV module) results in both a cost and energy increase as the dyed component is replaced over the lifetime of the LSC module. When this is accounted for, it is found that the PMMA and PC LSC modules uniformly exhibit a comparable or higher (worse) cost and energy than glass/glass laminates with either matched illuminance or efficiency. Expressed another way, given any particular configuration of PMMA or PC LSC module, it is always possible to construct a glass/glass laminate module which achieves a comparable or lower (better) cost and energy. In reality, the situation is even worse, since experimental efficiencies will always be lower than simulated values, which increases the cost and energy still further.

6.4 Conclusions

The Rot 305 dye used for the analysis in this chapter represents a near-perfect organic dye for use in LSCs. It has both a wide absorption range and near-unity quantum yield, even at high concentrations. Despite this, there are no significant advantages in terms of cost and energy of a Rot 305-based LSC over conventional laminates. It would therefore appear that, unfortunately, LSCs based on organic dyes cannot compete with glass/glass laminate modules.

If the efficiencies of LSCs are to be increased so that they become a viable alternative, this will require the development of novel NIR-emitting fluorophores with wide absorption ranges, low self-absorption, high (>50 %) quantum yields, good photostability (5-10 years), and also the reduction or elimination of host absorption losses. Rare-earth complexes represent a promising step in this direction, since they can exhibit zero self-absorption and high quantum yields[140], but NIR-emitting complexes still lack the required performance and their photostability is unknown.

Based on the optimisation simulations performed in this chapter, several LSC modules are now constructed and their performances measured.

Chapter 7

LSC performance

In the previous chapter, the effects of a range of module parameters on the efficiency, cost and embodied energy of LSCs were studied. Optimum dye concentrations were determined using ray-tracing simulations. Based on these results, several LSC modules of two different sizes were constructed containing different dye mixtures. Details of their performance under solar illumination are presented in this chapter. The effect of short-term accelerated weathering on PMMA samples containing the Lumogen dyes is also discussed.

7.1 Small modules (10 cm square)

The first five modules constructed in the project (see Sections 2.6.3 to 2.6.5) were all based on 10 cm x 10 cm x 0.3 cm square LSC sheets. It was therefore possible to measure the I-V characteristics of these modules using the Oriel solar simulator described previously (Section 2.7.1), which has an illuminated area of 12 cm x 12 cm square. This allowed the both the performance of individual modules and also the effectiveness of the different construction methods to be determined. The solar-to-electric efficiencies of the LSC modules were then calculated as described below.

The I-V curves of each cell attached to an LSC module were measured individually, so as top take into account slight variations in the characteristics of the cells on the edges of the modules resulting from differences such as cell efficiency, optical coupling

and contact resistance. I-V curves of the modules with all of the edge cells connected in parallel were also measured. A parallel connection was chosen so as to minimise the effect that a single "bad" cell could have on the overall output (a series connection, while theoretically resulting in the same maximum output power, would suffer more from the effects of a "bad" cell, as all the current has to flow through that one cell).

The overall module efficiency was calculated from the maximum power generated by the module and the incident solar power, which for modules 1 to 5 was 10 W (area of 100 cm^2). However, there are several different ways of calculating the module efficiency, depending on whether cells were measured individually or in parallel. In total, there are three different module efficiencies which can be calculated. These are designated Type 1, 2 & 3 and are described below.

Type 1. The maximum power output of an individual edge cell is measured and then multipled by four to obtain the output power from the module, assuming that cells with equal output were also placed on the other three edges. For example, if a single cell outputs 40 mW maximum, then the module output power is 160 mW and the module efficiency is 1.6 %. This efficiency is most useful, for example, when several of the edge cells perform poorly and calculations have to be based on the output of one individual edge cell.

Type 2. The maximum power outputs of each edge cell are measured individually and then added together to obtain the power output from the module as a whole. For example, if the outputs from each cell (in mW) were 23, 27, 46 & 32, the total module output would be 128 mW and the efficiency 1.28 %.

Type 3. All edge cells are connected in parallel and the maximum power output measured. This is then the power output of the module. Note that the result will be different from Type 2 (most likely less) as mis-match between the cells will reduce the power output of the parallel combination. For example, the maximum power point of each cell may occur at a slightly different voltage because of variations between cells, yet when connected in parallel all cells are forced to operate at the same voltage. Therefore, not all cells will be operating at their maximum power-point and overall power (and efficiency) will be reduced.

Comparison between the results obtained by calculating the different types of efficiencies is useful in determining how well the edge cells are matched to each other and how much power it is possible to produce (for example, by calculating the Type 1 efficiency for the best-performing edge cell). If Type 2 & 3 efficiencies are close, then this is a sign that the cells have roughly equal maximum power points and are matched well when connected in parallel.

In addition to the module efficiency, which is of most interest, several other parameters were also calculated. Their symbols and descriptions are listed below.

I_{SC}	Short-circuit current
J_{SC}	Short-circuit current density, obtained by dividing I_{SC} by the cell area
V_{OC}	Open-circuit voltage
FF	Fill factor
P_{MAX}	Power at maximum power point
R_{SERIES}	Series resistance in solar cell
R_{SHUNT}	Shunt (parallel) resistance across solar cell

Different back reflectors were used to study their effect on the power output. These are denoted by Black (B), Specular (S), Semi-specular (SS) and Diffuse (D).

Black. Heavy black card, normally used for shielding optical components from stray light. It has a rough surface, so therefore reflects very little light.

Specular. Polyester film coated with an aluminium reflector. This acts as a specular reflective mirror.

Semi-specular. The aluminised polyester film was crumpled to texture it and create different angles of reflective planes.

Diffuse. White copy paper, which acts as a diffuse reflector. Any ray striking it is reflected in a random direction.

Three different visits were made to NaREC to measure the performance of the various

modules. The results are grouped by visit and are presented in the next three sections. The first and second non-optimised modules were measured on the first two visits and are described in Sections 7.1.1 & 7.1.2, respectively. The three optimised modules (constructed in Section 2.6.5) were measured on the third visit and results from these are given in Section 7.1.3.

7.1.1 First module

This was the first LSC module made in the project and was built mainly to see what problems would be encountered in construction and what kind of efficiency could be expected. Constructional details are given in Section 2.6.3. Since simulations to determine the optimum mixture of dyes had not yet been performed, a sheet containing a mixture of four of the Lumogen dyes was cast. Their concentrations are shown in Table 7.1. Sheet dimensions were 10 cm x 10 cm x 0.3 cm.

Table 7.1: First module dye concentrations

Dye	Concentration (ppm)
Violett 570	190
Gelb 083	130
Orange 240	90
Rot 305	215

It was found later from simulations that the addition of the Gelb 083 and Orange 240 actually resulted in a reduced efficiency compared with only Violett 570 and Rot 305 present on their own. The predicted efficiency with only the above concentrations of Violett 570 and Rot 305 present is 4.05 %. This drops to 3.89 % when Gelb 083 and Orange 240 are added to the mixture. Both efficiencies are for a LSC with a diffuse white back reflector.

I-V characteristics were measured of individual cells and the parallel combination of all of them with different back reflectors. Results are presented in Table 7.2.

Table 7.2: I-V results for module 1

#	Description	Reflector	Cell area[a] (cm^2)	I_{SC} (A)	J_{SC} (mA/cm^2)	V_{OC} (V)	FF (%)	P_{MAX} (mW)	R_{SERIES} (mΩ)	R_{SHUNT} (Ω)	Efficiency[b] Type	%
	Secondary ref. cell "Ref1_2"	-	142.9	4.801	33.60	0.611	79.2	2323.3	5.5	20	-	16.26
1	All cells[c]	Black[d]	12	0.444	37.00	0.554	68.5	168.5	73	190	3	1.69
2	All cells, repeat 1	"	12	0.400	33.33	0.553	67.6	149.6	-[e]	-	3	1.49
3	All cells, repeat 2	"	12	0.403	33.58	0.551	56.5	125.5	-	-	3	1.25
4	Cell A	"	3	0.058	19.26	0.562	72.4	23.6	130	23	1	0.94
5	Cell B	"	3	0.078	26.10	0.543	56.4	23.9	130	24	1	0.96
6	Cell C	"	3	0.057	19.08	0.556	75.6	24.0	160	8400	1	0.96
7	Cell D	"	3	0.127	42.27	0.550	72.2	50.4	160	270	1	2.02
8	Cell D	Specular[f]	3	0.136	45.17	0.553	72.0	54.2	160	320	1	2.17
9	Cell D	Semi-specular[g]	3	0.137	45.50	0.553	72.2	54.7	160	250	1	2.19
10	Cell D	Diffuse[h]	3	0.150	49.93	0.559	72.9	61.1	150	290	1	2.45

[a] Total area of cell(s), used for calculating J_{SC}. Note, this is an approximate value.

[b] Overall module efficiency, assuming incident intensity of $100\,mW/cm^2$. See text (p. 278) for description of different efficiency types.

[c] Cracking heard during this measurement.

[d] Matt black card.

[e] Series and shunt resistances were not available for measurements 2 & 3 because of a file corruption problem.

[f] Aluminised polyester film.

[g] Same aluminised polyester film, but crumpled to create different reflection angles.

[h] White copy paper.

Initially, all cells were connected in parallel and measured with a black rear reflector (measurements 1-3). The first module efficiency measured was 1.69 %. However, during measurement #1, cracking sounds were heard from the sheet. The measurement was repeated twice (#2 & #3) and the efficiency decreased sharply both times (from 1.69 % to 1.49 % to 1.25 %). The fill factor also decreased.

The cracking sounds and the drop in efficiency & fill factor were caused by the stress set up by the different expansion rates of the PMMA sheet and silicon cells as they heated up under illumination by the solar simulator. The cyanoacrylate adhesive used to bond the cells, while providing a good mechanical joint, is brittle and cannot withstand this stress. On inspection, the cells had separated from the edge of the LSC sheet at several points and this resulted in a drop in the coupling efficiency of the edge-emitted light into the cell. As was found later, several of the cells also had electrical problems. A contrast-enhanced image of one of the cells is shown in Fig. 7.1 and shows several areas of separation of the cell from the sheet edge. These areas appear bright, indicating that fluorescence emission is being reflected by the air gap rather than being absorbed by the cell.

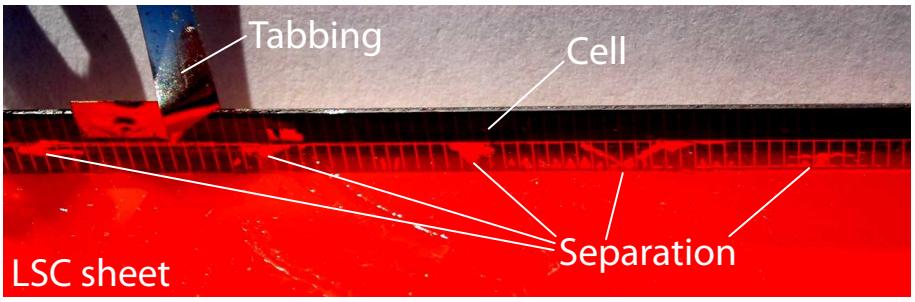

Figure 7.1: Contrast-enhanced image showing cell separation

The reference cell shows a fill factor of 79 %, yet the edge cells of the module have a fill factor of only ∼69-72 %. This is a result of poor electrical contact to the cells, as tabbing connections were only made at one point on the busbar and the busbar resistance will decrease the fill factor. It will be shown later in Section 7.1.3 that proper electrical contact can restore the fill factor to its normal value.

Fig. 7.2 shows the corresponding I-V curves for the first three measurements. The current decreases with successive measurements. In the third measurement, there is a sudden drop in current at around 0.3 V. This is a sign of an intermittent electrical

connection to one or several of the cells caused again by thermal stresses.

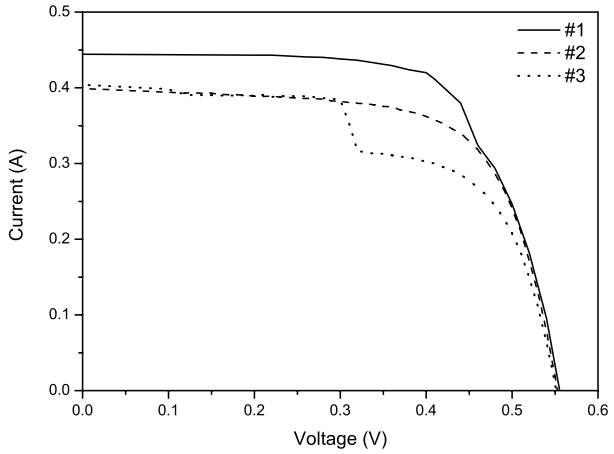

Figure 7.2: Successive I-V curves of first module, all cells in parallel

The cells were then disconnected and the I-V curve of each measured individually (measurements 5-8) to see which cells were damaged and if any were still usable. Fig. 7.3 shows the curves. Clearly, cells A, B & C are all damaged, as is evident from their low power output. Cells A & B have a low shunt resistance, indicating an internal short - these cells should have a shunt resistance of several hundred ohms. Fortunately, cell D still performs satisfactorily and its output was used to study the effect of the various back reflectors.

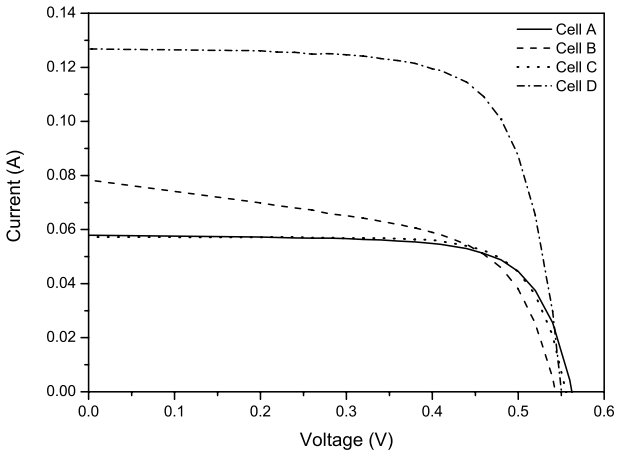

Figure 7.3: I-V curves of each cell of first module

Fig. 7.4 shows the curves of cell D with four different back reflectors - black, specular,

semi-specular and diffuse. Several points are worthy of note. First, any back reflector (specular, semi-specular or diffuse) improves the efficiency by reflecting unabsorbed incident illumination and rear-surface escape-cone losses back into the sheet. The semi-specular reflector is a slight improvement over the specular reflector, as the different reflection angles increase the probable pathlength of reflected light inside the sheet and the chances of its being re-absorbed. The diffuse reflector results in the highest efficiency. Part of this efficiency increase is due to unabsorbed solar radiation being reflected directly on to the cells, without being absorbed by the LSC sheet. Evidence for this will be shown in the next section.

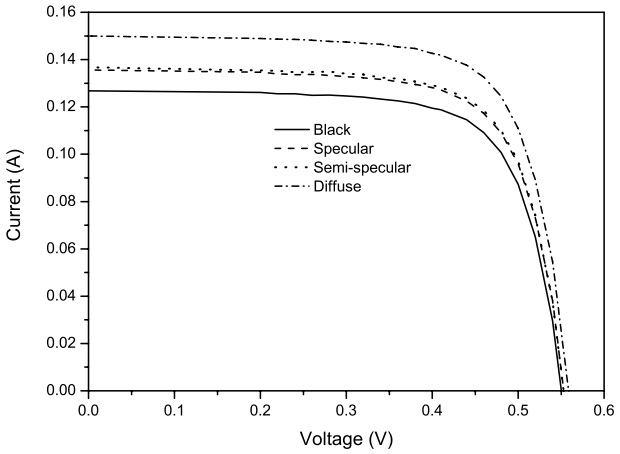

Figure 7.4: I-V curves of cell D with different back reflectors

The percentage relative efficiency increases resulting from the specular reflector and the diffuse reflector are 7 % (2.02 % to 2.17 %, measurement 8) and 21 % (2.02 % to 2.45 %, measurement 10) respectively. The Monte-Carlo simulation model in Section 6.1.2 predicted relative increases of 11 % and 19 % for specular and diffuse reflectors. The experimental improvements are in good agreement with the model.

The Type 1 efficiencies calculated for the individual cell D (measurements 7-10) are much higher than the Type 3 efficiencies obtained for all cells connected in parallel (measurements 1-3). This is a result of poor matching between cells. The best module efficiency obtained is 2.45 % (measurement 10, with a diffuse back reflector). In view of the problems of thermal stresses and poor electrical connection to the cells, there is clearly room for improvement.

7.1.2 Second module

Constructional details of this module are given in Section 2.6.4. A dye concentration of 300 ppm Violett 570 and 900 ppm Rot 305 was used in a 10 cm x 10 cm x 0.3 cm sheet, although it was subsequently found through simulations that these concentrations were unnecessarily high.

I-V results from the second module are shown in Table 7.3. Note that a different secondary reference cell was used ("Ref2_4"), as the previous cell ("Ref1_2") had suffered damage in the time between visits to NaREC. However, this does not affect the results, as each secondary reference cell is calibrated against the same primary reference cell, which is characterised by the Fraunhöfer Institute for Solar Energy Systems.

Again, all the cells were initially connected in parallel. The efficiency obtained was 1.40 % (measurement 1) - much lower than the first module. The largest factor in this lower efficiency is the poor quality of the aluminium coating on the mirrored strips near the edges. As nearly all of the edge-emitted light reflects from the mirrored strips, this will reduce the amount of light reaching the cells.

The first observation was that no cracking was heard from the module when it was under illumination by the simulator. This is because the cells were attached using epoxy resin rather than cyanoacrylate. This is more resilient and can accomodate thermal stresses. However, as found later, there were still electrical-connection problems to some of the cells.

Table 7.3: I-V results for module 2

#	Description	Reflector	Cell area (cm^2)	I_{SC} (A)	J_{SC} (mA/cm^2)	V_{OC} (V)	FF (%)	P_{MAX} (mW)	R_{SERIES} (mΩ)	R_{SHUNT} (Ω)	Efficiency Type	Efficiency %
	Secondary ref. cell "Ref2_4"	-	142.9	4.828	33.79	0.609	77.4	2275.8	6.1	13	-	15.92
1	All cells	Black	12	0.395	32.90	0.560	63.3	140.1	210	37	3	1.40
2	All cells	Specular	12	0.421	35.08	0.561	62.8	148.3	210	37	3	1.48
3	All cells	Semi-specular	12	0.425	35.42	0.560	62.6	149.0	210	38	3	1.49
4	All cells	Diffuse	12	0.441	36.77	0.559	62.3	153.7	210	37	3	1.54
5	All cells, no R_{WIRE} [a]	Black	12	0.394	32.83	0.559	70.6	155.5	110	38	3	1.55
6	All cells, no R_{WIRE}	Semi-specular	12	0.421	35.08	0.557	70.7	165.8	76	37	3	1.66
7	All cells, no R_{WIRE}	Diffuse	12	0.439	36.58	0.559	70.5	173.0	74	39	3	1.73
8	Cell 1	Black	3	0.100	33.33	0.549	72.2	39.6	250	1700	1	1.59
9	Cell 2	"	3	0.093	30.93	0.548	38.0	19.3	12000	74	1	0.77
10	Cell 3	"	3	0.101	33.63	0.556	69.9	39.2	270	96	1	1.57
11	Cell 4	"	3	0.095	31.80	0.552	65.5	34.5	420	73	1	1.38
12	Cell 4, no R_{WIRE}	"	3	0.095	31.67	0.552	68.3	35.8	250	73	1	1.43
13	Cell 1, no R_{WIRE}	"	3	0.099	33.13	0.555	75.2	41.5	87	11000	1	1.66
14	Cell 1, no R_{WIRE}	Semi-specular	3	0.106	35.23	0.555	75.5	44.3	89	1700	1	1.77
15	Cell 1, no R_{WIRE}	Diffuse	3	0.112	37.27	0.555	75.4	46.8	92	1300	1	1.87
16	Cell 1, no R_{WIRE}, no heat [b]	"	3	0.112	37.20	0.560	75.8	47.4	86	3200	1	1.89
17	Cell 3, no R_{WIRE}	Black	3	0.100	33.43	0.560	72.8	40.9	86	95	1	1.64
18	Cell 3, no R_{WIRE}	Semi-specular	3	0.108	36.07	0.554	72.4	43.4	110	100	1	1.74
19	Cell 3, no R_{WIRE}	Diffuse	3	0.111	37.10	0.558	73.1	45.4	120	100	1	1.82

[a] Electrical connections were made directly to cell tabbing instead of via long flying wire leads. Same for all other measurements with "no R_{WIRE}".

[b] Module was left to cool for around 30 min before measurement, as the illumination caused the module and cells to gradually heat up.

The addition of a specular reflector resulted in a 6 % relative increase in the efficiency to 1.48 % (measurement 2) - roughly the same as with the first module. The semi-specular reflector was also a slight improvement over the specular reflector, as before. However, the increase of 11 % (1.40 % to 1.54 %) when a diffuse reflector is added (measurement 4) is much smaller than before. As explained previously, much of the improvement that results with a diffuse reflector is from sunlight being reflected directly on to the cells. This happens predominantly in a region near the edge, with a width approximately the same as the thickness of the sheet. The mirrored strips on the faces of this module block this directly-reflected light, and this explains the smaller increase in efficiency with the diffuse reflector.

To prevent stress on the tabbing attached to the cells, electrical connection between the sourcemeter and the module consisted of two long (50 cm) wire leads of approximately 0.5 mm diameter. The resistance of this long, thin connection reduced the efficiency of the module. Measurements were then made without these wire leads, with connections made instead as near to the cells as possible. This resulted in around a 12 % relative increase in efficiency compared with before (measurements 5-7). The series resistance was approximately half of that with the wire lead connections.

As before, the cells were now disconnected and measured individually (measurements 8-12). Cell 2 had an extremely large series resistance, indicating poor connection to that cell. Cells 2-4 also had a low shunt resistance which, while not as low as cells A & B of the first module, still indicates shorting within the cell. Cell 1 is the only remaining cell which has both a low series resistance and a high shunt resistance. It was measured with different back reflectors. The relative increases with semi-specular (7 %, from 1.66 % to 1.77 %) and diffuse reflectors (13 %, from 1.66 % to 1.87 %) are comparable to the increases obtained when all cells were connected in parallel.

There was the possibility that the entire module heated up during the measurement due to the incident illumination. As temperature rises, the efficiency of the cells will drop. To see if this was happening, Cell 1 was re-measured after allowing the module to cool for 30 min to room temperature. There is a only a slight increase in efficiency from 1.87 % to 1.89 % (measurements 15 & 16), indicating that long illumination times have little effect on the measured efficiencies.

The short-circuit current density reaches a maximum of 37.27 mA/cm^2 (measurement 15) which is not considerably greater than the 1-sun density of 33 mA/cm^2. This indicates that the cells are operating at roughly 1-sun illumination intensity. However, these cells were designed for a 5-sun illumination intensity and, as a result, have a smaller finger spacing which produces more shading of the cell. A 1-sun cell could equally be used and would benefit from lower shading losses. The low concentration ratio is partly a result of the LSC's small size.

From the results, it can be concluded that both the mirroring of the strips near the edges and the use of conductive silver paint to make electrical connections have reduced the efficiency of the module. The maximum efficiency is 1.89 % (measurement 16).

7.1.3 Third, fourth and fifth modules

The dye mixtures and concentrations chosen for the third set of modules are based on the simulations performed in Section 6.1.1. Three modules were made - mixed visible dyes only, mixed visible & NIR dyes and NIR dye only. The dye concentrations used for each of the three modules are listed in Table 7.4. Module 3 contained the optimum mixture of only visible dyes (Violett 570 and Rot 305). Module 4 contained the same visible mixture as module 3, but with the addition of a small amount of NIR-emitting dye, NIR3. Its main purpose is to demonstrate the detrimental effect that adding an NIR dye has on the efficiency of a visible sheet. Module 5 contains only an NIR dye (NIR3) and was used in conjunction with module 3 in a stacked LSC arrangement. Constructional details of these modules are given in Section 2.6.5.

Table 7.4: Third set of modules - dye concentrations

	Dye concentration (ppm)		
Dye	Module 3	Module 4	Module 5
Violett 570	50	49	-
Rot 305	368	358	-
NIR3	-	32	78

Each cell of each module was measured with three different back reflectors (black,

semi-specular and diffuse). All cells on individual modules were then connected in parallel, and measurements again taken with different back reflectors. Finally, modules 3 & 5 were stacked to form a 2-layer LSC and the individual cell outputs measured, again with three different reflectors.

The same results are presented in slightly different formats in Table 7.5 and Table 7.6. Table 7.5 contains a chronological list of all measurements and shows all I-V curve parameters for each measurement (current, voltage, fill factor, power, resistance). The format is the same as for the first and second modules.

Table 7.6 presents the three different calculated module efficiency types for all the measurements. Each efficiency is calculated for the three different back reflectors studied, which allows an easy comparison of the effects of the reflectors. Results for single and stacked modules are presented in separate sections of the table. Table 7.6 also shows the ratios between the power outputs obtained with different back reflectors, both semi-specular to black and diffuse to black. This shows the relative improvement in power output when using these back reflectors.

First, note the small variation between the different cells on the edges of individual modules. For example, the cells on module 3 vary in output power (with a diffuse rear reflector) from 74.9 mW to 80.5 mW (measurements 9-12) - a variation of only 7 % and this is the greatest variation of all the sheets. Compare this with the cell-to-cell variation in the edges of the first and second modules which were 50-100 %. Both the cell soldering and cell gluing techniques ensure this uniformity between cells.

There is also little variation between Type 2 and Type 3 efficiencies - the variation is no more than 5 %. This means that the same power output can be achieved by either adding the individual powers of each cell or by connecting all cells in parallel. This is another indication of the uniformity of the cells.

Table 7.5: I-V results for modules 3, 4 and 5

#	Description Module[a]	Cell[b]	Reflector	Cell area (cm^2)	I_{SC} (A)	J_{SC} (mA/cm^2)	V_{OC} (V)	FF (%)	P_{MAX} (mW)	R_{SERIES} (mΩ)	R_{SHUNT} (Ω)
	Secondary ref.	cell "Ref2_4"	-	142.9	4.856	33.98	0.608	77.2	2277.7	7	19
				Single module - module 3							
1	Module 3	Cell 1	Black	3	0.151	50.37	0.573	76.0	65.8	240	520
2	"	Cell 2	"	3	0.148	49.30	0.577	79.1	67.5	220	1200
3	"	Cell 3	"	3	0.149	49.70	0.577	78.5	67.6	220	420
4	"	Cell 4	"	3	0.143	47.73	0.571	76.7	62.7	250	450
5	"	Cell 1	Semi-specular	3	0.168	55.87	0.569	75.6	72.1	170	540
6	"	Cell 2	"	3	0.165	54.93	0.572	79.2	74.7	160	570
7	"	Cell 3	"	3	0.165	54.97	0.572	79.0	74.5	160	360
8	"	Cell 4	"	3	0.159	53.13	0.567	76.7	69.3	170	380
9	"	Cell 1	Diffuse	3	0.178	59.47	0.573	76.2	77.9	160	320
10	"	Cell 2	"	3	0.176	58.67	0.577	79.2	80.5	220	620
11	"	Cell 3	"	3	0.176	58.67	0.578	79.0	80.4	220	250
12	"	Cell 4	"	3	0.171	56.87	0.569	77.1	74.9	170	350
13	"	All cells	Black	12	0.579	48.27	0.567	76.2	250.0	48	110
14	"	All cells	Semi-specular	12	0.651	54.25	0.566	75.6	278.6	50	130
15	"	All cells	Diffuse	12	0.690	57.52	0.568	75.8	297.0	49	110
				Single module - module 4							
16	Module 4	Cell 1	Black	3	0.094	31.25	0.561	70.2	36.9	220	51
17	"	Cell 2	"	3	0.089	29.87	0.561	72.8	36.5	220	95
18	"	Cell 3	"	3	0.096	32.00	0.558	69.8	37.4	200	62
19	"	Cell 4	"	3	0.095	31.81	0.560	74.5	39.8	200	130
20	"	Cell 1	Semi-specular	3	0.107	35.80	0.559	71.0	42.7	210	52
21	"	Cell 2	"	3	0.105	34.9	0.557	73.6	42.9	210	96
22	"	Cell 3	"	3	0.113	37.53	0.558	71.4	44.9	210	62
23	"	Cell 4	"	3	0.110	36.63	0.557	74.8	45.8	210	150
24	"	Cell 1	Diffuse	3	0.117	39.13	0.563	71.5	47.3	190	50
25	"	Cell 2	"	3	0.113	37.70	0.561	73.8	46.9	200	98
26	"	Cell 3	"	3	0.122	40.63	0.562	71.9	49.2	200	64
27	"	Cell 4	"	3	0.119	39.50	0.562	75.2	50.1	190	140
28	"	All cells	Black	12	0.370	30.82	0.554	71.5	146.6	59	20

Continued...

Table 7.5 – Continued

#	Description Module[a]	Cell[b]	Reflector	Cell area (cm^2)	I_{SC} (A)	J_{SC} (mA/cm^2)	V_{OC} (V)	FF (%)	P_{MAX} (mW)	R_{SERIES} (mΩ)	R_{SHUNT} (Ω)
29	”	All cells	Semi-specular	12	0.439	36.61	0.557	72.0	176.2	60	20
30	”	All cells	Diffuse	12	0.470	39.15	0.561	72.7	191.4	56	20
				Single module - module 5							
31	Module 5	Cell 1	Black	3	0.069	23.09	0.557	70.3	27.1	300	90
32	”	Cell 2	”	3	0.063	20.96	0.551	73.2	25.4	230	250
33	”	Cell 3	”	3	0.066	21.87	0.549	73.2	26.4	230	190
34	”	Cell 4	”	3	0.064	21.35	0.549	74.9	26.3	230	400
35	”	Cell 1	Semi-specular	3	0.086	28.52	0.552	71.9	34.0	220	92
36	”	Cell 2	”	3	0.080	26.59	0.548	72.9	31.8	240	300
37	”	Cell 3	”	3	0.081	27.14	0.548	73.8	33.0	240	190
38	”	Cell 4	”	3	0.080	26.69	0.549	75.3	33.1	230	390
39	”	Cell 1	Diffuse	3	0.094	31.25	0.558	72.5	38.0	210	97
40	”	Cell 2	”	3	0.087	29.06	0.554	74.2	35.9	220	250
41	”	Cell 3	”	3	0.089	29.68	0.554	74.5	36.8	220	210
42	”	Cell 4	”	3	0.088	29.49	0.556	75.2	37.0	210	390
43	”	All cells	Black	12	0.260	21.65	0.547	71.5	101.6	56	43
44	”	All cells	Semi-specular	12	0.325	27.07	0.549	72.7	129.6	59	44
45	”	All cells	Diffuse	12	0.361	30.07	0.554	73.0	146.0	55	45
				Stacked modules - module 3 on top of module 5[c]							
46	Module 3	Cell 1	Black	3	0.153	50.97	0.572	75.7	66.2	250	510
47	”	Cell 2	”	3	0.150	50.03	0.574	78.7	67.7	240	810
48	”	Cell 3	”	3	0.151	50.30	0.572	78.9	68.1	170	470
49	”	Cell 4	”	3	0.146	48.77	0.566	76.5	63.4	180	540
50	Module 5	Cell 1	”	3	0.047	15.52	0.542	66.5	16.8	250	92
51	”	Cell 2	”	3	0.040	13.46	0.534	70.4	15.2	250	300
52	”	Cell 3	”	3	0.043	14.22	0.535	71.6	16.3	260	290
53	”	Cell 4	”	3	0.040	13.43	0.536	72.6	15.7	260	440
54	Module 3	Cell 1	Semi-specular	3	0.161	53.80	0.566	75.5	68.9	180	650
55	”	Cell 2	”	3	0.158	52.70	0.568	78.8	70.8	170	730
56	”	Cell 3	”	3	0.161	53.67	0.566	78.8	71.8	170	470
57	”	Cell 4	”	3	0.155	51.50	0.563	76.5	66.6	190	450
58	Module 5	Cell 1	”	3	0.052	17.38	0.541	69.1	19.5	250	110

Continued...

Table 7.5 – Continued

#	Description Module[a]	Cell[b]	Reflector	Cell area (cm^2)	I_{SC} (A)	J_{SC} (mA/cm^2)	V_{OC} (V)	FF (%)	P_{MAX} (mW)	R_{SERIES} (mΩ)	R_{SHUNT} (Ω)
59	”	Cell 2	”	3	0.049	16.24	0.535	71.0	18.5	270	320
60	”	Cell 3	”	3	0.050	16.68	0.535	71.4	19.1	270	230
61	”	Cell 4	”	3	0.050	16.77	0.540	73.0	19.9	250	410
62	Module 3	Cell 1	Diffuse	3	0.165	55.03	0.567	75.4	70.6	170	450
63	”	Cell 2	”	3	0.163	54.43	0.570	79.2	73.7	160	560
64	”	Cell 3	”	3	0.164	54.60	0.569	78.9	73.6	170	430
65	”	Cell 4	”	3	0.158	52.77	0.566	76.8	68.8	180	660
66	Module 5	Cell 1	”	3	0.059	19.83	0.546	70.0	22.7	240	100
67	”	Cell 2	”	3	0.059	19.63	0.544	72.2	23.1	240	350
68	”	Cell 3	”	3	0.056	18.63	0.542	72.3	21.9	250	230
69	”	Cell 4	”	3	0.058	19.45	0.544	74.2	23.6	240	360
Stacked modules - module 5 on top of module 3[d]											
70	Module 3	Cell 3	Diffuse	3	0.110	36.83	0.567	77.9	48.8	270	1000
71	Module 5	Cell 3	”	3	0.086	28.57	0.555	74.1	35.3	220	180

[a]The module (3, 4 or 5) being measured.
[b]Which cell (1, 2, 3 or 4) is being measured. “All cells” indicates all cells are connected in parallel.
[c]Light strikes module 3 first.
[d]Light strikes module 5 first.

Table 7.6: Efficiencies of modules 3, 4 and 5

Description		Measured P_{MAX} (mW)			Ratios[a]		Type 1 efficiency (%)			Type 2 efficiency (%)			Type 3 efficiency (%)		
Module	Cell	B[b]	SS	D	SS:B	D:B	B	SS	D	B	SS	D	B	SS	D
Single modules															
Module 3	Cell 1	65.8	72.1	77.9	1.096	1.184	2.63	2.88	3.12	2.64	2.91	3.14	-	-	-
”	Cell 2	67.5	74.7	80.5	1.107	1.193	2.70	2.99	3.22	-	-	-	-	-	-
”	Cell 3	67.6	74.5	80.4	1.102	1.189	2.70	2.98	3.22	-	-	-	-	-	-
”	Cell 4	62.7	69.3	74.9	1.105	1.195	2.51	2.77	3.00	-	-	-	-	-	-
Module 4	Cell 1	36.9	42.7	47.3	1.157	1.282	1.48	1.71	1.89	1.51	1.76	1.94	-	-	-
”	Cell 2	36.5	42.9	46.9	1.175	1.285	1.46	1.72	1.88	-	-	-	-	-	-
”	Cell 3	37.4	44.9	49.2	1.201	1.316	1.50	1.80	1.97	-	-	-	-	-	-
”	Cell 4	39.8	45.8	50.1	1.151	1.259	1.59	1.83	2.00	-	-	-	-	-	-
Module 5	Cell 1	27.1	34.0	38.0	1.255	1.402	1.08	1.36	1.52	1.05	1.32	1.48	-	-	-
”	Cell 2	25.4	31.8	35.9	1.252	1.413	1.02	1.27	1.44	-	-	-	-	-	-
”	Cell 3	26.4	33.0	36.8	1.250	1.394	1.06	1.32	1.47	-	-	-	-	-	-
”	Cell 4	26.3	33.1	37.0	1.259	1.407	1.05	1.32	1.48	-	-	-	-	-	-
Module 3	All cells	250.0	278.6	297.0	1.114	1.188	-	-	-	-	-	-	2.50	2.79	2.97
Module 4	All cells	146.6	176.2	191.4	1.202	1.306	-	-	-	-	-	-	1.47	1.76	1.91
Module 5	All cells	101.6	129.6	146.0	1.276	1.437	-	-	-	-	-	-	1.02	1.30	1.46
Stacked modules - module 3 on top of module 5															
Module 3	Cell 1	66.2	68.9	70.6	1.041	1.066	3.32[c]	3.54	3.73	3.29[d]	3.55	3.87	-	-	-
”	Cell 2	67.7	70.8	73.7	1.046	1.089	3.32	3.57	3.87	-	-	-	-	-	-
”	Cell 3	68.1	71.8	73.6	1.054	1.081	3.38	3.64	3.82	-	-	-	-	-	-
”	Cell 4	63.4	66.6	68.8	1.050	1.085	3.16	3.46	3.70	-	-	-	-	-	-
Module 5	Cell 1	16.8	19.5	22.7	1.161	1.351	-	-	-	-	-	-	-	-	-
”	Cell 2	15.2	18.5	23.1	1.217	1.520	-	-	-	-	-	-	-	-	-
”	Cell 3	16.3	19.1	21.9	1.172	1.344	-	-	-	-	-	-	-	-	-
”	Cell 4	15.7	19.9	23.6	1.268	1.503	-	-	-	-	-	-	-	-	-
Stacked modules - module 5 on top of module 3															
Module 3	Cell 3	-	-	48.8	-	-	-	-	3.36	-	-	-	-	-	-
Module 5	Cell 3	-	-	35.3	-	-	-	-	-	-	-	-	-	-	-

[a] Relative ratios of semi-specular to black powers (SS:B) and diffuse to black powers (D:B).

[b] Reflector abbreviations: B = black, SS = semi-specular, D = diffuse.

[c] P_{MAX} of corresponding cells on both modules added together for these calculations, e.g. 3.32 % efficiency contains contributions from cell 1 of both modules 3 and 5.

[d] Same as footnote *c* - power output of all cells on *both* modules added together.

The fill factor of the cells is also much improved compared to the first and second modules with values (e.g. 79.1 % for measurement 2) equal to or greater than that of the secondary reference solar cell (77.2 %). The shunt resistances of the cells on module 3 are also high (300-600 Ω, measurements 1-12). Both are a result of the soldering technique, which ensures both low-resistance contact to the entire length of the busbar and a low residual stress as both sides are soldered simultaneously.

Module 3 shows the highest efficiency for a single-sheet device, with a maximum value of 3.22 % (Type 1 using cell 2 or 3 with a diffuse back reflector). The relative improvements when using semi-specular and diffuse back reflectors are 10 % and 19 %. These are close matches to the values obtained from simulation (9 % & 19 %, respectively). The actual efficiency of 3.22 % is lower than that predicted by the model (3.75 %, Table 6.7 Chapter 6), but exact agreement cannot be expected, as the model does not take into account factors such as increased finger shading, edge recombination losses or non-uniform cell illumination. In addition, there are some locations along the edge where fluorescence emission is coupled out of the sheet by the presence of a glue fillet between the sheet surface and the cell.

Module 4 contains the NIR dye. There is a large drop in efficiency from module 3 to module 4. Module 4 efficiencies without a back reflector are approximately 57 % of the corresponding module 3 efficiencies (for example, the type 2 efficiency with no back reflector decreases from 2.64 % for module 3 to 1.51 % for module 4). The low-PLQY NIR dye absorbs the fluorescence photons emitted by the Rot 305 dye and reduces the number reaching the cells. The simulation predicts a module 4 efficiency of 53 % of module 3. This is in agreement with the experimental value. Clearly, combining low-PLQY NIR dye with a visible dye mixture in the same sheet is not beneficial, even with an extremely low NIR concentration.

Although module 5 was intended for use in a stacked structure along with module 3, it was also measured on its own. Maximum efficiency was around 1.5 % with a diffuse back reflector. The efficiencies from module 5 with no back reflector were around 37 % of the module 3 efficiencies. This is again in agreement with the simulation, which predicts 33 %.

The relative improvements in the efficiency of module 5 with semi-specular or diffuse

back reflectors are higher than for module 3. While module 3 absorbs over 80 % of incident solar photons in the range 300-600 nm in a single pass through the sheet as it contains a high concentration of the Rot 305 dye, module 5 only has strong absorption in the range 600-700 nm. Module 5 transmits more light to the back reflector and will therefore absorb more when this light is reflected back.

Modules 3 and 5 were then stacked on top of each other to form a two-layer LSC module, with 3 on top of 5 (light incident on module 3 first). Each cell was again measured individually. When calculating the efficiencies, the power outputs from corrsponding cells on each module were added together, for example the output from module 3, cell 3 added to that from module 5, cell 3. The best efficiency obtained was 3.87 % with a diffuse back reflector, compared with 4.76 % predicted by the model (Table 6.7, Chapter 6).

The relative improvement in the outputs of the cells on module 3 with different back reflectors is less in the stacked configuration. The back reflector is placed behind the entire stack, so light transmitted or emitted by module 3 has to pass through module 5 before reaching the back reflector. Some will be absorbed by module 5 and lost because of the poor PLQY of the NIR dye. There will therefore still be an improvement, but not as great.

Modules 3 and 5 were also stacked with module 5 on top. However, this resulted in a lower efficiency (3.36 %) as a large fraction of incident light is absorbed by the low-PLQY NIR dye in module 5 before it can reach module 3. It is clearly better to stack multiple sheets so that incident light strikes sheets containing higher PLQY dyes first.

In moving from a single to a two-sheet LSC module, the amount of materials (LSC sheet and silicon) used in the construction doubles, as each sheet is identical in shape & size. The embodied energy in the module will therefore also double. However, the *efficiency* increases by only around 20 %. The effect of the extra embodied energy outweighs the benefit of the slight improvement in efficiency. For a two-layer LSC to have a better embodied energy per peak watt, the efficiency would need to at least double compared with a single sheet module, which is clearly not the case. If embodied energy is the deciding factor in choosing a LSC design, a single-sheet

module will provide the best results. This is in agreement with the results obtained from the simulations in Section 6.2. A two-sheet module may offer some advantages in terms of greater insulative properties compared with a single sheet (if it is to be used as a window in a building) and this would need to be accounted for.

The maximum short-circuit current density obtained was around 60 mA/cm^2. Since the current density for a cell under 1-sun AM1.5 illumination is 33 mA/cm^2, this is a concentration of only 1.8x. The cells used on the edges were designed for 5x concentration and as a result have a smaller finger spacing and higher shading losses. If, instead, cells optimised for 1-sun illumination (i.e. no concentration) were used, the shading fraction decreases from 7.9 % to 2.3 %. The corresponding relative increase in the amount of light reaching the cell is then 6 %, and there would be a corresponding increase in the module efficiency. The maximum efficiency obtained of 3.22 % for module 3 would increase to 3.41 %. However, this increase is only possible because of the low concentration ratio of the LSC module. Larger modules *would* require cells designed for higher concentrations, with a corresponding increase in shading losses.

7.2 Large module (60 cm square)

The LSC modules tested thus far have been small, based on 10 cm x 10 cm PMMA sheets. However, simulations have shown that the optimum square LSC size is in the range of 20-60 cm square (Section 6.2). Therefore, to determine both the constructional feasibility and performance of a larger device, the final LSC constructed in the project was based on a 60 cm x 60 cm square PMMA sheet. The nominal thickness was, once again, 0.3 cm.

Prior to the construction of this module, it had been found from accelerated weathering measurements on PMMA samples containing the Lumogen dyes (Section 7.3) that the Violett 570 dye exhibited a poor photostability. Although the optimum dye mixture has previously been determined to be 50 ppm Violett 570 + 350 ppm Rot 305 (Section 6.1.1), it would appear that the Violett 570 dye in this mixture would have a short lifetime in outdoor use. Therefore, since the Rot 305 showed a high photostability, it was decided to remove the violet dye from the mixture and increase the concentration of the Rot 305 dye to 400 ppm to compensate, resulting in a simulated module efficiency of 2.9 % (with no back reflector).

As a result of the large size of the module and the limited length of the solar cells used (10 cm, Section 2.5), several solar cells need to be attached to each edge of the sheet. In addition, to achieve adequate operating voltages, the cells on all of the edges need to be connected in series[166]. However, if all cells are of identical dimensions, the phenomenon of non-uniform edge illumination, which has been widely described previously by other researchers[12, 165, 166, 169, 170, 298, 6, 176], will result in different short-circuit currents from each cell, with lower currents being obtained from cells nearer the corners of the sheet and higher currents from those near the middle of the edges. Since the current in a series-connected string of cells is limited by the cell with the lowest short-circuit current, non-uniform illumination will reduce the total power output of the module and hence the efficiency[166]. Despite this problem being widely acknowledged, there has been little suggestion as to a solution. A logical answer is to vary the dimensions of the cells to achieve similar short-circuit currents from each cell ("current matching") so that they can subsequently be connected in

series without a loss in efficiency. Since the width of the cells is fixed by the thickness of the LSC sheet, the length can be varied to obtain the desired short-circuit current, as has been proposed recently[169]. The present module provides an ideal opportunity to test this idea.

The simulation program "Raytracer" was used to determine the photon intensity distribution along the edge of the LSC using a total of 100,000,000 (100 million) initial photons. The program directly records the locations on the edge where a photon is detected, and a histogram of these locations versus position gives the intensity distribution. Fig. 7.5 shows the resulting plot. In addition to the simulated data points, a fourth-order polynomial has been fitted to the data to obtain a smooth curve suitable for performing integration on later. The intensity at the extreme ends of the edge is ∼60 % of that in the middle.

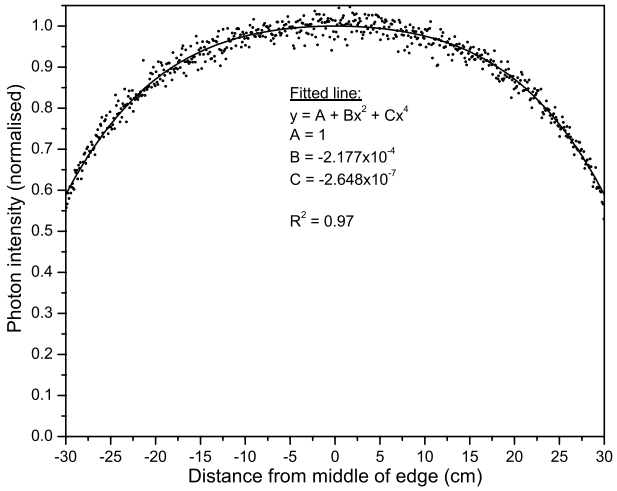

Figure 7.5: Intensity along one edge of a 60 cm x 60 cm LSC sheet, showing simulated values (points) and fitted polynomial (line)

In order to determine the total number of photons incident on a particular length of solar cell and hence the short-circuit current, the polynomial expression in Fig. 7.5 is simply integrated over the length of the cell. If x_1 and x_2 denote the ends of the cell in terms of distance from the middle of the edge, I_{SC} (in arbitrary units) can be calculated from Eqn. (7.1). By using an iterative process, it is possible to calculate a group of cell lengths which both achieve similar I_{SC} and also fit exactly into a 60 cm-long edge. These results are presented in Table 7.7, which lists cell lengths and both

absolute and normalised I_{SC} for three different cell matching schemes.

$$\begin{aligned} I_{SC} &= \int_{x_1}^{x_2} A + Bx^2 + Cx^4\, dx \\ &= \left[Ax + B\frac{x^3}{3} + C\frac{x^5}{5} \right]_{x_1}^{x_2} \\ &= A(x_2 - x_1) + \frac{B}{3}(x_2^3 - x_1^3) + \frac{C}{5}(x_2^5 - x_1^5) \end{aligned} \tag{7.1}$$

For reference, the currents from a set of six unmatched cells (all 10 cm length) are shown under "Unmatched". There is a large variation in the currents of ∼24 %. If the cell lengths are adjusted to obtain the closest possible matching (within the limits of the iteration process, which is 0.01 cm), the results shown under "Matched (perfect)" are obtained. The number of cells required has increased to seven because of the shorter cells in the middle. A variation of 0.2 % is now obtained - a considerable improvement. However, note that the maximum cell length used is 10.15 cm. Since the maximum length of the cells available is only 10 cm, some compromise in the cell lengths is required. This is shown under "Matched (compromised)", where the cell lengths have been adjusted to obtain a maximum length of 10 cm, while still fitting exactly into a 60 cm-long edge. The variation in currents (2.9 %) is larger than the perfectly-matched case, but is still much lower than the unmatched cells.

Table 7.7: Predicted short-circuit currents for different matching schemes

Unmatched			Matched (perfect)			Matched (compromise)		
Length (cm)	I_{SC} (a.u.)	I_{SC} (norm.)	Length (cm)	I_{SC} (a.u.)	I_{SC} (norm.)	Length (cm)	I_{SC} (a.u.)	I_{SC} (norm.)
10.00	7.504	0.756	10.15	7.635	0.998	10.00	7.504	0.971
10.00	9.328	0.940	8.25	7.644	0.999	8.35	7.726	1.000
10.00	9.922	1.000	7.77	7.650	1.000	7.85	7.728	1.000
10.00	9.922	1.000	7.66	7.652	1.000	7.60	7.592	0.982
10.00	9.328	0.940	7.77	7.650	1.000	7.85	7.728	1.000
10.00	7.504	0.756	8.25	7.644	0.999	8.35	7.726	1.000
			10.15	7.635	0.998	10.00	7.504	0.971
Variation: (min-max)		24.4 %			0.2 %			2.9 %

Fig. 7.6 plots the short-circuit currents listed in Table 7.7 versus the centre position of the respective cell. The variations in current can clearly be seen. The relative increase in power which can be expected from using matched cells can be estimated by considering the magnitudes of the current obtained and the number of cells. In both matched and unmatched situations, the short-circuit currents are similar, since the lowest current of the unmatched cells (which determines the total current in a series-connected string) is similar to the currents from the matched cells. However, seven matched cells are used, compared with only six unmatched cells. Since the open-circuit voltage remains relatively constant, regardless of length or illumination intensity, the power output of a matched string should be 7/6 of that of an unmatched string, which corresponds to a relative increase of ∼16 %.

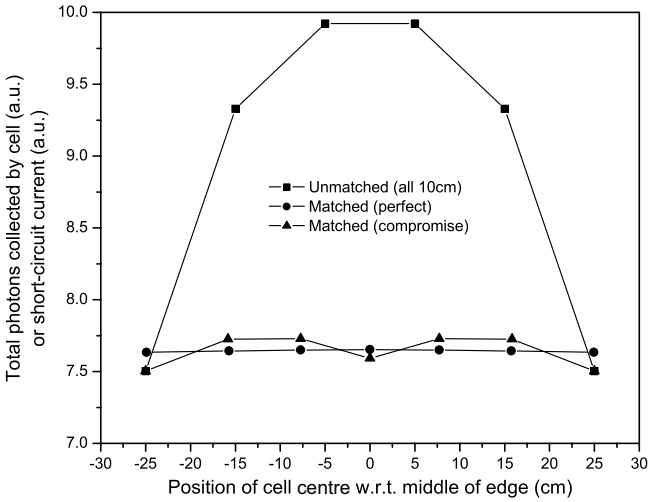

Figure 7.6: Total collected photons (or short-circuit current) of cells attached to 60 cm LSC edge, obtained by integrating the curve in Fig. 7.6 over the length of each cell. Shown for three different matching schemes - unmatched, perfectly matched, and a compromise to obtain a maximum 10 cm cell length.

In order to compare the relative performance of umatched and matched cells on the LSC module, it was decided to apply unmatched cells to two adjacent edges and matched cells to the other two. Fig. 7.7 shows the final layout used. Edges 1 & 2 use six unmatched cells each, while edges 3 & 4 use seven matched cells each. All cells round the entire perimeter were connected in series. This enables the measurement of either individual cells, a complete edge or edges, or the entire module. For constructional details of this module, see Section 2.6.6.

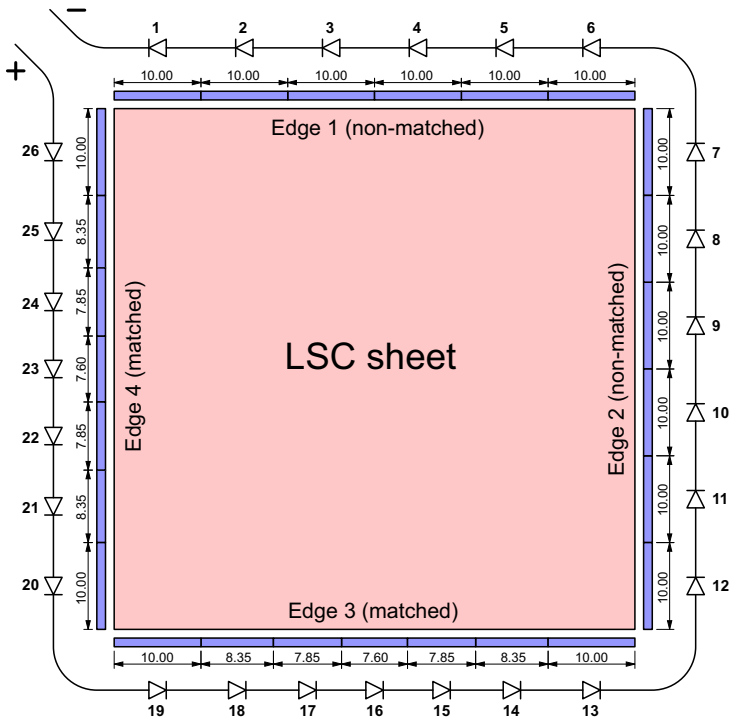

Figure 7.7: Cell layout around edges of LSC sheet. Cell lengths (in cm) and polarities shown.

A total of 26 cells were cut to the appropriate lengths (only those <10 cm needed cut) and tabbed. Before they were attached to the edge of the LSC sheet, their short-circuit currents were measured under AM1.5g illumination at normal incidence to determine if any had been damaged during the cutting process and also whether I_{SC} is proportional to the length of the cell. The measured currents are shown in Fig. 7.8.

There are no damaged cells, as all of the measured currents are near the fitted line. The spread in values obtained (for example, at 10 cm length) can be explained by the slight variation in the position of the cell busbar relative to the outline of the cell - two different laser processes are used for finger patterning and scribing, and relative alignment between these processes can vary, resulting in a variation in the illuminated area of the cell.

I_{SC} is indeed proportional to the cell length, as expected. It is of interest to calculate the short-circuit current density, J_{SC} of the cells. The illuminated width of the cells is 0.37 cm, including part of the busbar which is also illuminated. From the gradient of the fitted line, each cell produces a lineal current density of 12.97 mA/cm. Therefore,

the area current density is $J_{SC} = 12.97/0.37 \approx 35\,\mathrm{mA/cm^2}$. This is close to the measured $J_{SC} \approx 34\,\mathrm{mA/cm^2}$ of full-wafer LGBC cells (see, for example, the reference cells used in the first row of Tables 7.2, 7.3 & 7.5), giving a further indication that all cells are functioning properly.

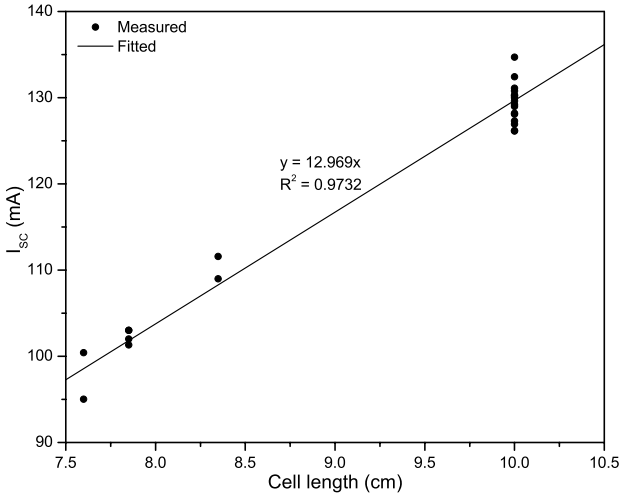

Figure 7.8: Short-circuit currents of edge cells, measured under 1-sun illumination before attachment to LSC edge.

The I-V characteristcs of individual cells, edges and entire module were measured using the SPI-SUN flash tester (Section 2.7.2). Table 7.8 lists the relevant electrical characteristics for each measurement. The short-circuit current, current density (where relevant), open-circuit voltage, fill factor, maximum power, series and shunt resistance, and AM1.5g module efficiency are all shown. Module efficiency is only meaningful for measurements performed on an entire edge, edges or the entire module, and is calculated from the P_{MAX} of an individual measurement. The correction factor of 1.055 has been used in the calculation of efficiency to obtain a value which is valid for AM1.5g illumination (Section 2.7.2). The results of these measurements are described in detail below.

Individual cells were measured first. The most immediate observation is that the current density is in the range 140-190 $\mathrm{mA/cm^2}$, indicating that they are operating under concentrating conditions. The average J_{SC} of all the edge cells is $168\,\mathrm{mA/cm^2}$. Therefore, since $J_{SC} \approx 34\,\mathrm{mA/cm^2}$ for a cell under 1-sun illumination, the overall concentration ratio of the LSC is $168/34 \approx 5$x. The cells, which were designed for 5x

Table 7.8: Sixth module electrical characteristics

Description	I_{SC} (A)	J_{SC} (mA/cm^2)	V_{OC} (V)	FF (%)	P_{MAX} (W)	R_{SERIES} (mΩ)	R_{SHUNT} (Ω)	Efficiency (%)
Cell 1	0.430	143	0.615	76.4	0.202	175	68	-
Cell 2	0.541	180	0.624	77.4	0.261	135	71	-
Cell 3	0.576	192	0.627	77.6	0.280	128	36	-
Cell 4	0.562	187	0.624	76.7	0.269	125	66	-
Cell 5	0.534	178	0.628	78.7	0.264	149	64	-
Cell 6	0.467	156	0.618	77.5	0.224	123	35	-
Cell 7	0.427	142	0.617	77.5	0.204	153	63	-
Cell 8	0.520	173	0.620	76.2	0.246	136	29	-
Cell 9	0.547	182	0.625	75.1	0.257	141	52	-
Cell 10	0.548	183	0.622	78.0	0.266	123	44	-
Cell 11	0.534	178	0.623	68.7	0.228	154	28	-
Cell 12	0.421	140	0.617	78.9	0.205	159	68	-
Cell 13	0.424	141	0.616	78.6	0.205	139	57	-
Cell 14	0.429	171	0.624	79.2	0.212	133	73	-
Cell 15	0.408	173	0.625	79.2	0.202	127	107	-
Cell 16	0.403	177	0.624	75.6	0.190	169	63	-
Cell 17	0.409	174	0.623	79.6	0.203	129	59	-
Cell 18	0.394	157	0.620	79.2	0.194	139	50	-
Cell 19	0.429	143	0.616	77.6	0.205	140	68	-
Cell 20	0.445	148	0.614	78.7	0.215	127	44	-
Cell 21	0.458	183	0.621	77.6	0.220	122	72	-
Cell 22	0.436	185	0.624	79.2	0.215	137	82	-
Cell 23	0.436	191	0.619	80.0	0.216	136	266	-
Cell 24	0.446	189	0.623	78.9	0.219	116	43	-
Cell 25	0.462	184	0.621	79.4	0.228	116	50	-
Cell 26	0.439	146	0.615	78.5	0.212	150	62	-
Edge 1	0.432	-	3.751	86.2	1.398	632	365	1.64
Edge 1 (2)	0.435	-	3.747	83.6	1.361	705	228	1.60
Edge 2	0.434	-	3.751	83.5	1.359	976	162	1.59
Edge 2 (2)	0.429	-	3.741	83.1	1.332	666	294	1.56
Edge 3	0.399	-	4.387	81.1	1.421	837	314	1.67
Edge 4	0.439	-	4.408	81.2	1.572	795	416	1.84
Edges 1+2	0.429	-	7.495	83.3	2.680	1524	369	1.57
Edges 3+4	0.396	-	8.789	81.5	2.389	1732	320	1.66
All edges	0.393	-	16.243	82.9	5.294	3107	530	1.55
All edges with refl.	0.437	-	16.237	80.4	5.704	2661	491	1.67

concentration (Section 2.5) are therefore an ideal match to the intensity at the sheet edge. This concentration ratio is less than the predicted 7.5x (Fig. 6.15), but, again, exact agreement cannot be expected for the reasons discussed previously in Section 7.1.3.

It should be noted that cell 11 was damaged during the attachment process (cracked near one end) which is the reason for its unusually low fill factor (68.7 %, compared with 76-80 % for the rest of the cells). An examination of the I-V curve for this cell

showed that the shunt resistance was nearly half that of the other cells. However, despite this, both I_{SC} and V_{OC} are comparable to other cells in a similar location (cells 2, 5, 8) and the performance of the rest of the module was not affected.

The short-circuit currents of the individual cells are plotted in Fig. 7.9 versus the centre position of each cell. The cells on edges 1 and 2, which are unmatched, exhibit a wide variation in I_{SC} between the middle and end of the edge, with a difference of ∼25 %. This is in close agreement with the simulated value of 24.4 %. The line (**– –**) shows the simulated distribution of cell currents along the unmatched edges (obtained from Fig. 7.6). The measured values for edges 1 and 2 are in good agreement with this.

Edges 3 and 4, which use matched cells, exhibit good current matching between cells, with a min-max variation of ∼8.2 % and ∼5.6 %, respectively. The average short-circuit current from cells on these edges (0.41-0.43 A) is close to the minimum current obtained from the cells on the unmatched edges (cells 1, 6, 7, 12), as expected. The simulated distribution of currents for a string of matched cells (also obtained from Fig. 7.6) is shown by the line (**----**) and is a close match with edges 3 and 4. The min-max variations are greater than those predicted in Table 7.7 because of the random distribution in cell currents, even among cells of identical lengths (seen in Fig. 7.8), a result of variation in properties (ARC coating, edge defects, contact resistance etc) between cells.

Unfortunately, the cells on edge 3 all exhibit a lower current than those on edge 4, despite both edges using identical cell lengths and layout. Currents are on average ∼10 % lower. This is explained by two problems which occurred during the attachment of cells to that edge of the module. Since the 60 cm x 60 cm sheet was cut from a larger 120 cm x 90 cm sheet (the original size cast), there was some thickness variation across the sheet (the glass mould plates deflect slightly during casting). As a result, the thickness of the each edge was slightly different (0.28, 0.29, 0.32 and 0.29 cm), with edge 3 having the greatest thickness of 0.32 cm. This is at the limit of the active width of the cell, also 0.32 cm. When combined with the slight planar bend in the cells caused by contraction of the soldered tabbing, some of the cells did not cover the entire width of the LSC edge, causing light to be lost. This problem was most

pronounced with cells 15-18, which also exhibit the lowest I_{SC} of the cells on that edge. In addition, cells on edge 3 exhibited a higher proportion of adhesive defects (regions of the cell not coupled to the sheet edge because of a lack of adhesive) than any of the other edges. The reasons for this are unknown, although it may be related to the greater thickness of that particular edge - the cell attachment process seems to perform better with thinner sheet edges. These problems are far less evident with the other edges, which were thinner and have much better adhesive coverage.

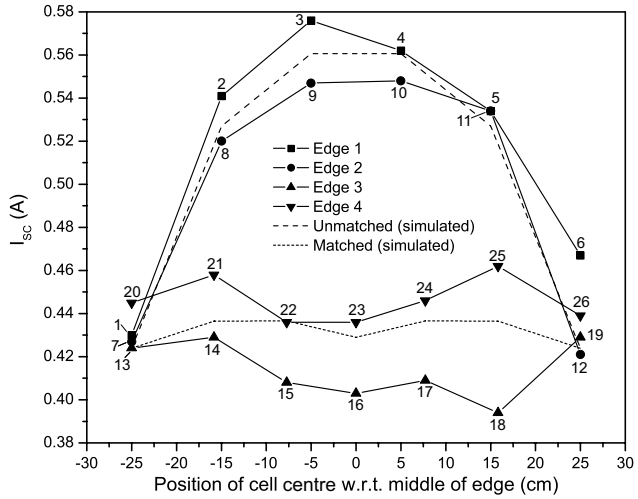

Figure 7.9: Measured I_{SC} of cells on all edges of LSC. The predicted currents (scaled from Fig. 7.6) are indicated by the dashed and dotted lines. Numbers at data points indicate the corresponding cell.

Next, individual edges were measured. As expected, the I_{SC} of an entire edge is limited by the cell with the lowest I_{SC}, and the V_{OC} of the entire edge is the sum of the V_{OC} of the individual cells. Edges 1 and 2 have comparable power outputs and the calculated module efficiencies are correspondingly similar (in the range 1.56-1.64 %). Edge 3 displays only a slightly higher power output than 1 and 2, as a result of the low I_{SC} of the individual cells. However, edge 4 has a significantly higher power output, ∼15 % greater than that of the unmatched edges, which is in close agreement with the predicted increase of 16 % obtained earlier. The corresponding module efficiency was 1.84 %, the highest of all measurements. Although this is less than predicted by the model (as was seen before for the other modules), several experimental factors can account for the difference. For example, although the minimum possible amount of adhesive was applied to the edges of the sheet, some inevitably formed a fillet

which covered the surface slightly (∼0.05 cm) once the cell was applied. In addition, several cells showed areas where there was an air space between the cell surface and the edge of the sheet where adhesive was not present. Both factors result in losses, and a reduction in efficiency.

The two pairs of edges (1+2 in series and 3+4 in series) were then measured. However, because of the low I_{SC} of the cells on edge 3, no significant increase in the power output of edges 3+4 compared with edges 1+2 was observed, despite the higher power output of edge 4 measured alone.

Finally, all edges were connected in series. As expected, the resulting I_{SC} was limited by edge 3 and the module efficiency was similar to that obtained from the unmatched edges alone. To conclude the measurements, a diffuse white back reflector was placed behind the module and a relative increase in power of ∼8 % was observed. Since the cells in this module are shielded from directly-reflected sunlight by the wooden frame, this increase is in agreement with that observed previously for modules where the cells have also been shielded, for example module 2 (Section 7.1.2) where a mirrored strip was used.

7.3 Dye weathering

Samples of PMMA containing the Lumogen dyes were subjected to an accelerated weathering regime using the QUV tester (Section 2.8) to measure their photostabilities. Exposure times were in one-week intervals with a maximum of five weeks. Two different concentrations of each dye were exposed, as listed in Table 7.9. In addition, a sample of clear (undoped) PMMA and a sample containg a mixture of 350 ppm Violett 570 + 900 ppm Rot 305 were also exposed. None of the samples contained UV stabiliser, since this made measurements of the absorption spectrum of the violet dye impossible because of the strong UV stabiliser absorption below 420 nm. The main objective is to determine the relative photostabilities of the dyes, and the presence of UV stabiliser would make this impossible since it would "protect" the dye from UV radiation.

As it is impossible to know the concentration of dye remaining in the sheet, it is not possible to calculate the mass absorption coefficient (ppm^{-1} cm^{-1}). Therefore, the absorption coefficient of the sheet as a whole (cm^{-1}) was calculated. The surface reflectivity of the samples was corrected for. The PMMA will degrade as it is exposed and its absorption spectrum will change. However, the extent of this will depend on whether a dye is present in the sample and in what concentration. Corrections cannot be made for the PMMA absorption, because the degradation of the PMMA is altered by the presence of the dye. The absorption coefficients plotted in the following figures are therefore a combined coefficient which includes both dye and PMMA absorption.

Table 7.9: Sample concentrations for weathering

Dye	Concentration (ppm)
Violett 570	65
“	194
Gelb 083	35
“	105
Gelb 170	35
“	105
Orange 240	25
“	195
Rot 305	70
“	210

The spectra of the clear sample are shown in Fig. 7.10. As exposure progresses, there is a change in absorption in the region 300-500 nm. There is initially an increase in absorption (up to 3 weeks) as the PMMA degrades and breakdown products are formed which absorb in this region. However, after three weeks, the absorption begins to decrease. This is possibly due to the breakdown products from the first three weeks being themselves degraded. The effect is visible - after 3 weeks the sample showed a brownish colouration, but this had faded in the 5 week sample.

The PMMA degradation is caused by light in the blue/UV region of the spectrum, as only this region has sufficient energy to cause damage to the bonds and structures of the PMMA or dyes[265, 264, 263, 325]. A UV stabiliser acts by absorbing light in this region, preventing it reaching the dye. As is seen later, some of the fluorescent dyes can act as UV stabilisers because they have strong absorption in this region.

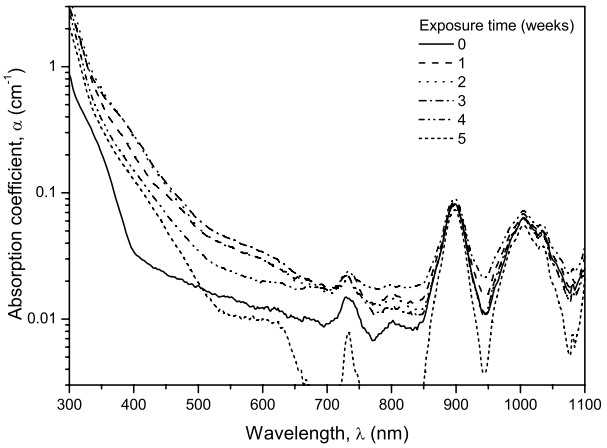

Figure 7.10: Weathered clear PMMA absorption spectra. Note logarithmic vertical scale.

Figs. 7.11-7.15 show the progression in absorption spectra for each of the five Lumogen dyes. Parts a) and b) of each figure show the low and high concentration samples respectively.

Violett 570 showed a rapid decrease in absorption with exposure time (Fig. 7.11a). The peak absorption dropped to around 40 % of its initial value over the five week exposure time. There were changes in two other regions of the spectrum. From 300 nm to around 330 nm, there was again the sign of PMMA degradation, with the absorption increasing up to week 1 and then decreasing. However, the magnitude of the increase is less than for the clear PMMA sample, indicating that the violet dye is protecting the PMMA by absorbing harmful wavelengths. It is therefore acting as a UV stabiliser.

There was a steady increase at wavelengths above 420 nm caused by a combination of increased absorption from both dye and PMMA breakdown products. This increase was also present in the undoped PMMA sample and will lead to an increase in re-absorption losses. It is not so critical for the first four Lumogen dyes used in this experiment, as they are not likely to be used in an LSC sheet on their own so their fluorescence is more likely to be absorbed by another dye rather than by the breakdown products because of the higher probability of absorption by the second dye.

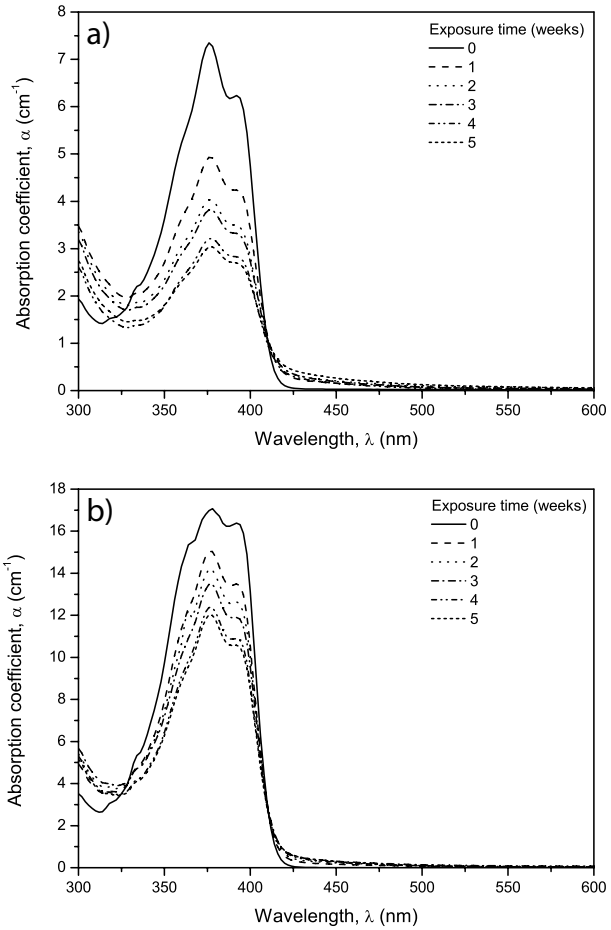

Figure 7.11: Weathered Violett 570 absorption spectra a) 65 ppm b) 194 ppm

The higher concentration of dye (Fig. 7.11b) still shows degradation, but to a lesser degree. Peak absorption decreases to 70 % of its initial value over five weeks. Degradation has less effect simply because there are more dye molecules present in the sample.

Gelb 083 (Fig. 7.12 a & b) also shows a decrease in dye absorption, although not as much as with Violett 570. A higher dye concentration again leads to less of a decrease. An increase above 500 nm is present, which will increase re-absorption losses. The increased concentration reduces the amount of PMMA degradation, as seen from the increase around 300 nm.

Gelb 170 (Fig. 7.13 a & b) is similar to Gelb 083. The absorption above 550 nm is increased by the degradation.

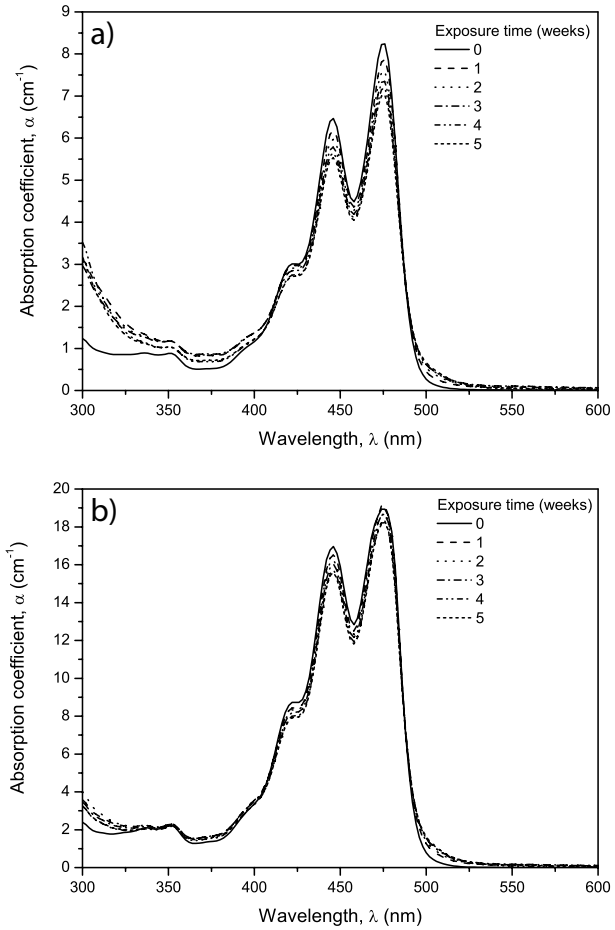

Figure 7.12: Weathered Gelb 083 absorption spectra a) 35 ppm b) 105 ppm

Spectra for Orange 240 are shown in Fig. 7.14 a & b. Note the much greater increase in PMMA absorption from 300-400 nm. The absorption of the Orange 240 dye is weaker in the UV compared with the other dyes and will therefore protect the PMMA less against degradation.

Several absorption peaks appear at long wavelengths as exposure progresses, at 700 nm & 800 nm (shown in the inset of Fig. 7.14b). These are caused by breakdown products of the dye. The absorption increases until week 3 and then decreases, indicating that the breakdown products are being degraded. These peaks are several orders of magnitude greater in strength than the tail absorption of the dye on its own and will cause severe re-absorption. Seybold[48] also observed this behaviour.

Fig. 7.15 shows spectra for Rot 305. Little degradation of the dye is evident. There is hardly any degradation of the PMMA, especially with the higher concentration of

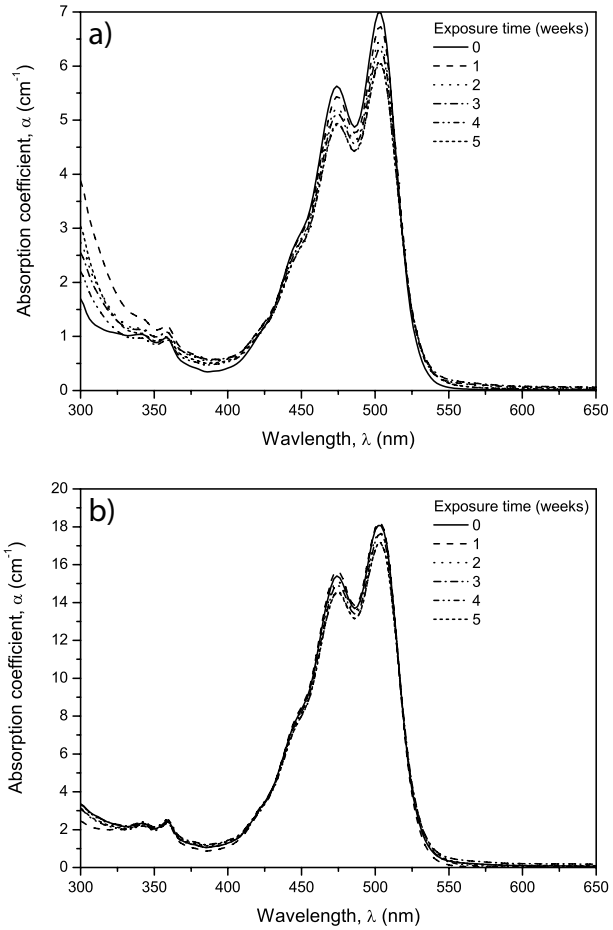

Figure 7.13: Weathered Gelb 170 absorption spectra a) 35 ppm b) 105 ppm

dye. The Rot 305 dye has an high absorption coefficient in the blue/UV and will, therefore, protect the PMMA from damage. This is an extremely beneficial feature, as extra UV stabilisers do not have to be added to the sheet to protect it.

There is no sign of any increased absorption in the tail from breakdown products (above 650 nm). This is especially important for Rot 305, as it will normally be the longest-wavelength dye used in an LSC and re-absorption will be most pronounced.

Fig. 7.16 shows the progression of absorption spectra for the mixed-dye sample containing 350 ppm Violett 570 + 900 ppm Rot 305. However, because of the extremely high absorption, no trends are detectable as exposure time is increased.

The peak absorption coefficients of the spectra from Figs. 7.11-7.15 are plotted together in Fig. 7.17. Low and high concentrations have been separated into parts a)

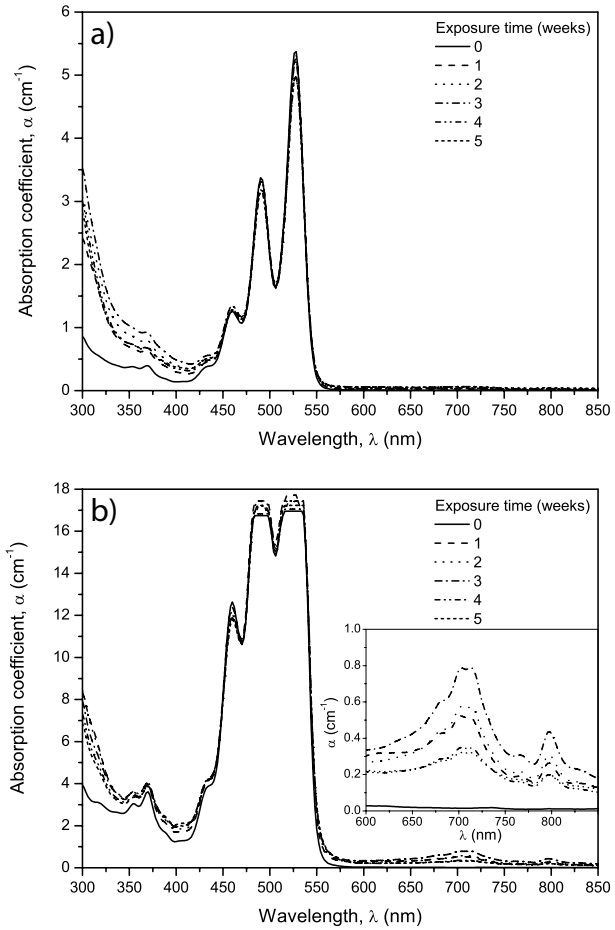

Figure 7.14: Weathered Orange 240 absorption spectra a) 25 ppm b) 195 ppm. Inset shows close-up of 600-850 nm region. Clipping at the top of the graph is caused by the sensitivity limit of the spectrophotometer.

& b) respectively. The error in the normalised peak absorption coefficients is ±0.01, although error bars have not been shown on the graph for clarity. Clearly, Violett 570 is the worst-performing dye. Absorption drops to only 40 % of its initial value after 5 weeks. The most stable dye is Rot 305, which drops to 93 % after five weeks. At higher concentrations (210 ppm), absorption coefficient for the Rot 305 dye remains unchanged. Van Sark *et. al.*[62] also found Rot 305 to be the most stable dye.

A higher dye concentration results in a lower rate of decay of the absorption coefficient. This is shown in Fig. 7.18 for two different concentrations. Instead of dropping to 40 %, the absorption coefficient of the higher concentration drops to around 70 %.

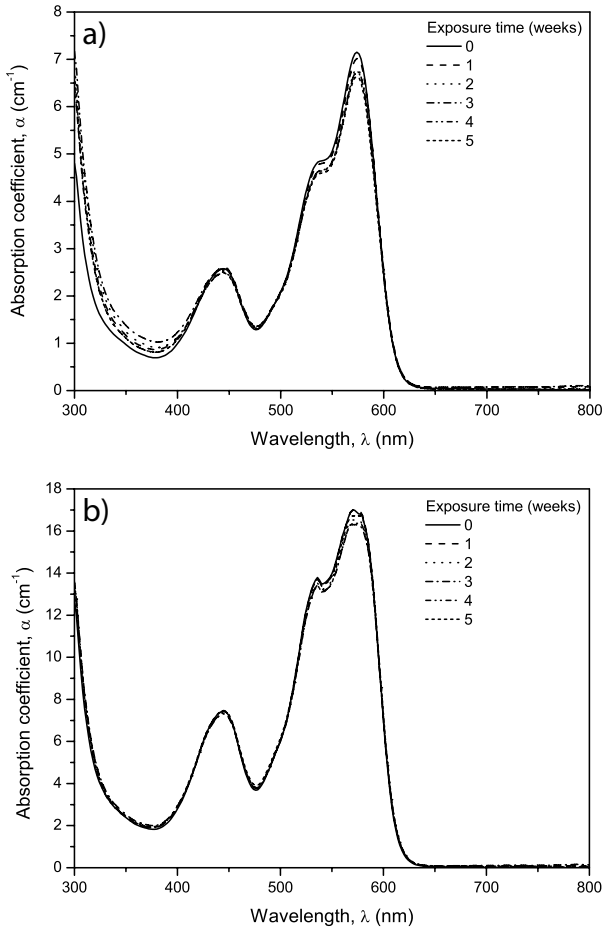

Figure 7.15: Weathered Rot 305 absorption spectra a) 70 ppm b) 210 ppm

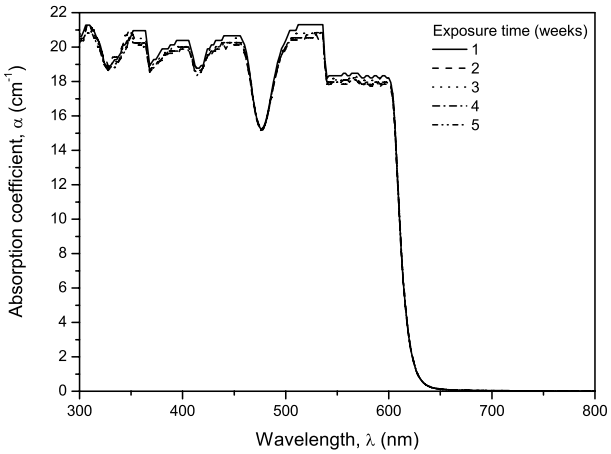

Figure 7.16: Weathered mixed-dye absorption spectra. Clipping at the top of the graph is caused by the sensitivity limit of the spectrophotometer.

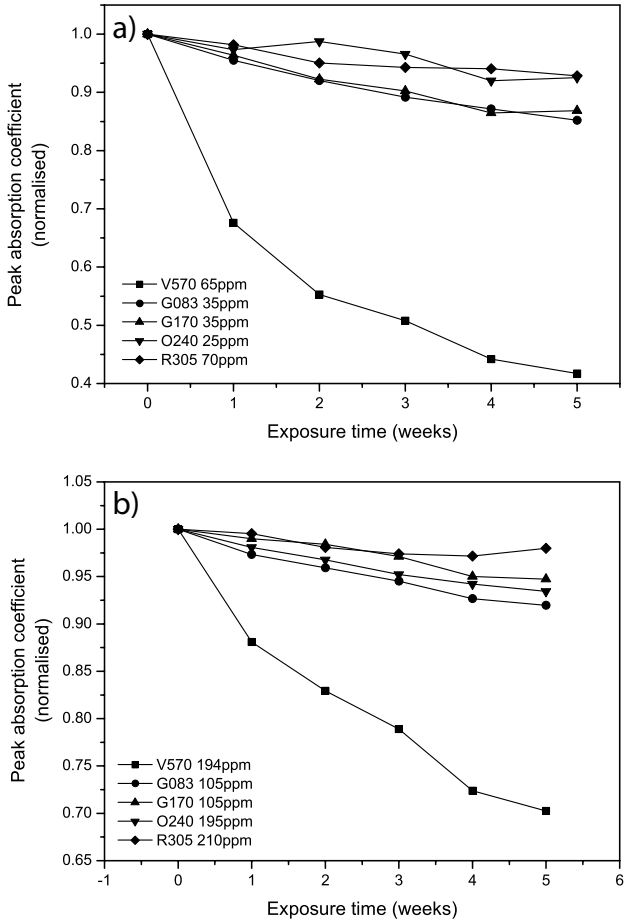

Figure 7.17: Peak absorption coefficient progression a) low concentrations b) high concentrations

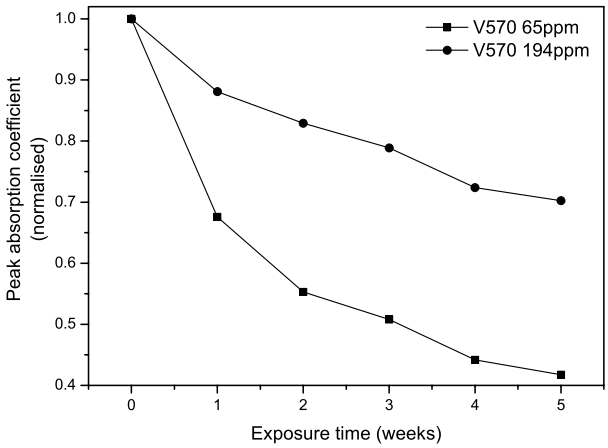

Figure 7.18: Effect of violet dye concentration on absorption decay rate

To try to obtain some correlation between the time for which the samples were exposed in the accelerated weathering machine and an equivalent time in real-world conditions, another sample containing 65 ppm Violet 570 was exposed (July to September 2008 inclusive) for a total of four months outside in San Francisco, California. The peak absorption coefficient of the same was measured after exposure and this was compared with the previous data obtained from the QUV tester. Fig. 7.19 shows the results, with an exponential decay fitted to the QUV data. The peak absorption coefficient measured from the California sample was $2.43\,\mathrm{cm}^{-1}$, which corresponds to an exposure time in the QUV machine of 7.2 weeks. In other words, a time of 7.2 weeks in the QUV tester is equivalent to four months (17.2 weeks) exposure in California. Therefore, the acceleration factor of the weathering is 2.4 times greater than real life. This should only be viewed as an approximate figure, however, since accurate correlation between real-world and accelerated weathering is only possible if a sample is placed outside for several years' exposure to experience the full range of climatic conditions. Correlation coefficients are notoriously difficult to determine because of wide variations in climatic conditions (illumination, temperature, humidity, duration) over time and between locations, and also differences in material sensitivity (for example, between different dyes and host materials)[267, 266].

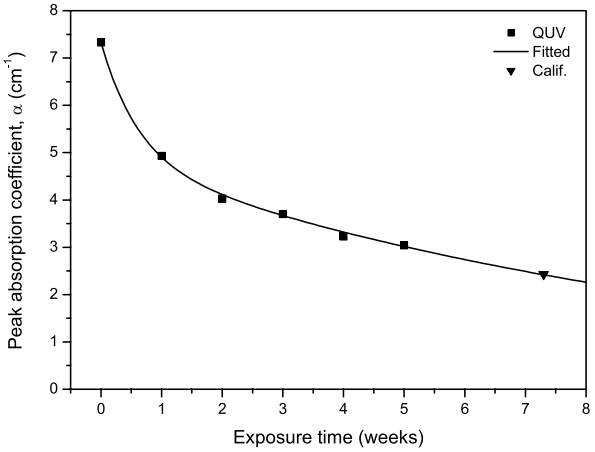

Figure 7.19: Comparison with exposure in California

7.4 Angular and light distribution sensitivity

The angular dependence of the power output of an LSC and its sensitivity to sunny/cloudy conditions were measured and compared with a standard mc-Si module. For angular dependence measurements, both the LSC and the mc-Si module were mounted on a computer-controlled rotary table[240], as shown in Fig. 7.20. Illumination was provided by a tungsten-halogen lamp (Section 2.2.4) and the power output was measured with a sourcemeter (Section 2.7.3). The lamp was positioned at a distance of approximately 3 m from the module under illumination to ensure uniform intensity across the sample.

The table was stepped in 10° increments and the I-V curve measured at each position. From this, the maximum power output at each position was calculated. Fig. 7.21 shows a plot of this versus angle for both the LSC and mc-Si module. The incident power on the device as it is rotated is related to the cosine of the incident angle. The best angular performance that can be expected from the device is also a cosine. This theoretical limit is also plotted in Fig. 7.21. 0° corresponds to light normally incident on the module.

The LSC performs closest to the cosine, with two deviations. At angles below 50°, the output is greater than the theoretical cosine. The LSC collects light from all directions, including light from the lamp which is scattered from objects around the

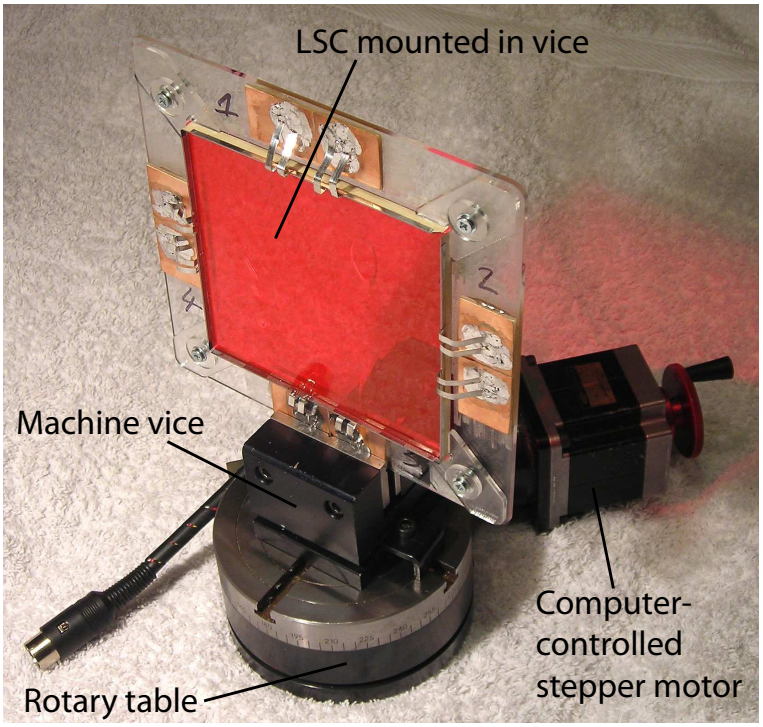

Figure 7.20: LSC mounted on computer-controlled rotary table

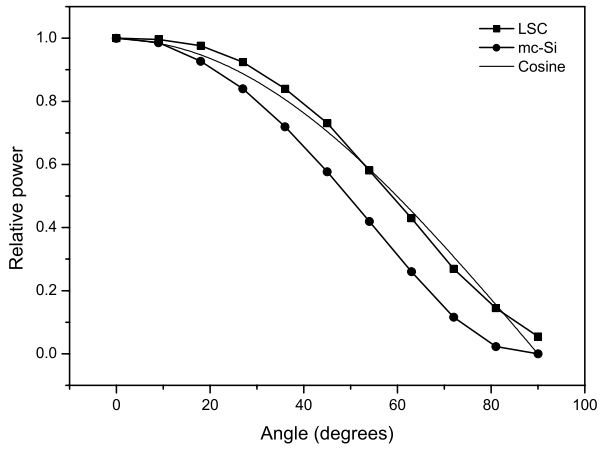

Figure 7.21: Angular variation of output power

laboratory. Despite surrounding the measurement setup with black cloth, there was still sufficient scattered light to increase the power output above the theoretical maximum. This is also the reason for the non-zero power obtained from the LSC at 90°, when it is collecting purely scattered light. In addition, although the tungsten-halogen is at a sufficient distance to ensure uniform illumination, it does not represent a point source. The angle subtended at the sample by the bulb is approximately 2°

(a 10 cm-long filament at a distance of 3 m). The module will therefore still receive some illumination even at 90° incident angle. This contributes to the non-zero power detected at 90° incident angle. At large incident angles, there is a greater loss because more incident light is reflected from the surface of the LSC or mc-Si module.

If the power is integrated over all angles, the LSC results in an 18 % higher output power compared with the mc-Si module. This is in agreement with data obtained by Friedman[12, 13] which showed a 20 % greater integrated energy output over a day's exposure compared with a mc-Si module.

The relative performance of the LSC and mc-Si module under different illumination (direct or diffuse) was measured by recording I-V curves of both devices simultaneously outside under both sunny and cloudy conditions. The maximum power points were then calculated. Table 7.10 shows the results obtained.

Table 7.10: Direct/diffuse power outputs (W)

	Direct	Diffuse	Direct/diffuse ratio
LSC	0.113	0.008	14.1
mc-Si	1.175	0.060	19.6

The direct/diffuse ratio for the LSC is 28 % smaller than that for the mc-Si, meaning that the LSC performs 28 % better than the mc-Si when going from direct to diffuse lighting conditions. This is due to the LSC's better ability to collect diffuse light and the concentration provided at the edges.

7.5 Conclusions

Based on the theoretical simulations of optimum dye concentrations in Section 6.1.1 , a range of LSC modules was constructed using a variety of constructional techniques. The highest single-sheet module efficiency achieved was 3.22 %, obtained from a 10 cm x 10 cm sheet containing only Rot 305 and Violett 570 and with a diffuse back reflector. This is the highest efficiency achieved thus far for an LSC module of practical size using a bulk-doped sheet and silicon solar cells. By adding a second sheet containing an NIR-emitting dye, the efficiency was increased to 3.87 %, again with a diffuse back

reflector.

A large, 60 cm x 60 cm module based on a sheet containing 400 ppm of only the Rot 305 dye was constructed and exhibited a maximum efficiency of 1.84 %. Most importantly, it successfully demonstrated the possibility of current-matching the edge cells to maximise the output power by varying their lengths. When current-matched cells were used, a ∼15 % increase in the output power was obtained. This is in agreement with predictions.

Accelerated weathering was also performed on the full range of Lumogen F dyes. The results show that Rot 305 is the most photostable of the entire range. In addition, because of its strong UV absorption, it acts as a UV stabiliser since the degradation of the PMMA itself was less in samples containing Rot 305. Violett 570 also acts as a UV stabiliser. Since proprietary UV stabilisers absorb nearly all light below 400 nm (determined from transmission measurements on commercial PMMA samples) and turn it to heat, a reduction in efficiency would result if UV stabiliser had to be deliberately added to the sheet. However, both Violett 570 and Rot 305 can make use of the UV radiation, avoiding the need for a UV stabiliser.

Chapter 8

Conclusion

8.1 Summary

This thesis has presented an in-depth study of a range of aspects of LSC devices, including measurement of the optical properties of fluorophores, analysis of re-absorption losses in LSC sheets, cost and energy analysis, and the design, construction and performance of several LSC modules. The important findings are summarised below.

Thermal lens

Despite extensive study, the thermal-lens technique proved unreliable for measuring the PLQY of dye-doped PMMA samples. However, it should not be discounted entirely, as it offers several distinct advantages over the integrating-sphere technique. The chief advantage is the ability to probe an extremely small region of the sample (of the order of 100 μm), which greatly reduces the effects of self-absorption, in contrast to the integrating-sphere technique where a self-absorption correction is required even for low sample concentrations because of the multiple reflections inside the sphere. Further investigation of the thermal-lens technique would be advantageous, with specific focus on measurements in solid samples, since it has been utilised successfully by other researchers [270, 271, 272, 205, 204, 273, 274, 275, 276, 277, 278, 279, 280, 281, 282, 212, 211, 109, 269, 283, 213, 284].

Fluorophores

Both organic and inorganic fluorophores have been studied in this thesis. The Lumogen F range of visible-emitting organic dyes all exhibited high (>95 %) quantum yields and had absorption wavelengths ranging from 300 nm to 650 nm (Section 4.1). They were also easily incorporated into different organic hosts. Most importantly, they retained their high PLQY even at high concentrations or in mixtures with each other, indicating the possibility of using several dyes in a mixture to absorb a wide range of solar wavelengths. Several NIR-emitting organic dyes were studied but these all exhibited much lower PLQYs (60-80 %) than the visible-emitting dyes (Section 4.4.1). When used in an LSC, these result in greater losses because of the low PLQY and the multiple re-absorption/re-emission events which occur.

The most suitable organic visible-emitting dye is Rot 305, with its wide absorption range (300-650 nm), near-unity PLQY, and the highest photostability of all the Lumogen F dyes. Since it retains its near-unity PLQY even at concentrations as high as 1600 ppm, a high concentration of this dye alone can be used in an LSC sheet to absorb a wide range of solar wavelengths. Accelerated weathering results demonstrated that both Rot 305 and Violett 570 can act as UV-stabilising agents, protecting the host PMMA from degradation, as a result of their strong absorption in the UV region (Section 7.3).

Measurements of the optical properties of Rot 305 at different excitation wavelengths, including excitation in the absorption tail, showed that the PLQY was independent of excitation wavelength (Section 4.3), thus lending further support to the possibility of a single-dye LSC containing only Rot 305. The emission spectral profile was found to be constant at excitation wavelengths within the main absorption spectrum and showed a red-shift at excitation wavelengths in the absorption tail, due to excitation of dye aggregates. Since all re-absorption effects result in excitation in the absorption tail, this red-shift results in a reduction in re-absorption losses.

All of the Lumogen F dyes exhibit an absorption tail, due to the combined effects of absorption from thermal levels and aggregate absorption, which extends to wavelengths several hundred nanometers above the end of the main absorption spectrum. Despite the low magnitude of this tail, its effect is significant - up to a 15 % rel-

ative loss in edge-collected photons in an LSC containing 600 ppm of Rot 305 dye (Fig. 5.15). Measurements on strip LSC samples have shown that the largest fraction of re-absorption occurs in the first few centimeters of pathlength, and subsequent re-absorption is due to the low-magnitude tail.

Rare-earth complexes appear to provide an ideal solution to the problem of re-absorption, due to their large Stokes shift between absorption and emission. Although their PLQY is less than that of organic dyes, this is less of a concern because there is no re-absorption. The europium-containing complex studied here had a PLQY of 86 % and, as was shown in Section 5.3.3, this resulted in a higher optical efficiency for an LSC sheet than the Rot 305 organic dye, despite the lower PLQY of the complex. The PLQY of complexes with NIR-emitting ions is currently low (1-2 %), but if this can be increased (by the use of, for example, deuterated ligands or hosts), RE complexes provide an extremely promising means for increasing LSC efficiency[88, 154].

LSC design

The efficiency, cost and embodied energy of LSC modules were simulated using the ray-tracing program over a wide range dye mixtures, concentrations, sheet sizes, thicknesses and aspect ratios.

For a single-sheet LSC module, the dye mixture which resulted in the highest module efficiency was, as expected, one containing a high concentration of Rot 305 dye. The optimum concentration was in the region of 350 ppm for a 0.3 cm-thick LSC sheet (Section 6.1.1). Addition of a small amount (50 ppm) of Violett 570 dye was found to improve the efficiency slightly by increasing the absorption of the LSC sheet around 370 nm, where the absorption of Rot 305 is lowest. This optimum dye mixture is in line with results from other researchers, who also found a high Rot 305 concentration to be optimum[19, 299, 67]. The optimum concentration is a balance between absorbing sufficient incident solar radiation whilst keeping re-absorption losses within the sheet to a minimum. For a 10 cm x 10 cm sheet, the predicted efficiency is 3.75 % with the use of a back reflector.

The addition of NIR-emitting dyes to the Rot 305/Violett 570 mixture in an attempt to increase the absorption range of the sheet results in a sharp decrease in

the efficiency, even at low concentrations. The addition of only 15 ppm of KF402, the NIR-emitting dye with the highest PLQY of 78 %, results in a ∼38 % relative decrease in the module efficiency of a 10 cm x 10 cm LSC module (Section 6.1.1). Despite the increase in absorption range, this is outweighed by the greater losses within the sheet due to the low PLQY of the NIR-emitting dye. Unless the NIR-emitting dye also has near-unity PLQY, its use in a single-sheet LSC is not possible.

When the NIR-emitting dye is placed in a separate sheet to form a two-sheet LSC module, an efficiency increase can be achieved, as the low-PLQY NIR dye does not interfere with the fluorescence from the high-PLQY visible dyes in the first sheet. The predicted efficiency of a 10 cm x 10 cm two-sheet module, with the first sheet containing 350 ppm Rot 305 + 50 ppm Violett 570 and the second sheet containing 80 ppm of NIR3, was 4.62 % (with a back reflector) - a significant increase over the single-sheet module.

A diffuse back reflector is an important means of increasing the LSC efficiency, capable of achieving relative improvements of ∼10 % relative[28]. It acts both by reflecting back unabsorbed sunlight and also rear escape-cone losses, giving them a chance to be re-absorbed by the sheet. There is an additional benefit of directly reflecting sunlight on to the edge-mounted solar cell, although this effect is only significant for small modules (Section 6.1.2).

The efficiency decreases steadily with increasing sheet sizes as a result of the increased re-absorption losses and host absorption, but increases with larger sheet thicknesses because of the larger number of absorbed solar photons. Although rectangular sheets (as originally proposed by Weber and Lambe[8]) showed an increased efficiency, the effect is only significant at aspect ratios <0.2 where the module shape is impractically long and narrow.

The cost and embodied energy of LSC modules were compared with glass/glass laminate modules with either matched transmitted illuminance or matched efficiency. Both bulk (PMMA and PC) and thin-film (BF33 and low-iron) LSCs were simulated. The results show that thin film on glass devices have a much greater (worse) cost and energy than polymeric bulk devices. Most importantly, it was found that the LSCs did not offer any significant reduction in cost or energy compared with the laminate

modules, suggesting that LSCs based on organic fluorescent dyes cannot achieve a high enough efficiency to compete with conventional modules.

LSC construction & performance

A total of six different LSC modules were constructed using different techniques and dye mixtures as information was learned from the project. The highest efficiency measured from a 10 cm x 10 cm module was 3.22 % for a sheet containing 50 ppm Violett 570 + 350 ppm Rot 305. This increased to 3.87 % when a second sheet containing 80 ppm of NIR3 was placed behind the first.

A large 60 cm x 60 cm module was also constructed to demonstrate the technique of current-matching a series string of edge-mounted cells to maximise the power output. A relative increase of ∼15 % in power output was achieved when current-matching was used. The maximum efficiency obtained for the large module was 1.84 %.

8.2 Future research

During the course of this project, several areas emerged which merit further investigation. These are described briefly below.

In the cost and energy analysis performed in Section 6.2, a major unknown factor is the lifetime of the Lumogen dyes. Although there have been several reports of the photodegradation rate of these dyes[48, 62, 71, 325], there has been no attempt to correlate real-world with accelerated weathering. This is essential if any meaningful prediction is to be made of an LSC's lifetime outdoors. If the correlation were made with a range of different dyes and concentrations, by exposing identical dyed samples to both weathering scenarios, it would allow a more accurate prediction of the lifetime of the dye and hence the overall cost and embodied energy of the LSC module.

Another unknown is the actual efficiency of total internal reflection. Throughout this thesis, it has been assumed that TIR is 100 % efficient, with no losses. However, it has been found in some situations that losses can occur during TIR. These can be caused by, for example, surface microstructure[37]. In addition, the LSC's sensitivity to the effects of surface damage is unknown. As a result of the large number of reflections

which occur in an LSC, a non-unity TIR efficiency or the presence of surface dust and scratches could have a significant effect. Measurement of the TIR efficiency would allow for more accurate modelling of LSC performance. The presence of scattering by either the host or the dye will also result in losses, and measurement of the amount of scattering present would be extremely useful. If it were found that no great reduction in efficiency occured as a result of surface damage, the LSC could then be mounted without protective covers, reducing the cost and embodied energy.

8.3 Conclusion

It has been shown that, despite the optimum optical properties of the Rot 305 organic dye (good solubility, wide absorption range, near-unity PLQY and good photostablilty), LSCs based on this dye do not exhibit any advantages over conventional glass/glass laminate PV modules on grounds of either cost or embodied energy. It is unlikely that any organic dye could be developed which has superior properties to Rot 305, since all dyes suffer from the effects of re-absorption. Therefore, it is highly unlikely that LSCs based on organic dyes in general will ever be competitive with traditional technologies.

Dye-based LSCs are limited in efficiency because of the effects of re-absorption losses, which are present with all organic dyes. If any improvement in LSC efficiency is to be made, it must come from the use of fluorophores which exhibit low or zero re-absorption. The most promising means of achieving this is by the use of rare-earth complexes. As has been shown in this thesis, these can result in a higher optical efficiency than organic dyes as a result of their complete lack of re-absorption. However, the quantum yields of RE complexes which can absorb in the visible and emit in the NIR are currently low, and must be improved significantly (to at least 50 %) if they are to be suitable for LSC use.

Bibliography

[1] J. Houghton. *Global Warming (3rd ed.)*. Cambridge University Press, 2005.

[2] Henning Wicht and Stefan de Haan. PV Raw Materials Q2 2009 Market Tracker. Market research carried out by iSuppli. Abstract available from `http://www.isuppli.com/Abstract/P11583_20090727110425.pdf` (last accessed 12/11/09).

[3] Gary Homan. The Silicon Supply Chain. Presented on behalf of Hemlock Semiconductor Group at Intersolar North America 2009, 14-16 July 2009. Available from `http://www.semiconwest.org/cms/groups/public/documents/web_content/ctr_030778.pdf` (last accessed 12/11/09).

[4] I. Antón, D. Pachón, and G. Sala. Characterization of optical collectors for concentration photovoltaic applications. *Prog. Photovolt: Res. Appl.*, 11:387–405, 2003.

[5] J.G. Fossum and F.A. Lindholm. The dependence of open-circuit voltage on illumination level in p-n junction solar cells. *IEEE Trans. Elecron. Devices*, 24(4):325–329, 1977.

[6] A. Goetzberger and W. Greubel. Solar energy conversion with fluorescent collectors. *Appl. Phys.*, 14:123–139, 1977.

[7] T.K. Mallick and P.C. Eames. Design and fabrication of low concentrating second generation PRIDE concentrator. *Solar Energy Materials & Solar Cells*, 91:597–608, 2007.

[8] W.H. Weber and J. Lambe. Luminescent greenhouse collector for solar radiation. *Appl. opt*, 15(10):2299–2300, 1976.

[9] A. Goetzberger. Fluorescent solar energy collectors: Operating conditions with diffuse light. *Appl. Phys.*, 16:399–404, 1978.

[10] A. Goetzberger and O. Shirmer. Second stage concentration with tapers for fluorescent solar collectors. *Appl. Phys.*, 19:53–58, 1979.

[11] W.A. Shurcliff and R.C. Jones. The trapping of fluorescent light produced within objects of high geometrical symmetry. *J. Opt. Soc. Am.*, 39(11):912–916, 1949.

[12] P.S. Friedman. Luminescent solar concentrators. *Opt. Eng.*, 20(6):887–892, 1981.

[13] P.S. Friedman. Luminescent solar concentrator development. Final subcontract report. Technical report, US Dept. of Energy. Contract No. DE-AC02-83CH10093, 1987.

[14] J.S. Batchelder, A.H. Zewail, and T. Cole. Luminescent solar concentrators. 1: Theory of operation and techniques for performance evaluation. *Appl. Opt.*, 18(18):3090–3110, 1971.

[15] A.M. Hermann. Luminescent solar concentrators - a review. *Solar Energy*, 29(4):323–329, 1982.

[16] J.S. Batchelder, A.H. Zewail, and T. Cole. Luminescent solar concentrators. 2: Experimental and theoretical analysis of their possible efficiencies. *Appl. Opt.*, 20(21):3733–3754, 1981.

[17] V. Wittwer, W. Stahl, and A. Goetzberger. Fluorescent planar concentrators. *Sol. Energy Mater.*, 11(3):187–197, 1984.

[18] P.S. Friedman. Progress on the development of luminescent solar concentrators. In *Proc. SPIE Role of electro-optics in photovoltaic conversion technology*, volume 248, pages 98–104, 1980.

[19] L.H. Slooff, E.E. Bende, A.R. Burgers, T. Budel, M. Pravettoni, R.P. Kenny, E.D. Dunlop, and A. Büchtemann. A luminescent solar concentrator with 7.1 % power conversion efficiency. *Phys. Stat. Sol. (RRL)*, 2(6):257–259, 2008.

[20] J.C. Goldschmidt, M. Peters, A. Bösch, H. Helmers, F. Dimroth, S.W. Glunz, and G. Willeke. Increasing the efficiency of fluorescent concentrator systems. *Solar Energy Materials & Solar Cells*, 93:176–182, 2009.

[21] E.E. Bende, L.H. Slooff, A.R. Burgers, W.G.J.H.M. van Sark, and M. Kennedy. Cost & efficiency optimisation of the fluorescent solar concentrator. In *Proceedings of the 23rd European Photovoltaic Solar Energy Conference, Valencia, Spain*, pages 461–469, 2008.

[22] K. Barnham. Quantum-dot concentrator and thermodynamic model for the global redshift. *Appl. Phys. Lett.*, 76(9):1197–1199, 2000.

[23] M.J.V. Werts, J.W. Hofstraat, F.A.J. Geurts, and J.W. Verhoeven. Fluoroscein and eosin as sensitizing chromophores in near-infrared luminescent ytterbium(III), neodymium(III) and erbium(III) chelates. *Chem. Phys. Lett.*, 276:196–201, 1997.

[24] V. Sholin, J.D. Olson, and S.A. Carter. Semiconducting polymers and quantum dots in luminescent solar concentrators for solar enegry harvesting. *J. Appl. Phys.*, 101(12):123114–1–123114–9, 2007.

[25] M.G. Debije, D.J. Broer, and C.W.M. Bastiaansen. Effect of dye alignment on the output of a luminescent solar concentrator. In *Proceedings of the 22nd European Photovoltaic Solar Energy Conference and Exhibition, Milan*, pages 87–89, 2007.

[26] U. Rau, F. Einsele, and G.C. Glaeser. Efficiency limits of photovoltaic fluorescent collectors. *Appl. Phys. Lett.*, 87(17):171101–1–171101–3, 2005.

[27] A. Goetzberger and V. Wittwer. Fluorescent planar collector-concentrators: a review. *Solar Cells*, 4:3–23, 1981.

[28] M.G. Debije, J.-P. Teunissen, M.J. Kastelijn, P.P.C. Verbunt, and C.W.M. Bastiaansen. The effect of a scattering layer on the edge output of a luminescent solar concentrator. *Solar Energy Materials and Solar Cells*, 93:1345–1350, 2009.

[29] J.C. Goldschmidt, M. Peters, L. Prönneke, L. Steidl, R. Zentel, B. Bläsi, A. Gombert, S. Glunz, G. Willeke, and U. Rau. Theoretical and experimental analysis of photonic structures for fluorescent concentrators with increased efficiencies. *Phys. Stat. Sol. A*, 205(12):2811–2821, 2008.

[30] B.S. Richards, A. Shalav, and R.P. Corkish. A low escape-cone loss luminescent solar concentrator. In *Proceedings of the 19th European Photovoltaic Solar Energy Conference, Paris, France*, pages 113–116, 2004.

[31] M. Peters, J.C. Goldschmidt, P. Loeper, A. Gombert, and G. Willeke. Application of photonic structures on fluorescent concentrators. In *Proceedings of the 22nd European Photovoltaic Solar Energy Conference, Milan, Italy*, pages 177–181, 2007.

[32] M. Peters, J.C. Goldschmidt, P. Loeper, B. Bläsi, and G. Willeke. Light trapping with angular selective filters. In *Proceedings of the 23rd European Photovoltaic Solar Energy Conference, Valencia, Spain*, pages 353–357, 2008.

[33] A. Luque, A. Marti, A. Bett, V.M. Andreev, C. Jaussaud, J.A.M. van Roosmalen, J. Alonso, A. Räuber, G. Strobl, W. Stolz, C. Algora, B. Bitnar, A. Gombert, C. Stanley, P. Wahnon, J.C. Conesa, W.G.J.H.M. van Sark, A. Meijerink, G.P.M. van Klink, K. Barnham, R. Danz, T. Meyer, I. Luque-Heredia, R. Kenny, C. Christofides, G. Sala, and P. Benitez. FULLSPECTRUM: A new PV wave of more efficient use of the solar spectrum. *Solar Energy Materials & Solar Cells*, 87:467–479, 2005.

[34] B.S. Richards and K.R. McIntosh. Ray-tracing simulations of luminescent solar concentrators containing multiple luminescent species. In *Proceedings of the 21st EU PVSEC, Dresden*, pages 185–188, 2006.

[35] N.A. Bakr, A.F. Mansour, and M. Hammam. Optical and thermal spectroscopic studies of luminescent dye doped poly(methyl methacrylate) as solar concentrator. *J. Appl. Polym. Sci.*, 74(14):3316–3323, 1999.

[36] J. Ballato, S.H Foulger, and D.W. Smith Jr. Optical properties of perfluorocyclobutyl polymers. II. Theoretical and experimental attenuation. *J. Opt. Soc. Am. B*, 21(5):958–967, 2004.

[37] W.R.L. Thomas, J.M. Drake, and M.L. Lesiecki. Light transport in luminescent solar concentrators: the role of matrix losses. *Appl. Opt.*, 22(21):3440–3450, 1983.

[38] J.R. Lakowicz. *Principles of fluorescence spectroscopy.* Plenum Press, 1983.

[39] R.W. Olson, R.F. Loring, and M.D Fayer. Luminescent solar concentrators and the reabsorption problem. *Appl. Opt.*, 20(7):2934–2940, 1981.

[40] J. Sansregret, J.M. Drake, W.R.L. Thomas, and M.L. Lesiecki. Light transport in planar luminescent solar concentrators: the role of DCM self-absorption. *Appl. Opt.*, 22(4):573–577, 1983.

[41] R. Reisfeld, M. Eyal, V. Chernyak, and R. Zusman. Luminescent solar concentrators based on thin films of polymethylmethacrylate on a polymethylmethacrylate support. *Solar Energy Materials*, 17:439–455, 1988.

[42] M.G. El-Shaarawy, A.F. Mansour, S.M. El-Bashir, M.K. El-Mansy, and M. Hammam. Electrical conduction and dielectric properties of poly(methyl methacrylate)/perylene solar concentrators. *J. Appl. Poly. Sci.*, 88:793–805, 2003.

[43] J.M. Drake, M.L. Lesiecki, J. Sansregret, and W.R.L. Thomas. Organic dyes in PMMA in a planar luminescent solar concentrator: a performance evaluation. *Appl. Opt.*, 21(6):2945–2952, 1982.

[44] A. Zastrow. The physics and applications of fluorescent concentrators:A review. In *Proc. SPIE*, volume 2255, pages 534–547, 1994.

[45] A. Zastrow, K. Heidler, R.E. Sah, V. Wittwer, and A. Goetzberger. On the conversion of solar radiation with fluorescent planar concentrators(FPCs). In *Proceedings of the 3rd International Photovoltaic Solar Energy Conference, Cannes, France*, pages 413–417, 1980.

[46] F.O. Holtrup, G.R.J. Müller, H. Quante, S. de Feyter, F.C. de Schryver, and K. Müllen. Terrylenimides: New NIR fluorescent dyes. *Chem. Eur. J.*, 3(2):219–225, 1997.

[47] F. Nolde, J. Qu, C. Kohl, N.G. Pschirer, E. Reuther, and K. Müllen. Synthesis and modification of terrylenediimides as high-performance fluorescent dyes. *Chem. Eur. J.*, 11:3959–3967, 2005.

[48] G. Seybold and G. Wagenblast. New perylene and violanthrone dyestuffs for fluorescent collectors. *Dyes and Pigments*, 11:303–317, 1989.

[49] L. Fan, Y. Xu, and H. Tian. 1,6-disubstituted perylene bisimides: concise synthesis and characterization as near-infrared fluorescent dyes. *Tetrahedron Lett.*, 46:4443–4447, 2005.

[50] Y. Geerts, H. Quante, H. Platz, R. Mahrt, M. Hopmeier, Arno Böhm, and K. Müllen. Quaterrylenebis(dicarboximide)s: near infrared absorbing and emitting dyes. *J. Mat. Chem.*, 8(11):2357–2369, 1998.

[51] N.G. Pschirer, C. Kohl, F. Nolde, J. Qu, and K. Müllen. Pentarylene- and hexarylenebis(dicarboximide)s: near-infrared-absorbing polyaromatic dyes. *Angew. Chem. Int. Ed.*, 45:1401–1404, 2006.

[52] H. Quante, Y. Geerts, and K. Müllen. Synthesis of soluble perylenebisamidine derivatives. Novel long-wavelength absorbing and fluorescent dyes. *Chem. Mater.*, 9:495–500, 1997.

[53] R.E. Sah and G. Baur. Influence of the solvent matrix on the overlapping of the absorption and emission bands of solute fluorescent dyes. *Appl. Phys.*, 23:369–372, 1980.

[54] B.A. Swartz, T. Cole, and A. Zewail. Photon trapping and energy transfer in multiple-dye plastic matrices: an efficient solar energy concentrators. *Optics Letters*, 1(2):73–75, 1977.

[55] D.V. Roberts, B.P. Wittmershaus, Y.-Z. Zhang, S. Swan, and M.P. Klinosky. Efficient excitation energy transfer among multiple dyes in polystyrene microspheres. *J. Lumin.*, 79:225–231, 1998.

[56] S.T. Bailey, G.T. Lokey, M.S. Hanes, J.D.M. Shearer, J.B. McLafferty, G.T. Beaumont, T.T. Baseler, J.M. Layhue, D.R. Broussard, Y.-Z. Zhang, and B.P.

Wittermershaus. Optimized excitation energy transfer in a three-dye luminescent solar concentrator. *Solar Energy Materials & Solar Cells*, 91:67–75, 2007.

[57] V. Petrova-Koch, R. Hezel, and A. Goetzberger. *High-Efficient Low-Cost Photovoltaics, Chapter 10 "Fluorescent solar energy concentrators: Principle and present state of development"*. Springer-Verlag, 2009.

[58] A.J. Boehm, A. Glaser, and K. Muellen. The quaterrylimides - highly efficient NIR absorbers for plastics. In *Proceedings of ANTEC 2003 (Society of Plastics Engineers), Nashville, USA*, pages 3687–3691, 2003.

[59] A.J. Boehm and P. Blaschka. Perylimide fluorescent dyestuffs - speciality colorants with a brilliant future. In *Proceedings of ANTEC 2003 (Society of Plastics Engineers), Nashville, USA*, pages 2474–2478, 2003.

[60] A.J. Boehm, A. Glaser, and O. Koch. Nanocolorants - more than colored nanoparticles. In *Proceedings of ANTEC 2003 (Society of Plastics Engineers), Nashville, USA*, pages 2419–2422, 2003.

[61] A.A. Earp, G.B. Smith, P.D. Swift, and J. Franklin. Maximising the light output of a luminescent solar concentrator. *Solar Energy*, 76:655–667, 2004.

[62] W.G.J.H.M. van Sark, K.W.J. Barnham, L.H. Slooff, A.J. Chatten, A. Büchtemann, A. Meyer, S.J. McCormack, R. Koole, D.J. Farrell, R. Bose, E.E. Bende, A.R. Burgers, T. Budel, J. Quilitz, M. Kennedy, T. Meyer, C. De Mello Donegá, A. Meijerink, and D. Vanmaekelbergh. Luminescent solar concentrators - a review of recent results. *Opt. Exp.*, 16(26):21773–21792, 2008.

[63] BASF Lumogen F dyes product datasheets. Available from `http://www.dispersions-pigments.basf.com/portal/basf/ien/dt.jsp?setCursor=1_422514` (last accessed 05/01/10).

[64] L.H. Slooff, R. Kinderman, A.R. Burgers, J.A.M. van Roosmalen, A. Büchtemann, R. Danz, M. Schleusener, A.J. Chatten, D. Farrell, and K.W.J. Barnham. The luminescent solar concentrator: a bright idea for spectrum conversion? In *Proceedings of the 20th European Photovoltaic Solar Energy Conference and Exhibition, Barcelona, Spain*, pages 413–416, 2005.

[65] L.H. Slooff, T. Budel, A.R. Burgers N.J. Bakker, A. Büchtemann, R. Danz, T. Meyer, and A. Meyer. The luminescent concentrator: stability issues. In *Proceedings of the 22nd European Photovoltaic Solar Energy Conference and Exhibition, Milan*, pages 584–588, 2007.

[66] L.H. Slooff, R. Kinderman, A.R. Burgers, A. Büchtemann, R. Danz, T.B. Meyer, A.J. Chatten, D. Farrell, K.W.J. Barnham, and J.A.M. van Roosmalen. The luminescent concentrator illuminated. In *Proc. SPIE*, volume 6197, page 61970K, 2006.

[67] M.G. Debije, P.P.C. Verbunt, B.C. Rowan, B.S. Richards, and T.L. Hoeks. Measured surface loss from luminescent solar concentrator waveguides. *Appl. Opt.*, 47(36):6763–6768, 2008.

[68] P.D. Swift and G.B. Smith. Color considerations in fluorescent solar collector stacks. *Appl. Opt.*, 42(25):5112–5117, 2003.

[69] P.D. Swift, G.B. Smith, and J.B. Franklin. Light-to-light efficiencies in luminescent solar concentrators. In *Proc. SPIE conference on solar optical materials XVI*, volume 3789, pages 21–28, 1999.

[70] A.A. Earp, G.B. Smith, J. Franklin, and P. Swift. Optimisation of a three-color luminescent solar concentrator daylighting system. *Solar Energy Materials & Solar Cells*, 84:411–426, 2004.

[71] R. Kinderman, L.H. Slooff, A.R. Burgers, N.J. Bakker, A. Büchtemann, R. Danz, and J.A.M. van Roosmalen. I-V performance and stability study of dyes for luminescent plate concentrators. *J. Sol. Energy Eng.*, 129:277–282, 2007.

[72] A.F. Mansour, H.M.A. Killa, S.A. El-Wanees, and M.Y. El-Sayed. Laser dyes doped with poly(ST-Co-MMA) as fluorescent solar collectors and their field performance. *Polym. Test.*, 24:519–525, 2005.

[73] R. Reisfeld, D. Shamrakov, and C. Jorgensen. Photostable solar concentrators based on fluorescent glass films. *Solar Energy Materials & Solar Cells*, 33:417–427, 1994.

[74] N. Tanaka, N. Barashkov, J. Heath, and W.N. Sisk. Photodegradation of polymer-dispersed perylene di-imide dyes. *Appl. Opt.*, 45(16):3846–3851, 2006.

[75] H. Du, C. Chen, R. Krishnan, T.D. Krauss, J.M. Harbold, F.W. Wise, M.G. Thomas, and J. Silcox. Optical properties of colloidal PbSe nanocrystals. *Nano Lett.*, 2(11):1321–1324, 2002.

[76] O.I. Mićić, H.M. Cheong, H. Fu, A. Zunger, J.R. Sprague, A. Mascarenhas, and A.J. Nozik. Size-dependent spectroscopy of InP quantum dots. *J. Phys. Chem. B*, 101:4904–4912, 1997.

[77] E.H. Sargent. Infrared quantum dots. *Adv. Mat.*, 17(3):515–522, 2005.

[78] Evident Technologies quantum dots product information. Available from `http://www.evidenttech.com` (last accessed 17/11/09).

[79] Nanoco Group quantum dots product information. Available from `http://www.nanocotechnologies.com` (last accessed 17/11/09).

[80] D.J. Farrell, A.J. Chatten, A. Büchtemann, and K.W.J. Barnham. Fabrication, characterisation & modelling of quantum dot solar concentrator stacks. In *Proceedings of the IEEE 4^{th} World Conference on Photovoltaic Solar Energy Conversion, Waikoloa, Hawaii*, pages 217–220, 2006.

[81] E. Klampaftis, D. Ross, K.R. McIntosh, and B.S. Richards. Enhancing the performance of solar cells via luminescent down-shifting of the incident spectrum: A review. *Solar Energy Materials & Solar Cells*, 93:1182–1194, 2009.

[82] S.J. Gallagher, B.C. Rowan, J. Doran, and B. Norton. Quantum dot solar concentrator: Device optimisation using spectroscopic techniques. *Solar Energy*, 81:540–547, 2007.

[83] X. Wang, J. Zhang, A. Nazzal, and M. Xiao. Photo-oxidation-enhanced coupling in densely packed CdSe quantum dot films. *Appl. Phys. Lett.*, 81(1):162–164, 2003.

[84] M. Lomascolo, A. Creti, G. Leo, L. Vasanelli, and L. Manna. Exciton relaxation processes in collodial core/shell ZnSe/ZnS nanocrystals. *Appl. Phys. Lett.*, 82(3):418–420, 2003.

[85] S.J. Gallagher, P.C. Eames, and B. Norton. Predicting the behaviour of quantum dot solar concentrators using a ray trace approach. *Int. J. Ambient Energy*, 25(1):47–56, 2004.

[86] B.C. Rowan. *Development of a quantum dot solar concentrator*. PhD thesis, Dublin Institute of Technology, 2007.

[87] O.I. Mićić. Synthesis and characterization of InP quantum dots. *J. Phys. Chem.*, 98(19):4966–4969, 1994.

[88] B.C. Rowan, L.R. Wilson, and B.S. Richards. Advanced material concepts for luminescent solar concentrators. *IEEE J. Selected Topics in Quantum Electronics*, 14(5):1312–1322, 2008.

[89] S.J. Gallagher, B. Norton, and P.C. Eames. Quantum dot solar concentrators: Electrical conversion efficiencies and comparative concentrating factors of fabricated devices. *Solar Energy*, 81:813–821, 2007.

[90] M. Kennedy, S.J.McCormack, J. Doran, and B. Norton. Improving the optical efficiency and concentration of a single-plate quantum dot solar concentrator using near infra-red emitting quantum dots. *Solar Energy*, 83:978–981, 2009.

[91] A.J. Chatten, K.W.J. Barnham, B.F. Buxton, and N.J. Ekins-Daukes. Quantum dot solar concentrators. *Semiconductors*, 38(8):909–917, 2004.

[92] A. Schüler, M. Python, M. Valle del Olmo, and E. de Chambrier. Quantum dot containing nanocomposite thin films for photoluminescent solar concentrators. *Solar Energy*, 81(9):1159–1165, 2007.

[93] S.M. Reda. Synthesis and optical properties of CdS quantum dots embedded in silica matrix thin films and their applications as luminescent solar concentrators. *Acta Materialia*, 56:259–264, 2008.

[94] R. Bose, D.J. Farrell, A.J. Chatten, M. Pravettoni, A. Büchtemann, and K.W.J. Barnham. Novel configurations of luminescent solar concentrators. In *Proceedings of the 22nd European Photovoltaic Solar Energy Conference and Exhibition, Milan*, pages 210–214, 2007.

[95] R. Reisfeld and Y. Kalisky. Nd^{3+} and Yb^{3+} germanate and tellurite glasses for fluorescent solar energy collectors. *Chem. Phys. Lett.*, 80(1):178–183, 1981.

[96] R. Reisfeld. Spectroscopy and nonradiative phenomena of rare earths in glasses: future applications. *Inorganica Chimica Acta*, 95:69–74, 1984.

[97] R. Reisfeld. Future technological applications of rare-earth-doped materials. *J. Less-Common Metals*, 93:243–251, 1983.

[98] V. Sytko and M. Pershina. Phosphate glasses with great concentration of uranyl and rare earth ions and its films for solar cell concentrators. In *Proc. SPIE*, volume 2531, pages 272–280, 1995.

[99] R. Reisfeld. Potential uses of chromium(III)-doped transparent glass ceramics in tunable lasers and luminescent solar concentrators. *Mat. Sci. Eng.*, 71:375–382, 1985.

[100] A. Buch, M. Ish-Shalom, R. Reisfeld, A. Kislev, and E. Greenberg. Transparent glass ceramics: preparation, characterization and properties. *Mat. Sci. Eng.*, 71:383–389, 1985.

[101] R. Reisfeld. Prospects of sol-gel technology towards luminescent materials. *Opt. Mat.*, 16:1–7, 2001.

[102] J. Lin and C.W. Brown. Sol-gel glass as a matrix for chemical and biochemical sensing. *Trends Anal. Chem.*, 16(4):200–211, 1997.

[103] A. Hinsch, A. Zastrow, and V. Wittwer. Sol-gel glasses: a new material for solar fluorescent planar concentrators? *Solar Energy Materials*, 21:151–164, 1990.

[104] T. Jin, S. Tsutsumi, Y. Deguchi, K.-ichi Machida, and G.-ya Adachi. Luminescence characteristics of the lanthanide complex incorporated into an ORMOSIL matrix using a sol-gel method. *J. Electrochem. Soc.*, 143(10):3333–3335, 1996.

[105] T. Jin, S. Inoue, S. Tsutsumi, K.-ichi Machida, and G.-fya Adachi. Luminescence properties of lanthanide complexes incorporated into sol-gel derived inorganic-organic composite materials. *J. Non-cryst. Solids*, 223:123–132, 1998.

[106] C.K. Jorgensen and R. Reisfeld. Luminescence yields, minimal photodegradation of organic and inorganic species in sol-gel glass and modalities of confinement. In *Proc. SPIE*, volume 2288, pages 208–215, 1994.

[107] R. Reisfeld. Fluorescent dyes in sol-gel glasses. *J. Fluor.*, 12(3-4):317–325, 2002.

[108] A. Rosencwaig and E.A. Hildum. Nd^{3+} fluorescence quantum-efficiency measurements with photoacoustics. *Phys. Rev. B*, 23(7):3301–3307, 1981.

[109] S.M. Lima, A.A. Andrade, R. Lebullenger, A.C. Hernandes, T. Catunda, and M.L. Baesso. Multiwavelength thermal lens determination of fluorescence quantum efficiency of solids: Application to Nd^{3+}-doped fluoride glass. *Appl. Phys. Lett.*, 78(21):3220–3222, 2001.

[110] T. Kushida and J. Geusic. *Phys. Rev. Lett.*, 21:1172, 1968.

[111] P.F. Liao and H.P. Weber. *J. Appl. Phys.*, 45:2931, 1974.

[112] D.F. de Sousa, F. Batalioto, M.J.V. Bell, S.L. Oliveira, and L.A.O. Nunes. Spectroscopy of Nd^{3+} and Yb^{3+} co-doped fluoroindogallate glasses. *J. Appl. Phys.*, 90(7):3308–3313, 2001.

[113] G.A. Hebbink, L. Grave, L.A. Woldering, D.N. Reinhoudt, and F.C.J.M. van Veggel. Unexpected sensitization efficiency of the near-infrared Nd^{3+}, Er^{3+}, and Yb^{3+} emission by fluorescein compared to eosin and erythrosin. *J. Phys. Chem. A*, 107:2483–2491, 2003.

[114] F. Liégard, J.L. Doualan, R. Moncorgé, and M. Bettinelli. $Nd^{3+} \rightarrow Yb^{3+}$ energy transfer in a codoped metaphosphate glass as a model for Yb^{3+} laser operation around 980 nm. *Appl. Phys. B*, 80:985–991, 2005.

[115] C. Lurin, C. Parent, G. Le Flem, and P. Hagenmuller. Energy transfer in a Nd^{3+}-Yb^{3+} borate glass. *J. Phys. Chem. Solids*, 46(9):1083–1092, 1985.

[116] C. Lurin, C. Parent, G. Le Flem, and M. Couzi. Kinetic study of the neodymium fluorescence and of the $Nd^{3+} \rightarrow Yb^{3+}$ energy transfer in lithium lanthanum metaphosphate-like glasses. *J. Less-Common Metals*, 126:155–160, 1986.

[117] C. Parent, C. Lurin, G. Le Flem, and P. Hagenmuller. $Nd^{3+} \rightarrow Yb^{3+}$ energy transfer in glasses with composition close to $LiLnP_4O_{12}$ metaphosphate (Ln=La, Nd, Yb). *J. Lumin.*, 36:49–55, 1986.

[118] V. Lupei, A. Lupei, and A. Ikesue. Transparent Nd and (Nd, Yb)-doped Sc_2O_3 ceramics as potential new laser materials. *Appl. Phys. Lett.*, 86:111118–1–111118–3, 2005.

[119] N. Neuroth and R. Haspel. Glasses for luminescent solar concentrators. *Solar Energy Materials*, 16:235–242, 1987.

[120] E. Łukowiak, W. Stręk, and B. Jeżowska-Trzebiatowska. Optical properties of Cr (III)-doped glasses. *Optica Applicata*, 18(4):281–286, 1988.

[121] E. Łukowiak, W. Stręk, A. Hejduk, and B. Jeżowska-Trzebiatowska. Spectral characteristics of the Cr(III), Nd(III) and Yb(III) triple co-doped inorganic glasses. *Mat. Sci.*, 17(3):63–67, 1991.

[122] W.G. Quirino, M.J.V. Bell, S.L. Oliveira, and L.A.O. Nunes. Effects of non-radiative processes on the infrared luminescence of Yb^{3+} doped glasses. *J. Non-Cryst. Solid.*, 351:2042–2046, 2005.

[123] H. Lu and J. Ballato. Synthesis and characterization of Eu^{3+}-doped sol-gel silica containing vanadium oxide nanotubes. *J. Am. Ceram. Soc.*, 89(11):3573–3576, 2006.

[124] H. Lu and J. Ballato. Luminescence properties of Eu^{3+}-doped silica containing silver nanoparticles. *Phys. Chem. Glasses: Eur. J. Glass Sci. Technol. B*, 47(2):96–100, 2006.

[125] J.R. DeMaio, B. Kokuoz, and J. Ballato. White light emissions through down-conversion of rare-earth doped LaF_3 nanoparticles. *Optics Express*, 14(23):11412–11417, 2006.

[126] J.R. DiMaio, B. Kokuoz, T.L. James, and J. Ballato. Structural determination of light-emitting inorganic nanoparticles with complex core/shell architectures. *Adv. Mat.*, 19:3266–3270, 2007.

[127] J.R. DiMaio, B. Kokuoz, T.L. James, T. Harkey, D. Monofsky, and J. Ballato. Photoluminescent characterization of atomic diffusion in core-shell nanoparticles. *Optics Express*, 16(16):11769–11775, 2008.

[128] J.R. DeMaio, C. Sabatier, B. Kokuoz, and J. Ballato. Controlling energy transfer between multiple dopants within a single nanoparticle. *Proc. Nat. Acad. Sci.*, 105(6):1809–1813, 2008.

[129] G.A. Kumar, R.E. Riman, and E. Snitzer. Solution synthesis and spectroscopic characterization of high Eu^{3+}-content LaF_3 for broadband 1.5 μm amplification. *J. Appl. Phys.*, 95(1):40–47, 2004.

[130] G.A. Kumar, R.E. Riman, S. Banerjee, A. Kornienko, J.G. Brennan, S. Chen, D. Smith, and J. Ballato. Infrared fluorescence and optical gain characteristics of chalcogenide-bound erbium cluster-fluoropolymer nanocomposites. *Appl. Phys. Lett.*, 88:091902, 2006.

[131] G.A. Kumar, C.W. Chen, R.E. Riman, S. Chen, D. Smith, and J. Ballato. Optical properties of a transparent CaF_2:Er^{3+} fluoropolymer nanocomposite. *Appl. Phys. Lett.*, 86:241105, 2005.

[132] J. Ballato, R.E. Riman, and E. Snitzer. Sol-gel synthesis of rare-earth-doped lanthanum halides for highly efficient 1.3 μm optical amplification. *Opt. Exp.*, 22(10):691–693, 1997.

[133] Sigma-Aldrich chemicals. Available from `http://www.sigmaaldrich.com` (last accessed 17/02/10).

[134] Y. Hasegawa, K. Sogabe, Y. Wada, T. Kitamura, N. Nakashima, and S. Yanagida. Enhanced luminescence of lanthanide(III) complexes in polymer matrices. *Chem. Lett.*, CL-980670:35–36, 1999.

[135] Y. Hasegawa, K. Sogabe, Y. Wada, and S. Yanagida. Low-vibrational luminescent polymers including tris(bis-perfluoromethane and ethanesulfonylaminate)neodymium(III) with 8-coordinated DMSO-6. *J. Lumin.*, 101:235–224, 2003.

[136] M.H.V. Werts, R.T.F. Jukes, and J.W. Verhoeven. The emission spectrum and the radiative lifetime of Eu^{3+} in luminescent lanthanide complexes. *Phys. Chem. Chem. Phys.*, 4:1542–1548, 2002.

[137] S. Biju, D.B.A. Raj, M.L.P. Reddy, and B.M. Kariuki. Synthesis, crystal structure, and luminescent properties of novel Eu^{3+} heterocyclic β-diketonate complexes with bidentate nitrogen donors. *Inorg. Chem.*, 45:10651–10660, 2006.

[138] M.H.V. Werts, J.W. Verhoeven, and J.W. Hofstraat. Efficient visible light sensitisation of water-soluble near-infrared luminescent lanthanide complexes. *J. Chem. Soc., Perkin Trans.*, 2:433–439, 2000.

[139] M. Xiao and P.R. Selvin. Quantum yields of luminescent lanthanide chelates and far-red dyes measured by resonance energy transfer. *J. Am. Chem. Soc.*, 123:7067–7073, 2001.

[140] O. Moudam, B.C. Rowan, M. Alamiry, P. Richardson, B.S. Richards, A.C. Jones, and N. Robertson. Europium complexes with high total photoluminescence quantum yields in solution and in PMMA. *Chem. Commun.*, pages 6649–6651, 2009.

[141] S. Marchionna, F. Meinardi, M. Acciarri, S. Binetti, A. Papagni, S. Pizzini, V. Malatesta, and R. Tubino. Photovoltaic quantum efficiency enhancment by light harvesting of organo-lanthanide complexes. *J. Lumin.*, 118:325–329, 2006.

[142] N.M. Shavaleev, R. Scopelliti, F. Gumy, and J.-C.G. Bünzli. Visible-light excitation of infrared Lanthanide luminescence via intra-ligand charge-transfer state in 1,3-diketonates containing push-pull chromophores. *Eur. J. Inorg. Chem.*, pages 1523–1529, 2008.

[143] S. Faulkner, M.-C. Carrié, S.J.A. Pope, J. Squire, A. Beeby, and P.G. Sammes. Pyrene-sensitised near-IR luminescence from ytterbium and neodymium complexes. *Dalton Trans.*, pages 1405–1409, 2004.

[144] P.B. Glover, A.P. Bassett, P. Nockemann, B.M. Kariuki, R. van Deun, and Z. Pikramenou. Fully fluorinated imidodiphosphinate shells for visible- and NIR-emitting Lanthanides: hitherto unexpected effects of sensitizer fluorination on Lanthanide emission properties. *Chem. Eur. J.*, 13:6308–6320, 2007.

[145] S. Bucella, P. Riello, B.F. Scremin, P. Calvelli, R. Polloni, A. Speghini, M. Bettinelli, and A. Benedetti. Synthesis and luminescent properties of ZrO_2 and ZrO_2/SiO_2 composites incorporating Eu(III)-phenanthroline complex prepared by a catalyst-free sol-gel process. *Opt. Mat.*, 27:249–255, 2004.

[146] R. Shunmugam and G.T. Tew. Unique emission from polymer based Lanthanide alloys. *J. Am. Chem. Soc.*, 127:13567–13572, 2005.

[147] R. van Deun, P. Fias, P. Nockemann, K. van Hecke, L. van Meervelt, and K. Binnemans. Visible-light-sensitizes near-infrared luminescence from rare-earth complexes of the 9-hydroxyphenalen-1-one ligand. *Inorg. Chem.*, 45:10416–10418, 2006.

[148] S. Yanagida, Y. Hasegawa, and Y. Wada. Remarkable luminescence of novel Nd(III) complexes with low-vibrational hexafluoroacetylacetone and DMSO-d_6 molecules. *J. Lumin.*, 87-89:995–998, 2000.

[149] N.M. Shavaleev, L.P. Moorcraft, S.J.A. Pope, Z.R. Bell, S. Faulkner, and M.D. Ward. Sensitized near-infrared emission from complexes of Yb^{III}, Nd^{III} and Er^{III} by energy-transfer from covalently attached Pt^{II}-based antenna units. *Chem. Eur. J.*, 9:5283–5291, 2003.

[150] H. Xu, L.-H. Wang, X.-H. Zhu, K. Yin, G.-Y. Zhong, X.-Y. Hou, and W. Huang. Applicationof chelate phosphine oxide ligand in Eu^{III} complex with mezzo triplet energy level, highly efficient photoluminescent, and electroluminescent performances. *J. Phys. Chem. B*, 110:3023–3029, 2006.

[151] L.H. Slooff, A. van Blaaderen, A. Polman, G.A. Hebbink, S.I. Klink, F.C.J.M. van Veggel, D.N. Reinhoudt, and J.W. Hofstraat. Rare-earth doped polymers for planar optical amplifiers. *J. Appl. Phys.*, 91(7):3955–3980, 2002.

[152] A.P. Bassett, S.W. Magennis, P.B. Glover, D.J. Lewis, N. Spencer, S. Parsons, R.M. Williams, L. de Cola, and Z. Pikramenou. Highly luminescent, triple- and quadruple-stranded, dinuclear Eu, Nd, and Sm(III) Lanthanide complexes based on bis-diketonate ligands. *J. Am. Chem. Soc.*, 126:9413–9424, 2004.

[153] B.C. Rowan and B.S. Richards. Near-infrared emitting lanthanide complexes for luminescent solar concentrators. In *Proceedings of the 23rd European Photovoltaic Solar Energy Conference and Exhibition, Valencia*, pages 700–703, 2008.

[154] B.C. Rowan, L.R. Wilson, and B.S. Richards. Visible and near-infrared emitting Lanthanide complexes for luminescent solar concentrators. In *Proceedings of the 24th European Photovoltaic Solar Energy Conference and Exhibition, Hamburg*, pages 346–349, 2009.

[155] M. Latva, H. Takalo, V.-M. Mukkala, C. Matachescu, J.C. Rodriguez-Ubis, and J. Kankare. Correlation between the lowest triplet state energy level of the ligand and lanthanide(III) luminescence quantum yield. *J. Lumin.*, 75:149–169, 1997.

[156] A.R. Burgers, L.H. Slooff, A. Buchtemann, and J.A.M. van Roosmalen. Performance of single layer luminescent concentrators with multiple dyes. In *Proceedings of IEEE 4th WCPEC, Waikoloa, HI*, pages 198–201, 2006.

[157] L.G. Rainhart and W.P. Schimmel Jr. Effect of outdoor aging on acrylic sheet. *Solar Energy*, 17:259–264, 1975.

[158] T. Kaino, M. Fujiki, S. Oikawa, and S. Nara. Low-loss plastic optical fibers. *Appl. Opt.*, 20(17):2886–2888, 1981.

[159] Y.Hasegawa, Y. Wada, and S. Yanagida. Strategies for the design of luminescent Lanthanide(III) complexes and their photonic applications. *J. Photochem. Photobiol. C: Photochem. Rev.*, 5(3):183–202, 2004.

[160] J. Gordon, J. Ballato, J. Jin, and D.W Smith Jr. Spectroscopic properties as a function of fluorine content in Eu^{3+}:PMMA. *J. Poly. Sci. B*, 44:1592–1596, 2006.

[161] J. Gordon, J. Ballato, D.W. Smith Jr., and J. Jin. Optical properties of perfluorocyclobutyl polymers. III. Spectroscopic characterization of rare-earth-doped perfluorocyclobutyl polymers. *J. Opt. Soc. Am. B*, 22(8):1654–1659, 2005.

[162] J. Ballato, S.H. Foulger, and D.W. Smith Jr. Optical properties of perfluorocyclobutyl polymers. *J. Opt. Soc. Am. B*, 20(9):1838–1843, 2003.

[163] M. Yamane, S. Aso, and T. Sakaino. Preparation of a gel from metal alkoxide and its properties as a precursor of oxide glass. *J. Mat. Sci.*, 13, 1978.

[164] D. Avnir, D. Levy, and R. Reisfeld. The nature of the silica cage as reflected by spectral changes and enhanced photostability of trapped rhodamine 6G. *J. Phys. Chem.*, 88(24):5956–5959, 1984.

[165] E. Loh and D.J. Scalapino. Luminescent solar concentrators: effects of shape on efficiency. *Appl. Opt.*, 25(2):1901–1907, 1986.

[166] M. Sidrach de Cardona, M. Carrascosa, F. Meseguer, F. Cusso, and F. Jaque. Edge effect on luminescent solar concentrators. *Solar Cells*, 15:225–230, 1985.

[167] S.R. Dhariwal, R.K. Mathur, and R. Gadre. Voltage reduction in a non-uniformly illuminated solar cell. *J. Phys. D: Appl. Phys.*, 14:1325–1329, 1981.

[168] Z.H. Lu, Q. Song, S.Q. Li, Q. Yao, and A. Othman. The effect of non-uniform illumination on the performance of conventional polycrystalline silicon solar cell. In *Proceedings of the ISES World Congress*, pages 1445–1448, 2007.

[169] J. Mapel, M. Currie, T.D. Heidel, M. Baldo, and S. Goffri. US Patent Application US2009/0235974A1 (paragraph 138), 2009.

[170] R. Soti, E. Farkas, M. Hilbert, Z. Farkas, and I. Ketskemety. Photon transport in luminescent solar concentrators. *J. Lumin.*, 68:105–114, 1996.

[171] J. Roncali and F. Garnier. New luminescent back reflectors for the improvement of the spectral response and efficiency of luminescent solar concentrators. *Solar Cells*, 13:133–143, 1984.

[172] T. Markvart. Detailed balance method for ideal single-stage fluorescent collectors. *J. Appl. Phys.*, 99:026101–1–026101–3, 2006.

[173] Lightwave Power (2D photonic crystals). Available from `http://www.lightwavepower.com` (last accessed 14/01/10).

[174] C.F. Rapp and N.L. Boling. Luminescent solar concentrators. In *Proceedings of the 13th IEEE Photovoltaic Specialists Conference, Washington*, pages 690–693, 1978.

[175] W. Viehmann and R.L. Frost. Thin film wafeshifter coatings for fluorescent radiation converters. *Nucl. Inst. Meth.*, 167:405–415, 1979.

[176] R. Reisfeld and C.K. Joergensen. Luminescent solar concentrators for energy conversion. *Struct. Bond.*, 49:1–36, 1982.

[177] G. Hammond and C. Jones. Inventory of Carbon & Energy. Available from `http://www.bath.ac.uk/mech-eng/sert/embodied` (last accessed 14/01/10).

[178] M. Lenzen. Greenhouse gas analysis of solar-thermal electricity generation. *Solar Energy*, 65(6):353–368, 1999.

[179] G. Baird, A. Alcorn, and P. Haslam. The energy embodied in building materials - updated New Zealand coefficients and their significance. In *IPENZ transactions, Vol 24., No. 1*, pages 46–54, 1997.

[180] G. Burgess, J.G. Fernández-Velasco, and K. Lovegrove. Materials, geometry, and net energy ratio of tubular photobioreactors for microalgal hydrogen production. In *16th World Hydrogen Energy Conference, 13-16 June, Lyon, France,* 2006. Available from `http://stwp.cecs.anu.edu.au/wp-content/uploads/WHEC-Burgess-biohydrogen.pdf` (last accessed 04/04/10).

[181] Ian Boustead. Eco-profiles of the European Plastics Industry: Polymethyl Methacrylate. Published by PlasticsEurope (2005). Available from `http://www.lca.plasticseurope.org/download/pmma.zip` (last accessed 14/01/10).

[182] K. Daimatsu, H. Sugimoto, Y. Kato, E. Nakanishi, K. Inomata, Y. Amekawa, and K. Takemura. Perparation and physical properties of flame retardant acrylic resin containing nano-sized aluminium hydroxide. *Polym. Degrad. Stab.*, 92:1433–1438, 2007.

[183] M.M.K. Khan, C.J. Hildao, S. Agarwal, and R.K. Gupta. Flammability properties of virgin and recycled polycarbonate (PC) and acrylonitrile-butadiene-styrene (ABS) recovered from end-of-life electronics. *J. Polym. Environ.*, 15:188–194, 2007.

[184] K.R. McIntosh, G. Lau, J.N. Cotsell, K. Hanton, D.L. Bätzner, F. Bettiol, and B.S. Richards. Increase in external quantum efficiency of encapsulated silicon solar cells from a luminescent down-shifting layer. *Prog. Photovolt.: Res. Appl.*, 17:191–197, 2009.

[185] C.M. Garner, F.W. Sexton, and R.D. Nasby. High efficiency silicon cells for luminescent solar concentrators. *Solar Cells*, 4:37–46, 1981.

[186] A. Goetzberger and W. Greubel. Apparatus for converting light energy into electrical energy. US Patent 4110123, 1978.

[187] N.L. Boling. Luminescent solar collector structure. US Patent 4164432, 1979.

[188] N.L. Boling. Luminescent solar collector structure. US Patent 4190465, 1980.

[189] A.H. Zewail and J.S. Batchelder. Luminescent solar energy concentrator devices. US Patent 4227939, 1980.

[190] J.N. Demas and G.A. Crosby. The measurement of photoluminescent quantum yields. A review. *J. Phys. Chem.*, 75(8):991–1024, 1971.

[191] S.I. Vavilov. *Z. Phys.*, 22:266, 1924.

[192] W.H. Melhuish. *New Zealand J. Sci. Tech.*, 37:142, 1955.

[193] W.H. Melhuish. *J. Opt. Soc. Am.*, 54:183, 1964.

[194] G. Weber and F.W.J. Teale. *Trans. Faraday Soc.*, 53:646, 1957.

[195] D.M. Hercules and H. Frankel. *Science*, 131:1611, 1960.

[196] H.V. Drushel, A.L. Sommers, and R.C. Cox. *Anal. Chem.*, 35:2166, 1963.

[197] C.A. Parker and W.T. Rees. *Analyst (London)*, 85:587, 1960.

[198] M.A. Alentsev. National Research Council of Canada Technical Translation TT-433. *Журнал Экспериментальной и Теоретической Физики (Journal of Experimental and Theoretical Physics)*, 21:133, 1951.

[199] T. Meites, L. Meites, and J.N. Jaitly. *J. Phys. Chem.*, 73:3801, 1969.

[200] R.A. Gudmundsen, O.J. Marsh, and E. Matovich. *J. Chem. Phys.*, 39:272, 1963.

[201] M. Kasha. *J. Opt. Soc. Am.*, 38:929, 1948.

[202] J. Olmsted III. Calorimetric determinations of absolute fluorescence quantum yields. *J. Phys. Chem.*, 83(20):2581–2584, 1979.

[203] P. Michel, J. Dugas, J.M. Cariou, and L. Martin. Thermal variations of refractive index of PMMA, polystyrene and poly(4-methyl-1-pentene). *J. Macromol. Sci. - Phys.*, B25(4):379–394, 1986.

[204] C. Hu and J.R. Whinnery. New thermooptical measurement method and comparison with other methods. *Appl. Opt.*, 12(1):72–79, 1973.

[205] J.P. Gordon, R.C.C. Leite, R.S. Moore, S.P.S. Porto, and J.R. Whinnery. Long-transient effects in lasers with inserted liquid samples. *J. Appl. Phys.*, 36(1):3–8, 1965.

[206] C.A. Carter and J.M. Harris. Comparison of single- and dual-beam configurations for thermal lens spectrometry. *Anal. Chem.*, 55:1256–1261, 1983.

[207] C.A. Carter and J.M. Harris. Comparison of models describing the thermal lens effect. *Appl. Opt.*, 23(3):476–481, 1984.

[208] M. Franko and C.D. Tran. Analytical thermal lens instrumentation. *Rev. Sci. Inst.*, 67(1):1–18, 1996.

[209] R.D. Snook and R.D. Lowe. Thermal lens spectrometry - a review. *Analyst*, 120:2051–2068, 1995.

[210] A. Chartier, J. Georges, and J.M. Mermet. Limitation of the thermal-lens method in fluorescence quantum yield measurements. *Chem. Phys. Lett.*, 171(4):347–352, 1990.

[211] J. Georges. Advantages and limitations of thermal lens spectrometry over conventional spectrophotometry for absorbance measurements. *Talanta*, 48:501–509, 1999.

[212] M. Terazima, M. Horiguchi, and T. Azumi. Limitation of absorbance measurements using the thermal lens method. *Anal. Chem.*, 61:883–888, 1989.

[213] A. Kurian, N.A. George, B. Paul, V.P.N. Nampoori, and C.P.G. Vallabhan. Studies on fluorescence efficiency and photodegradation of rhodamine 6G doped PMMA using a dual beam thermal lens technique. *Laser Chem.*, 20(2-4):99–110, 2002.

[214] J.C. de Mello, H.F. Wittmann, and R.H. Friend. An improved experimental determination of external photoluminescent quantum efficiency. *Adv. Mater.*, 9(3):230–232, 1997.

[215] N.C. Greenham. Measurement of absolute photoluminescence quantum efficiencies in conjugated polymers. *Chem. Phys. Lett.*, 241(1-2):89–96, 1995.

[216] L.-O. Pålsson and A.P. Monkman. Measurements of solid-state photoluminescence quantum yields of films using a fluorimeter. *Adv. Mater.*, 14(10):757–758, 2002.

[217] L. Porres, A. Holland, L.-O. Pålsson, A.P. Monkman, C. Kemp, and A. Beeby. Absolute measurements of photoluminescence quantum yields of solutions using an integrating sphere. *J. Fluor.*, 16(2):267–273, 2006.

[218] T. Aimono. 100 % fluorescence efficiency of 4,4'bis[(N-carbazole)styryl]biphenyl in a solid film and the very low amplified spontaneous emission threshold. *Appl. Phys. Lett.*, 86:071110–1–071110–3, 2005.

[219] Y. Kawamura. 100 % phosphorescence quantum efficiency of Ir(III) complexes in organic semiconductor films. *Appl. Phys. Lett.*, 86:071104–1–071104–3, 2005.

[220] A.R. Johnson and S.-J. Lee. Absolute photoluminescence quantum efficiency measurement of light-emitting thin films. *Rev. Sci. Inst.*, 78:096101, 2007.

[221] G.B. Smith and J.B Franklin. US Patent 5548490, 1996.

[222] I. Rudiger and G. Seybold. US Patent 4618694, 1986.

[223] Farbmittel für Kunststoffeinfärbungen. Available from `http://www.functionalpolymers.basf.com/portal/streamer?fid=421644` (last accessed 05/01/10).

[224] F.L. Pedrotti and L.S. Pedrotti. *Introduction to Optics 2nd Edition*. Prentice-Hall, 1993.

[225] S.E. Braslavsky. Glossary of terms used in photochemistry 3rd edition. *Pure. Appl. Chem.*, 79(3):293–465, 2007.

[226] Optical-grade Spectralon material SRM-990 datasheet. Available from `http://www.labsphere.com/data/userFiles/Optical%20Grade%20Spectralon%%20datasheet_1.pdf` (last accessed 12/01/10).

[227] R. Viewveg and F. Esser. *Kunststoff-Handbuch Bd. IX Polymethacrylate*, volume 9. Hanser Verlag, 1975.

[228] O. Rohm. US Patent 2091615, 1937.

[229] O. Rohm. US Patent 2154639, 1939.

[230] R.O. Ebewele. *Polymer Science and Technology*. CRC Press, 2000.

[231] Neil Kirtley (Lucite International). Personal communication, 2009.

[232] J.S. Batchelder. *The Luminescent Solar Concentrator*. PhD thesis, California Institute of Technology, 1982.

[233] P.S. Friedman. LSC Contract Report. Technical report, Owens-Illinois SERI Contract XS-9-8216-1, 1980.

[234] MicroChem NANO^{TM} PMMA resist. Available from `http://www.microchem.com/products/pdf/PMMA_Data_Sheet.pdf` (last accessed 14/01/10).

[235] Metricon Corporation prism coupler instruments. Available from `http://www.metricon.com` (last accessed 14/01/10).

[236] R. Ulrich and R. Torge. Measurement of thin film parameters with a prism coupler. *Appl. Opt.*, 12(12):2901–2908, 1973.

[237] R.T. Kersten. A new method for measuring refractive index and thickness of liquid and deposited thin films. *Opt. Comm.*, 13(3):327–329, 1975.

[238] Artcoe Frisk Film low-tack self-adhesive masking film. Available from `http://www.artcoe.com/frisk-film.html` (last accessed 14/01/10).

[239] K2 Devices, Inc. Available from `http://www.k2cnc.com` (last accessed 14/01/10).

[240] Sherline Products, Inc. Available from `http://www.sherline.com` (last accessed 14/01/10).

[241] Mutronic Präzisionsmaschinen GmbH & Co. KG. Available from `http://www.mutronic.de` (last accessed 14/01/10).

[242] A.R. Burgers, L.H. Slooff, R. Kinderman, and J.A.M. van Roosmalen. Modelling of luminescent concentrators by ray-tracing. In *Proceedings of the 20th EU PVSEC, Barcelona*, pages 394–397, 2005.

[243] M. Carrascosa, S. Unamuno, and F. Agullo-Lopez. Monte Carlo simulation of the performance of PMMA luminescent solar collectors. *Appl. Opt.*, 22(20):3236–3241, 1983.

[244] M. van Gurp and Y. Levine. Determination of transition moment directions in molecules of low symmetry using polarized fluorescence. *J. Chem. Phys.*, 90:4095–4102, 1989.

[245] C. Sánchez, B. Villacampa, R. Cases, R. Alcalá, C. Martínez, L. Oriol, and M. Pinol. Polarized photoluminescence and order parameters of 'in situ' photopolymerized liquid crystal films. *J. Appl. Phys.*, 87:274–279, 2000.

[246] NaREC - New and Renewable Energy Centre, Blyth, U.K. Available from `http://www.narec.co.uk` (last accessed 14/01/10).

[247] M.A. Green, A.W. Blakers, S.R. Wenham, S. Narayanan, M.R. Willison, M. Taouk, and T. Szpitalak. Improvements in silicon solar cell efficiency. In *Proceedings of the 18th IEEE Photovoltaic Specialists Conference*, pages 39–42, 1985.

[248] S.R Wenham. Buried-contact silicon solar cells. *Progress in Photovoltaics*, 1:3–10, 1993.

[249] T.M Bruton, N.B. Mason, and J.G. Summers. Towards production of high-efficiency terrestrial solar cells. In *Proceedings of the 6th International Photovoltaic Science and Engineering Conference*, pages 11–16, 1992.

[250] T.M. Bruton. Fabrication of laser-grooved buried-contact Si solar cells. In *Proceedings of the 1st E.U. International Workshop on Crystalline Silicon Solar Cells*, volume 1, 1994.

[251] S. Narayanan, J. Creager, S. Roncin, R. Rohatgi, and Z. Chen. Process improvements for large area polycrystalline silicon buried-contact solar cell sequence. In *Proceedings of the 1st World Conference on Photovoltaic Energy Conversion, New Jersey, 1984*, pages 1319–1322, 1984.

[252] M. Vivar, C. Morilla, I. Antón, J.M. Fernández, and G. Sala. Laser grooved buried contact cells optimised for linear concentrator systems. *Solar Energy Materials & Solar Cells*, 94:187–193, 2010.

[253] A. Cole, K.C. Heasman, A. Mellor, S. Roberts, and T.M. Bruton. Laser grooved buried contact solar cells for concentration factors up to 100x. In *Proceedings of IEEE 4th WCPEC, Waikoloa, HI*, pages 834–837, 2006.

[254] D.W.K. Eikelboom, J.H. Bultman, A. Schöneker, M.H.H. Meuwissen, M.A.J.C van den Nieuwenhof, and D.L. Meier. Conductive adhesives for low-stress interconnection of thin back-contact solar cells. In *Proceedings of the 29th IEEE Photovoltaic Specialists Conference, New Orleans*, pages 403–406, 2002.

[255] P.C. de Jong, D.W.K. Eikelboom, J.A. Wienke, M.W. Brieko, and M.J.H. Kloos. Low-stress interconnections for solar cells. In *Proceedings of the 20$^{\text{th}}$ European Photovoltaic Solar Energy Conference and Exhibition, Barcelona, Spain*, 2005.

[256] F. Dross, E. Van Kerschaver, and G. Beaucarne. Solar modules of back-contact cells connected with lamination-curing conductive adhesive. In *Proceedings of the 21st EU PVSEC, Dresden*, pages 2143–2145, 2006.

[257] J.H. Bultman, D.W.K. Eikelboom, R. Kinderman, A.C. Tip, C.J.J. Tool, A.W. Weeber, M.A.C.J. van den Nieuwenhof, C. Schoofs, and F.M. Schuurmans. Fast and easy single step module assembly for back-contacted c-Si solar cells with conductive adhesives. In *Proceedings of the IEEE 3rd World Conference on Photovoltaic Solar Energy Conversion, Osaka, Japan*, pages 979–982, 2003.

[258] P.C. de Jong, D.W.K. Eikelboom, R. Kinderman, A.C. Tip, J.H. Bultman, M.H.H. Meuwissen, and M.A.C.J. van den Nieuwenhof. Single step laminated full size PV modules made with back contacted mc-Si cells and conductive adhesives. In *Proceedings of the 19th European Photovoltaic Solar Energy Conference, Paris, France*, 2004.

[259] Ulbrich PV tabbing ribbon specifications. Available from `http://www.ulbrich.com/files/pvribbon09.pdf` (last accessed 24/01/10).

[260] Spire Solar Corporation. Available from `http://www.spirecorp.com` (last accessed 14/04/10).

[261] Keithley Instruments, Inc. basic measurement circuits. Available from `http://www.keithley.com/re/cel` (last accessed 14/01/10).

[262] Q-Lab QUV Accelerated Weathering Tester. Available from `http://www.q-lab.com/QUV.html` (last accessed 14/01/10).

[263] P.F. Conforti and B.J. Garrison. Electronic structure calculations of radical reactions for poly(methyl methacrylate) degradation. *Chem. Phys. Lett.*, 406:294–299, 2005.

[264] T. Mitsuoka, A. Torikai, and K. Fueki. Wavelength sensitivity of the photodegradation of poly(methyl methacrylate). *J. Appl. Poly. Sci.*, 47(6):1027–1032, 1993.

[265] A. Torikai, M. Ohno, and K. Fueki. Photodegradation of poly(methyl methacrylate) by monochromatic light: Quantum yield, effect of wavelengths, and light intensity. *J. Appl. Poly. Sci.*, 41(5-6):1023–1032, 1990.

[266] D.M. Grossman. Q-Lab Technical Bulletin LU-0833: Correlation questions & answers. Available on request from `http://www.q-lab.com` or `http://www.degradable.net/downloads/Q_Panel.pdf` (last accessed 17/01/10).

[267] Q-Lab Corporation "Lab Notes" newsletter, issue 1, pp. 2-4, 2009. Available from `http://www.q-lab.com/EN_Weblit/LabNotes2009_1.pdf` (last accessed 17/01/10).

[268] K.E. Rieckhoff. Self-induced divergence of CW laser beams in liquids - a new nonlinear effect in the propagation of light. *Appl. Phys. Lett.*, 9(2):87–88, 1966.

[269] K.L. Jansen and J.M. Harris. Double-beam thermal lens spectrometry. *Anal. Chem.*, 57:2434–2436, 1985.

[270] D. Magde, J.H. Brannon, T. L. Cremers, and J. Olmsted III. Absolute luminescence yield of cresyl violet. A standard for the red. *J. Phys. Chem.*, 83(6):696–699, 1979.

[271] J.H. Brannon and D. Magde. Absolute quantum yield determination by thermal blooming. Fluorescein. *J. Phys. Chem.*, 82(6):705–709, 1978.

[272] J.R. Whinnery. Laser measurement of optical absorption in liquids. *Acc. Chem. Res.*, 7:225–231, 1974.

[273] D. Magde, R. Wong, and P. Seybold. Fluorescence quantum yields and their relation to lifetimes of Rhodamine 6G and Fluorescein in nine solvents: improved absolute standards for quantum yields. *Photochem. Photobiol.*, 75(4):327–334, 2002.

[274] A. Marcano, H. Cabrera, M. Guerra, R.A. Cruz, C. Jacinto, and T. Catunda. Optimizing and calibrating a mode-mismatched thermal lens experiment for low absorption measurement. *J. Opt. Soc. Am. B*, 23(7):1408–1413, 2006.

[275] M.L. Baesso, A.C. Bento, A.A. Andrade, J.M. Sampaio, E. Pecoraro, L.A.O. Nunes, T. Catunda, and S. Gama. Absolute thermal lens method to determine fluorescence quantum efficiency and concentration quenching of solids. *Phys. Rev. B*, 57(17):10545–10549, 1998.

[276] V. Pilla, T. Catunda, S.M. Lima, A.N. Medina, M.L. Baesso, H.P. Jenssen, and A. Cassanho. Thermal quenching of the fluorescence quantum efficiency in colquiriite crystals measured by thermal lens spectrometry. *J. Opt. Soc. Am. B*, 21(10):1784–1791, 2004.

[277] V. Pilla, L.P. Alves, E. Munin, and M.T.T. Pacheco. Radiative quantum efficiency of CdSe/ZnS quantum dots suspended in different solvents. *Opt. Comm.*, 280:225–229, 2007.

[278] V. Pilla, T. Catunda, H.P. Jenssen, and A. Cassanho. Fluorescence quantum efficiency measurements in the presence of Auger upconversion by the thermal lens method. *Opt. Lett.*, 28(4):239–241, 2003.

[279] V. Pilla, E. Munin, L.P. Alves, and M.T.T. Pacheco. Thermal-lens study of thermo-optical properties of CdSe/ZnS quantum dots embedded into PMMA matrix. In *Proc. SPIE*, volume 6481, pages 648105–1–648105–8, 2007.

[280] V. Pilla, D.T. Balogh, R.M. Faria, and T. Catunda. Thermal-lens study of thermo-optical and spectroscopic properties of polyaniline. *Rev. Sci. Inst.*, 74(1):866–868, 2003.

[281] C.V. Bindhu, S.S. Harilal, V.P.N. Nampoori, and C.P.G. Vallabhan. Solvent effect on absolute fluorescence quantum yield of rhodamine 6G determined using transient thermal lens technique. *Mod. Phys. Lett. B*, 13(16):563–576, 1999.

[282] M. Fischer and J. Georges. Fluorescence quantum yield of rhodamine 6G in ethanol as a function of concentration using thermal lens spectrometry. *Chem. Phys. Lett.*, 260:115–118, 1996.

[283] C.V. Bindhu, S.S. Harilal, G.K. Varier, R.C. Issac, V.P.N. Nampoori, and C.P.G. Vallabhan. Measurement of the absolute fluorescence quantum yield of rhodamine B solution using a dual-beam thermal lens technique. *J. Phys. D: Appl. Phys.*, 29:1074–1079, 1996.

[284] M.L. Lesiecki and J.M. Drake. Use of the thermal lens technique to measure the luminescent quantum yields of dyes in PMMA for luminescent solar concentrators. *Appl. Opt.*, 21(3):557–560, 1982.

[285] J.M. Cariou, J. Dugas, L. Martin, and P. Michel. Refractive index variations with temperature of PMMA and polycarbonate. *Appl. Opt.*, 25(3):334–336, 1986.

[286] S.J. Sheldon, L.V. Knight, and J.M. Thorne. Laser-induced thermal lens effect: a new theoretical model. *Appl. Opt.*, 21(9):1663–1669, 1982.

[287] D. Magde, G.E. Rojas, and P. Seybold. Solvent dependence of the fluorescence lifetimes of xanthene dyes. *Photochem. Photobiol.*, 70:737–744, 1999.

[288] ISS Fluorescence quantum yield standards. Available from `http://www.iss.com/resources/yield.html` (last accessed 14/01/10).

[289] B.C. Rowan, L.R. Wilson, and B.S. Richards. Advanced concepts for luminescent solar concentrators. *IEEE J. Select. Top. Quantum Electron.*, 14:1312–1322, 2008.

[290] P.-S. Shaw, Z. Li, U. Arp, and K.R. Lykke. Ultraviolet characterization of integrating spheres. *Appl. Opt.*, 46(22):5119–5128, 2007.

[291] T.-S. Ahn, R.O. Al-Kaysi, A.M. Muller, K.M. Wentz, and C.J. Bardeen. Self-absorption correction for solid-state photoluminescence quantum yields obtained from integrating sphere measurements. *Rev. Sci. Inst.*, 78:086105, 2007.

[292] F. Wurthner, C. Thalacker, D. Siegmar, and C. Tschierske. Fluorescent J-type aggregates and columnar mesophases of perylene bisimide dyes. *Chem. Eur. J.*, 7:2245–2253, 2001.

[293] F. Wurthner. Perylene bisimide dyes as versatile building blocks for functional supramolecular architectures. *Chem. Commun.*, pages 1564–1579, 2004.

[294] G. Lifante, F. Cusso, F. Meseguer, and F. Jaque. Solar concentrators using total internal reflection. *Appl. Opt.*, 22(24):3966–3970, 1983.

[295] G. Smestad and P. Hamill. Concentration of solar radiation by white backed photovoltaic panels. *Appl. Opt.*, 23(23):4394–4402, 1984.

[296] G. Smestad, H. Ries, R. Winston, and E. Yablonovitch. The thermodymanic limits of light concentrators. *Solar Energy Materials*, 21:99–111, 1990.

[297] J. Roncali and F. Garnier. Photon-transport properties of luminescent solar concentrators: anaylsis and optimization. *Appl. Opt.*, 23(16):2809–2817, 1984.

[298] K. Heidler. Efficiency and concentration ratio measurements of fluorescent solar concentrators using a xenon measurement system. *Appl. Opt.*, 20(5):773–777, 1981.

[299] Marcus Zettl (General Electric). Personal communication, 2009.

[300] F. Galluzzi and E. Scafé. Spectrum shifting of sunlight by luminescent sheets: Performance evaluation of photovoltaic applications. *Solar Energy*, 33(6):501–507, 1984.

[301] E. Yablonovitch. Thermodynamics of the fluorescent planar concentrator. *J. Opt. Soc. Am.*, 70(11):1362–1363, 1980.

[302] Suntech Power "See-Thru" modules. Available from `http://www.suntech-power.com/products/docs/See%20Thru%20Brochure.pdf` (last accessed 29/03/10).

[303] Schott Solar ASI modules. Available from http://www.schottsolar.com/fileadmin/media/sales-services/downloads/product-information/thin-film-modules/data-sheets/english/SCHOTT%20ASI%2095-97-100-103%20EN.pdf (last accessed 29/03/10).

[304] H. Maurus, M. Schmid, B. Blersch, P. Lechner, and H. Schade. PV for buildings: Benefits and experiences with amorphous silicon in BIPV applications. *Refocus*, 5(6):22–27, 2004.

[305] Suntech Power "Light-Thru" modules. Available from http://www.suntech-power.com/products/docs/Light%20Thru%20Brochure.pdf (last accessed 29/03/10).

[306] A. Henemann. BIPV: Built-in solar energy. *Renewable Energy Focus*, 9(6):14–19, 2008.

[307] G. Marsh. BIPV: innovation puts spotlight on solar. *Renewable Energy Focus*, 9(3):62–67, 2008.

[308] J. Benemann, O. Chehab, and E. Schaar-Gabriel. Building-integrated PV modules. *Solar Energy Materials & Solar Cells*, 67:345–354, 2001.

[309] Schott Borofloat 33 datasheet. Available from http://www.schott.com/hometech/english/download/brochure_borofloat_e.pdf (last accessed 29/03/10).

[310] Saint-Gobain "Diamant". Available from http://www.saint-gobain-glass.com/FO/uk/pdf/SGG%20DIAMANT%AE.pdf (last accessed 29/03/10).

[311] Pilkington "Optiwhite". Available from http://www.pilkington.com/resources/optiwhiteanddsjune08.pdf (last accessed 29/03/10).

[312] Saint-Gobain Glass. Personal communication, 2010.

[313] Romag "PowerGlaz" solar modules. Available from http://www.romag.co.uk/~powergla/ (last accessed 04/04/10).

[314] Technal MX Curtain Walling Brochure. Available from http://www.technal.co.uk/downloads.php4 (last accessed 29/03/10).

[315] Neil Kirtley (Lucite International). Personal communication, 2010.

[316] Gilbert Curry Industrial Plastics Co Ltd. Available from `http://www.gcip.co.uk` (last accessed 04/04/10).

[317] Schott Glass. Personal communication, 2010.

[318] Alex Cole (NaREC). Personal communication, 2010.

[319] E.A. Alsema and M.J. de Wild-Scholten. Reduction of the environmental impacts in crystalline silicon module manufacturing. In *Proceedings of the 22nd European Photovoltaic Solar Energy Conference, Milan, Italy*, pages 829–836, 2007.

[320] Technal Ltd. Personal communication, 2010.

[321] Etimex Solar GmbH. Personal communication, `http://www.etimex-solar.com` (last accessed 29/03/10), 2010.

[322] K. Kato, T. Hibino, K. Komoto, S. Ihara, S. Yamamoto, and H. Fujihara. A life-cycle analysis on thin-film CdS/CdTe PV modules. *Solar Energy Materials & Solar Cells*, 67:279–287, 2001.

[323] E.A. Alsema and M.J. de Wild-Scholten. The real environmental impacts of crystalline silicon PV modules: an analysis based on up-to-date manufacturers' data. In *Proceedings of the 20th European Photovoltaic Solar Energy Conference, Barcelona, Spain*, 2005.

[324] CIE standard luminosity functions. Available from either `http://www.cie.co.at/main/freepubs.html` or `http://www-cvrl.ucsd.edu` (last accessed 24/03/10).

[325] A.A. Earp, T. Rawling, J.B. Franklin, and G.B. Smith. Perylene dye photodegradation due to ketones and singlet oxygen. *Dyes and Pigments*, 84:59–61, 2010.